Author:
Wood, Jacob O

Title:
An elusive impurity

studying hydrogen in natural diamonds

An elusive impurity: studying hydrogen in natural diamonds

Jacob O. Wood

Supervisors: Simon C. Kohn & Richard Brooker

A dissertation submitted to the University of Bristol in accordance with the requirements for award of the degree of Doctor of Philosophy in the Faculty of Science

Department of Earth Sciences

14/09/2020

Word Count: 33821

Abstract

Diamonds are a valuable tool for petrologists in order to study the lithospheric mantle. Diamond's unique material properties enable it to act as a record of the conditions within the mantle from which diamonds grow, through mineral inclusions and crystallographic defects within the lattice. One impurity often observed is hydrogen, with the most common form being the N_3VH centre, seen in the IR spectra of many natural diamonds. Despite its ubiquity, it is not well understood. This work initially presents an attempt at quantification of the amount of hydrogen present in natural diamonds and how it relates to the amount of N_3VH. The results suggest that most hydrogen within diamonds is not contained in the N_3VH defect, with the concentrations observed over 20 times higher than predicted using IR alone. High-quality IR and UV-vis line scans are then used to interrogate the effect of hydrogen on the nitrogen aggregation sequence in diamonds, specifically using the concentration of N3, a minor aggregate. This enables generation of proportionality constants within each diamond and suggests that the primary formation mechanism of N_3VH is through direct protonation of N3. A methodology is laid out for studying the availability of hydrogen within diamond-forming fluids through the study of the relative abundance of N3 and N_3VH within a diamond. A minor IR peak at 3236 cm^{-1} is also investigated through comparison with other IR features, and some evidence is found for aggregated nitrogen and platelets in the defect structure.

Covid-19 statement

In late February 2020 I was due to visit the Gemmological Institute at the China University of Geosciences in Wuhan on a research trip to collect UV-vis line scans on 10-20 diamonds (time permitting). This trip did not go ahead due to the travel ban during the Covid pandemic. This work would have contributed to chapter 4. It was possible to send five samples to be studied once the worst of the pandemic had passed, but a significantly larger dataset would have been presented here if not for the pandemic.

In January, test PL experiments were performed with a cold stage installed on the equipment. There were plans to collect a number of targeted measurements on previously studied diamonds at close to liquid nitrogen temperature. This could not be carried out due to lack of access to the lab facilities during the pandemic. These would have contributed to chapter 6, potentially allowing for the investigation of additional PL centres to the ones discussed. As such, it was only possible to include PL measurements taken at room temperature within this thesis.

Author’s declaration

I declare that the work in this dissertation was carried out in accordance with the requirements of the University's Regulations and Code of Practice for Research Degree Programmes and that it has not been submitted for any other academic award. Except where indicated by specific reference in the text, the work is the candidate's own work. Work done in collaboration with, or with the assistance of, others, is indicated as such. Any views expressed in the dissertation are those of the author.

Jacob O. Wood

14/09/2020

Acknowledgements

I would like to wholeheartedly thank everyone who has supported me throughout the duration of this project. My first thanks must go to my primary supervisor, Simon Kohn, who has been exceptionally supportive throughout what has not always been an easy project for either of us. His guidance, responsiveness and intelligence have helped me form a project that I feel I can be proud of. Alongside Simon, Richard Brooker has been there whenever needed, and I thank him for his support.

I would like to thank David Fisher of De Beers and Galina Bulanova for the provision of samples during this work. I am also grateful to EPSRC and De Beers Technologies for the provision of financial support.

Thanks are also due to other members of the diamond group, in particular Laura Speich for helping to train me on various pieces of equipment, and allowing me to learn how to approach life as a PhD researcher. Alongside is the invaluable support of everyone in G9, especially Ailsa Naismith and George Rowland, for making the work environment one I enjoyed being in. I also must thank the numerous other PhD students in the department for many enjoyable lunch discussions and pub trips, and also my friends from the Diamond CDT in Warwick for making me feel part of a scientific community.

Finally, to my friends (Shakey in particular for putting up with me as a flatmate for 4 years), family and to Molly. I couldn't have done this without the love and support from everyone around me, and I will be forever grateful.

Table of contents

List of tables

List of figures

5.4 Graphs showing the relationships between 3107 cm^{-1} peak intensity against the 2786 cm^{-1} and 3236 cm^{-1} peak intensities for the single spectra

5.5 Plots displaying I(3236 cm^{-1}) (cm^{-2}) against nitrogen related features for the Argyle line scans

5.6 Plots displaying log(3236/3107) against nitrogen related features for the Argyle line scans

5.7 A plot of the 3107 cm^{-1} vs. 3236 cm^{-1} peak intensity for the Argyle line scans

5.8 Plots of the platelet related features against I(3236 cm^{-1}) (cm^{-2}) for the Argyle line scans

5.9 Plots of the platelet related features against log(3236/3107) for the Argyle line scans

5.10 Plots displaying I(3236 cm^{-1}) (cm^{-2}) against nitrogen related features for the Diavik line scans

5.11 Plots displaying log(3236/3107) against nitrogen related features for the Diavik line scans

5.12 A plot of the 3107 cm^{-1} vs. 3236 cm^{-1} peak intensity for the Diavik line scans

5.13 Plots of the platelet related features against I(3236 cm^{-1}) (cm^{-2}) for the Diavik line scans

5.14 Plots of the platelet related features against log(3236/3107) for the Diavik line scans

5.15 The spatial variation of the IR features against I(3236 cm^{-1}) (cm^{-2}) for the Argyle line scans

5.16 The spatial variation of the IR features against log(3236/3107) for the Argyle line scans

5.17 The spatial variation of the IR features against I(3236 cm^{-1}) (cm^{-2}) for the Diavik line scans

5.18 The spatial variation of the IR features against log(3236/3107) for the Diavik line scans

1. Introduction and background

1.1 Why study diamond?

Diamonds have long fascinated humanity due to their brilliance as a gemstone. There is a global production of ca. 150 million carats of rough diamonds per year, with a global demand of US $76 bn for diamond jewellery and polished diamonds in 2018 (De Beers Group, 2019). Aside from their gemmological interest, diamond also displays a wide array of extreme material properties. These properties include the highest thermal conductivity of any solid, at ~ 2000 W m^{-1} K^{-1} (five times higher than that of copper), as well as a high refractive index ($\eta \approx 2.4$ compared to ~ 1.5 for glass) and a range of optical transparency that extends from the ultraviolet (UV) to the far infrared (IR) (Field, 1992) – the latter two, along with high dispersion, are the reason for the striking appearance of cut gem-quality diamonds. This unique set of properties has led to intense focus on diamond for technological applications and a wide array of research areas. With the advent of synthetic diamonds via high-pressure high-temperature (HPHT) (Bundy et al., 1955) and later chemical vapour deposition (CVD) (Ashfold et al., 1994) came the capability to tailor the properties of diamonds to fit numerous applications. These range from diamond as a Raman laser (Nikkinen et al., 2018) to electrodes for sensing (Hutton et al., 2013; Read et al., 2019) and even through to potential quantum computing applications using the nitrogen-vacancy defect as a qubit (Chen et al., 2019; Jelezko et al., 2004).

Natural diamonds have provided a valuable source of information on the geological history of Earth processes, due to their range of deep mantle origins and ages ranging back throughout Earth history (Harris et al., 1997). They have long been studied as unique records of conditions within the Earth.

Along with its well-known exceptional hardness – diamond represents the top of the Mohs scale of mineral hardness with a value of 10 – diamond is unique as a material due to its resistance to changes in its environment from a chemical standpoint. Brought to the surface by fast-moving kimberlite and lamproite magmas as xenocrysts, diamond's unique properties

enable it to remain chemically unchanged well outside its high-pressure stability field, despite the volatile-rich nature of these magmas. Whilst xenoliths are often highly altered by mantle metasomatism and transportation to the surface of the Earth, individual diamonds can preserve a significant amount of information about the conditions from which they were grown, and their subsequent residence within the mantle.

Information stored within the diamond tends to be studied in two main ways: by the composition of mineral inclusions captured during the growth of the crystals, or through the properties and characteristics of the host diamond lattice itself – including the lattice defects that are the subject of this thesis. Whilst there has been significant development in the study of inclusions, both mineral (Stachel et al., 2005; Thomson et al., 2016) and fluid (Klein-BenDavid et al., 2007; Smith et al., 2015) in nature, there is still a significant amount of information yet to be gleaned from more detailed studies of the diamonds themselves.

1.1.1 Diamond formation and geological setting

Diamond hosted in kimberlite was first discovered in South African deposits in the early 1870s. Initially, diamond formation was linked to reactions of the kimberlite magmas that bring diamonds to the surface with carbonaceous shale fragments. This would make diamond a high-pressure phenocryst within the kimberlite (Lewis, 1887). Although there was evidence of a xenocrystic origin as early as 1899, based upon the observation of diamondiferous eclogite xenoliths (Bonney, 1900), this phenocryst theory was widely accepted until geochemical studies of inclusions and radiometric dating of diamond became prevalent. These both provided evidence of crystallisation in the Earth's mantle, unrelated to the magmatism of the kimberlite within which the diamonds were hosted (Kramers, 1979; Sobolev et al., 1969). Once it had been recognised that diamond was a mantle-derived xenocryst, the concept emerged of its formation via redox reactions occurring during a melt or fluid traveling through the mantle host rock (Rosenhauer et al., 2019; Taylor and Green, 1986). This means that diamond is now

considered to be a metasomatic mineral (Stachel and Harris, 1997), although the exact nature of the fluids or melts from which diamonds precipitate is poorly understood. There is much to be learned about the composition or redox character of these fluids, making further study crucial in order to further constrain these mantle conditions.

The mineralogy of the rocks in which diamond is hosted in the mantle is well characterised from studies of the mineral inclusions (Shirey et al., 2013; Stachel and Harris, 2008). Results from these studies suggest that diamonds are derived from two locations: the first, and most common, of these is the subcontinental lithospheric mantle (this reaches depths at which diamond is stable at around 200 km deep) (Boyd and Gurney, 1986), or, more rarely from the sublithospheric mantle at depths of up to 700 km (Harte, 2010, 1994; Stachel et al., 2005). These sublithospheric diamonds consist of less than 1 % of global diamond production by mass (Stachel and Harris, 2008). A schematic of the geological setting for diamond formation and ascent to the surface is provided in figure 1.1 (Shirey et al., 2013).

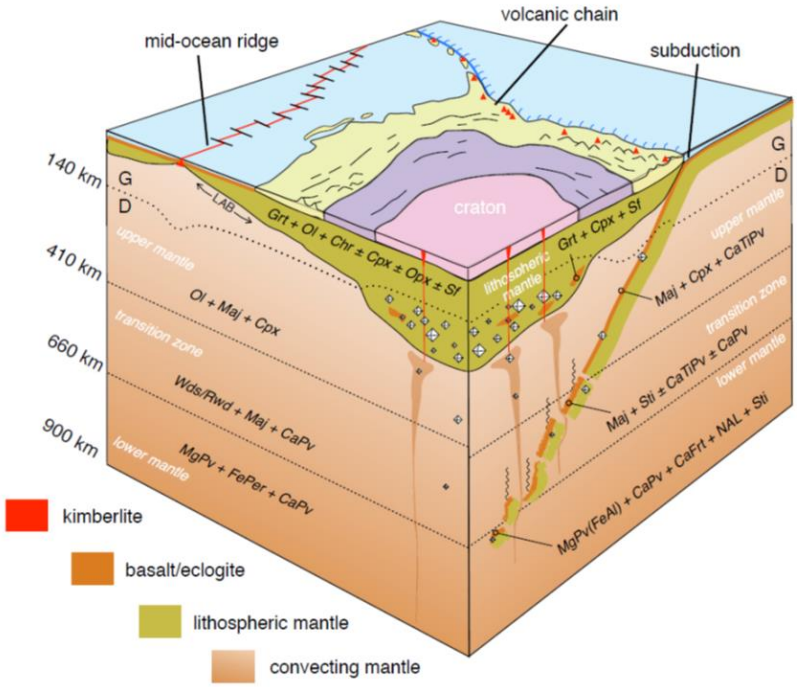

Figure 1.1: A schematic showing the geological setting for the formation of diamonds, with the relationship between the craton, lithospheric mantle keel and diamond stable regions within, along with the convecting mantle. G is graphite, D is diamond and LAB is the lithosphere/asthenosphere boundary. Diagram from Shirey et al., 2016 (mineral assemblage information and abbreviations can be found within).

According to the mineral inclusions present, diamonds from the lithospheric mantle can be divided into 3 suites or parageneses: i) peridotitic (65 % of all diamonds), ii) eclogitic (33 %) and iii) websteritic (2 %) (Stachel and Luth, 2015). The 33 % of diamonds from eclogitic sources greatly exceeds the estimated 1 – 5 % abundance by volume of eclogite within the lithospheric mantle beneath cratons (Dawson and Stephens, 1975) This may suggest that eclogite is a preferred substrate for the growth of diamond (Grütter et al., 2004), and that this paragenesis has some genetic significance. This is supported by the observation of different carbon isotope fractionation in diamonds of peridotitic and eclogitic parageneses (Gurney, 1986). Peridotitic diamonds have been observed to display a narrow range of $\delta^{13}C$ values (Deines et al., 1984), meaning that diamonds found to be either isotopically heavy or light can be considered as of eclogitic or unknown paragenesis.

The robust and inert nature of diamonds suggest that they can provide a closed system. This means that isolated single-phase mineral inclusions within diamonds (known as non-touching

inclusions) are assumed to have remained unchanged since their encapsulation within the diamond crystal, in the absence of visible exsolution features. There are some exceptions where disequilibrium has been observed in inclusions incorporated in environments with significant chemical evolution (Bulanova, 1995). The pressure-temperature conditions under which diamond is formed are primarily calculated from a number of geothermobarometers, using data from the silicate inclusions. Within the region at which diamond is stable and at temperatures of over 1000 °C, diamond is capable of conveying changes in the ambient pressure of its growth medium to included minerals via plastic deformation (De Vries, 1975). This means that the minerals included will re-equilibrate with the surroundings if changes in the pressure-temperature conditions occur, and so they can be considered to reflect the conditions under which the diamond is stored within the mantle. Two primary geothermobarometers can be considered as appropriate to a relatively large amount of inclusions for peridotitic diamonds: a combination of an Al exchange barometer (Brey and Köhler, 1990) and a Mg-Fe exchange thermometer (Harley, 1984) can be used for pairs of garnet and orthopyroxene inclusions, and a single crystal geothermobarometer for clinopyroxene inclusions (Nimis and Taylor, 2000). Based on 157 independent estimates using these geothermobarometers to study lithospheric diamonds (Stachel and Luth, 2015), the average peridotitic diamond is derived from 5.3 ± 0.8 GPa and 1130 ± 140 °C. For eclogitic diamonds, the most widely used thermometer is one using garnet-clinopyroxene Mg-Fe exchange (Krogh, 1988). A reliable barometer does not currently exist for mantle eclogites and the corresponding eclogitic inclusions in diamond. It has therefore been assumed that these diamonds form at similar pressures to those of peridotitic origin (Abbott, 2018; Nimis and Grütter, 2010). A previous study examined 144 garnet-clinopyroxene pairs using this method, with an average temperature produced of 1170 ± 110 °C (Stachel and Luth, 2015). This is in excellent agreement with temperatures derived from 164 pairs of garnet and olivine inclusions in peridotitic diamonds (O'Neill and Wood, 1979), the

study of which yields a mean derivation of 1160 ± 110 °C. This agreement suggests that peridotite and eclogite hosted diamonds originate from the same source within the diamond stable region of the lithospheric mantle.

1.1.2 Diamond-forming processes

There are a variety of proposed processes in the mantle which might lead to diamond formation. These include precipitation from a carbon-rich fluid or melt, or via redox reactions involving species derived from carbonate or methane. Alongside this is the potential direct conversion of graphite to diamond, although without the presence of a solvent or catalyst this requires overcoming of a significant activation energy; experiments have shown that temperatures and pressures exceeding 12 GPa and 1800 °C are required to undergo this reaction (Irifune et al., 2004). Industrial syntheses of diamond use nickel, iron or cobalt melts as growth media in order to precipitate diamond out of solution, and it is possible that melts such as these could account for diamond growth within the mantle. Below ca. 250 km it appears that conditions are reducing enough to stabilise the presence of metal, whereas at shallower depths, the conditions are typically too oxidised (Frost and McCammon, 2008). There is currently no evidence for the ability of elemental carbon to dissolve in silicate or carbonate melts. This suggests that diamond precipitation requires a redox reaction to take place. This could potentially involve the reduction of an oxidised carbon species such as CO_2 or CO_3^{2-}, along with the alternative of oxidation of a reduced carbon species, for example methane.

Discussion of the redox conditions of diamond-forming processes normally uses the concept of oxygen fugacity (fO_2), which is a representation of the partial pressure of oxygen present in an environment available for reaction with other redox-active elements that are capable of existing in a number of valence states. This concept originates from the use of oxygen buffers to control the oxygen content and availability in early petrological experiments (Eugster, 1957), such as the following:

$$2x\ Fe + \ O_2 \ \rightleftharpoons 2\ Fe_xO\ (iron - w\ddot{u}stite; IW) \quad (1.1)$$

$$4\ Fe_3O_4 + \ O_2 \ \rightleftharpoons 6\ Fe_2O_3\ (magnetite - hematite; MH) \quad (1.2)$$

$$3\ Fe_2SiO_4 + \ O_2 \ \rightleftharpoons 2\ Fe_3O_4 + 3\ SiO_2\ (fayalite - magnetite - quartz; FMQ) \quad (1.3)$$

An equilibrium expression can then be written for these reactions, and, using the standard free energy for the reaction, an expression for fO_2 (conventionally represented as $\log_{10}(fO_2)$) can be produced and related to the activity of the components (a), such as for the magnetite-hematite (MH) system:

$$logfO_2(MH) = \frac{\Delta_r G^0}{2.303RT} + 6\ loga_{Fe_2O_3} - 4\ loga_{Fe_3O_4} \quad (1.4)$$

The temperature dependence can be discounted through the use of a reference reaction, most commonly the fayalite-magnetite-quartz (FMQ) reaction, giving

$$\Delta \log fO_2\ (FMQ) = \log fO_2\ (sample) - \log fO_2\ (FMQ) \quad (1.5)$$

These buffer reactions also have a degree of pressure dependence. This dependence must also be considered while using values of $\Delta logfO_2$, especially where a compressible, volatile species is involved. Evidence alluding to the oxidation state of the mantle in regions in which diamond is stable comes from a number of sources. The most commonly used are garnet-bearing peridotites, which can accommodate Fe^{2+} and Fe^{3+} to variable extents, most notably in garnet and pyroxenes. Reactions involving these minerals can be used as 'oxybarometers' (Luth et al., 1990). The oxygen fugacity of the mantle is consistent with the presence of a metasomatic liquid dominated by one of an H_2O- or silicate-rich melt (Stagno et al., 2013). It has been determined through study of a large body of xenolith samples from the diamond stability field that the ambient cratonic lithosphere likely has a low enough fO_2 that carbon can exist as diamond (Shirey et al., 2013). The highest oxygen fugacity – and therefore most oxidising conditions – that diamonds can be stable is represented by the enstatite-magnetite-olivine-

diamond (EMOD) buffer, at which diamond becomes stable over magnesite or carbonate in peridotitic assemblage. Without the presence of olivine, diamond could potentially coexist at higher fO_2 values with fluids richer in CO_2. At low oxygen fugacities the potential for diamond growth is inhibited by the presence of metallic Fe, and subsequent dissolution of carbon into the metal (Luth and Stachel, 2014). Whilst these buffers represent well-defined places in P-T-fO_2 space, they present some difficulty for the study of diamonds due to the lack of touching inclusions present in the majority of samples.

1.1.3 Carbon and hydrogen speciation in the mantle

Some carbon bearing fluids within the mantle can be considered as part of the C-O-H system, which comprises mixtures of species such as H_2, H_2O, CO, CO_2, CH_4, O_2 and C_2H_6. These can play significant roles in a wide variety of geologically significant processes, from fluid-rock interactions (McCollom and Shock, 1998) through to mantle melting (Dasgupta and Hirschmann, 2010; Eggler, 1983; Watson and Brenan, 1987) and magma degassing (Wallace, 2003). A number of thermodynamic modelling studies have been undertaken alongside high pressure high temperature experiments in an attempt to predict the compositions of these fluids and model their behaviour (Sokol et al., 2004; Zhang and Duan, 2009). Some of the results are displayed in figure 1.2. It can be seen that fluids coexisting with diamond can have a variety of properties. Under reduced conditions, the fluids would be CH_4-rich. At the 'water maximum' the fluids would be almost pure H_2O. At the highest oxygen fugacity under which diamond would be stable (EMOD), the fluids would be a water-rich mixture of CO_2 and H_2O. However, it must be noted that such a fluid would likely interact with the host peridotite or eclogite and lead to a saline melt. The idea of diamond formation through carbonate-bearing high-density fluids is corroborated through the observation of saline fluid inclusions within diamonds from a variety of localities (Jablon and Navon, 2016; Krebs et al., 2019; Weiss et al., 2015).

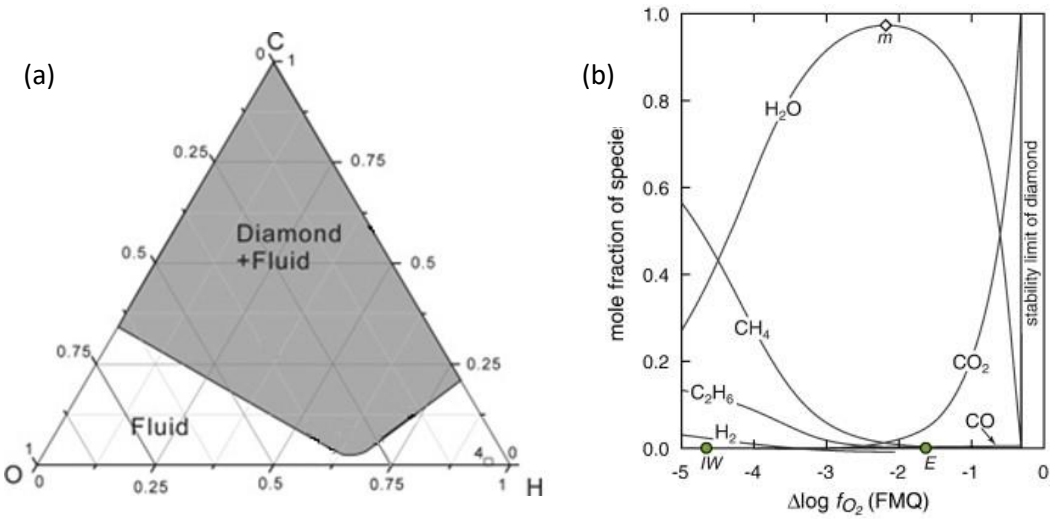

Figure 1.2: (a) Diamond crystallisation in the C-O-H fluid system, displaying data from experiments and calculations at 1693.15 K and 5.7 GPa. The curve displayed represents the carbon saturated line generated through calculations. Diagram adapted from Zhang and Duan, 2009. (b) The speciation of C-O-H fluids in equilibrium with diamond, plotted as a function of $\Delta logfO_2$. The diamond 'm' represents the 'water maximum' and the vertical line labelled 'stability limit of diamond' on the right of the diagram is representative of the reaction $C + O_2 \rightleftharpoons CO$. This reaction defines the highest oxygen fugacity at which diamond is stable in this system. Diagram from Stachel and Luth, 2015.

Some evidence for diamond formation from methane-rich fluids with a reduced oxidation state is that the ambient fO_2 of the lithospheric mantle at depths below ~ 150 km lies below an fO_2 capable of supporting CO_2-rich fluids (Frost and McCammon, 2008). Along with this comes the observation of some diamonds exhibiting fluid inclusions containing $CH_4 \pm H_2$, which can be interpreted as direct evidence of the role methane may play in some instances of diamond formation (Smit et al., 2016a; Smith et al., 2018). It must also be noted that fluid inclusions in diamonds are often observed to contain precipitated carbonates (Izraeli et al., 2004, 2001). Recent experimental work has provided further suggestions of the viability of diamond growth from such reduced methane-rich fluids (Matjuschkin et al., 2020). In this study, the diamond crystallisation was not related to a significant change in redox state, instead forming from processes such as interactions between H_2 and olivine and pyroxene, along with graphite 'etching'. The implication of this study suggests that CH_4-rich fluids could be more common than is often believed. They may also represent a significant source of carbon for diamond formation in the mantle. Alongside this, the associated H_2 present is believed to hold an important role in diamond forming processes.

Under the reduced conditions within the mantle, hydrogen is likely not present in an oxidised form as H_2O, but instead as H_2. Retention of this hydrogen may then only be possible via the direct dissolution of H_2 into mantle minerals. Studies on He solubility in olivine suggested this may not be implausible (Parman et al., 2005). Further studies on olivine, orthopyroxene, clinopyroxene and garnets have demonstrated that molecular H_2 does indeed have an appreciable solubility in these mantle minerals (Yang et al., 2016). It has also been demonstrated that water and molecular hydrogen are immiscible within the mantle through the generation of synthetic fluid inclusions in olivines (Bali et al., 2013). This could potentially offer an explanation as to why magmas generated from the lower mantle contain significant amounts of hydrogen, despite the fact that minerals derived from this region are almost completely anhydrous.

As the experimental and observational evidence suggests that diamond forming fluids are oxidised, whereas the ambient mantle is very reduced, it must be considered where the oxidised material is derived from. The likeliest source is through subduction, whereby oxidised material from the surface is brought down to deeper within the Earth.

1.1.4 Water in the mantle

The cycling of water throughout the exosphere and the different reservoirs in the mantle is a critical process when it comes to the description and understanding of the Earth's geochemical evolution. Despite this, the exact distribution of H_2O and the mechanisms of the transport of water between the different reservoirs still require further examination. An example of this is the uncertainty in the total amount of H_2O stored in the mantle. Estimates produced have ranged from roughly a quarter of an ocean mass (the total mass of H_2O in the world's oceans) to ca. 4 ocean masses (Ahrens, 1989; Bolfan-Casanova, 2005; Bolfan-Casanova et al., 2000; Hirschmann, 2006; Jambon and Zimmermann, 1990). H_2O storage in the mantle can take place in the form of solid, H_2O-containing minerals, or it can be present in the form of hydrous fluids

or melts; the latter are crucial when it comes to mass transfer and differentiation within the mantle. Figure 1.3 displays a schematic of areas in which hydrous melting may occur in the mantle (Hirschmann, 2006). The right of the diagram presents a representation of the total storage capacity by depth, with gradually increasing H_2O storage capacity with depth until the discontinuity at 410 km. The capacity within the transition zone is much higher, and the lower mantle below 670 km has a significantly lower storage capacity than the rest of the mantle.

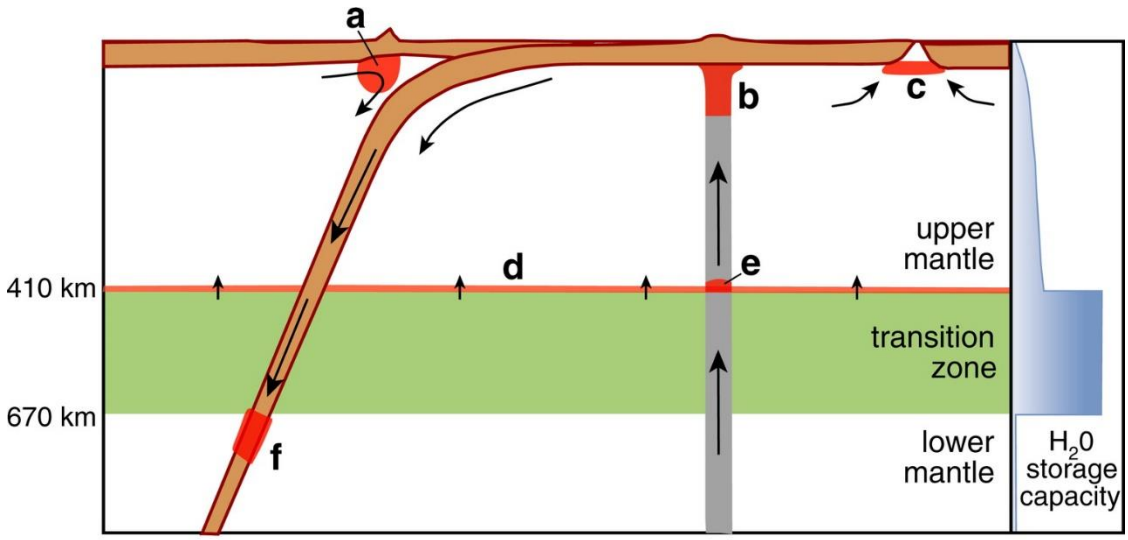

Figure 1.3: A schematic displaying theorised regions of hydrous melting in the mantle (a) melting triangular shaped regions of mantle above areas of subduction, (b) melting in deep oceanic island basalts, (c) melting in the deeper portions of mid ocean-ridge basalt source regions, (d) melting in regions above the discontinuity at 410 km, (e) melting above the 410 km discontinuity, situated in localised upwellings, and (f) melting below the discontinuity at 670 km in downwellings. The section on the right shows an illustrative image of the variation of storage capacity with depth. Diagram from Hirschmann, 2016.

The predominant phase in the upper mantle (above the transition zone at 410 km) is olivine, and the H_2O storage capacity is well-characterised for mantle phases (Demouchy and Bolfan-Casanova, 2016). Olivine storage capacity was originally found to increase significantly with water fugacity (and thereby with depth) by Kohlstedt et al., with their studies showing an increase from ~ 25 ppm at a depth of 10 km to ~ 1300 ppm at 410 km (Bai and Kohlstedt, 1993; Kohlstedt et al., 1996). Later work then lead to an increase in these values by a factor of 3-3.5 after a reconsideration of the analytical techniques involved in the analysis and a comparison between the relevant infrared and SIMS analyses (Bell et al., 2003; K. Koga et al., 2003). Storage capacities for other upper mantle assemblages such as pyroxene and garnet are not as

well characterised as that of olivine. However, it has been observed that at low pressure the storage capacity of pyroxene is significantly higher than in olivine (Aubaud et al., 2004). This suggests that pyroxene is likely the main host of water in the upper mantle, although it is not known whether or not this is the case at depth. If this is indeed the case, then the H_2O storage capacity of the lower regions of the upper mantle could reach up to 1 % (Hirschmann et al., 2005).

Studies of diamond have provided some valuable information when it comes to the study of water in the mantle, due to the possibility of observing hydrous mineral inclusions (those with water bound within the crystal structure of the mineral). For example, there has been some evidence of aqueous fluid deep in the mantle in the transition zone with the observation of ice-VII inclusions in diamonds sourced from this depth (Tschauner et al., 2018). This ice is thought to have crystallised upon ascent as a residue of aqueous fluid present during the growth of the diamond, which points to the potential existence of fluid-rich areas within the transition zone. There are also limited observations of hydrous ringwoodite inclusions observed within super deep diamonds that suggest of the existence of deep water within the transition zone, potentially constraining on the ascension rate of diamond from depths of at least 525 km (Nestola and Smyth, 2016; Pearson et al., 2014). Aside from inclusions, hydrogen within the diamond lattice is another potential indicator of the water content in the deep mantle and is the focus of this thesis. Information gleaned from the study of hydrogen could be applied to a wide array of samples due to its ubiquity in the IR spectrum, and could lead to the ability to study variations across different localities.

1.2 Defects in diamond

1.2.1 The mechanism of diamond growth and the incorporation of defects

Most natural diamonds are thought to crystallise in layer-by-layer mechanisms. This leads to zoned internal growth structures which can be complex, containing any number of different

growth zones, from the most common octahedral growth, to non-faceted growth on curved surfaces. The latter averages out to a mean orientation defined by simple indices, termed as 'cuboid growth'. Alongside this are also dissolution and overgrowth features (Bulanova, 1995). The zonation found in diamonds contains valuable information regarding the geological history of the crystal, with spatial variation in isotopic composition (Thomson et al., 2014) and infrared absorption features (Kohn et al., 2016; Palot et al., 2013) commonly being observed.

A pure diamond, while valuable to gemmologists, is less interesting to geologists. An imperfect diamond can be thought of as a record, with the imperfections observed providing a wealth of information about the growth history of individual crystals. Infrared features observed in diamonds often arise from defects within the crystal structure, which are one way in which the crystals can retain information from the growth environment during diamond growth. Lattice defects can take two primary forms, the first being point defects. These are defects that occur at or around a single point within the crystal lattice. There are also extended defects, such as stacking faults (Lang, 1974a) and dislocations (Hanley et al., 1977; Lang, 1977), which exist as larger-scale defects within the lattice. Due to the strong C-C bonds and small interatomic spacing in the diamond lattice, the incorporation of foreign elements should be difficult, with the most common impurities being smaller elements such as boron, nitrogen and hydrogen. The latter is the focus of this thesis. Point defects can be investigated using optical spectroscopy techniques such as photoluminescence (PL) or Fourier-transform infrared (FTIR) spectroscopy, and variations in the spectroscopic features can be used to investigate differences within single samples, or to detect variations between populations of diamonds from differing localities or of different types.

1.2.2 Nitrogen in diamond

Nitrogen is the most abundant and well-studied impurity in natural diamonds, and can be present in quantities of up to 3500 ppm (Cartigny, 2005). Absorption peaks in the FTIR

spectrum of diamond were first related to nitrogen in the 1950s (Kaiser and Bond, 1959), and, over time, an aggregation sequence of diamond was determined.

The simplest mechanism for nitrogen incorporation into diamond is as single nitrogen atoms substituted into the lattice for carbon atoms during growth (Dyer et al., 1965), forming defects known as C-centres. Under typical mantle temperatures, these single nitrogen atoms are mobile, and migrate within the lattice to form pairs of nitrogen atoms occupying neighbouring lattice sites known as A-centres (Davies, 1976). In natural diamonds, this reaction continues to completion at typical mantle conditions over geological timescales. This means that the majority of, but not all (Hainschwang et al., 2006), natural samples do not contain measurable amounts of C-centres, although they are common in synthetic HPHT diamonds due to their high nitrogen content (Collins, 2001; Reinitz et al., 2000). The A-centre pairs can then aggregate further to form groups of four nitrogen atoms around a carbon vacancy (Bursill, 1983), known as B-centres. The structure of these is displayed in figure 1.4. These IR-active defects have been studied in great detail to develop the quantification of defect concentrations (Boyd et al., 1995, 1994). In addition, the kinetics of the interconversions between these species has become the intense focus of much research (Chrenko et al., 1977; Evans and Qi, 1982).

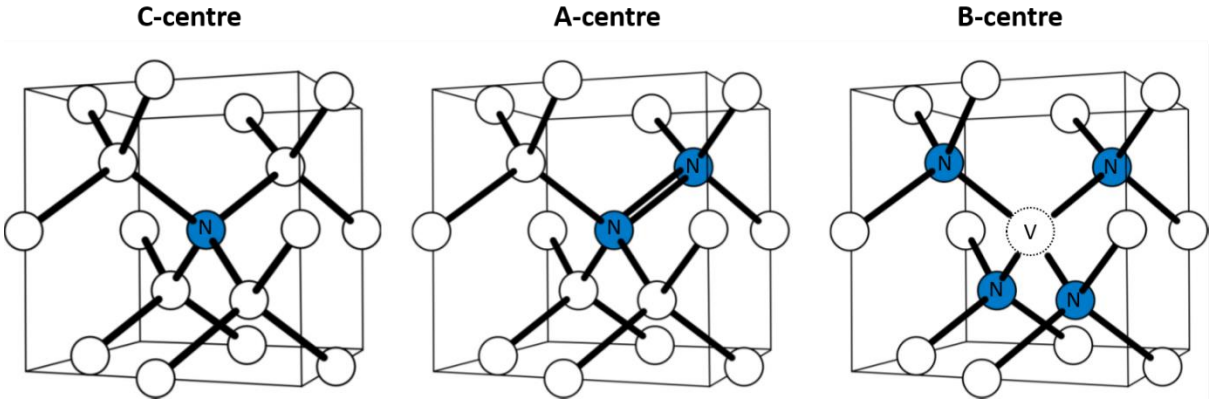

Figure 1.4: Schematic models of the three most common nitrogen aggregates in diamond. White is carbon, the blue atoms represent nitrogen atoms and the dashed circle is a vacancy. The aggregates are displayed in the order of the nitrogen aggregation sequence, from single substitutional nitrogen (C-centres), to nitrogen pairs (A-centres) through to four nitrogen atoms around a vacancy (B-centres). These centres are all IR-active.

Alongside these three major aggregates are a number of other IR inactive nitrogen containing species, for example the N3 centre, which consists of a trio of substitutional nitrogen atoms around a vacancy (Zaitsev, 2013). Species such as this are thought to be in minor abundance when compared to the other aggregates (Kiflawi and Bruley, 2000). The N3 centre and its role in the nitrogen aggregation sequence will be discussed in greater detail in chapter 4. The final population of aggregation states achieved within a diamond is more dependent on temperature than time. This means that, for a diamond with a known formation age and a known time at which the diamond was exhumed (kinetically frozen), the aggregation state can function as a geothermometer and provide a temperature history of the crystal's residence within the mantle (Evans and Harris, 1989; Kohn et al., 2016).

Diamonds have long been classified according to the presence (or, indeed, absence) of impurities within the crystal (Robertson et al., 1933). The ubiquitous system classifies individual samples based on the existence of nitrogen and/or boron defects within the stone (Breeding and Shigley, 2009), and is presented in figure 1.5. Type I diamonds contain nitrogen, whereas type II diamonds do not have a measurable amount of nitrogen present. Type I diamonds are further divided into type Ia and Ib. Type Ia comprises the majority of natural

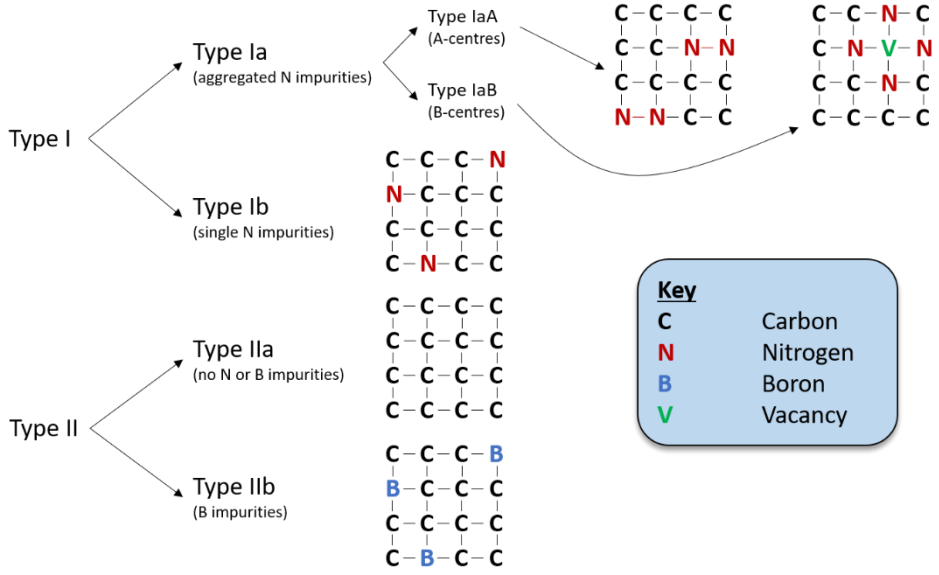

Figure 1.5: A schematic of the type classification system for diamonds, based on the presence or absence of boron and nitrogen defects.

diamonds and contains nitrogen in its aggregated forms. This may be further split into type IaA and IaB classifications, used to distinguish between those with majority A centres and B centres respectively. Type Ib contain non-aggregated nitrogen in the form of C-centres. These type Ib stones rarely occur naturally but are common amongst synthetic samples. Type II diamonds are similarly subdivided into type IIa, consisting of diamonds that are entirely free from impurities, and type IIb, which comprises diamonds that contain substitutional boron as an impurity.

The three major nitrogen aggregates in diamond are all IR-active, with their characteristic absorption spectra having known shapes and an intensity that is dependent on the concentrations of the defects present (Mendelssohn and Milledge, 1995). The absorption at 1282 cm^{-1} was initially discovered to be proportional to nitrogen concentration in diamonds using combustion techniques combined with mass spectrometry (Kaiser and Bond, 1959). However, nitrogen contained within different species can also contribute to this intensity. In order to obtain concentrations of the underlying defects, the spectrum must be decomposed into several overlapping components, which are displayed in figure 1.6, along with the D feature, which is related to platelets (see Section 1.2.3).

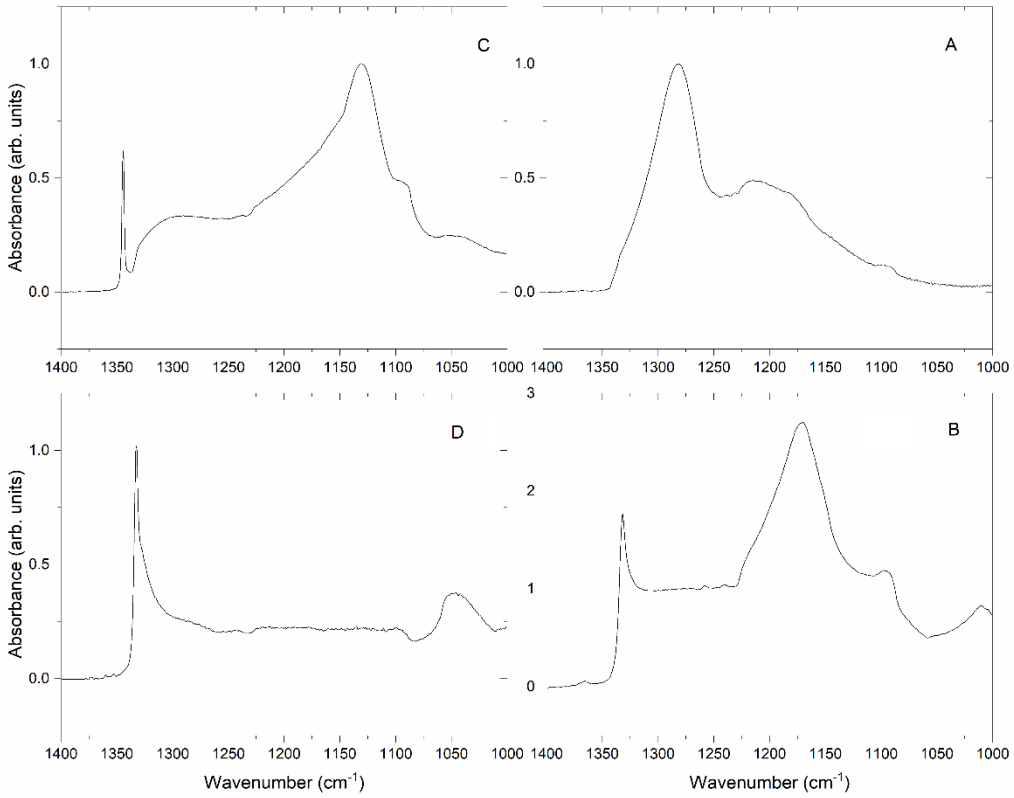

Figure 1.6: IR absorption spectra of the most common nitrogen-bearing defects in diamond (as displayed in figure 1.4) along with the D feature, related to platelets. Data is taken from the CAXBD Excel spreadsheet (D. Fisher, De Beers Technologies, Maidenhead)

The deconvolution of IR spectra was first undertaken in 1981 using spectra of diamonds dominated by either A- or B- centres (Davies, 1981), although it was later found that an additional component, known as the D component, was necessary in order to successfully model the observed range of data in diamonds. This D component has since been attributed to platelets (Woods, 1986) – these will be discussed in section 1.2.2 and in chapter 5.

Once decomposed, the relationship between the absorption intensity and the concentration of the defect responsible can be used to measure defect concentrations. This relationship can be described using an extinction coefficient, usually termed *k*, in the following form

$$c = k.\mu \tag{1.6}$$

Where c is the concentration of the defect and μ is the absorption coefficient measured at a specific wavenumber. The values of this extinction coefficient used within this thesis are as follows

$$k_C(1330\ cm^{-1}) = 25.0\ \pm 2\ {}^{ppm}/_{cm^{-1}} \tag{1.7}$$

$$k_A(1282\ cm^{-1}) = 16.5\ \pm 1\ {}^{ppm}/_{cm^{-1}} \tag{1.8}$$

$$k_B(1282\ cm^{-1}) = 79.4\ \pm 8\ {}^{ppm}/_{cm^{-1}} \tag{1.9}$$

For k_C this is derived from Kiflawi et al., 1994 and k_A and k_B are from Boyd et al., 1994. The comprehensive procedure used for spectral deconvolution is provided in chapter 2.

1.2.3 Platelets

Platelets are amongst the most commonly observed impurities in natural diamonds and take the form of extended planar defects containing nitrogen in aggregated forms. They are frequently observed in FTIR studies of natural diamonds (Bulanova et al., 2018; Speich et al., 2018, 2017), but despite this, their formation at high temperatures is not fully understood. Current understanding is that platelets are formed of a thin layer of carbon interstitials in the {100} plane (J P Goss et al., 2003; Humble, 1982). This suggests that nitrogen is not a fundamental component of the platelet structure, but can instead be considered an impurity (Speich et al., 2018). Proposed formation mechanisms are varied. One is the potential release of interstitials during the formation of B-centres, which could lead to platelet formation (Woods, 1986). Ab initio calculations have also suggested that the most favourable mechanism is through the production of vacancies. The vacancies are subsequently trapped by A-centres, forming VN_2, and then B-centres by trapping another A-centre (J P Goss et al., 2003). These mechanisms are quite different, but both highlight the links between platelet formation and the nitrogen aggregation sequence.

Comprehensive studies of the relationship between the most prominent IR feature (referred to as the B' peak) and IR features related to the presence of nitrogen aggregates shows that most diamonds exhibit a positive linear correlation between the B-centre absorption and the integrated B' peak (Woods, 1986). There is a variation in peak width and symmetry that is probably a result of the relationship between average platelet radius and position of the platelet peak (Clackson et al., 1990; Speich et al., 2017).

Diamonds are commonly observed as showing weaker platelet absorption than predicted by the relationship with B-centres. This is commonly thought to be a result of platelet degradation caused by short-lived events occurring at high temperature (Hunt et al., 2009; Melton et al., 2013). This behaviour can be considered as a first order rate equation of the following form

$$P_t = P_0 \times e^{-k_P t} \tag{1.10}$$

Where P_t is the amount of platelets detected represented as peak area (cm^{-2}), P_0 is the initial amount of platelets, $k_P t$ is the rate constant for the process of platelet degradation and t is the duration. In order to calculate the deviation from expected platelet behaviour, the following relationship can be used (Speich, 2017; Speich et al., 2018)

$$Platelet\ Degradation = 100 \times \left(1 - \frac{[N_B]/0.806}{I(B')}\right) \tag{1.11}$$

Where $[N_B]$ is the concentration of nitrogen present as B-centres (ppm) and $I(B')$ is the integrated intensity of the platelet peak (cm^{-2}). This will be discussed further and used to interrogate another IR feature in chapter 5.

1.2.3 Hydrogen in diamond

Hydrogen was first observed as an impurity in diamonds in the 1950s (Charette, 1959), with the first evidence of hydrogen (in the form H_2) found during mass spectrometry measurements

on escaped gases from a number of high-quality gem diamond crystals (Kaiser and Bond, 1959). Although studies using this destructive method were carried out for some time afterwards (Melton and Giardini, 1975, 1974), a non-destructive spectroscopic method is desirable in order to get better spatial information and allow for complimentary investigations of samples.

Hydrogen is thought to be a ubiquitous impurity in natural diamonds, with nuclear rection analysis (NRA) suggesting that diamonds can contain anywhere between 500 – 3500 ppm (Sideras-Haddad et al., 2001). Chemical analysis using an ion beam has suggested that the concentration of hydrogen in natural diamond could reach up to 1 atomic % (or 10,000 atomic ppm) (Hudson and Tsong, 1977). These previous attempts at hydrogen quantification in diamond will be discussed in greater detail in chapter 3, which also presents efforts using a technique that has not been previously attempted on natural diamonds.

There are more than 90 sharp lines or absorption systems in the IR and UV-visible ranges in natural diamonds that have been at least tentatively related to the presence of hydrogen within the crystal (Fritsch et al., 2007). However, despite the ubiquity of hydrogen in diamond, there is a relative paucity of information as to the environments involved. In the structurally analogous silicon crystal, for example, complexes such as an interstitial H_2 dimer (Pritchard et al., 1998) and a series of hydrogen-silicon-vacancy complexes (Bech Nielsen et al., 1995) have been characterised. This is not the case in diamond. The hydrogen contents proposed by Sideras-Haddad *et al.* (2001) and Hudson and Tsong (1977) are bulk techniques that consider any and all forms of hydrogen in diamond, whether it is optically active or not.

Hydrogen is also commonly observed in synthetic diamond. In particular, it is often incorporated into CVD-grown diamond (Titus et al., 2006). Hydrogen is also capable of passivating boron acceptors in doped synthetic diamond, and can also influence other electronic properties in these synthetic samples (Chevallier et al., 1998; Uzan-Saguy et al., 2001).

However, its incorporation into synthetic diamonds is often different than in natural samples. For example, some hydrogen-related defects such as the NVH centre (which will be discussed in section 3.1) have only been observed in synthetic samples.

1.2.3.1 The 3107 cm^{-1} peak

By far the most widely observed and well characterised hydrogen related defect in diamond is the centre responsible for a vibrational mode at 3107 cm^{-1}. This feature is seen in almost all type Ia natural diamonds (Fritsch et al., 2007). This defect is amongst the first hydrogen related defects to have been observed in diamond and original interpretations involved either an N-H stretch, a C-H stretch or even a vinylidene group (>C=CH_2) due to comparable positions of the vibrational frequencies (Runciman and Carter, 1971). Assignment was then refined to a C-H stretch due to the presence of a peak at 3097.8 cm^{-1} with the relative intensity and wavenumber expected of an isotopically-shifted ^{13}C band, along with a corresponding bending mode at 1405 cm^{-1} (Woods and Collins, 1983). This was also indicated by the lack of shift with isotopic substitution of nitrogen, although the intensity of the 3107 cm^{-1} was found to increase with the nitrogen content in the diamond (Kiflawi et al., 1996). The lack of isotopic shift suggested that nitrogen was not bonded to a hydrogen atom, or even to a carbon atom upon which a H atom is decorated, but that nitrogen was part of the defect in some fashion. It was thought for a long time that the 3107 cm^{-1} defect could not be observed in synthetic diamonds. However, it has now been shown that, upon annealing of CVD and HPHT samples at temperatures upwards of 1900 °C, this spectral feature can develop (Fuchs et al., 1995; Kiflawi et al., 1996). Uniaxial stress studies that showed a trigonal defect along the [1 1 1] crystal axes (J P Goss et al., 2014), which combined with the previous information suggests a possible link to the N3 and B centres – this will be discussed in chapter 4. The peak was eventually assigned to a defect referred to as N_3VH, consisting of three substitutional nitrogen atoms around a vacancy, with the dangling

carbon bond having been decorated by a hydrogen atom (J P Goss et al., 2014). The structure of this defect is displayed in figure 1.7.

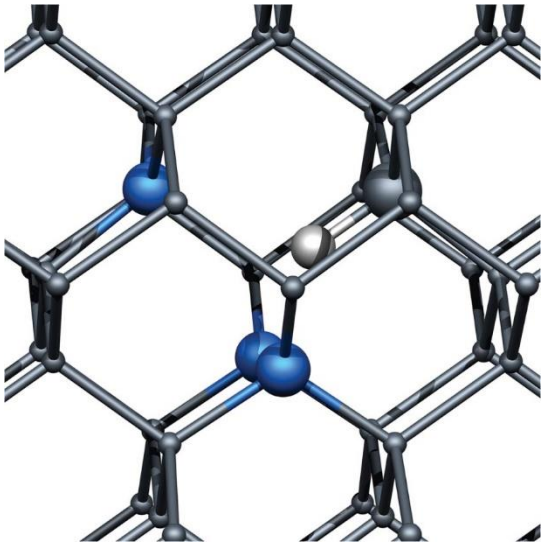

Figure 1.7: A representation of the structure of the N_3VH centre which causes the 3107 cm^{-1} IR absorption feature in diamond. The larger spheres indicate sites surrounding the vacancy, consisting of one carbon atom and three nitrogen atoms (in blue). The carbon is decorated with a hydrogen atom (smaller white sphere). The smaller grey spheres constitute the carbon atoms in the diamond lattice. (Goss et al., 2014)

Although the structure of this defect has been characterised, the identity of a vast number of other peaks attributed to hydrogen within the diamond spectrum is as yet unknown. Whilst the majority of IR-active hydrogen is believed to be contained within the N_3VH defect, there is still much to be learned from the study of the other minor features that could potentially lead to information about the environment in which diamonds grow. The viability of the 3107 cm^{-1} as a proxy for total hydrogen content in natural diamonds will be considered in chapter 3.

The term 'hydrogen-rich', or 'H-rich' was originally coined in the early 1990s (Fritsch and Scarratt, 1993) and has been used to refer to diamonds with an unusually high amount of IR-active hydrogen, where the intensity of the 3107 cm^{-1} absorption is higher than that of the intrinsic diamond absorption located at 2450 cm^{-1}. This can often lead to diamonds with unusual gemmological properties, for example specific and unique colouration (van der Bogert et al., 2009).

1.2.3.2 Hydrogen and cuboid growth

The features associated with hydrogen in diamonds often tend to be associated with cuboid growth. This can be observed both in purely cubic or cuboid crystals (Welbourn et al., 1989) or in the cuboid sectors of diamonds containing various mixed growth zones, most strikingly observed in asteriated samples (Rondeau et al., 2004). Studies of the difference between growth sectors in mixed-habit diamonds has observed that the formation of platelets is diminished in cuboid growth sectors (Lang, 1974b; Rondeau et al., 2004), and it has thereby been proposed that hydrogen could play a part in the quenching of nitrogen aggregation. However, it is possible that, in the case that there is more nitrogen in the octahedral sectors than in the cuboid sectors of these mixed-habit stones, the formation of platelets could simply be more probable in octahedral sectors as a result (Fritsch et al., 2007 and ref. within). This relationship will be examined further in chapter 6.

1.2.3.3 Hydrogen diffusion

Natural diamond can host hydrogen-bearing fluid inclusions and nominally anhydrous minerals (NAMS) with a small but important OH content that provide valuable information about the 'wetness' of the source mantle (Ohtani, 2015; Tomlinson et al., 2007). This information relies heavily on the assumption that the diamond is a perfect sealed container and that hydrogen has not entered or escaped since the inclusion was captured. As a result, understanding hydrogen diffusion within the crystals is an essential step in validating models based on these inclusions. It has often been assumed that this process is too slow to warrant consideration for geologically relevant conditions and timescales. However, this assumption may be completely incorrect, as discovered with the advent of chemical vapour deposition (CVD) techniques for production of synthetic diamond substrates for technological applications (Gicquel et al., 2001). Due to the fact that hydrogen is present within the carrier gas used for CVD synthesis, and potentially has an effect on the chemical and electronic properties of the diamond (both at the surface and within the bulk), it has become important to better quantify and understand hydrogen diffusion.

Past studies of H in diamond and how it relates to the material properties have focused on the effect of H in doped, semiconducting CVD diamond, both p- and n-type. This showed that, in p-type diamond, the neutral boron acceptors present were compensated by H donors, ionising the hydrogen to protons, which are fast donors with a migration energy of 0.1 – 0.2 eV (Chevallier et al., 1998; Saguy, 2004). In undoped and n-type diamond the diffusion was thought to be slower due to a higher migration energy and a lower solubility of both H^0 and H^- compared to H^+ (Chevallier et al., 2002; Saguy et al., 2003).

Calculations of H diffusion through the diamond lattice have been undertaken to provide a diffusion coefficient, which can be used to calculate diffusion distances at temperatures between 500 – 1600 °C, using the temperature dependant Arrhenius relationship in the form

$$x \sim (D\ t)^{1/2} \tag{1.12}$$

Where *D* is the diffusion coefficient according to the Arrhenius relationship, *x* is the diffusion distance and *t* is the time (Crank, 1979). Data produced by Cherniak *et al.* in 2018 extrapolate to a diffusion of 50 µm in 300,000 years at a temperature of 500 °C and ~ 30 min at 1400 °C (Cherniak et al., 2018). By contrast, a 50 µm diffusion of a nitrogen atom at 1400 °C within diamond would take close to 1 billion years (K. T. Koga et al., 2003). H retention within diamond grains was also calculated, and this showed almost complete loss of hydrogen from the diamond on a geological timescale, assuming a spherical geometry of the diamond and a uniform initial H concentration (Cherniak et al., 2018). If this holds true for natural diamonds, it can be assumed that diamonds will equilibrate with ambient hydrogen in the mantle on the timescale of most mantle scale processes. However, it is also possible that there is some re-equilibration with the host kimberlite magmas as the diamonds are transported from source to surface on an hourly timescale (Canil and Fedortchouk, 1999; Kelley and Wartho, 2000; Peslier et al., 2008; Sparks et al., 2006). Modelling of the hydrogen diffusion during ascent has found

that the outcomes depend largely on the rate of ascent and cooling, with fractional losses ranging from 15 % within larger diamonds (ca. 1 mm radius) at an ascent rate of 45 m/s up to 70 % using an ascent rate of 5 m/s (Cherniak et al., 2018). This indicates that diamonds do not necessarily preserve the bulk of the hydrogen present within the lattice during their ascent. However, it is worth noting that these simple diffusion models only consider atomic hydrogen migrating through the diamond lattice. They do not consider the presence of inclusions, either fluid or mineral in nature, and also do not account for the possibility of the hydrogen being trapped by point defects present within the diamond lattice. If the decoration of a point defect with a hydrogen atom functions as a thermodynamic sink, then it could be expected that any retention of hydrogen is dependent on the presence of these pre-existing defects, rather than the availability of hydrogen within the growth medium. This has been studied in synthetic diamond, in particular boron-doped diamond. A combination of theory and experiments have observed that, in B-doped diamond, traps are likely a primary cause of low observed diffusion of hydrogen within the diamond lattice (J. P. Goss et al., 2003b; Teukam et al., 2003). This has also been investigated in undoped polycrystalline CVD diamond (Ballutaud et al., 2001). This study focussed on deuterium diffusion within the diamond, and it was found that the diffusion rate was primarily governed by trapping on defects. This data lends credence to defects as a primary mechanism of hydrogen retention within the diamonds.

1.2.3.4 Classification of diamonds through hydrogen-related features

By reviewing the hydrogen and nitrogen-related spectral features and their corresponding defect concentrations, along with gemmological properties such as visible colour, Fritsch et al. (2007) suggested that all diamonds containing hydrogen can be categorised as the following six groups:

1. Near-colourless type Ia diamonds – these contain weak features related to hydrogen, often only the 3107 cm^{-1} peak. These are commonly encountered, and it is rare to find a type Ia stone containing no hydrogen.

2. Yellow to brown to green diamonds, and white to grey diamonds (coloured by inclusions) – the spectra of these can vary significantly (Fritsch et al., 1991). There are often weaker hydrogen- and nitrogen-related IR features than in some of the subclassifications. The nitrogen in these diamonds is often present in a less aggregated form.

3. Grey to blue to violet diamonds – these diamonds contain exceptionally high hydrogen and nitrogen concentrations through IR. The nitrogen is found in an advanced aggregation state (van der Bogert et al., 2009), with the diamonds usually being almost pure type IaB. The most common source of these diamonds is the Argyle mine in Australia.

4. Chameleon diamonds – the most characteristic feature of these diamonds is their photo- and thermochromic properties, and the colour changes that this brings on. The nitrogen and hydrogen content is usually low-medium, with a low aggregation state. These diamonds are typically type IaA with Ib character (Hainschwang et al., 2005).

5. Intense yellow to orange type Ia diamonds – diamonds in this group display intense colouration. An intense 3107 cm^{-1} peak and high Ib character is usually observed. These diamonds have a nitrogen content and are usually pure type IaA.

6. Yellow to orange to brown type Ib and “ABC” diamonds – these samples are typically type Ib. They tend to exhibit a variety of peaks in the spectral regions corresponding to the hydrogen-related features (Hainschwang et al., 2006). These are very rarely found and are usually small in size and deep in colour.

This classification highlights the gemmological significance of hydrogen-related features in the IR spectra of diamonds and the importance of understanding the range of properties that they can display.

1.3 Project Aims and Thesis Structure

This project aims to extend our understanding of hydrogen in natural diamonds. Despite the common presence of impurity hydrogen within diamonds, there is surprisingly little knowledge of how much hydrogen there is within these crystals and within what environment it is contained. Water (and by extension, hydrogen) can affect mineralogical properties such as conductivity, strain rate and the deformation mechanism. Water content has implications for the bulk rock properties such as the location of the solidus, the viscosity and rheology which feed into the process of mantle convection. Given the importance of water in the mantle, the study of hydrogen in diamonds could potentially shed new light on unseen processes occurring deep within the Earth. Hydrogen and its incorporation also have a significant effect on the material properties for technological applications – for example, it can affect the electronic properties in ways which are crucial to understand for the potential use of doped diamond as a semiconducting material (Chevallier et al., 2002, 1998; Hutton et al., 2013). This means that there is a clear need to learn more about the incorporation of hydrogen into the structure of diamonds.

Chapter 2 describes the methodology used for preparing diamond plates for optical studies and their analysis using FTIR, the core technique used within this thesis. FTIR studies form the basis of all subsequent chapters.

Chapter 3 looks at the relationship between the 3107 cm^{-1} feature and the bulk hydrogen content, as measured using proton-proton scattering. This is a novel technique that has not been previously applied to the study of natural diamond samples. This chapter addresses the question

of whether or not the 3107 cm^{-1} peak can be used as a proxy for bulk hydrogen content, and by extension whether or not the majority of hydrogen is contained within this defect. Also examined is the accuracy of previous attempts to generate an extinction coefficient for H-containing defects in diamond.

Chapter 4 looks at the role hydrogen may play in the nitrogen aggregation sequence, and whether the formation of the N_3VH centre comes primarily through the protonation of an N3 centre. This chapter uses a combination of IR and UV-vis measurements to study systematics across a range of samples from different localities.

Chapter 5 provides a detailed characterisation of a minor H-related IR peak at 3236 cm^{-1}. This chapter uses comparisons between a number of IR-measurable features to provide clues as to the origin of this feature, and what sort of defect it may represent.

Chapter 6 compares IR studies with photoluminescence results in order to probe the growth conditions in internally zoned diamonds at high spatial resolution. Links between nickel- and hydrogen-related features are investigated.

Chapter 7 contains discussion about the impact of the work presented here and ideas for future work that can continue the investigations started within this thesis.

2. Methods

2.1 Sample Preparation

Original studies on diamonds used whole stones in their research, using properties such as birefringence of photoluminescence in order to provide information, although the internal inhomogeneity of diamonds means that this can be insufficient when attempting to draw conclusions from such data. Although it results in loss of a significant portion of the diamond crystal, the use of polished plates provides the opportunity to study and constrain the growth history through the comparison of properties throughout the zones. Thus, samples within this work were studied as thin plates.

The diamonds, predominantly octahedral in morphology, were polished on two parallel {110} faces on an industrial diamond impregnated scaif, in order to yield thin plates (Bulanova et al., 2005), according to the anisotropic hardness of diamond as a material. A schematic of this process is displayed in Figure 2.1. The thickness of the plates varies between 300 µm and ca. 1000 µm, in order to provide optimal thickness for Fourier Transform Infrared (FTIR) analysis – thin enough to provide sufficient signal when passing the light through, but not thin enough to suffer any significant negative effects from interference fringes.

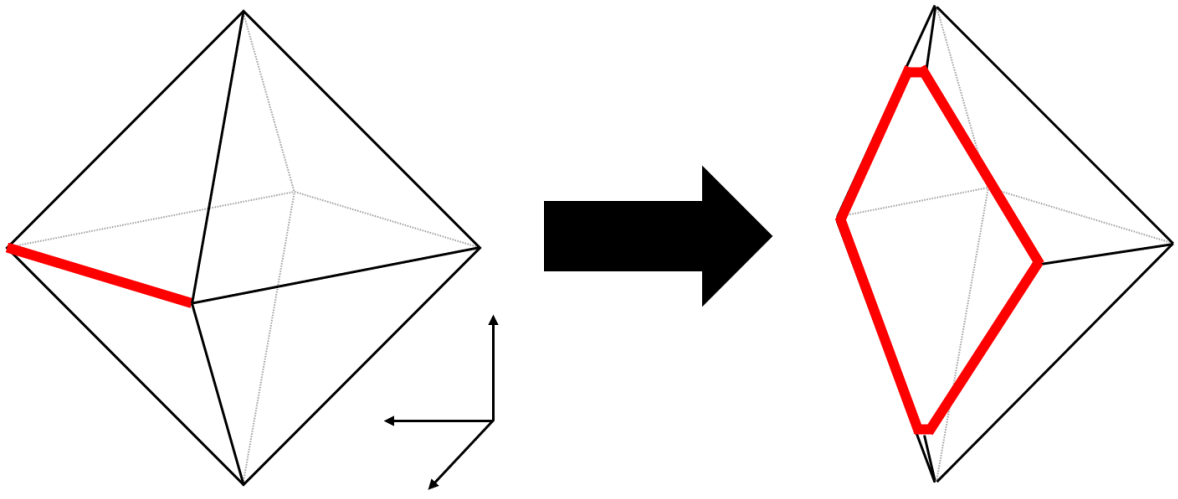

Figure 2.1: A schematic of the polishing of an octahedral diamond along the {110} direction in order to produce a parallel plate. The face being polished is indicated by the thick, red line and the crystal indices are displayed at the bottom of the figure on the left.

2.2 Optical Spectroscopy

Optical spectroscopy techniques, involving the transitions between electronic states within the sample being studied, are undeniably valuable in the study and identification of point defects in diamond (Walker, 1979). Optical spectroscopy encompasses two main areas, emission-based techniques (also known as luminescence) and optical absorption. A schematic of these is displayed in Figure 2.2. For emission techniques, a number of different sources can be used to generate the luminescence which is measured. This includes photoluminescence – where a photon beam (or light) acts as the source – and cathodoluminescence, which generates emission using an electron beam. Other excitation modes are possible, such as chemiluminescence (the production of light via a chemical reaction), triboluminescence (where light is produced through material stress), or thermoluminescence, where light emission is stimulated through heating a sample. Luminescence techniques can be highly sensitive. It can be possible to detect optical centres present at levels below 1 ppb. However, optical absorption is unaffected by non-radiative processes at the luminescence centres (Willardson et al., 1998). This means that it can be thought of as the more fundamental technique. Photoluminescence techniques will be discussed in greater detail in section 6.2.

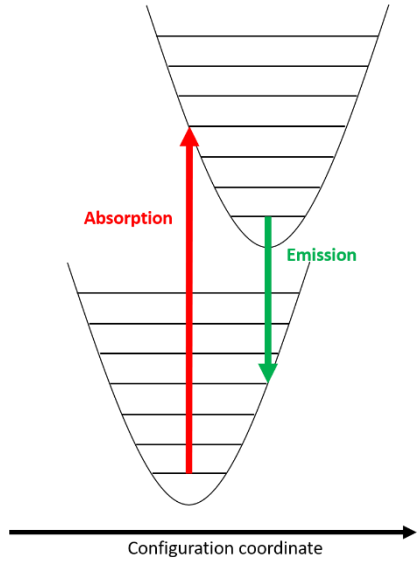

Figure 2.2: A schematic of the processes involved in optical spectroscopy. The techniques involve either excitation to an excited electronic state through absorption of a photon (in red), such as in IR, or the relaxation of an excited state through emission of a photon (in green), such as in photoluminescence.

2.2.1 Fourier Transform Infrared Spectroscopy

FTIR Spectroscopy was performed according to previous work (Kohn et al., 2016). Prior to analysis, diamonds were cleaned using laboratory-grade ethanol in order to remove surface contaminants such as dust or adhesive residue. Samples were dried and then secured on to a knife-edge aperture over the hole in the sample holder, as displayed in Figure 2.3. This procedure ensures that spectra collected do not contain any signal from organic material, and the lack of a carrier material eliminates the possibility of reflections from the interface between carrier and sample obscuring the spectra. All FTIR analyses in this work were performed using a Nicolet iN10 MX microscope, with a liquid nitrogen cooled mercury cadmium telluride (MCT-A) detector.

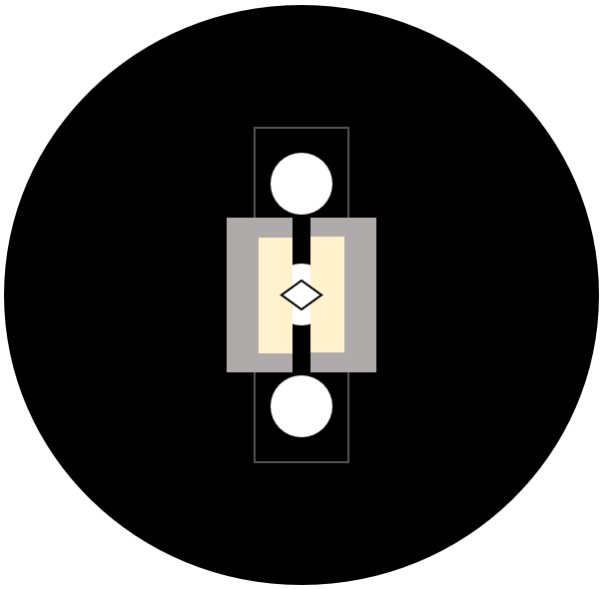

Figure 2.3: A schematic of the sample holder used during FTIR analyses, with the polished diamond plate secured on a knife-edge aperture.

Two modes of data collection were used: either a 1-dimensional high-resolution line scan or a 2-dimensional high-resolution map. In the former, a fast, low-resolution map was initially obtained via the instrument's ultrafast mapping capability, using a 16 cm^{-1} spectral resolution between 650 – 4000 cm^{-1}. This can produce a map with high spatial resolution (typically a step size of 20 µm and a 30 µm aperture) in less than 30 minutes for the majority of samples. Whilst these maps cannot be used for quantification, they provide a good overview of zonation within

a sample, which can be used to target high quality line scans acquired at a higher spatial resolution of 2 cm^{-1}, typically using 64 or 128 scans per spectrum and a step size of 30 µm and a 40 µm aperture. For high quality 2D maps, a spectral resolution of 2 cm^{-1} was used, with a typical step size of 50 µm and a 60 µm aperture. Depending on the size of the specific sample, these maps can consist of up ca. 7000 individual spectra. As the liquid nitrogen tank used to cool the detector lasts for approximately 21 hours, any measurement lasting longer than this required the data acquisition to be paused in order to replenish the liquid nitrogen.

2.2.2 Spectral Deconvolution

In order to quantify the components that compose a spectrum, spectral deconvolution must be performed. An IR spectrum of a typical diamond is displayed in Figure 2.4. There are 3 main regions of interest when studying the IR spectra of diamonds. The region below 1500 cm^{-1} contains a variety of peaks which arise because of different nitrogen species present within the diamond, as well as the platelet peak, which varies in position with the size of the platelets. The region from 1800 – 2700 cm^{-1}, known as the two-phonon region, contains the main absorptions associated with the intrinsic diamond lattice. The 3107 cm^{-1} peak associated with the N_3VH defect is also indicated (J P Goss et al., 2014). This is typically the predominant high-wavenumber feature in IR spectra of natural diamonds.

The most prevalent method of IR spectral deconvolution uses the CAXBD97n Excel spreadsheet produced by David Fisher (De Beers Technologies, Maidenhead). Whilst this is useful for smaller datasets of up to 100 spectra, the large number of data points acquired during map collection requires automated processing. This processing is accomplished using the program Quantification of Infrared active Defects in Diamond and Inferred Temperatures (QUIDDIT) (Speich, 2017; Speich and Kohn, 2020).

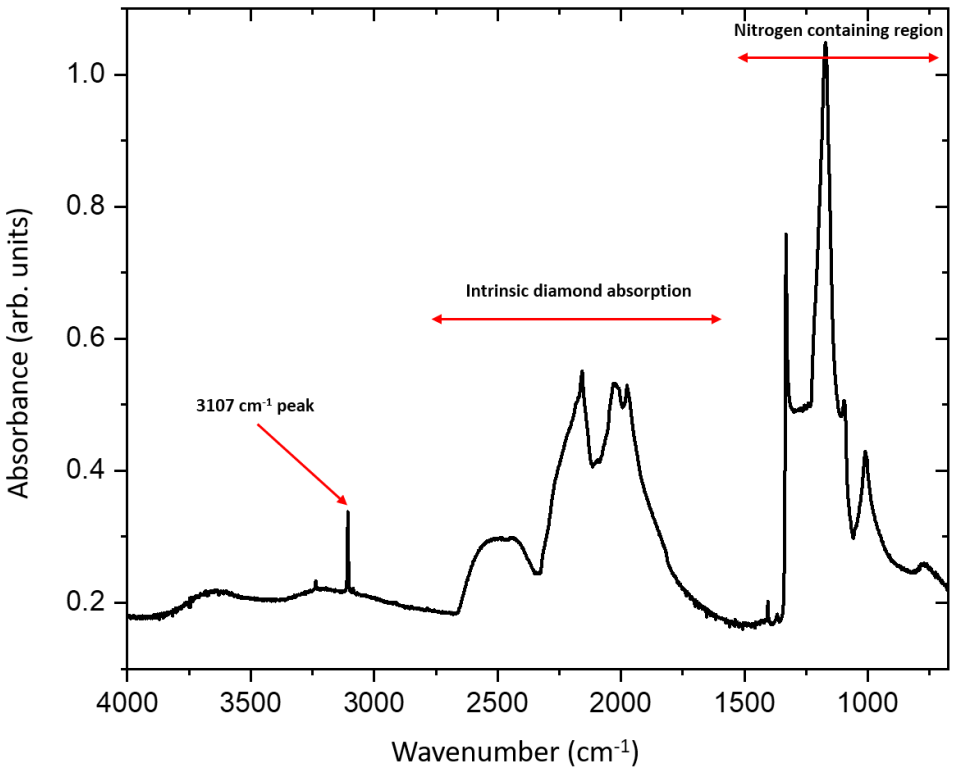

Figure 2.4: A typical IR spectrum of a diamond. Indicated on the diagram are the three primary regions of interest: the nitrogen containing region below 1500 cm^{-1}, the intrinsic diamond region at 1800 – 2700 cm^{-1} and the 3107 cm^{-1} peak.

As an initial preparatory step, the dataset is split into individual CSV files. The OMNIC Picta (Thermo Scientific) software attached to the IR spectrometer is capable of dividing the map files into SPA files, which are a proprietary format used by Thermo Scientific. These are converted to CSV files using a simple macro that preserves spatial information by setting each file name to the x-y coordinates from which the spectrum was collected, e.g. "X-123.4 Y 567.8". Spectra from the edge of the samples or on inclusions are removed manually in order to minimise the influence of certain artefacts in the spectra.

Baseline correction must then be performed. The initial correction consists of a constant baseline subtraction, which is based off of the absorption at 4000 cm^{-1} in the collected spectrum. Alongside this, a simultaneous normalisation is performed to 1 cm diamond thickness. This is achieved by locating the absorption value at 1992 cm^{-1} and calculating a normalisation factor, which is then used to normalise to an absorption value of 12.3 at 1992 cm^{-1}.

Three areas of this spectrum are then linearly interpolated before a final correction is applied. These are the regions spanning 1500 to 2312 cm^{-1}, 2391 to 3000 cm^{-1} and 3800 to 4000 cm^{-1}. Interpolation ensures that data with any data spacing can be processed. The two-phonon region contains features arising from the intrinsic diamond, but the low wavenumber tail of this absorption can extend below 1500 cm^{-1}, potentially obscuring several features of interest. This baseline correction is aimed at eliminating the effect of this tail in order to accurately measure features within the one-phonon region. The three regions mentioned above are fitted to a spectrum of a Type IIa diamond which contains no IR-active nitrogen. This spectrum is normalised as discussed above to 1 cm thickness and only contains the intrinsic diamond peaks, with no other absorptions present. This fitting uses a least-squares routine (Zhu et al., 1997) implemented in SciPy (Virtanen et al., 2020). A first order polynomial baseline is also included. The reference spectrum and calculated polynomial baseline are subsequently subtracted from the corrected spectrum. Figure 2.5 displays an example of this process. The corrected spectra are produced as CSV files for further processing.

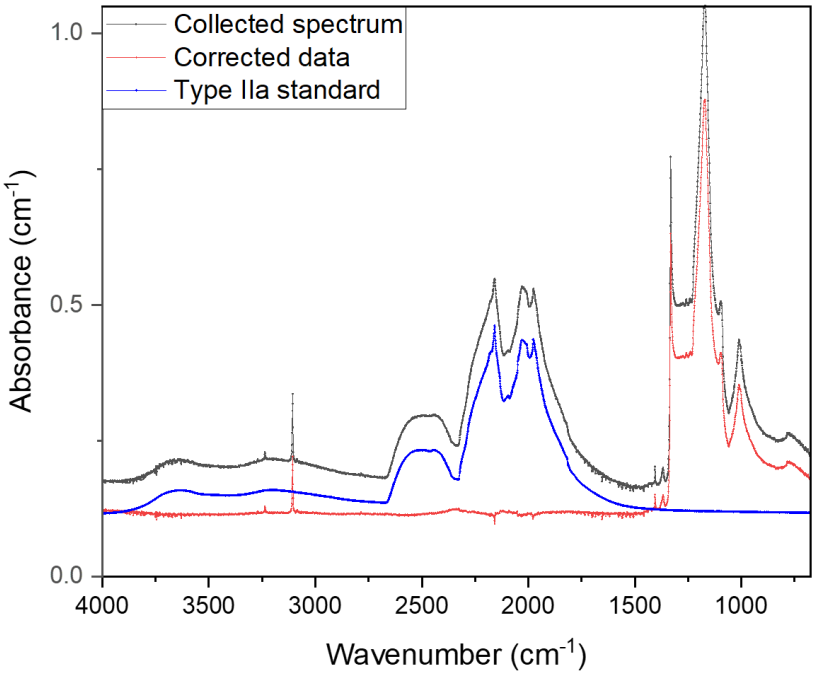

Figure 2.5: An illustrative example of the baseline correction and normalisation procedure used in the processing of FTIR data. At the top, in black, is a collected spectrum from one of the diamonds studied here, Argyle 78. In the middle, in blue, is the type IIa spectrum used as a reference for fitting, and at the bottom, in red, is the result of the fitting, subtraction and normalisation to 1 cm^{-1} thickness.

Once corrected spectra have been obtained, several distinct regions of the spectrum are analysed to interrogate factors such as nitrogen impurities, the width and position of the platelet peak and the 3107 cm^{-1} peak. This involves the fitting of a pseudo-Voigt function to the collected data. In IR spectra, the bands should be Lorentzian in shape, although instrumental factors can potentially add a Gaussian component to the peak shape (Seshadri and Jones, 1963), and thus a pseudo-Voigt function is used. This is a linear combination of a Gaussian (G(x)) and a Lorentzian (L(x)) distribution, which takes the form

$$P(x) = \eta \, . L(x) + (1 - \eta) . G(x) \tag{2.1}$$

Where η is the Lorentzian contribution to the peak shape, and $0 \leq \eta \leq 1$.

The 3107 cm^{-1} peak will be used as an illustration on how to fit high wavenumber peaks, as the technique is analogous for other peaks studied. Initially, the region between 3000 and 3200 cm^{-1} is extracted, before fitting a third order polynomial baseline. The area around the peak itself is excluded. The baseline is subtracted from the spectrum, and the peak is fitted using a pseudo-Voigt function. Peak height and area are written into the results file produced by QUIDDIT. This file also contains features such as peak width, along with any parameters produced by the local correction around the 3107 cm^{-1} peak.

The one-phonon region is fitted using the CAXBD97n Excel spreadsheet from David Fisher (De Beers Technologies, Maidenhead). This spreadsheet contains spectra of the A, B and D components, which can be interpolated and used as references. The area of the spectrum from 1000 to 1400 cm^{-1} is then extracted and subsequently interpolated. A least-squares method is used to minimise the difference between the collected spectrum and a combination of the individual component spectra. This takes the form

$$a \, . A(x) + b \, . B(x) + d \, . D(x) + constant \tag{2.2}$$

Where A(x), B(x) and D(x) are the reference spectra of the individual components (A, B and D) respectively and *a*, *b* and *d* are their respective absorption coefficients. The constant accounts for any remaining non-zero component after the baseline correction. The coefficients are constrained as positive as they relate to defect concentration. The concentrations of A- and B- centres are determined with the absorption coefficients at 1282 cm^{-1} (Boyd et al., 1995, 1994). The C component can be added to this procedure. However, in the majority of diamonds the concentration of C-centres is negligible, meaning that this is usually unnecessary.

Uncertainty assessment in the determination of nitrogen concentrations by FTIR can pose an issue when considering quantification, and it is not straightforwardly resolved. Several sources of random error exist, including interference fringes (which can be significant if the polished plate is thinner than ca. 200 μm), the inadequate removal of baselines and instrumental noise. These can interfere with automated fitting and reduce precision, particularly if total nitrogen concentration is low, although diamonds such as that are uncommon among those studied within this work.

There are also some systematic errors introduced by uncertainty in the absorption coefficients used to convert intensities into concentrations of A- and B- centres. A number of other factors also introduce uncertainties, including the determined activation energy and pre-exponential component, which are used in the kinetic equations determining nitrogen aggregation within diamonds. The calibration coefficients involved in the determination of A- and B- centre concentrations have uncertainties of ca. 6 and 10 % respectively (Boyd et al., 1995, 1994).

2.2.3 UV-vis spectroscopy

Due to the wavelength of the N3 absorption, which will be considered in detail in chapter 4, a UV-visible spectrometer is required to study the centre. Single measurements in chapter 4 were undertaken using a PerkinElmer LAMBDA 1050 UV-vis/NIR spectrometer at De Beers

Technologies, Maidenhead. Samples were mounted on a 1.5 mm aperture in order to increase signal by minimising signal loss from specular reflection and transmission through the transparent samples. The samples were then scanned over a range of wavelengths at room temperature. The thickness of the samples was also measured using calipers to allow for conversion between absorbance (A) and the attenuation coefficient (μ, in cm^{-1}) using the following relationship

$$\mu = \frac{\ln(10)}{t} \times A \tag{2.3}$$

Where *t* is the thickness in cm. Line scans, where obtained, were collected using a JASCO MSV5200 instrument in the Gemmological Institute at the China University of Geosciences in Wuhan, China. These used a 100 μm aperture and collected spectra using a step size between 50 – 15 μm. In order to quantify the N3 concentration, the following calibration can be used (Davies, 1999)

$$A_{N3\,(77\,K)} = 8.6 \times 10^{-17}\,[N3] \tag{2.4}$$

Where $A_{N3\,(77\,K)}$ is the area of the zero-phonon line of the N3 absorption in meV cm^{-1} and [N3] is the concentration of N3 in cm^{-3}. Areas are determined in $nm.cm^{-1}$, but this can be converted to $meV.cm^{-1}$ using the following equation (personal communications, David Fisher, De Beers Technologies, 2019)

$$A_{N3}\,(meV.cm^{-1}) = -0.0339 \times A_{N3}(nm.cm^{-1})^2 + 7.2209 \times A_{N3}(nm.cm^{-1}) \tag{2.5}$$

As this calibration has been determined for samples at 77 K, the following empirically derived equation can be used to convert from room-temperature to 77 K (personal communications, David Fisher, De Beers Technologies, 2019)

$$A_{N3\,(77\,K)} = 1.4928 \times A_{N3\,(RT)} \tag{2.6}$$

The concentration can now be converted to ppm using the following relationship

$$[N3](ppm) = \frac{[N3](cm^{-3})}{1.76 \times 10^{17}} \quad (2.7)$$

Where 1.76 x 10^{17} is the number of carbon atoms per cm^3 in diamond. This provides a way of quantifying N3 content in a similar way as other nitrogen aggregates, which, combined with the quantification of 3107 cm^{-1} as described in section 3.1 (Coxon et al., 2020) can be used to study nitrogen aggregation and the role hydrogen plays.

All UV-vis spectra were obtained as .csv files and were analysed using Origin 2019b. These were subsequently analysed and processed using the methods described above in order to produce [N3] values in ppm. A script was written to fit and subtract a linear baseline between 410 and 420 nm prior to numerical integration to produce a peak area. The peak area was then processed as discussed above to produce [N3] in ppm. Efforts were made to correlate features on the samples such as visual inclusions in order to accurately match the directions of the line scans for the FTIR and UV-vis experiments.

2.2.4 UV-vis data processing

When attempting to compare data from two separate analytical techniques, several factors must be considered. Firstly, in the majority of cases, it was only possible to collect a single UV-vis spectrum for each sample, using a 1 mm aperture. However, the collected IR data consists of high-quality line scans. Therefore, when comparing between the two, consideration must be given as to how best to represent the IR data. One simple way to do this is to simply average out all the individual points from the line scan, with the standard error then acting as a representative of inhomogeneity within an individual diamond. As the aperture size on the UV-vis instrument is known, points from outside this aperture can be excluded to provide a more representative comparison.

When correlating the UV-vis and IR line scans, it must be noted that there is potentially significant uncertainty introduced by human error. In order to match the directions as accurately as possible, features such as visual inclusions and the asymmetric shape of some of the diamonds were used. UV-vis spectra were provided with attached xy values. These can be assessed to provide a total length of the line scan. The IR line scan can be cropped to match this length, with visual inspection being used to assess where the discrepancy in length lies. Due to this element of visual inspection, there is potentially some errors introduced due to the human nature of the approach. In cases where a discrepancy was present in length, a best fit approach was used to attempt to correlate the line scans as best as possible. Where this has been undertaken, it will be noted within the text.

2.3 Proton-proton scattering

Proton-proton scattering (also known as hydrogen microscopy (Reichart et al., 2002)) experiments were performed using the Superconducting Nanoscope for Applied Nuclear (Kern-) physics Experiments (SNAKE) microprobe at the Maier-Leibnitz Laboratory of the Technical University of Munich in Garching, Munich. The technique involves the firing of a proton beam with energy E_o towards a hydrogen-containing sample within an evacuated chamber. The incoming protons collide with the nuclei of atoms within the sample, and collisions with protons lead to a unique scattering event due to the involvement of two particles of equal mass. The conservation of energy and momentum dictates that upon impact, the two protons will be deflected away at an angle of 90° from each other (see figure 3.1). The two scattered nuclei can be detected on time-coincidence detectors, and thereby any two protons arriving at 90° within a certain time interval at the detectors can be considered as referring to a hydrogen within the sample. The energy of the incident proton will be split upon the collision with a hydrogen nucleus within the sample, according to the following equation

$$E_0 = E_1 + E_2 \tag{2.8}$$

Where E_0 is the energy of the incident proton and E_1 and E_2 are the energies of the two scattered protons. In an ideal case where the protons are scattered at 45°, these two energies would be equal. However, some energy will be lost from the energy of the incident protons upon passing through the sample, leading to

$$E_1 + E_2 = E_0 - \Delta E \tag{2.9}$$

Where ΔE is the amount of energy lost during transmission through the sample. The value of this energy loss, determined by the detector, is dependent on the distance travelled through the sample and the energy of the incident protons. It is therefore also dependent on the position at which the collision takes place within the sample, allowing a spatial distribution of hydrogen in three dimensions to be reconstructed (Reichart et al., 2004; Wegdén et al., 2005).

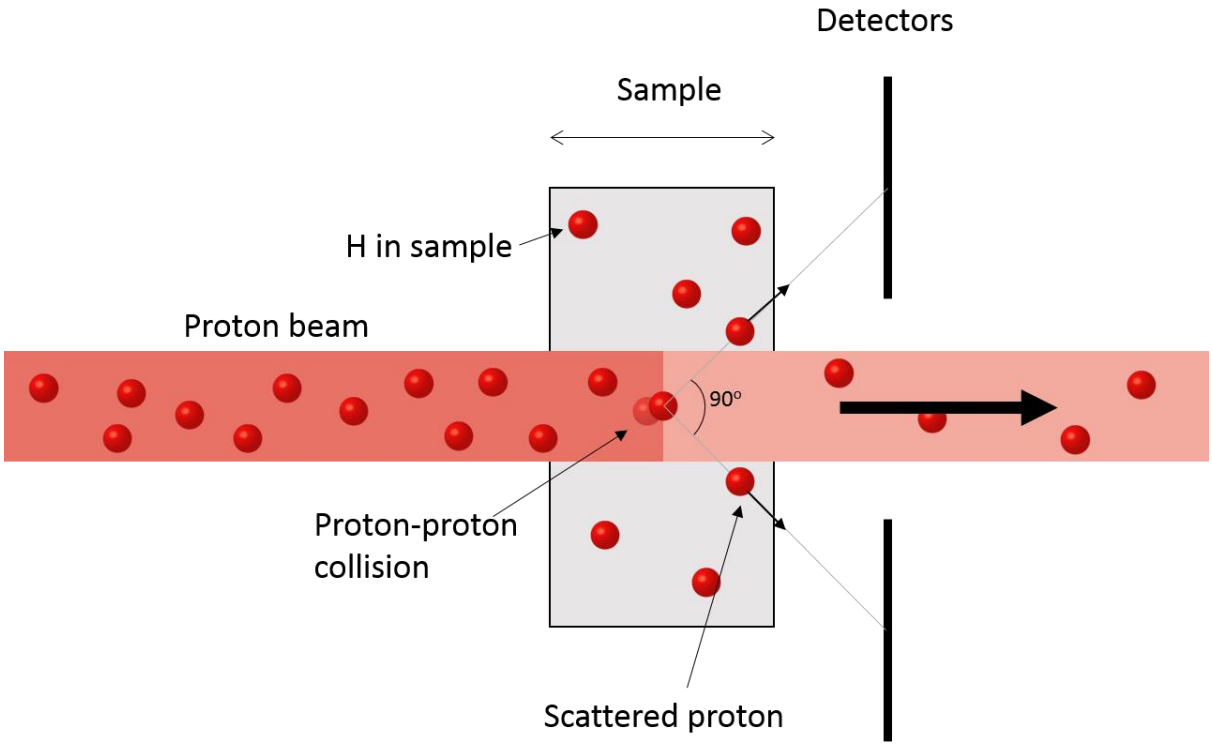

Figure 3.2: A schematic of the set-up for proton-proton scattering experiments. A proton beam is fired towards a hydrogen-containing sample. When the incident protons collide with hydrogen atoms within the sample, the nuclei are scattered at 90° to each other.

If a sample with thickness *t* is considered, with scattering events A and B at the surface closest to and furthest from the detectors respectively, the change energy can be described as follows:

$$\Delta E_A = \left(\frac{dE}{dx}\right)_{E_0} t \tag{2.10}$$

$$\Delta E_B = 2\left(\frac{dE}{dx}\right)_{\frac{E_0}{2}} \frac{t}{cos\theta} \tag{2.11}$$

Where $\left(\frac{dE}{dx}\right)_{E_{xy}}$ is the rate of energy loss per unit of distance at a certain energy, which is inversely proportional to E, and θ is the scattering angle of the particle relative to the direction of the incident beam. A particle scattered at point A will only experience loss by movement through the sample in the direction of the incident beam, but at point B, the energy loss will be due to diagonal movement of the two protons through the sample. If we consider a scattering event at a point, X, within the sample at a distance *d* from point A, the total energy change will contain a horizontal and diagonal component, resulting in the following equation:

$$\Delta E_X = \left(\frac{dE}{dx}\right)_{E_0} (t-d) + 2\left(\frac{dE}{dx}\right)_{\frac{E_0}{2}} \frac{d}{cos\theta} \tag{2.12}$$

As $\frac{dE}{dx} \propto 1/E$, if a sufficiently high E_0 is used, the change in energy will be very small. It can also be assumed that $\left(\frac{dE}{dx}\right)_{E_{0/2}} \approx 2\left(\frac{dE}{dx}\right)_{E_0}$, and equation 2.12 can thereby be simplified to

$$\Delta E_X \approx \left(\frac{dE}{dx}\right)_{E_0} (t-d) + 4\left(\frac{dE}{dx}\right)_{E_0} \frac{d}{cos\theta} \tag{2.13}$$

This constitutes the basic principle of the method, although other factors must be considered when undertaking full analyses. As the incident protons enter the sample, they will not only hit hydrogen atoms within the sample, but also other nuclei. This can lead to multiple scattering events for both the incident and outgoing protons. If a proton undergoes a non-proton collision before a proton-proton collision, the consequences are minimal; while the emerging protons will propagate at different angles than the ideal, the overall angle sum will still be 90 °, and an

appropriate time coincidence interval can still be used to determine that a scattering event took place. The steepest deflection of the scattering angles, alongside the change in energy dependent on the path determine the maximum sample thickness that can be used with this technique. More issues arise when considering multiple scattering events on the emerging protons, since this could lead to them escaping detection. It is possible to undertake some correction for these multiple collisions during the analysis, to minimise the effects on the acquired data. The deflection angle of a proton (α) in a collision depends on the rough relationship

$$\alpha \approx \left(1.8\ \frac{Z\ \Delta E}{E}\right)^{0.5} \tag{2.14}$$

Where Z is the atomic number of the atom involved in the collision. This provides some evidence that knowledge of the sample composition can help when undertaking the corrections. An exponential decay in count rate can also be assumed from the entrance of the beam to exit of the sample. The value of this exponent can be measured by observing the difference in signal upon rotation of the sample through 180°, and can be corrected for as such (Cohen et al., 1972). Analytical error due to multiple collision events can be minimised by using as large a detector area as possible, in order to capture events from all scattering angles and avoiding the escape of particles.

This technique, with the potential to provide 3D spatial resolution of hydrogen, offers a number of advantages over other techniques used to measure hydrogen content within solid samples. Due to its depth resolution, it can distinguish between hydrogen adsorbed to the surface of the sample and hydrogen within the sample itself, and can determine trace concentrations of hydrogen (< 1 ppm) on a micrometre depth resolution (Reichart et al., 2004). This is a clear advantage in terms of sensitivity compared to the techniques previously discussed. Unlike secondary mass-ion spectrometry (SIMS), which is a technique commonly used to study

elemental distributions within solid samples, including diamonds (Bulanova et al., 2002; Hogberg et al., 2016), this technique is not matrix-dependent, and so does not require independent analytical calibration. Alongside this, the radiation damage inflicted through the use of the proton beam is minimal, and is the lowest possible irradiation damage of all ion beam analysis methods (Reichart et al., 2002). A negative aspect of this technique compared to others is the need for samples to be thin. Due to the stopping power of diamond, the samples are required to be freestanding and ≤ ~ 100 μm in order to allow the beam to pass through the sample, and to allow for the collection of sufficient statistics to be able to reduce uncertainties as much as possible.

The results are obtained in the form of integrated density of hydrogen, ρ_H (in cm^{-2}), which can be converted into ppm via the following equation:

$$[H]\ (ppm) = \frac{\rho_H / l}{\rho_M \times N_A} \tag{2.15}$$

Where l is the thickness of the sample in cm and ρ_M is the density of the matrix (in this case diamond) in g cm^{-3}.

Details of the data analysis and experimental parameters will be discussed in Chapter 3.

2.4 Laser machining

In order to study the samples using proton-proton scattering, a sample thickness of as close to 100 μm as possible is optimal due to the penetration of the proton beam at the energies used.

Parameter	Value
Laser frequency	30 kHz (~ 12 W)
Scan speed	0.1 mm/s
Hatch pitch	0.05 mm
Z-step	0.1 mm

Table 2.1: A table of the laser machining parameters used to mill diamonds. These parameters remove ~ 10 μm of material.

Samples of up to ~ 200 µm can be studied, although the uncertainties will be greater. Due to the brittle nature of diamonds, mechanical polishing down to this thickness is not possible without risking fracture of the sample, so laser-milling was used. This was performed on an Oxford Lasers A Series Laser micromachining system, which is equipped with a 1064 nm neodymium-doped yttrium orthovanadate ($Nd:YVO_4$) solid state laser, frequency doubled to 532 nm. The nominal power output is ~ 11.4 W at 40 kHz, with a pulse width of < 30 ns. The pulse energy is 250 µJ at 40 kHz, providing a peak power of approximately 8.3 kW. In order to determine appropriate parameters for milling the diamond down to ~ 100 µm, experiments were undertaken on faulty diamonds intended for diamond anvil cell (DAC) experiments and polishing off-cuts from some of the plates intended for further study. The variations in material properties between different samples lead to slight changes in experimental parameters for each sample, but initial parameters used are summarised in table 3.1. These parameters were for one pass using the in-built 'mill rectangle' macro and were found to be capable of removing 10 µm of material. Regions of the samples measuring approximately 300 x 300 µm were thinned down to the appropriate thickness in order to preserve the majority of the material for further study.

2.4.1 Acid cleaning

As the use of laser etching leaves a layer of graphitic material on the sample due to the nature of the ablation, the samples were acid cleaned to attempt to minimise surface contamination. This utilises a powerful oxidising agent to remove any sp^2 or sp^3 impurities (also known as non-diamond carbon - NDC). The procedure used in this work uses potassium nitrate (KNO_3) and sulphuric acid (H_2SO_4) to produce nitric acid as an oxidising agent. Care must be taken not to use more than the required amount of KNO_3, as the nitrate can degrade to form oxygen, which can hinder the cleaning process. The acid and diamond samples were heated under reflux conditions to temperatures of over 200 °C for up to three hours, before being cooled, washed with deionised water, and subsequently dried. This procedure not only removes NDC left from

the micromachining process (Prado et al., 2003), and has the additional effect of leaving the diamond surface oxygen terminated (Bachmann et al., 1991), which helps to minimise the effects of hydrogen on the diamond surface.

3. The relationship between the 3107 cm^{-1} peak and bulk hydrogen content in diamonds as measured by proton-proton scattering – is it a viable proxy?

Declaration

Data collection for the proton-proton scattering experiments was carried out with assistance from Patrick Reichart (Universität der Bundeswehr München). Data analysis according to the methods discussed here was undertaken by Patrick Reichart. Diamonds were polished for FTIR studies by Galina Bulanova, and further thinned prior to laser milling by Hugh Leach (De Beers Technologies, Maidenhead).

3.1 Introduction

The most well-characterised and widely observed hydrogen-containing defect in natural diamonds is the defect responsible for the 3107 cm^{-1} feature in the IR spectrum. This feature was originally observed and attributed to hydrogen in the 1970s (Runciman and Carter, 1971), and has since been recognised as the stretching mode of the tri-nitrogen vacancy hydrogen (N_3VH) defect. This consists of three substitutional nitrogen atoms around a carbon vacancy, with a single hydrogen atom decorating the remaining carbon (J. P. Goss et al., 2014), and is discussed in greater detail in section 1.2.3.1.

When the IR intensity of this feature is higher than that of the intrinsic diamond peaks, diamonds are referred to as being 'hydrogen-rich' (Fritsch et al., 2007; van der Bogert et al., 2009). However, in spite of its use as an indicator of hydrogen content, it is not currently known what proportion of hydrogen within the bulk is captured within the 3107 cm^{-1} centre, and what proportion may be in optically inactive sites. Despite the 3107 cm^{-1} defect being relatively well understood, the quantification of hydrogen content via optical experiments has poses a significant challenge, with no firm grasp of the amount of hydrogen present within diamonds. A number of techniques have previously been used to study hydrogen concentration in diamonds; these will be discussed below.

3.1.1 Ion beam spectrochemical analysis

Ion beam spectrochemical analysis (IBSCA) has been used to study the hydrogen concentration in diamond samples. This technique is a sputtering-based surface technique, somewhat analogous to secondary ion mass spectrometry. This involves the use of an ion beam, typically of positive noble gas ions (e.g. Ar^+), which penetrates the surface of a sample and produces excited sputtered particles, the fluence of which is considered as representative of the elemental composition of the near-surface region (Rupertus, 2011). Once sputtering has occurred, the mass loss can be weighed, and hydrogen concentration determined by measurement of a

specific hydrogen-related line and comparison with a standard, for example a mica sample with a known hydrogen content (Tsong and McLaren, 1975). Experiments found that all diamonds studied appeared possess ~ 1 atomic % of hydrogen, no matter the type or locality (Hudson and Tsong, 1977). This is inconsistent with expected results from optical studies, but it could be explained by the fact that IBSCA is a surface-specific technique, only studying the layers down to a depth of ca. 200 nm. The diamond surface naturally adsorbs hydrogen if under air, so this could be responsible for the lack of agreement with optical techniques. The discrepancy could also potentially arise from the result of luminescence excitation driving photon emission which could obscure the true value of hydrogen content.

3.1.2 Nuclear reaction analysis

Nuclear reaction analysis (NRA) is a technique that uses MeV ion beams to measure hydrogen content in samples using reactions that occur upon collision with protons, such as:

$$^{15}N + {}^{1}H \rightarrow {}^{12}C + {}^{4}He + gamma\ ray \quad (3.1)$$

The yield of characteristic gamma rays is detected, and due to the proportionality of the gamma rays with hydrogen concentration, the hydrogen concentration can be measured as a function of depth (Lanford, 1992). NRA studies on diamonds have previously suggested that diamonds can contain anywhere between 500 – 3500 ppm of hydrogen (Sideras-Haddad et al., 2001). With these measurements, the migration of hydrogen from the volume of the sample is believed to be significant, and hydrogen content measured by this method is also believed to be inconsistent with optical studies, with the bending and stretching vibrations observed only accounting for a small part of the total hydrogen present (Sellschop et al., 1992). It is worth noting that NRA is only capable of sampling depths of ca. 2000 Å (0.2 μm). This means that issues similar to those discussed above for IBSCA must also be considered due to the surface specific nature of the technique.

3.1.3 Elastic recoil detection analysis

Another technique that has been used to study hydrogen content within diamonds is elastic recoil detection analysis (ERDA). The energy-angle dependence of scattered particles in an elastic collision is well known (Chu et al., 1978). A depth profile of hydrogen within a thin sample can be measured through the use of an energetic ion beam being directed at a sample and detection of the recoiled atoms and their energies. In diamonds, the detection limit has been estimated at both trace level (< 1 wt %) (Doyle et al., 1997) and approximately 50 ppm (Sweeney et al., 1999). This technique has been applied to a number of diamond samples, including a range of hydrogen-implanted areas (10, 40, 150 and 1000 atomic ppm) within a natural type Ib sample (Sweeney et al., 1999). In this work, the 10 and 40 ppm implants were not resolved from the diamond background, suggesting sensitivity issues for the use of this technique if the concentration proves to be lower than 50 ppm. In the same study, the intensity of the 3107 cm^{-1} was also correlated with ERDA measurements within a series of natural samples from the Muskox (Canada) and Roberts Victor and Venetia (South Africa) localities. No correlation was observed between the infrared absorbances and bulk H as measured by ERDA. A potential issue arises in terms of the sensitivity of ERDA with respect to the expected hydrogen concentrations via optical studies, and also to relating the 3107 cm^{-1} peak to bulk hydrogen within diamonds. This chapter aims to investigate this further.

3.1.4 The NVH^0 defect

Before the recent calibration of N_3VH concentration from the IR absorption intensity, an estimate was derived for the neutral nitrogen-vacancy hydrogen (NVH^0) concentration. This defect has only been observed in synthetic diamonds, but is thought to be an intermediate involved in the formation of the N_3VH defect in CVD diamond (J. P. Goss et al., 2014). This calibration is based off its IR-active stretching mode at 3123 cm^{-1} and the change in the

absorption intensity with varying temperature (Liggins, 2010). The empirical relationship derived is as follows:

$$[NVH^0]_{ppb} = 200(15)ppb\ cm^2 \times I_{3123\ cm^{-1}} \quad (3.2)$$

where $I_{3123\ cm}{}^{-1}$ is the integrated intensity of the 3123 cm^{-1} local vibrational mode and [NVH^0] is the concentration of the NVH^0 defect. Given that the 3123 and 3107 cm^{-1} both arise from C-H stretching modes within trigonal (C_{3v}) defects. Although the NVH^0 defect is ostensibly C_{1h} symmetry, the hydrogen atom is believed to tunnel the 3 available sites, providing an average of a C_{3v} symmetry on spectroscopic timescales (J. P. Goss et al., 2003a). This means that it could be reasonably assumed that the extinction coefficients would be similar, and so it would be possible to provide an estimate of [N_3VH] using the equation and calibration displayed above. As this estimate only considers the 3107 cm^{-1} defect, there is an inherent assumption that the majority of the hydrogen within natural diamonds is contained in the form of the 3107 cm^{-1} defect. This must be considered when drawing conclusions and interpreting trends based upon this estimate.

3.1.5 Characterisation of the 3107 cm^{-1} extinction coefficient

Recent work has utilised time-resolved infrared spectroscopy in order to attempt to provide insight into the vibrational dynamics of the C-H stretch upon excitation using infrared light (Coxon et al., 2020). This work provided information about the energies of the vibrational states involved in the defect stretching mode, and, tied with theory, allowed for the generation of an extinction coefficient for the conversion of 3107 cm^{-1} peak area to defect concentration within diamond. This relationship was found to take the form

$$[N_3VH^0]_{ppb} = 110(10)ppb\ cm^2 \times I_{3107\ cm^{-1}} \quad (3.3)$$

Where $I_{3107\ cm}{}^{-1}$ is the integrated intensity of the 3107 cm^{-1} local vibrational mode and [N_3VH^0] is the concentration of the N_3VH^0 defect. This result was verified using two approaches. The

first was by corroboration with the known relationship between absorption strength and concentration for the NVH^0 defect as described in section 3.1.4, which provided values similar in magnitude to the results calculated for a specifically grown CVD sample, HPHT annealed to produce the N_3VH centre. The second method was to produce an estimate for a maximum [N_3VH^0] from the total nitrogen content in the synthesised sample, specifically any nitrogen concentrations which cannot be accounted for in defects other than N_3VH^0 after the sample had been HPHT annealed. This provided an estimate for maximum concentration consistent with the other results for the synthetic sample, providing some evidence of the produced extinction coefficient's accuracy.

An independent method of measuring bulk hydrogen would be able to investigate whether or not the intensity of the 3107 cm^{-1} peak can be used as a reliable proxy for bulk hydrogen content, and if so, whether or not the calibrations produced for [NVH^0] and [N_3VH^0] are useful when considering the amount of hydrogen present within diamonds. Obtaining a proxy for bulk hydrogen would allow for further study of how and why hydrogen content varies with locality, which could potentially shed light into differences in mantle chemistry across the parts of the world in which diamonds can be found.

The work in this chapter contains one main hypothesis to be tested. This is that the bulk of the hydrogen within natural diamonds is contained within the N_3VH centre, and thereby the 3107 cm^{-1} peak attributed to the N_3VH centre can be considered a viable proxy for the bulk hydrogen content in diamonds. If this hypothesis is true, then the expected results would be a linear trend when plotting 3107 cm^{-1} peak area vs. proton-proton [H]. In order to conclude that the majority of the hydrogen is indeed present in the N_3VH centre, then the results obtained from the proton-proton experiments would be expected to agree with the previous results for extinction coefficients for the relevant point defects in diamond. Either way, the results from these studies provide significant context as to the presence of this ubiquitous impurity within diamond, and

knowing whether or not there is one dominant hydrogen sink within the crystal is valuable information that can be taken forward by further work.

3.2 Materials and methods

3.2.1 FTIR

Section omitted for brevity. A full write up can be found in chapter 2. FTIR maps were collected over the regions of the diamond that were subsequently thinned using the laser machining techniques discussed below.

3.2.2 Samples

Samples were chosen based on the results of FTIR studies. The decision was taken to study samples which had regions of homogenous 3107 cm^{-1} intensity in order to test the relationship between the 3107 cm^{-1} intensity and bulk hydrogen concentration. The samples used in this work were RTD002 and RTD003 – two 'hydrogen-rich' samples from the Argyle mine in Australia – Argyle 16 which has a very low 3107 cm^{-1} intensity and Argyle 78 and Diavik 127 which have intermediate peak intensities. The hypothesis can thus be tested across a wide range of hydrogen contents. Microscopy images of the samples with the regions of interest highlighted are displayed in figure 3.1.

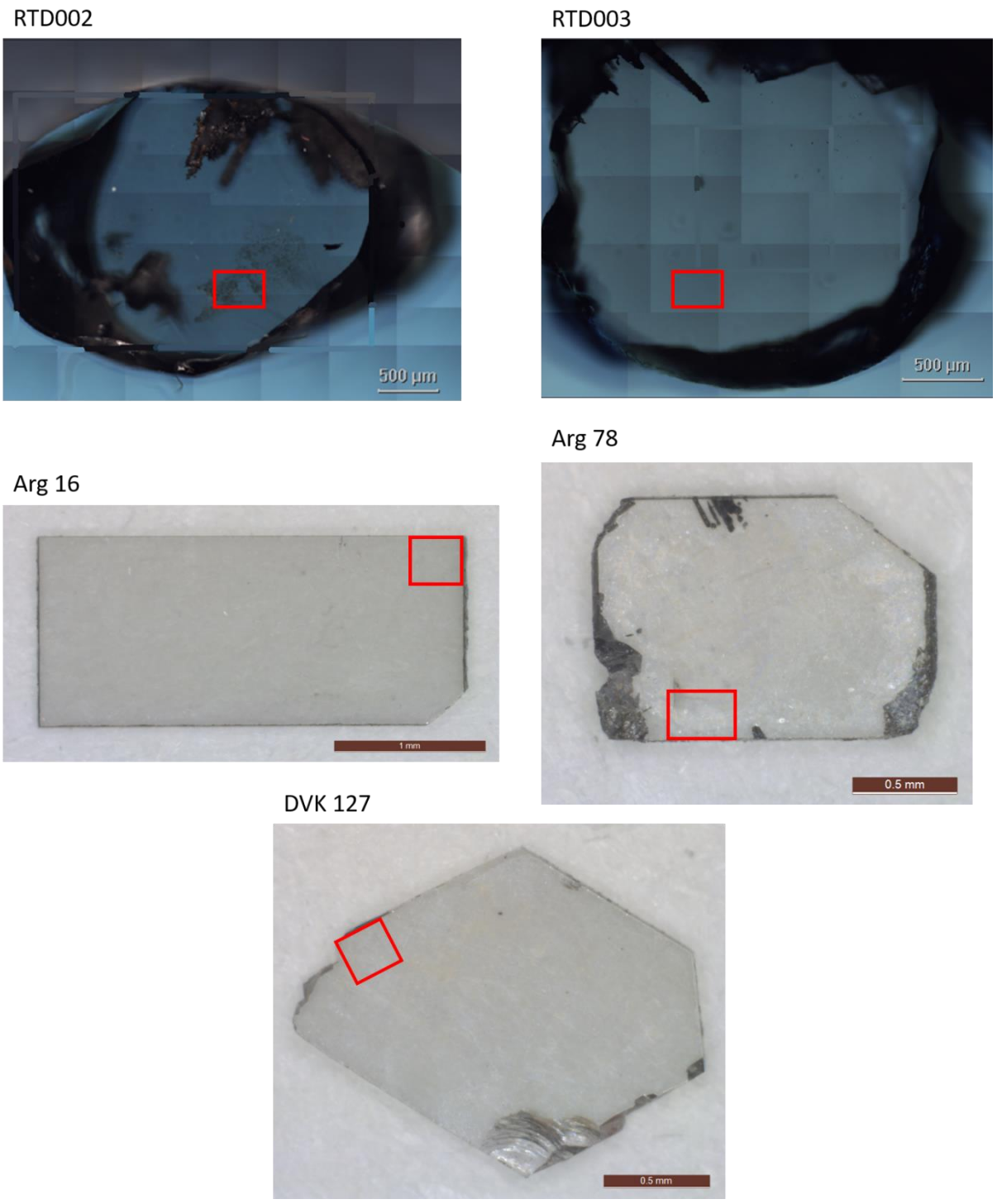

Figure 3.1: Microscopy images of the samples studied. The regions thinned for study via proton-proton scattering are highlighted in red.

3.2.3 Proton-proton scattering – data analysis

The experimental parameters for the proton beam for each sample are indicated below in table 3.2:

Sample	Beam energy (MeV)	Current (pA)	Time (min)
RTD003	20	15	225
RTD002	20	15	200
Arg 16	20	20	306
Arg 78	20	15	560
DVK 127	20	12	325

Table 3.2: A table displaying the parameters of the proton beam used for each sample studied, along with the time each run took to collect the data.

Analysis of the data was performed using a set of programs developed by Patrick Reichart at the Universität der Bundeswehr München. A list of the steps involved in this analysis is presented below. This will be presented for Arg 16 in the results section as an illustrative example of the analysis procedure (see figures 3.3 and 3.4).

1. Filter scattering events to isolate coincident protons using a time window of ~ 5 ns.
2. Angular filtering using vertical detector strips in order to produce a scattering plane.
3. Filter using horizontal detector strips to only include protons scattered at 90 ° to each other.
4. Correct the path length effect in the energy spectra in order to prepare a depth scale. A higher energy loss has been observed for protons scattered at higher angles, leading to a curved distribution of counts from any one depth (Moser et al., 2016; Reichart and Dollinger, 2009). This has been calculated using a Monte Carlo simulation to provide a correction. All deviations are then corrected to the zero point in order to remove the path length effect from the detector.

5. Correct for signal loss due to depth-dependent filter efficiency. For this work, many of the diamonds were too thick for previous efficiency corrections. RTD002 was used to produce a new calibration which can be applied to the other samples in this dataset. This requires the assumption of a constant H depth profile for this diamond. Based upon the FTIR studies, this is a reasonable assumption due to the homogeneity of the sample, but nevertheless must be considered. This will be discussed further in section 3.3.1.

6. Normalise coincidence counts to H-at/cm^2 using a well-known H-rich sample. The sample used in these analyses is a zoisite crystal of ~ 100 μm sample thickness. This sample is well-studied but still provides a significant source of uncertainty in the final values.

7. Produce a depth scale using the energy loss from the back surface, providing an approximation of the diamond thickness. The depth axis can then be rescaled using this thickness. This is a linear approximation but falls within the uncertainties of the technique.

8. Subtract the background. In the thicker samples presented here, the low energy background is ignored. This is due to the accidental coincidences from nuclear reactions with the carbon atoms in the diamond. These produce significant noise that must be corrected for.

Studies using this technique on natural diamonds have not been previously attempted. Alongside the geological processes investigated by the work, this study also tests whether or not proton-proton scattering is a viable technique for the analysis of natural diamonds.

3.3 Results

3.3.1 Proton-proton scattering

When studying natural diamonds using this technique, a number of problems arise. First is that the highest proton energies achievable using this set up of 25 MeV cannot be used to the nuclear resonances from carbon within the diamond (Reichart and Dollinger, 2009). Second is the difficulty of providing samples of a thickness below 100 µm due to the brittle nature of diamond. This means that the energy-loss of deep protons is too high to separate the signal from the front of the diamond from the accidental coincidences produced through nuclear reactions. In order to study these samples, a new depth-dependent calibration for signal loss was needed. RTD002 was selected to provide this calibration due to its assumed homogenous hydrogen depth profile.

Figure 3.2 shows the depth-dependent filter efficiency calibration derived from the measurements on RTD002. Assuming that the distribution of hydrogen is homogenous with depth, an exponential decay can be observed (linear on the logarithmic scale in the diagrams). This correction can then be applied to other diamonds in the data set to enable analysis of diamonds thicker than those that have been previously measured.

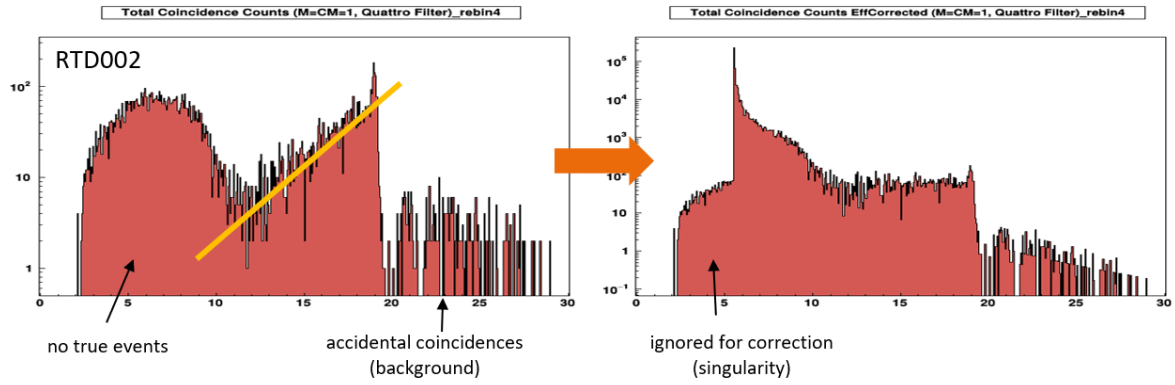

Figure 3.2: The measurements on RTD002 used to produce a calibration for the filter efficiency as a function of depth in thick diamonds. The count scale on the y-axes is logarithmic.

Figures 3.3 and 3.4 show an illustrative flow-chart of the analysis steps involved to produce a depth profile for Arg 16.

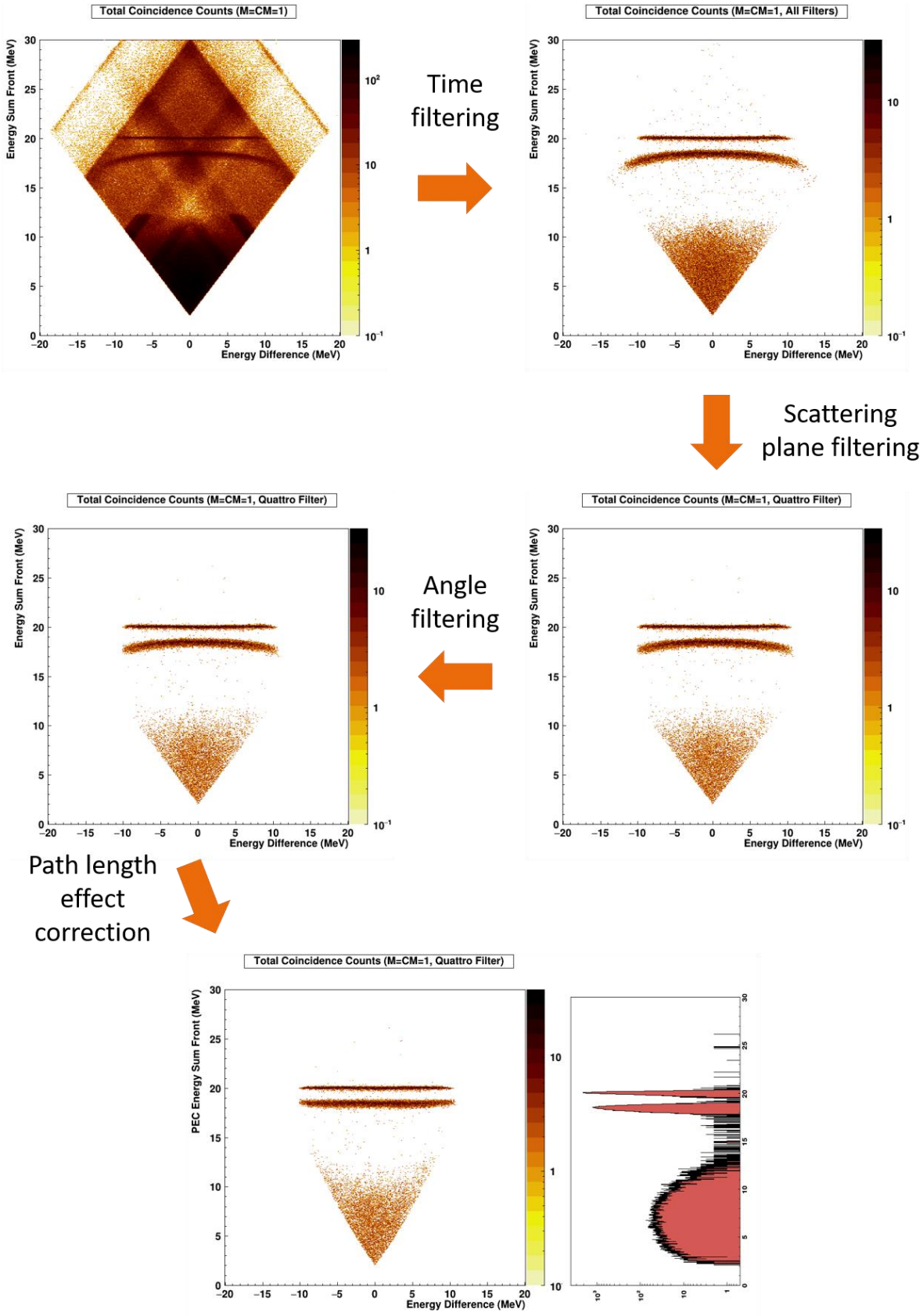

Figure 3.3: An illustrative flow chart displaying the analysis of proton-proton data for Arg 16. The initial diagram displays the total events using a time coincidence of 500 ns. Next is the scattering events once a coincidence filtering window of ~ 5 ns is applied. A filter using the vertical detectors to filter by scattering plane is applied. The final filtering uses the horizontal detectors to select events with a total angle of 90 °. A path length effect correction is then applied, and a depth profile is produced on the bottom right.

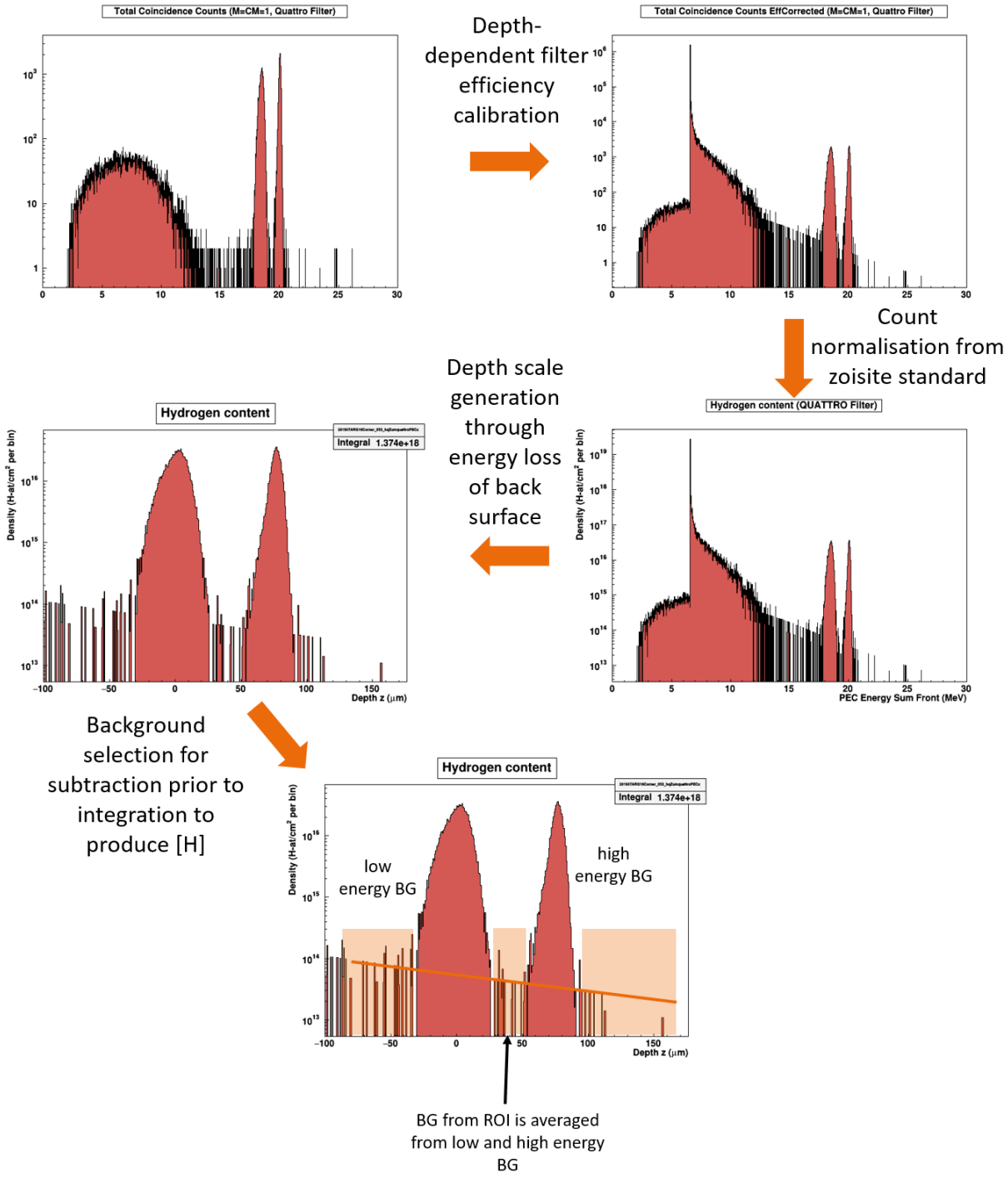

Figure 3.4: The second part of the flow chart for proton-proton analysis. Once a depth profile is produced, the depth-dependent filter efficiency calibration calculated from RTD002 is then applied. The counts are then normalised based on a zoisite standard. The depth scale is then generated through energy loss analysis from the back surface. Finally, a background is selected for subtraction as an average of the low- and high-energy backgrounds. The remaining counts are integrated to produce a final [H] in ppm.

Figure 3.5 displays the collected proton-proton data for RTD003. Fig. 3.5a shows the region of study, with the red crosshair indicating the area illuminated by the proton beam. The dimensions of the area studied are 50 x 50 µm. 3.5b displays the depth profile of integrated hydrogen concentration, in cm^{-2}, with contamination from the front and back surfaces highlighted. The region of interest (ROI) lies between these surfaces and is indicated by the grey shaded area. The hydrogen content appears homogenous with depth and in the xy plane.

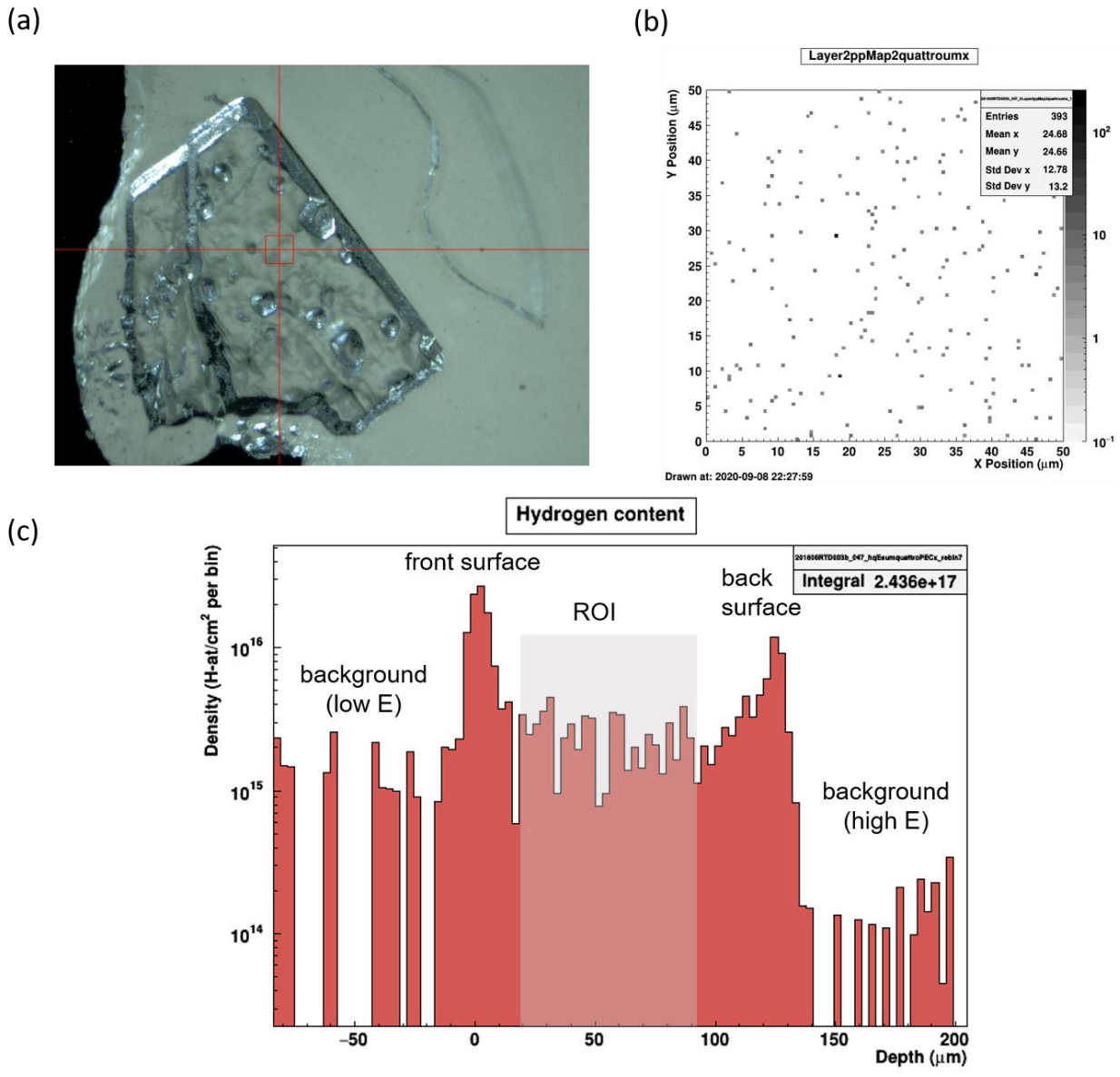

Figure 3.5: (a) An image of the thinned region of RTD003. The area scanned using the proton beam is indicated by the red crosshair. Its dimensions are 50 x 50 µm (b) an xy plot of the hydrogen counts within the ROI (c) A depth profile of the H density in cm^{-2} vs. the energy sum of the coincident protons, functioning as a measure of depth within the sample. The region of interest (ROI) is indicated by the grey box and the front and back surfaces are indicated.

Figure 3.6 displays the same data as figure 3.5 for RTD002. This sample was ~ 200 µm thick; to account for this a ROI was selected as far from the low energy background as possible. In this case, the low-E background contains noise from the nuclear reactions of carbon. To account for this, the low-E background was negated for background subtraction, and the high-E background was extrapolated in order to provide a baseline for the hydrogen content. The hydrogen content appears homogenous in depth and in the xy plane.

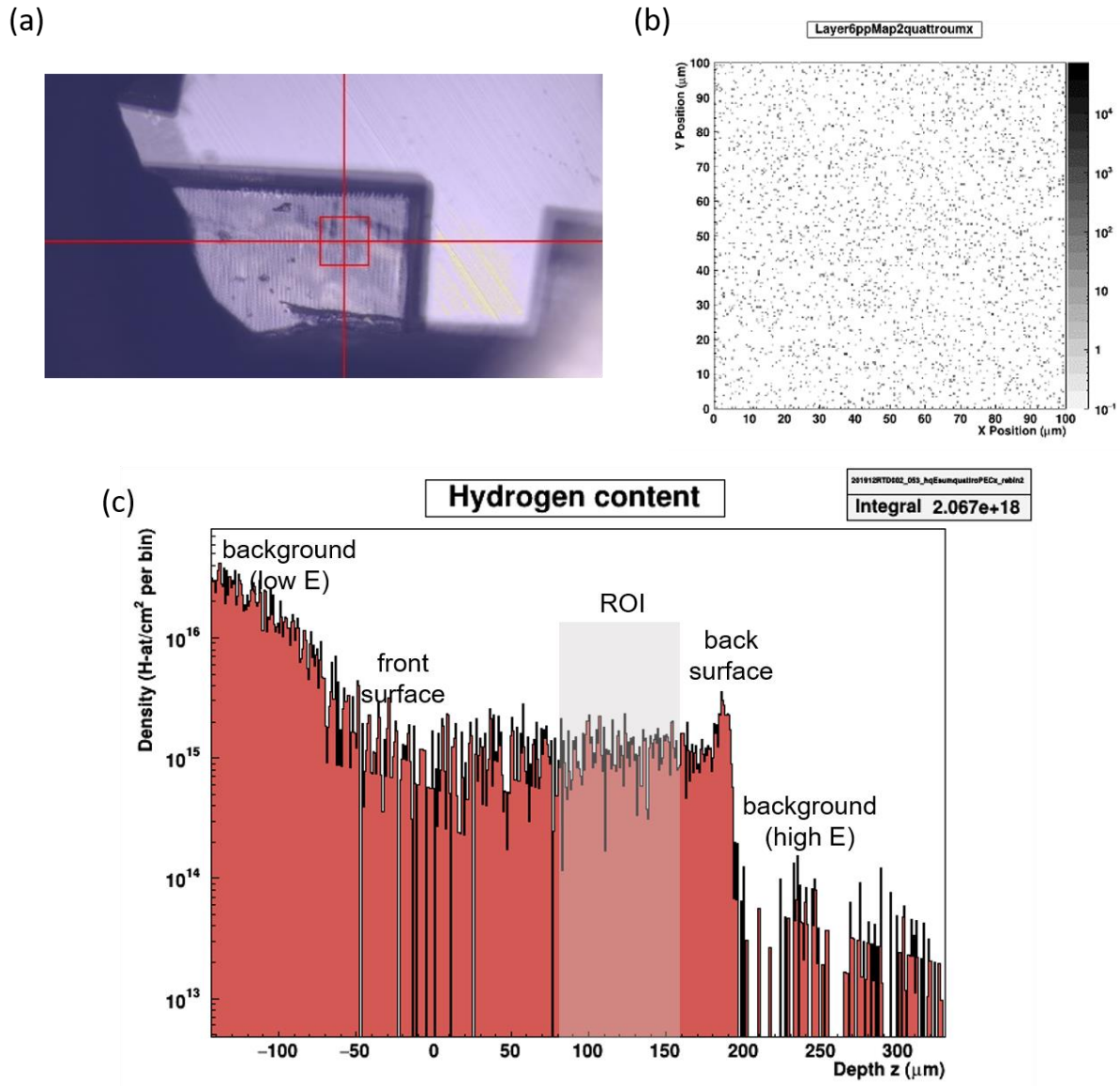

Figure 3.6: (a) An image of the thinned region of RTD002. The area scanned using the proton beam is indicated by the red crosshair. Its dimensions are 100 x 100 µm (b) an xy plot of the hydrogen counts within the ROI (c) A depth profile of the H density in cm^{-2} vs. the energy sum of the coincident protons, functioning as a measure of depth within the sample. The region of interest (ROI) is indicated by the grey box and the front and back surfaces are indicated.

Figure 3.7 shows the results for Arg 16. This sample shows very low statistics in the ROI, which can be clearly seen by the relative size of the surface peaks to the signal from within the diamond. These are not significantly above the background, and so the statistical error of the background and signal provide the limit for the result when producing [H]. It is not possible to comment on the homogeneity of the hydrogen distribution due to the low count rate.

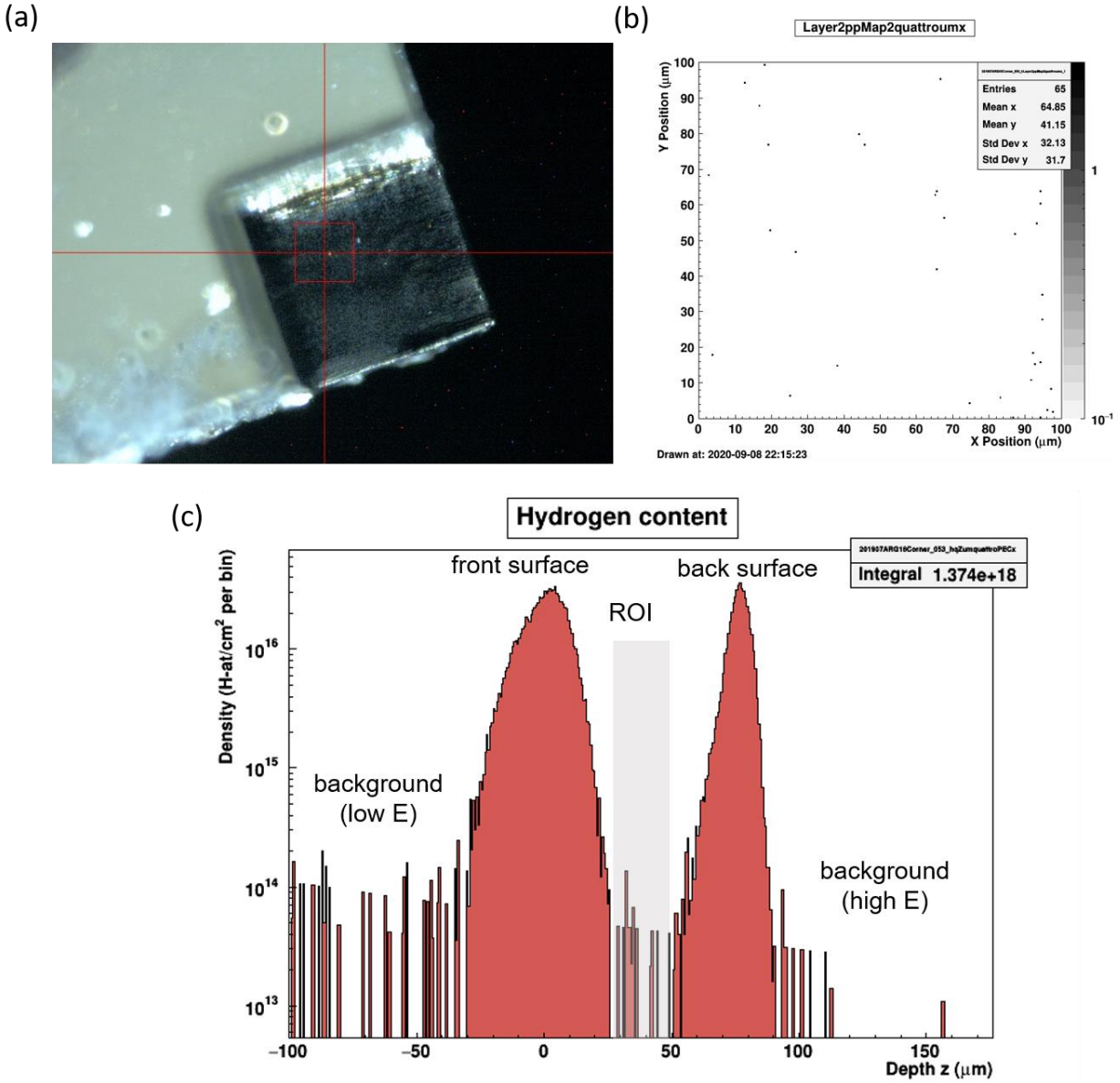

Figure 3.7: (a) An image of the thinned region of Arg 16. The area scanned using the proton beam is indicated by the red crosshair. Its dimensions are 100 x 100 μm (b) an xy plot of the hydrogen counts within the ROI (c) A depth profile of the H density in cm^{-2} vs. the energy sum of the coincident protons, functioning as a measure of depth within the sample. The region of interest (ROI) is indicated by the grey box and the front and back surfaces are indicated.

Figure 3.8 shows the DVK 127 results. It is apparent that the front surface is much rougher than the other samples, with the difference between the front and back surfaces being quite distinct. The ROI can be chosen closer to the back surface in order to reduce uncertainties introduced by the rough front surface. There could be some inhomogeneity present in figure 3.8b, but the count rate is too low to state this with certainty.

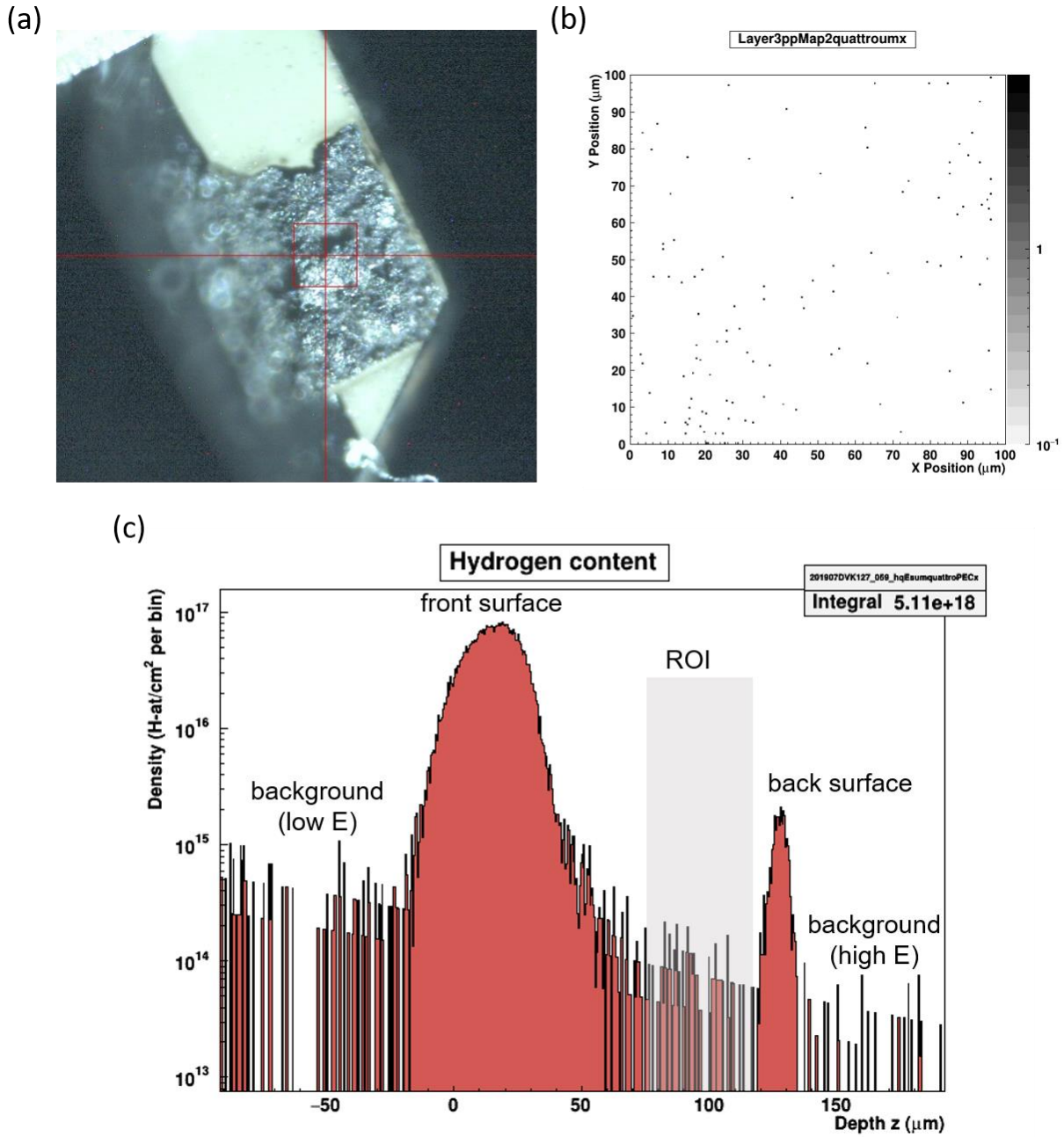

Figure 3.8: (a) An image of the thinned region of DVK 127. The area scanned using the proton beam is indicated by the red crosshair. Its dimensions are 100 x 100 µm (b) an xy plot of the hydrogen counts within the ROI (c) A depth profile of the H density in cm^{-2} vs. the energy sum of the coincident protons, functioning as a measure of depth within the sample. The region of interest (ROI) is indicated by the grey box and the front and back surfaces are indicated.

Figure 3.9 displays the proton-proton results for Arg 78. Once again, the sample is nearly 200 µm thick, meaning that the high energy background must be extrapolated in order to provide a background for the ROI. There appears to be some inhomogeneity with depth in this sample, as can be seen in the depth profile. There also appears to be some inhomogeneity in the xy plane, as presented in 3.9b and 3.9c, with some regions of the diamond seeming to have a higher concentration of hydrogen than others.

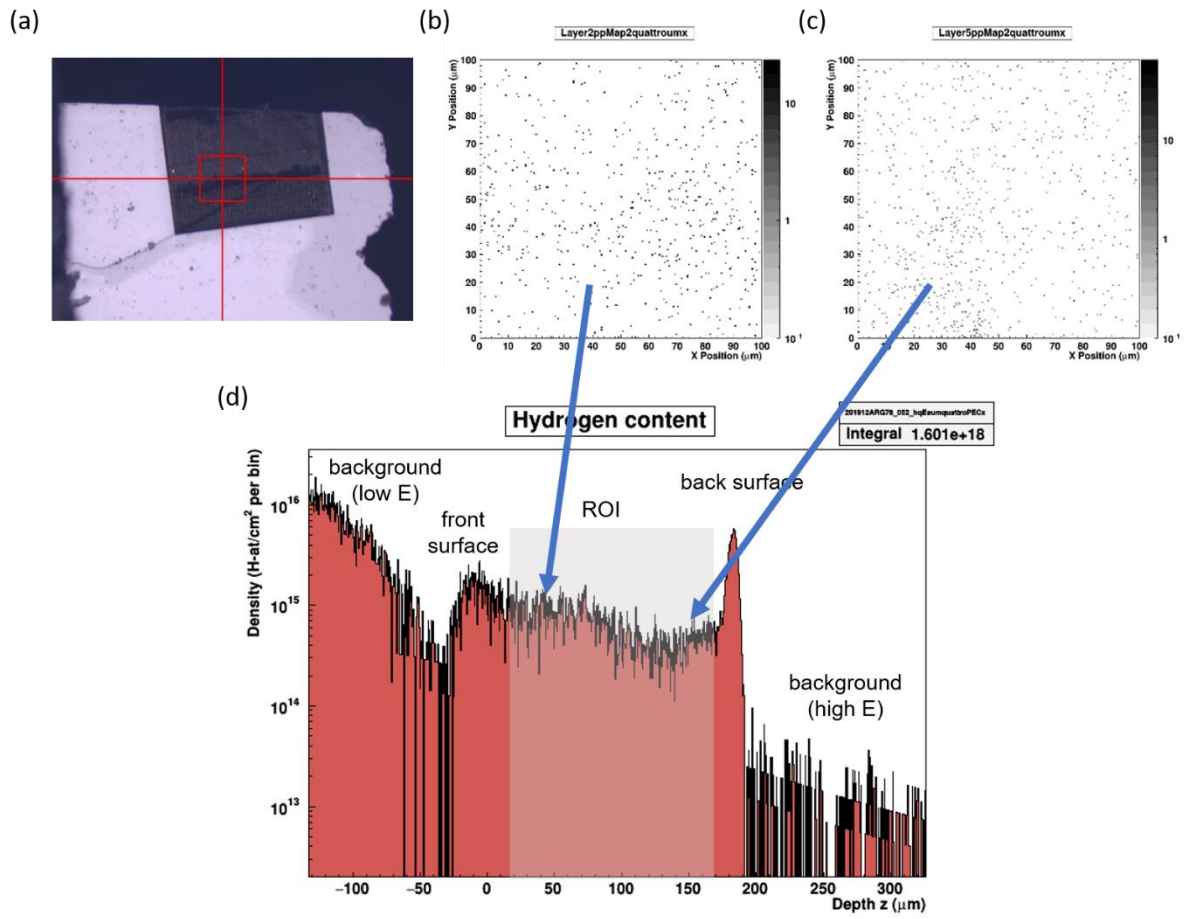

Figure 3.9: (a) An image of the thinned region of Arg 78. The area scanned using the proton beam is indicated by the red crosshair. Its dimensions are 100 x 100 µm (b) an xy plot of the hydrogen counts within the ROI towards the front surface (c) an xy plot of the hydrogen counts within the ROI towards the back surface (b) A depth profile of the H density in cm^{-2} vs. the energy sum of the coincident protons, functioning as a measure of depth within the sample. The region of interest (ROI) is indicated by the grey box and the front and back surfaces are indicated.

3.3.2 IR

Table 3.3 displays the results of the IR studies on the samples across the thinned regions. Presented are the concentrations of the various nitrogen aggregates, along with the integrated area of both the 3107 cm^{-1} peak and the platelet peak (B'). Uncertainties are derived from the standard deviation across the regions studied.

RTD002 and RTD003 show a very high concentration of nitrogen in its aggregated form, along with a very intense 3107 cm^{-1} and platelet peak. Arg 16 shows a significant amount of nitrogen and platelets, but a low 3107 cm^{-1}. Arg 78 also contains a significant amount of nitrogen, along with a moderately intense 3107 cm^{-1} peak, but has the lowest platelet content of all the samples. DVK 127 contains a less aggregated nitrogen content, a low platelet content and a low 3107 cm^{-1} intensity. The platelet degradation is also displayed, with Arg 16 containing the least degraded platelets, and Arg 78 containing the largest variation from expected behaviour.

Sample	$[N_A]$ (ppm)	$[N_B]$ (ppm)	$[N_t]$ (ppm)	I(3107) (cm^{-2})	I(B') (cm^{-2})	Platelet degradation (%)
RTD002	10.2(6.8)	1169.1(34.0)	1179.2(28.5)	253.9(6.9)	686.2(16.6)	27.2
RTD003	19.1(4.7)	1705.3(219.0)	1724.4(214.3)	205.0(22.7)	939.0(85.7)	31.7
Arg 16	223.2(32.7)	547.5(40.5)	770.8(72.4)	3.6(0.6)	433.9(16.7)	1.6
Arg 78	11.5(10.0)	709.5(119.6)	720.9(119.5)	48.9(5.1)	6.2(12.4)	98.9
DVK 127	826.4(21.5)	50.7(6.6)	877.1(27.0)	35.3(7.9)	23.0(2.6)	43.7

Table 3.3: A summary of the results from the IR scans over the regions that were subsequently thinned down in preparation for proton-proton scattering.

3.3.3 IR vs. proton-proton

Figure 3.10 is a plot of the 3107 cm^{-1} intensity in cm^{-2} against the concentration in ppm. The black squares represent the results from the proton-proton scattering experiments discussed within this chapter. The red circles and blue triangles represent the expected concentrations of the N_3VH centre as predicted by the Liggins and Coxon extinction coefficients respectively. Uncertainties on the x-axis are representative of inhomogeneity in the intensity of the 3107 cm^{-1} peak. These results are also summarised below in table 3.4. Immediately apparent is that the predicted values of [N_3VH] do not correlate with the values observed using proton-proton scattering. The values predicted using IR alone are typically 20 times lower than the values as measured by proton-proton scattering. The predicted trend from the IR experiments would be that the [H] for Arg 78 would be somewhere between the values measured for DVK 127 and RTD003. However, Arg 78 is observed to contain the highest [H] of all samples within this study. As such, there is no observation of a linear trend between 3107 cm^{-1} intensity and [H] when the whole data set is considered.

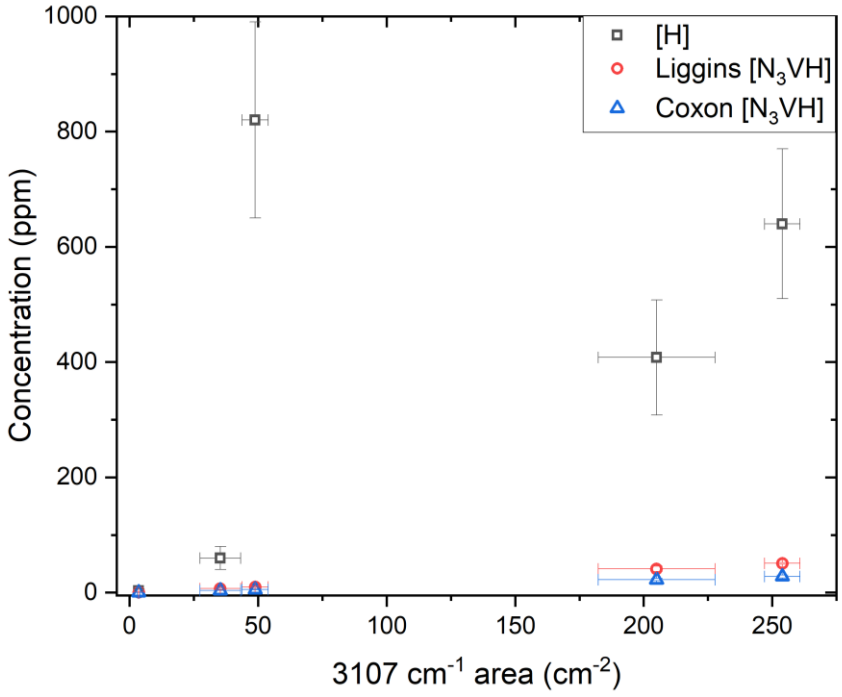

Figure 3.10: A plot of the 3107 cm^{-1} area in cm^{-2} against concentration in ppm. Black squares are from the proton-proton experiments, red circles are predicted [N_3VH] from Liggins, 2011 and blue triangles are predicted [N_3VH] from Coxon 2020. X-error bars are a representation of inhomogeneity in the 3107 cm^{-1} area within the region of interest and y-error bars are technique-specific.

Sample	[H] proton-proton (ppm)	[N_3VH] (Liggins) (ppm – 1 d.p.)	[N_3VH] (Coxon) (ppm – 1 d.p.)
RTD002	640(130)	48.8	26.8
RTD003	408(100)	44.8	24.7
Arg 16	< 3.3	0.7	0.4
Arg 78	820(170)	9.8	5.4
DVK 127	60(20)	5.1	2.8

Table 3.4: A summary of the results of the proton-proton scattering experiments within this study and how they compare to the predicted concentrations of the N_3VH defect previously discussed.

Figure 3.11a displays the relationship between the intensity of the platelet peak against the observed [H]. There is no observable relationship between the two, with the sample with the lowest I(B'), Arg 78 containing the highest [H]. Fig. 3.11b shows the relationship between % platelet degradation and the measured [H]. There appears to be a slight positive correlation, with the least platelet degraded diamond, Arg 16, containing the lowest [H], and the most platelet degraded, Arg 78, containing the highest [H]. Aside from this, there is some spread, with the three intermediate diamonds not falling on the trend between the two endmembers.

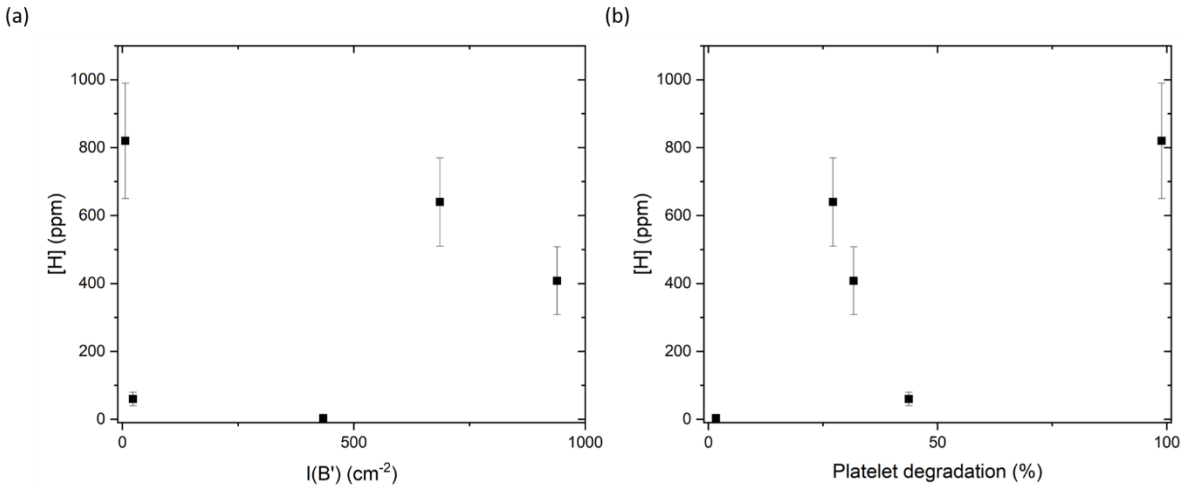

Figure 3.11: (a) A plot of the integrated area of the platelet peak (B') in cm^{-2} against hydrogen concentration in ppm as measured by proton-proton scattering. (b) percent platelet degradation against [H] in ppm

Figure 3.12 shows the concentrations of the various nitrogen aggregates against the [H] in ppm. Once again there appears to be no correlation between the concentrations of any specific nitrogen aggregate and the concentration of hydrogen measured.

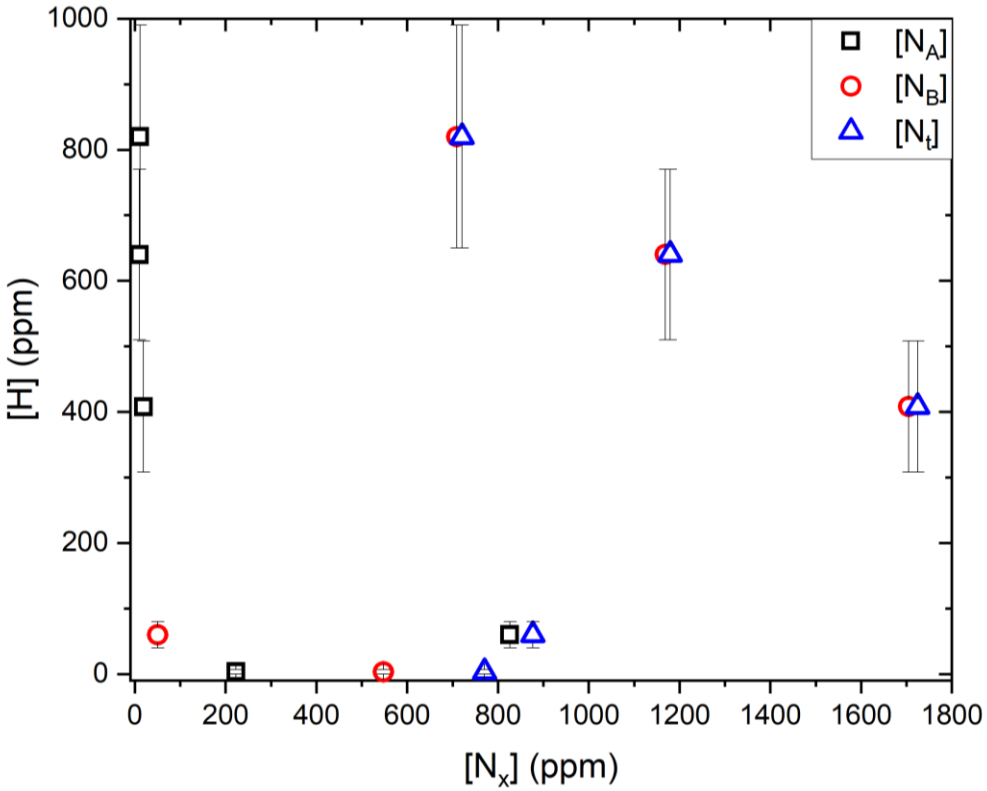

Figure 3.14: A plot of the concentrations of the various nitrogen aggregates in ppm against hydrogen concentration in ppm as measured by proton-proton scattering. Black squares represent [N_A], red circles represent [N_B] and blue triangles represent [N_t].

3.4 Discussion

One factor that must be noted about this work is the assumption that the hydrogen distribution within the diamond remains unchanged after laser machining to provide thinned regions. While the effect of the hydrogen beam used in proton-proton scattering is known to be the lowest of the ion-beam techniques (Reichart, 2004), the effect of the laser on hydrogen distribution is unknown. In order to test the behaviour of the 3107 cm^{-1} feature, it would be preferable to obtain FTIR spectra before and after thinning. Due to the surface left after laser machining, this was not possible, and it is therefore not known with certainty that the peak would maintain its intensity after thinning. It is also possible that the heat transfer from the laser would facilitate short-range hydrogen diffusion if the hydrogen is present in a form that can easily migrate. While the high thermal conductivity of diamond suggests that heat would be quickly transferred away from the diamond and in to the metal on which it is mounted, it has not been possible to rule out this scenario during this work.

The key results of this study are presented in figure 3.10. The values observed via proton-proton scattering indicate that the intensity of the 3107 cm^{-1} peak does not appear to provide a good indicator of the bulk hydrogen content within a sample. In all samples (aside from Arg 16, for which only an upper limit of [H] could be produced), the concentration of hydrogen present is at least order of magnitude higher than would be expected from IR studies alone.

The results from this study are lower than the estimates from past NRA studies of diamonds containing between 500 – 3500 ppm of hydrogen (Sideras-Haddad et al., 2001). In this work, the highest concentration of hydrogen observed was 820 ppm, with three out of five samples displaying a concentration below 100 ppm. This is also lower than previous ERDA studies, which showed a range of 100 – 4000 ppm (Sweeney et al., 1999). While these studies were only able to study the near-surface of the diamond, the results presented in this chapter have demonstrated the first measurements of bulk hydrogen within 100 – 200 μm of diamond. This

work supports the conclusions drawn within the ERDA and NRA studies that a significant portion of the H present in diamonds is not infrared-active. This suggests that determining the amount of hydrogen present in a diamond through the use of optical techniques alone may not be possible.

The value observed in Arg 16 is notably low, with a hydrogen content indistinguishable from the background of accidental coincidences leading to a value of < 3.3 ppm. This is comparable with the amount of hydrogen observed within the grain of polycrystalline CVD diamond of < 0.08 ppm (Reichart, 2004), although the difficulties involved in obtaining regions of diamond at ~ 100 μm lead to greater uncertainties when studying natural diamonds rather than synthetic samples.

If the 3107 cm^{-1} peak does not provide a good indicator, then this calls in to question the assignment of diamonds with a 3107 cm^{-1} peak more intense than the intrinsic diamond absorption as 'hydrogen-rich' (Fritsch et al., 2007). In this work, two of the diamonds would be classed as 'hydrogen-rich' through their IR spectra: RTD002 and RTD003. However, the diamond with the highest bulk hydrogen content measured by proton-proton scattering was Arg 78, which would not be 'hydrogen-rich' according to the classification proposed by Fritsch *et al*. This highlights an issue in terms of the classification of diamonds by their optical properties and how these properties relate to the presence of bulk impurities within the crystals.

It must be noted that, aside from Arg 78 there is a general increase of hydrogen content with increasing 3107 cm^{-1} intensity. However, the fact that Arg 78 is so far from the trend suggests one of two things: either Arg 78 is unique in its capability for hydrogen storage or there is not a consistent trend between samples. A possibility is that Arg 78 contains micro- and smaller fluid inclusions. Fluid inclusions have previously been observed to contain significant water contents (Klein-BenDavid et al., 2009; Logvinova et al., 2015; Navon et al., 1988), potentially

in the form of CH_4 (Smit et al., 2016b). If there are fluid inclusions present in this sample, then the value of [H] obtained through proton-proton scattering could not be considered as representative of the bulk. In the image of the scanned region of Arg 78 in figure 3.8a, a line can be seen parallel to the edge of the laser-milled region across the illuminated region. The cause of this is unknown. It may be a result of a change in material properties in the diamond across the milled region, leading to heterogenous absorbance of the laser and therefore variation in the amount of material removed. There is no obvious reason as to why this would be the case, but the fact that the line is parallel to the edge of the milled region, and not the edges of the diamond, suggest it is related to the milling rather than being a property of the diamond itself. For example, if it were caused by a different growth zone, it would be expected to lie parallel to the edges of the polished diamond plate.

The fact that the two diamonds containing the highest and lowest bulk [H] come from the Argyle mine indicates that the factors controlling the incorporation of hydrogen into the diamond can vary significantly on a local scale. The question then arises as to what causes this variation. There is clearly a difference in the availability of hydrogen during diamond growth for different samples. The consequences of this and how it may relate to the nitrogen aggregation sequence – specifically how it may affect the formation of the N_3VH defect – are discussed further in chapter 4.

An initial aim of this work was to assess the viability of the calibrations for the [N_3VH] previously produced (Coxon et al., 2020; Liggins, 2010). If the value from Arg 78 is indicative of the bulk [H] content then this is not possible to evaluate, as the calibration from proton-proton scattering does not appear to be possible. However, if Arg 78 is excluded from the dataset (due to the potential sampling of inclusions and inhomogeneities that may not be representative of the bulk diamond) then a value can be produced from the linear trend observed

within the other samples. Linear regression via an ordinary least-squares method, using a forced zero y-intercept due to assumed proportionality provides the following trend

$$[H]\ (ppm) = 2.30(0.15)\ \times I(3107\ cm^{-1})\ (cm^{-2}) \qquad (3.4)$$

This has an R^2 value of 0.9868 within a 95% confidence interval. This calibration is ~ 20 times higher than the values that are expected from the Coxon and Liggins calibrations. This has two potential connotations. The first is that the Coxon and Liggins calibrations provide an underestimation of the actual concentration of the hydrogen-containing defects within the diamond (assuming that the majority of hydrogen in natural diamonds is present in the form of the N_3VH centre). A simple consideration of the relative amounts of N_3VH expected compared to B-centre concentration tells us that the Coxon calibration is unlikely to have an error that significant. The second is predicated on the Coxon calibration being correct. If this is the case, then, while the 3107 cm^{-1} intensity is proportional to the bulk hydrogen content, there is still a significant amount of hydrogen contained within the crystal that cannot be accounted for. The question then arises as to where this hydrogen is stored. It could be possible that the numerous smaller peaks observed in the optical spectra of diamonds (Fritsch et al., 2007) are caused by defects with much larger extinction coefficients than that of the 3107 cm^{-1} peak. This would mean that the smaller peaks account for much larger amounts of hydrogen than would be expected. It is also possible that the excess hydrogen is not stored within optically active configurations. This could take the form of extended defects – see below – or potentially through nanometre-scale fluid inclusions that are unobservable via optical techniques.

Platelets have been theorised as potential reservoirs of hydrogen storage within diamonds (Gu et al., 2020). Arg 78 contains the smallest platelet peak but the largest concentration of hydrogen, suggesting that in this example, the platelets do not contain the hydrogen within the bulk of the diamond that cannot be accounted for by the optically observed features. It is

possible that incorporation of hydrogen into the platelet structure could quench the observable platelet features, leading to a lower platelet peak than would be expected from the nitrogen content. This will be discussed in greater detail in chapter 5, along with a candidate for a defect structure within which hydrogen could be contained. Aside from platelets themselves, there appears to be a slight positive correlation with the amount of platelet degradation and the [H] observed in the samples, with Arg 78 containing the most degraded platelets and the highest [H]. This could suggest that an aspect of the platelet degradation forms defects capable of trapping hydrogen. Platelet dissociation can lead to the formation of two primary features: voidites and dislocation loops. Voidites, described as such due to their appearance as small empty spaces, were initially studied in diamond in the 1980s (Barry, 1986; Hirsch et al., 1986). They are octahedral in shape and found inside or near the dislocation loops formed during platelet degradation. Their size ranges from a few nm up to several hundred nm, and large voidites have often been observed as elongated in {110} directions (Navon et al., 2017; Rudloff-Grund et al., 2016). Despite the term voidite, they are not in fact empty, and can in fact be considered as nano- and micro-scale inclusions. They have been observed as containing significant nitrogen contents theorised to be possibly NH_3-related (Rudloff-Grund et al., 2016) along with the observation of solid molecular N_2 under high pressure (Navon et al., 2017). This nitrogen has been theorised as either arising from platelet degradation (Kiflawi and Bruley, 2000) or from the breakdown of B-centres at high temperatures (Navon et al., 2017). If the voidites can function as a trap for hydrogen, then it could be possible that these nano-scale features contain a significant amount of hydrogen not accountable through IR alone. This could potentially explain the discrepancy from predicted trends, but confirmation of the presence of voidites within these samples, and the presence of hydrogen within them, would be needed to confirm this. It is also worth noting that, in the voidites in which nitrogen has been observed, the concentrations have been significant, with up to 350 ppm of nitrogen in some

nanoinclusions. Even if 10 % of that amount of hydrogen were to be incorporated, it would still not account for the discrepancies between IR and bulk [H] observed within this study.

The implications of this work may have significant consequences for the relation of spectral features to bulk impurity concentrations, with the presence of hydrogen-related features possibly not being indicative of the true hydrogen content. Significant work is needed in order to make inferences as to the nature of the fluids from which the diamonds are formed, including the speciation and availability of hydrogen. The range of bulk hydrogen concentrations observed within the four samples studied here from the Argyle locality indicate the wide variety of local conditions conducive to diamond growth, and the varying availability of hydrogen within diamond-forming fluids. It could be that the diamonds containing lower hydrogen concentration simply formed from hydrogen-poor fluids, or it may well be the case that hydrogen incorporation is dependent on trapping at optically inactive defects. For example, an as-yet unidentified extended defect could trap hydrogen within the crystal structure. Specific candidates for this are currently unknown.

3.5 Conclusions and future work

The primary conclusion of this study is clear: the 3107 cm^{-1} peak is not a viable proxy for bulk hydrogen concentration within diamonds, and the concentration of hydrogen does not appear to be significantly correlated with any IR-active features in the diamonds. This has significant gemmological implications and raises an issue when considering 'hydrogen-rich' diamonds, which are classed as such based on the intensity of the 3107 cm^{-1} peak. A theory has been discussed for voidites as a possible trap of hydrogen within diamonds, based upon the high hydrogen concentration in Arg 78, which contains the most degraded platelets.

A geological impact of this is that significant study is still needed to constrain the hydrogen content (both in terms of speciation and availability) within diamond-forming fluids in the lithospheric mantle. The production of a proxy would lead to a useful source in terms of probing this and how it varies with other observable features within diamonds, but this has not been possible from this work.

The fact that the majority of hydrogen does not appear to be contained within one defect lends itself to further study to determine the environment in which it is situated. Due to the decommissioning of the Munich facility in which this work was undertaken, further experiments at the SNAKE microprobe are not currently possible, but a similar technique has been developed at the Lund Ion Beam Analysis Facility (Borysiuk et al., 2013; Ros et al., 2015). This could be used to further the sample size for comparison between IR-active features and bulk hydrogen. The facility at Lund can only be used for samples with a thickness of ~ 15 µm, which would pose significant issues in the production of appropriate samples from natural diamond. Building up a larger dataset would likely provide further insights into this. Further experiments could build up the dataset to provide a better idea of how bulk hydrogen contents vary across localities. Further study could also potentially investigate inhomogeneity across

diamonds. One example would be to examine the variation in hydrogen content in different growth sectors of mixed habit diamonds.

Atom probe tomography (APT) has recently been developed as a promising technique for geochemical applications, capable of isotope analysis on an atomic scale (Reddy et al., 2020). This has been applied to the study of bulk diamond as grown by CVD (Schirhagl et al., 2015), but studies on natural diamonds could be used to add to the information on the environment of hydrogen. Typically, APT samples are studied as needle-like structures of < 100 nm in diameter. Due to this small size, targeting would be very important when considering sample selection for potential studies. For example, it may be possible to study hydrogen dynamics at the boundaries between growth zones within diamonds if an appropriate sample can be produced. However, locating a zone boundary with enough accuracy to produce an APT sample may prove difficult. Several APT samples could also be produced from one diamond in order to examine the variation in bulk hydrogen within one crystal. APT also has the added benefit of being able to study isotope distributions for all elements at once, and so studies not specifically aimed at the hydrogen contents could also be used to provide additional information. APT could also potentially investigate the idea of voidites containing significant hydrogen content, although sample selection and preparation could pose the same issues as discussed above.

Clearly there is still much to be learned from the study of hydrogen within diamonds, and many questions remain unanswered. This work has increased the knowledge around this pervasive impurity, but the implications suggest that hydrogen concentration within natural diamonds is a complex issue, and one that will not be resolved with ease.

4. The N3 and N_3VH centres and the role of hydrogen in the nitrogen aggregation sequence

Declaration

All samples were obtained as polished plates. Approximately half of the Argyle line scans were collected by Laura Speich (University of Bristol). This IR data was subsequently filtered to correspond with the UV-vis spectra collection and processed by me. UV-vis line scans in this chapter were collected by Tian Shao and Andy Shen (Gemmological Institute, China University of Geosciences, Wuhan). All data processing and subsequent analysis was done by me.

4.1 Introduction

As discussed in section 1.2.2, the nitrogen aggregates in diamond are most commonly found as pairs of neighbouring substitutional atoms (the A aggregate) or as groups of four substitutional atoms around a vacancy (the B aggregate). This nitrogen aggregation sequence has been discussed at great length due to its significance in determining the thermal history of diamonds. Alongside these major aggregates, however, there are lesser concentrations of minor aggregates. The minor aggregate that this chapter is concerned with consists of three substitutional nitrogen atoms in the (111) plane, bonded to a common carbon vacancy. This configuration gives rise to the optically active N3 centre (Davies, 1974) – given the N prefix to indicate that it is naturally occurring, which has an EPR analogue in the P2 centre (Smith et al., 1959), also known as the N_3V centre. The structure of the defect is displayed in Figure 4.1.

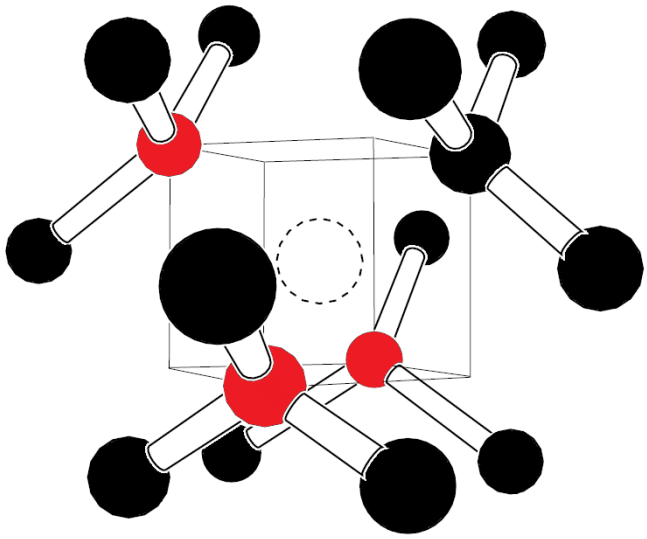

Figure 4.1: The structure of the N3 defect. This consists of three substitutional nitrogen atoms (red) around a carbon vacancy (dashed line). The black atoms are the carbon atoms constituting the host diamond lattice.

The presence of the N3 centre in EPR and luminescence spectra of natural diamonds poses many questions in relation to the nitrogen aggregation process. A correlation has been observed between the intensity of the N3 absorption and the absorption due to B centres (Woods, 1986). Woods attributed this correlation to the N3 defect being a side-product, occurring during the aggregation of A centres to B centres, which necessitates the assumption that the A centres

migrate as a unit. It has, however, also been suggested that this migration is unlikely to take place, and that instead A centres migrate through dissociation (Kiflawi and Bruley, 2000; Mainwood, 1994). Apart from the observed formation of N3 centres, there is no proof of this sort of dissociation. However, due to the fact that the N3 centre is seen to be absent during annealing experiments in which the formation of B centres is observed(Kiflawi and Bruley, 2000), it has been proposed that the N3 centre is an intermediate in this process, via the following method:

$$A \rightarrow N + N \tag{4.1}$$

$$N + A \rightarrow N3 + C_i \tag{4.2}$$

$$N + N3 \rightarrow B \qquad OR \qquad N + N + A \rightarrow B + C_i \tag{4.3}$$

Where C_i is a carbon interstitial (Kiflawi and Bruley, 2000). The fact that the concentration of nitrogen present as N3 centres is very small compared to the major aggregates could suggest that it is thermodynamically favourable for the N3 to capture a migrating N, compared to the analogous process for A centres. However, it must be noted that there is no direct proof of this. Also of note is that there are no single nitrogen centres observed in N3 and B centre-containing natural diamonds. This could potentially be due to the higher temperatures used in laboratory experiments compared to the temperatures involved in geological processes. It is as yet unknown whether the N3 centre is present in natural diamonds as a set fraction of the B centre concentration or whether there are other factors contributing to N3 content within diamonds.

It has been shown that N3 centres can be produced in diamonds through a number of annealing procedures. They can be introduced by heating diamonds which contain A centres and isolated N (Chrenko et al., 1977). They cannot be introduced in pure type IaA diamonds. However, they can also be produced by heating type IaB diamonds or type IaA + Ib diamonds at temperatures above 1960 °C (Brozel et al., 1978), or by annealing diamonds which contain only isolated N

atoms (Collins and Stanley, 1985; Satoh and Sumiya, 1995). The N3 centre can also be grown in to Type IIa diamonds through nitrogen ion implantation and then subsequent annealing at temperatures of over 1200 °C (Zaitsev, 2001). Once again, the temperatures considered here are significantly above the temperatures diamonds are stored at within cratons, which are typically in the region of 1000 – 1200 °C.

It has also been postulated that N3 centres can be formed due to plastic deformation of diamonds containing aggregated nitrogen, resulting in the destruction of the B centres which are present, due to the N3 luminescence often being seen localised at cracks or regions of plastic deformation (Kanda and Watanabe, 1999, 1997). Within these samples, the observed EPL and PL spectra of the N3 centre are broadened due to a distortion of the lattice near the dislocations present in highly plastically deformed diamond (Nadolinny et al., 2009; Rakhmanova et al., 2015). However, this does not account for the presence of the N3 centre in diamonds that do not contain any of the signs of plastic deformation, from direct observations to defects commonly associated with plastic deformation such as the H3 and H4 defects (Stepanov et al., 2011). This information has been used in experiments on samples from Kholomolokh in the northeast Siberian craton, which suggested that, at high temperatures (an annealing temperature of 2200 °C in this case), it is possible for B centres to dissociate into N_3V and C centres (often referred to as P1 centres when discussing their presence in EPR (Smith et al., 1959)), meaning that a high intensity of N3 absorption could possibly be an indication of a high-temperature annealing event after the aggregation of nitrogen into B centres. This has been attributed to a result of tectono-thermal events when superplumes rise (Nadolinny et al., 2020), although the temperatures considered here are significantly higher than the typical temperatures of diamond storage. The N3 center has also been observed to arise in brown diamonds containing stacking faults in (111) planes (Graham and Buseck, 1994).

A calibration has been produced for conversion of the integrated absorption in the zero-phonon line at 415.2 nm to a defect concentration (Davies, 1999); the full method of this conversion will be discussed in Section 4.2.2. This calibration was produced by comparing the strength of the P2 EPR signal (the EPR analogue of the N3 centre) and the P1 EPR signals. The P1 signal derives from N^0, and a calibration to [N^0] is known (Kiflawi et al., 1994); confirmation of this is provided in the form of charge-transfer effects, when excitation using a 514.5 nm Ar^+ light source produces an increase in N3 absorption, along with an increase in N^0 (Davies, 1999). Assuming the mechanism of $N3^- + N^+ \rightarrow N3^0 + N^0$, then the change in N^+ was shown to confirm the N3 calibration value.

As the most common hydrogen containing defect in diamonds, the N_3VH defect, takes the form of an N3 defect with the lone carbon atom surrounding the vacancy decorated with a hydrogen atom, it is easy to envisage a situation where the N_3VH defect is simply formed by the trapping of a hydrogen atom at an N3 centre. Computational studies have indeed suggested that the N_3VH can likely be formed either by the direct trapping of a hydrogen atom by an N3 centre or through the alternative mechanism of an NVH trapping an A-centre (J. P. Goss et al., 2014). While it is generally thought that the former would be the case in natural diamonds, and the latter in synthetic samples, there has been observation of the formation of NVH in HPHT-treated natural samples, along with a strong increase in 3107 cm^{-1} intensity within samples that do not generate B-centres (Lai et al., 2019). This possibly indicates the trapping of generated A-centres by NVH within these samples, thereby quenching the nitrogen aggregation process and leading to a reduced B-centre concentration. This also suggests that neither reaction pathway to N_3VH formation can be discounted in natural samples. There has yet to be any direct evidence of which proposed mechanism, if any, is the primary mechanism by which the N_3VH centre is formed. This means that it is difficult to provide proof as to the role that the N3

and N_3VH defects play in the wider nitrogen aggregation sequence, and whether hydrogen can potentially quench the aggregation.

Detailed optical study of a single diamond from the Ichetju placer in the northern Urals provided some more clues as to the N3 defect's place in the nitrogen aggregation scheme (Vasilev et al., 2019). In this unique sample, the core contains no N3 absorbance and a high 3107 cm^{-1} intensity (75 cm^{-1}), whereas the outer regions of the sample contain significant N3 absorbance and the associated blue luminescence. These observations could potentially be explained by the conversion of N3 to N_3VH through the trapping of a hydrogen atom. The authors of this study suggested that high-temperature annealing studies could be a useful way of examining and possibly confirming the supposed transformation of N3 centres to N_3VH. This has also been suggested in a subsequent study including two more diamonds from Uralian placers, which showed roughly inverse correlations between N3 and 3107 cm^{-1} intensity (Vasilev et al., 2020).

A relationship has previously been observed between the 3107 cm^{-1} peak area and the N_B concentration found in diamonds (Melton, 2013). This relationship takes the form of a 'limiting envelope', where for a diamond with a specific concentration of N_B, there is a maximum possible area of the 3107 cm^{-1} feature that could observed, seemingly entirely independent of the locality or paragenesis of the diamonds – this relationship is displayed in Figure 4.2. Such a defined limit is only weakly observed with A-centre concentrations, suggesting that the B-centre is crucial to whatever process is controlling the presence of this envelope. This relationship has been independently corroborated (Speich, 2017), and could be explained by the nitrogen aggregation mechanism affecting hydrogen defects, in order to convert them into optically active and therefore readily observable defects. If this is indeed the case, then the maximum 3107 cm^{-1} peak area could be considered a function of the amount of hydrogen available within the diamond, along with the nitrogen concentration and the degree of nitrogen

aggregation within the sample. Small 3107 cm^{-1} peak areas in diamonds with a high content of highly aggregated nitrogen could be accounted for by low concentrations of available hydrogen during growth. This could provide additional information about the conditions from which diamonds from different localities were grown.

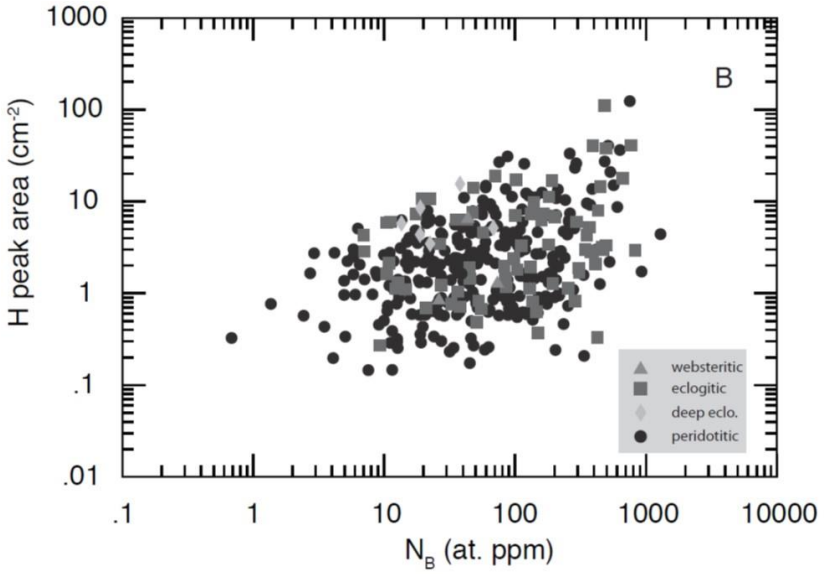

Figure 4.2: The 3107 cm^{-1} peak area versus [N_B] for a number of samples of differing parageneses, plotted on a logarithmic scale. This highlights the relationship between maximum 3107 cm^{-1} peak area and [N_B] concentrations, and the presence of a limiting envelope (Melton, 2013).

The work in this chapter is aimed at investigating the role of the N3 centre in the formation of the N_3VH defect, along with what role these two defects play in the nitrogen aggregation sequence in natural diamond. There are two main hypotheses to be tested:

- The N3 centre is formed at a set fraction of B-centre concentration.
- The primary formation mechanism of the N_3VH defect is from direct protonation of an N3 centre.

Along with these hypotheses come several predictions. If both hypotheses are correct, a plot of [N3] + [N_3VH] vs. [N_B] should produce a straight line fit, determining the proportionality constant. Due to the relative speed of hydrogen diffusion within diamonds (see section 1.2.3.3

for more detail), the amount of H present can be considered the limiting factor in N_3VH formation. Thereby, the limiting envelope displayed in figure 4.2 could be rationalised and explained with points closest to the limit containing no unprotonated N3, and points further away containing appreciable N3 contents. A schematic of these predictions is displayed below in figure 4.3 for ease of visualisation. Studying a number of diamonds from various points within this sample space should be able to shed light on whether or not the hypotheses provided above are accurate, and what this means in terms of how hydrogen fits into the nitrogen aggregation sequence as currently understood. The inclusion of spatially resolved studies will provide further detail as to the behaviour of the N3 and N_3VH defects. This can potentially add to our knowledge of the relationships between these optically active features in diamond. If the hypotheses are correct, then the relative abundance of N3 and N_3VH can function as a hygrometer within a diamond.

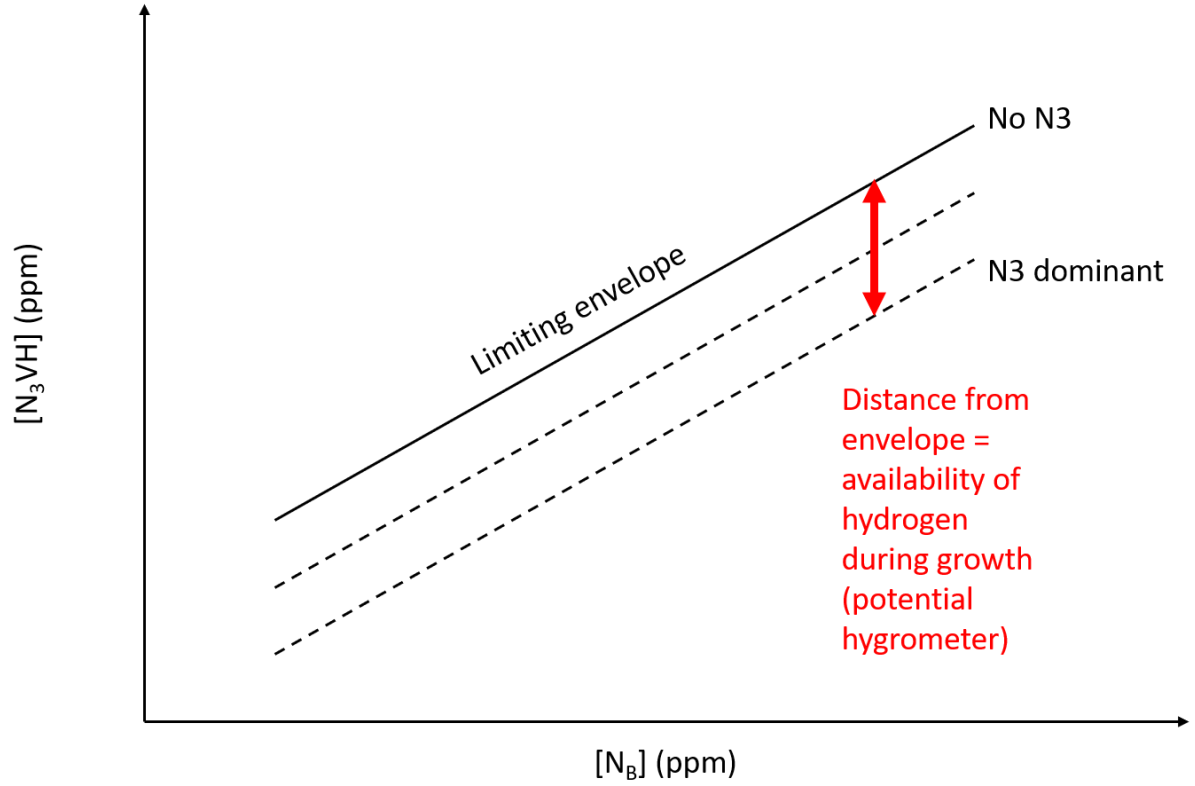

Figure 4.3: a schematic of the predictions made using the hypotheses presented in this work. The distance from the limiting envelope can potentially act as a hygrometer for the conditions under which the diamond was formed.

4.2 Methods

4.2.1 FTIR

A full, detailed write-up of the experimental setup used for FTIR studies can be found in chapter 2.

This section contains high quality line scans taken to study the inhomogeneity in 32 samples from a number of localities in order to probe systematics across these sample suites. A list of the diamonds and their thickness as measured by calipers is presented below in table 4.1:

Locality	Sample	Thickness (mm)	UV-vis line scan?
Argyle, Australia	Arg 13	1.09	N
	Arg 16	1.12	N
	Arg 25	1.13	N
	Arg 46	1.11	N
	Arg 56	1.06	N
	Arg 65	0.63	N
	Arg 72	1.09	N
	Arg 74	1.03	N
	Arg 75	0.85	N
	Arg 78	0.69	N
	Arg 90	0.88	N
	Arg 92	0.87	N
	Arg 93	0.93	N
	Arg 117	1.46	N
	Arg 118	1.20	**Y**
	Arg 136	1.70	N
	Arg 158	1.60	N
	Arg 167	1.47	N
Diavik, Canada	DVK 044	0.59	N
	DVK 076	0.44	N
	DVK 127	1.07	N
	DVK 143	0.54	**Y**
	DVK 159	0.55	**Y**
	DVK 160	0.39	**Y**
Mir, Russia	Mir 1164	0.54	N
Murowa, Zimbabwe	Mur 083	0.34	N
	Mur 112	0.28	N
	Mur 235	0.85	N
	Mur 265	0.34	N
Udachnaya, Russia	Udachnaya 2100	1.87	N
	Udachnaya 3009	0.63	N
	Udachnaya 3097	1.29	N
	Udachnaya 3143	0.71	**Y**

Table 4.1: A list of the samples used for this study, with indications as to whether or not a UV-vis line scan was collected.

4.3 Results

4.3.1 Single spectra

For measured values from both IR and UV-vis, see Appendix B.1. Figure 4.4 shows an example UV-vis spectrum displaying a moderately intense N3 centre absorption with the zero-phonon line (ZPL) highlighted, along with the vibronic sideband – specifically from Udachnaya 3097. Once the ZPL was fitted and the procedure described in Section 2.3 was carried out, the resulting concentration for this specific peak comes out as 1.6 ppm (2 s.f.).

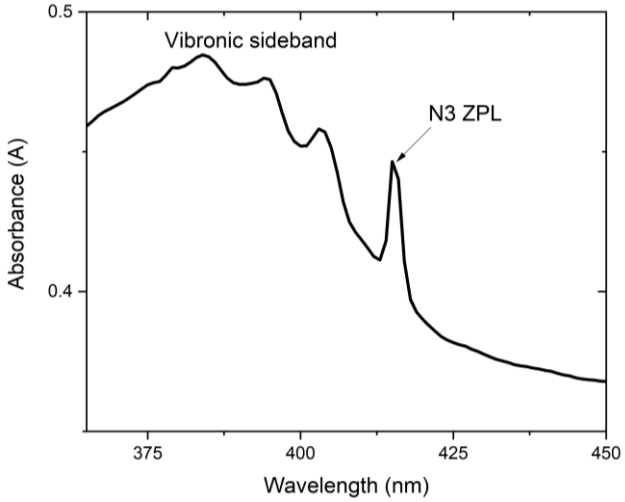

Figure 4.4: An example spectrum collected from Udachnaya 3097, displaying a moderately intense N3 absorption, with the zero-phonon line and vibronic sideband highlighted.

In the data set of single spectra, the concentrations observed range from 0 to the highest calculated [N3] of 5.2 ppm. By comparison, the [N_B] concentrations range from 47 to 1084 ppm. This emphasises the relatively low abundance of the N3 defect compared to the B centre.

Figure 4.5 displays a version of the plot in Figure 4.2 for this selection of 32 samples, with the summation from each IR line scan displayed as I(3107 cm^{-1}) in cm^{-2} against [N_B] in ppm. Each point is then colour-coded to show the observed [N3] (ppm) with the colour scale displayed to the right. Whilst there does appear to be an increase in samples with < 0 ppm of N3 towards the bottom-right of the plot (further from the limiting envelope), it is not a clear relationship, likely hindered by the lack of spatial resolution in the UV-vis measurements. One of the two diamonds with the highest [N3] – Udachnaya 3009 – appears close to the limit at the top of the envelope. This is contrary to what would be predicted by the hypotheses discussed earlier.

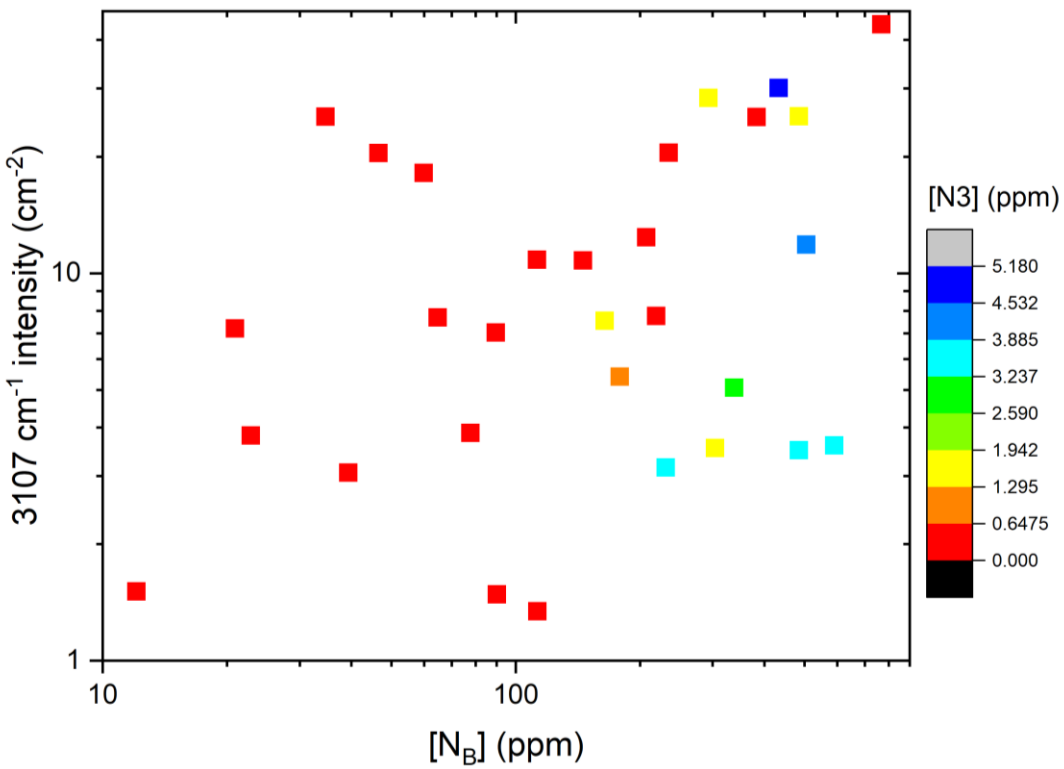

Figure 4.5: A graph showing the [N_B] (ppm) vs. 3107 cm^{-1} peak area (cm^{-2}) on a logarithmic scale. The data is colour-coded according to the [N3] (ppm) measured for each sample.

Figure 4.6 displays plots of [N_B] vs. [N3], [N_3VH] and ([N3] + [N_3VH]), and table 4.1 underneath displays some descriptive statistics from the fitting of the data. Error bars are representative of the standard error for the IR line scans, where the standard error = $\sigma/\sqrt{n}$ where σ is the standard deviation and n is the number of points averaged from the line scan. The extinction coefficient used to produce [N_3VH] is derived from studies of the vibrational dynamics of the infrared absorption (Coxon et al., 2020). Inspection of the data shows that all three plots show some element of a positive correlation, with the strongest relationship being observed in Fig. 4.5c for [N_B] vs. [N3] + [N_3VH]. This is also shown by the statistics in table 4.2. Fig. 4.5c produces the highest PMCC of 0.7026, indicating the strongest correlation. Linear regression of the data using a forced zero y-intercept produces an R^2 value of 0.4078 for [N_B] vs. [N3] + [N_3VH]. While this is the highest R^2 out of the three figures, it also shows that there is significant variation in the data that cannot be interpreted by a simple linear plot. This means that, while there is some evidence

supporting the hypothesis, the trend observed is not capable of quantifying the relationship between these three optical centres.

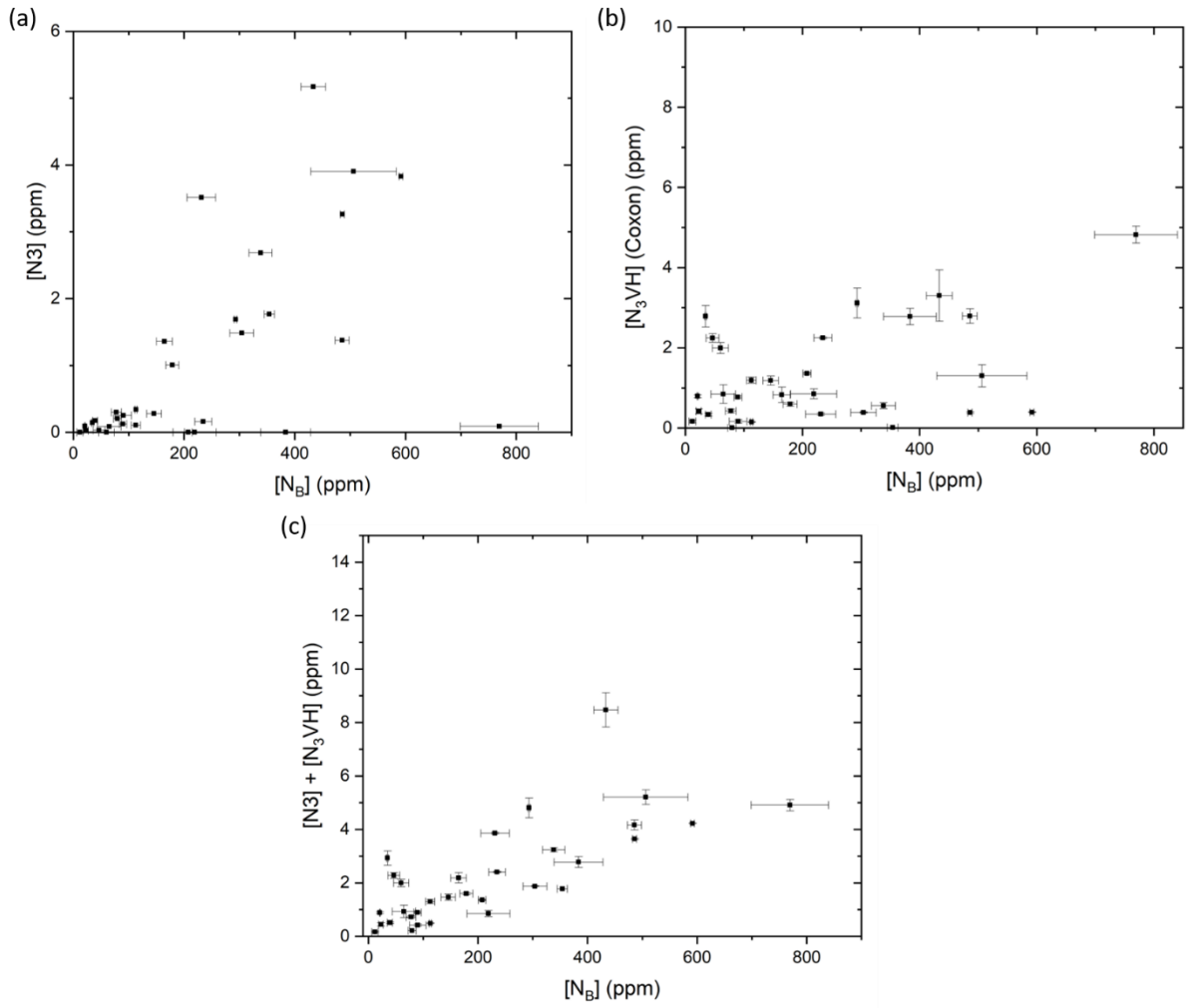

Figure 4.6: Plots of the various relationships between [N_B] (ppm) and (a) [N3] (ppm), (b) [N_3VH] (ppm) and (c) [N3] + [N_3VH] (ppm). The extinction coefficient used to produce [N_3VH] is derived from Coxon et al. (2020)

Relationship	PMCC	R^2 Value
[N_B] vs. [N3]	0.59947	0.3591
[N_B] vs. [N_3VH]	0.44345	0.079
[N_B] vs. [N3] + [N_3VH]	0.7026	0.4078

Table 4.2: Descriptive statistics for the data presented in Figure 4.6. This shows the PMCC values obtained along with the R^2 value obtained after linear regression with a forced zero y-intercept.

Figure 4.7 shows the observed relationship between the ratio between the intensity of the 3107 cm^{-1} peak and the [N_B] vs. the observed [N3]. There appears to be an indication that the concentration of N3 centres is only significant when the relative intensity of the 3107 cm^{-1} feature compared to the concentration of B centres is low. A plot of [N3]/[N_B] vs. [N_3VH]/[N_B] displays no observable relationship and so has not been included.

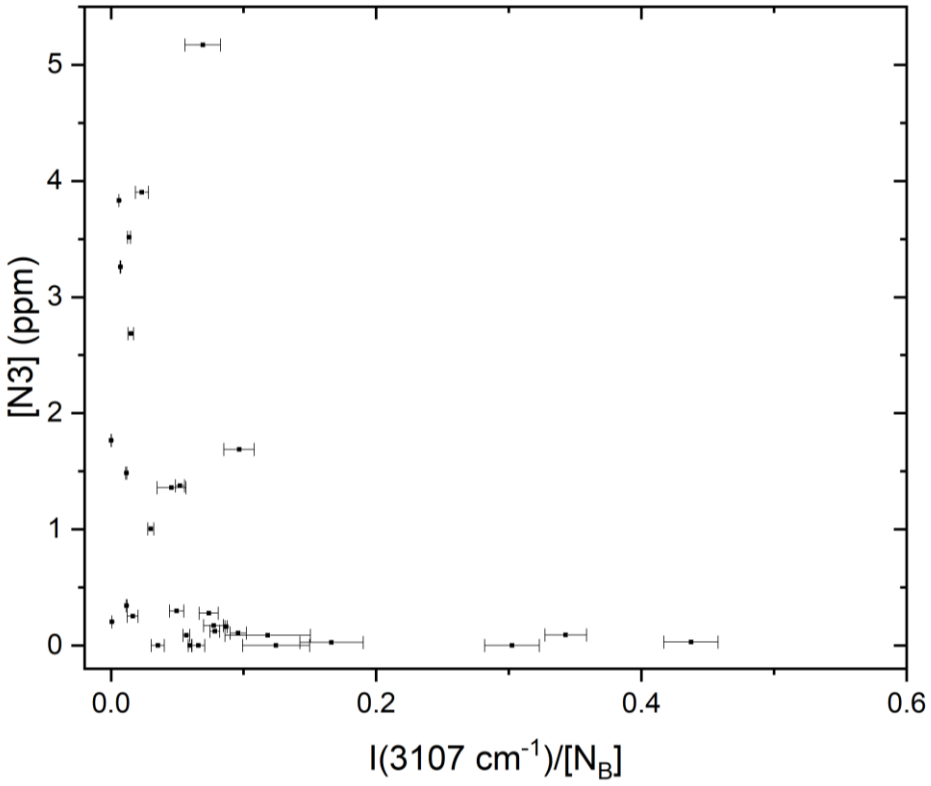

Figure 4.7: A plot showing the observed relationship between the ratio between the intensity of the 3107 cm^{-1} peak and the [N_B] vs. the observed [N3].

4.3.2 Line scans

Figure 4.8 displays the results from Arg 118. The diamond shows a higher [N_B] in the core of the diamond, and generally decreases in [N_B] from core to rim. There is a similar trend observed in [N3]. This sample is dominated by [N3]. The concentrations of N_3VH are very low, with the maximum concentration observed being two orders of magnitude lower than that of N3.

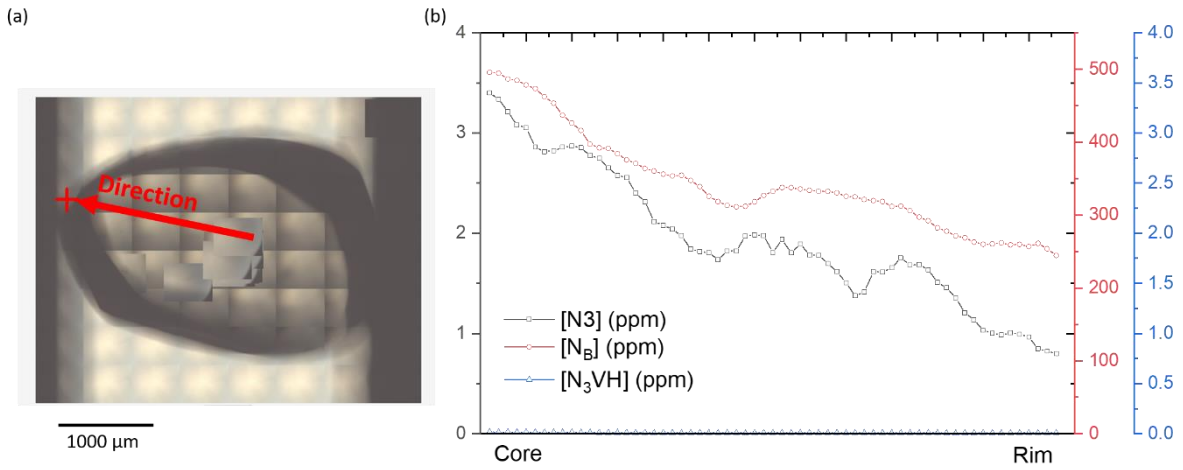

Figure 4.8: (a) an image of Arg 118 showing the testing direction for the line scans (b) a plot showing how the IR and UV-vis features vary spatially through the sample. The black line and squares represent [N3], the red line and circles represent [N_B] and blue triangles are [N3]. All numbers are in ppm. The line scans in 4.8b are across a length of 1575 µm.

Figure 4.9 displays the results of the line scans for DVK 143. This sample has a higher [N_B] in the core of the sample, with a low nitrogen rim. The N3 and N_3VH concentrations are similar in magnitude, with a max concentration of N3 of ~ 3.5 ppm and a max concentration of N_3VH of ~ 2 ppm. The peak observed in [N_3VH] to the left of the core occurs at a point when the [N3] lies lower than would be expected based on a proportional relationship with [N_B]. A similar trend can be seen in the centre, where a decrease in [N3] correlates with a spike in [N_3VH] in the core of the diamond.

Due to the symmetric shape of this diamond, there is slight uncertainty in terms of ensuring the scans were collected on the same face of the sample. While efforts have been made to ensure that this is the case, it must be noted.

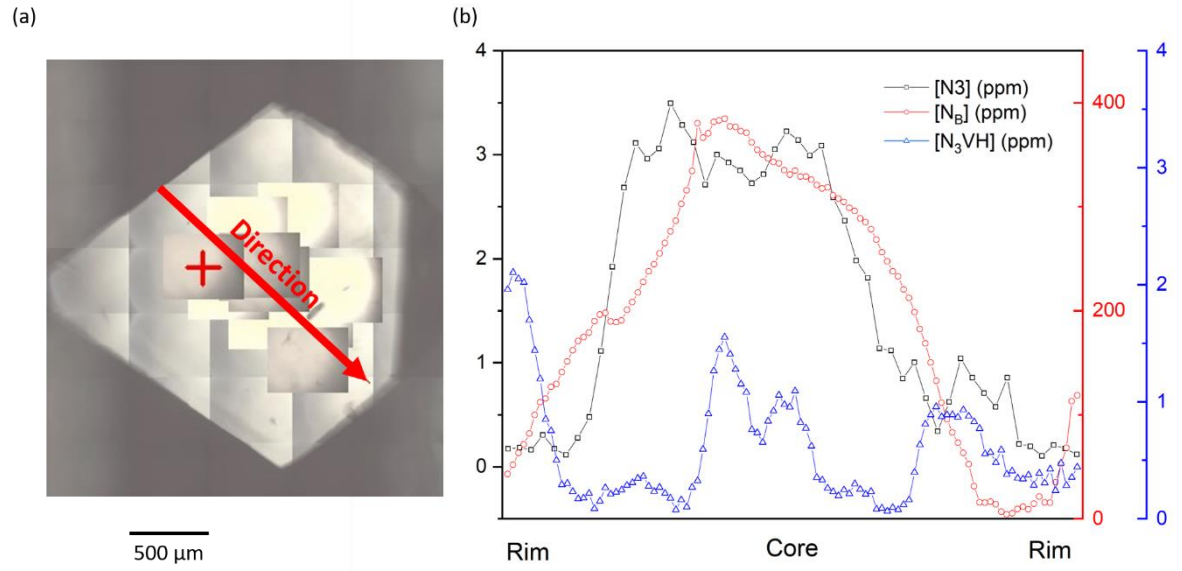

Figure 4.9: (a) an image of DVK 143 showing the testing direction for the line scans (b) a plot showing how the IR and UV-vis features vary spatially through the sample. The black line and squares represent [N3], the red line and circles represent [N_B] and blue triangles are [N3]. All numbers are in ppm. The line scans in 4.9b are across a length of 1600 µm.

Figure 4.10 presents the data from the line scans for DVK 159. This sample shows complex zonation, with a number of high and low nitrogen zones. The trend in [N_3VH] is clear, with a high intensity at both rims, and a low intensity within the core of the diamond. The [N3] shows a similarly complex zonation to [N_B], although of note is the point on the right of the diagram where the [N3] is low (~ 1 ppm), but the [N_3VH] peaks to ~ 4 ppm. The trend generally follows the trend observed in [N_B] aside from this point.

In this sample a discrepancy in the length of the IR and UV-vis line scans was observed. Visual inspection suggested that this lay to one end of the IR line scan. The data was cropped to produce both line scans across the same length scale.

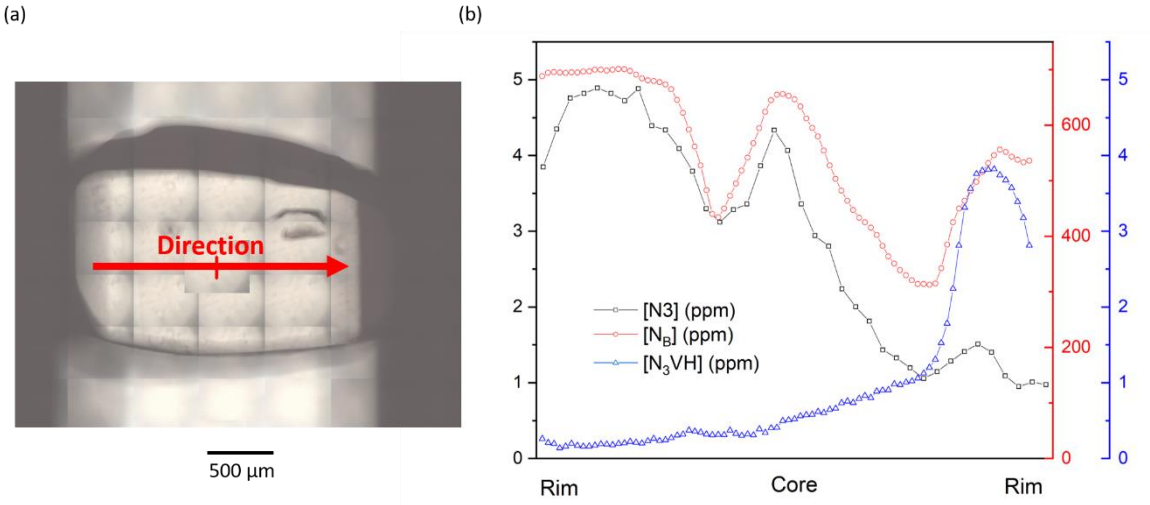

Figure 4.10: (a) an image of DVK 159 showing the testing direction for the line scans (b) a plot showing how the IR and UV-vis features vary spatially through the sample. The black line and squares represent [N3], the red line and circles represent [N_B] and blue triangles are [N3]. All numbers are in ppm. The line scans in 4.10b are across a length of 1660 µm.

Figure 4.11 displays the trends of the variation in the IR and UV-vis features of DVK 160. The [N_B] shows a high nitrogen core and a low nitrogen rim. The [N3] shows a similar trend, with a much higher concentration of N3 in the core. However, the concentration at the edge of the core is slightly diminished compared to what would be expected from a simple correlation with [N_B]. The [N_3VH] does not follow the same trend, with a similar concentration in the centre of the core as is found in the low nitrogen rim. The points at which an increased concentration of the [N_3VH] is found are those making up the boundary between the high nitrogen core and low nitrogen rim. Of particular interest is the distinct spike observed at the boundary between the high nitrogen core and the low nitrogen rim, where the [N_3VH] is ~ 4.5 ppm on one side and ~ 7 ppm on the other. This coincides with the point mentioned above where the [N3] is reduced compared to what would be expected from a simple correlation with [N_B]. Of note is that the spatial resolution of the UV-vis line scan is significantly lower than the IR, with only 10 points across the diamond. This could potentially obscure some nuances in the measured concentrations.

In this sample, the IR line scan contained several points outside the length of the UV-vis measurements. These were cropped out in order to match the length scales of the two techniques and to allow for ease of visualisation.

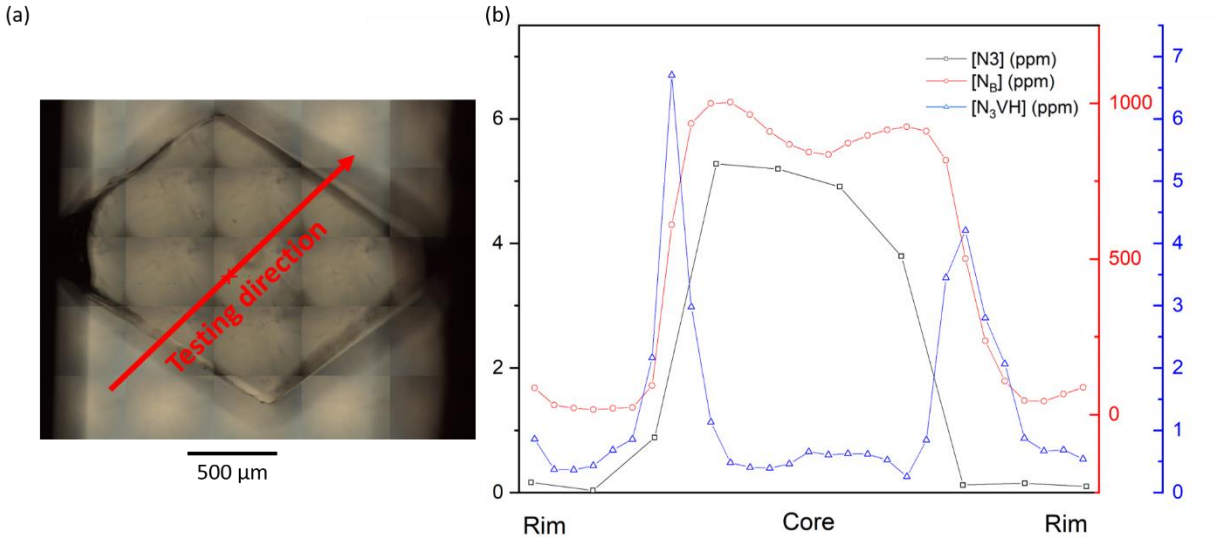

Figure 4.11: (a) an image of DVK 160 showing the testing direction (b) a plot showing how the IR and UV-vis features vary spatially through the sample. The black line and squares represent [N3], the red line and circles represent [N_B] and blue triangles are [N3]. All numbers are in ppm. The line scans in 4.10b are across a length of 1160 µm.

Figure 4.12 shows the measured data for Udachnaya 3143. The zonation in this sample is complex, much like the Diavik samples. There is a high nitrogen core and a low nitrogen rim, but there is additional complexity between these regions. The trends in [N_B] and [N3] correlate very well, with the concentration of N3 almost exactly following the trend in [N_B]. This is not the case for the [N_3VH]. The concentration of N_3VH is near-zero within the core. There are only significant concentrations in the low nitrogen rims. The rim to the left of the diagram shows a peak corresponding to the boundary between the high and low nitrogen zones. The only areas with appreciable concentrations of N_3VH contain very low concentrations of N3 compared to the rest of the sample. It is worth noting that the concentration of B-centres is also low at the points at which the peaks in [N_3VH] are observed, which goes against the predicted trends.

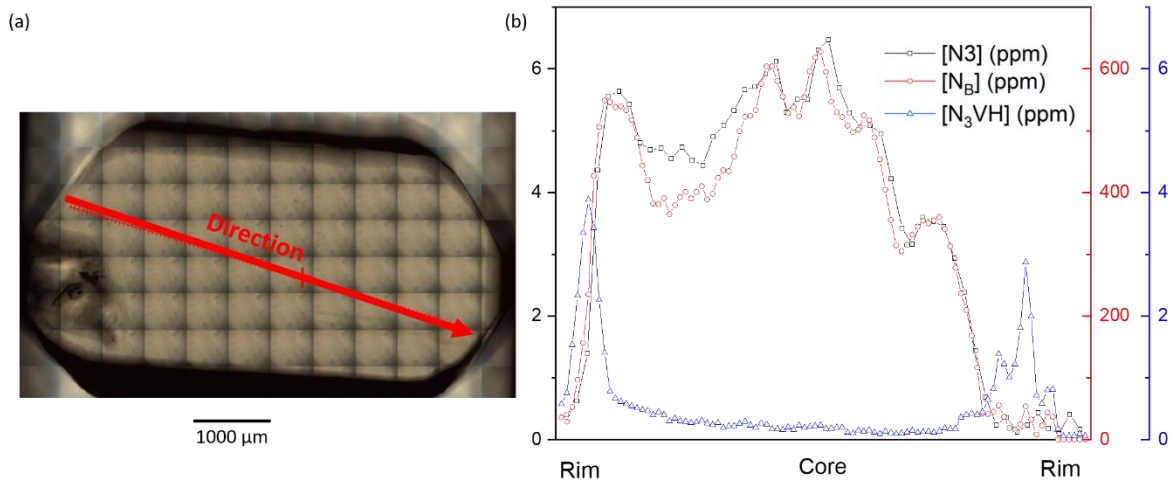

Figure 4.12: (a) an image of Udachnaya 3143 showing the testing direction (b) a plot showing how the IR and UV-vis features vary spatially through the sample. The black line and squares represent [N3], the red line and circles represent [N_B] and blue triangles are [N3]. All values are in ppm. The line scans in 4.12b are across a length of 5035 µm.

4.2.3 Attempts at quantification

In order to attempt to quantify the relationship between these nitrogen-containing defects, the line scans from the separate techniques must be combined. The IR line scans have a higher spatial resolution than those from UV-vis. In order to compare the two, points from the IR line scan can be selected that corresponded to the points from the UV-vis line scan. In the case of spectra not falling exactly on the same point, a simple linear interpolation can be used to provide a method of comparing the two. This comes with inherent uncertainties but enables an attempt at quantification to be made. Each sample will be discussed and evaluated individually, and then all samples will be considered as a combined dataset.

Figure 4.13 shows a plot of [N_B] vs. [N3] + [N_3VH] for Arg 118. The concentration of N_3VH is negligible, so the values are dominated by [N3].

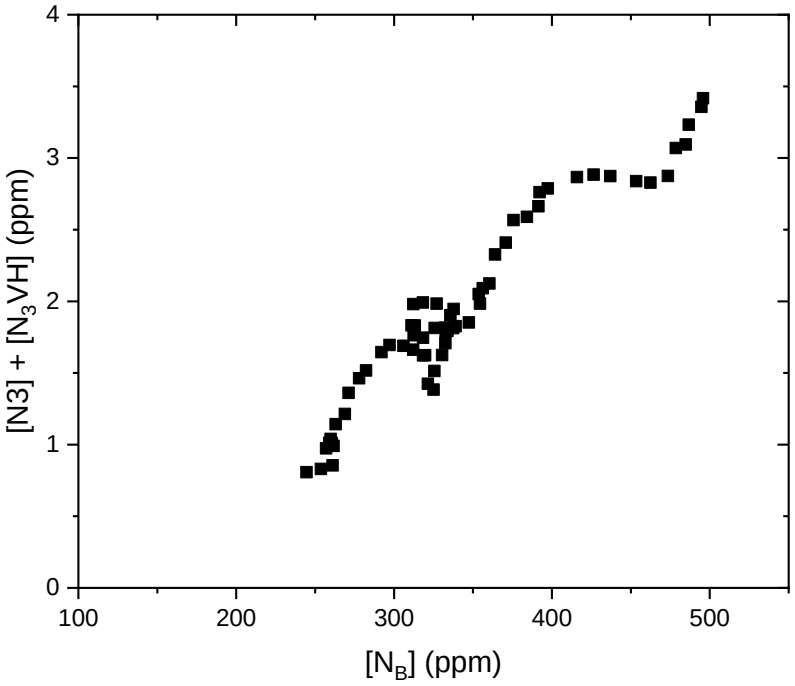

Figure 4.13: A plot of [N_B] vs. [N3] + [N_3VH] for Arg 118.

A linear regression of this data with a forced zero y-intercept provides the following relationship with a 95 % confidence interval

$$\left[N_{N3+N_3VH}\right](ppm) = 0.017(0.004) \times [N_B]\ (ppm) \qquad (4.9)$$

This relationship has an R^2 value of 0.95. This indicates that in this sample the concentration of nitrogen present as N3 and N_3VH centres is around 1.7 % of the nitrogen present as B centres.

Figure 4.14 shows a plot of $[N_B]$ vs. [N3] + $[N_3VH]$ for DVK 143. There is some scatter in terms of the proportionality between the defect concentrations compared to other samples.

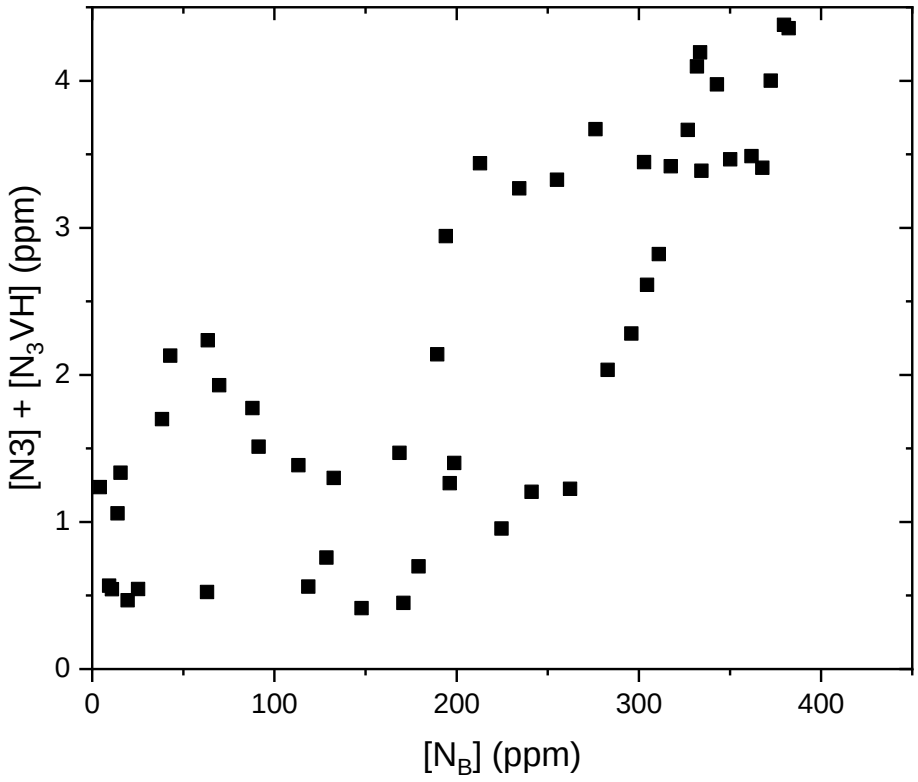

Figure 4.14: A plot of $[N_B]$ vs. [N3] + $[N_3VH]$ for DVK 143.

Linear regression of this with a forced zero y-intercept provides the following relationship

$$\left[N_{N3+N_3VH}\right](ppm) = 0.030(0.002) \times [N_B]\,(ppm) \qquad (4.10)$$

The R^2 of this relationship is 0.89, indicating a slightly less linear trend than for some of the other samples, which is consistent with what would be expected from simple visual inspection. In this sample, the concentration of nitrogen present as N3 and N_3VH centres is around 3.0 % of the nitrogen present as B centres.

Figure 4.15 displays a plot of [N_B] vs. [N3] + [N_3VH] for DVK 159.

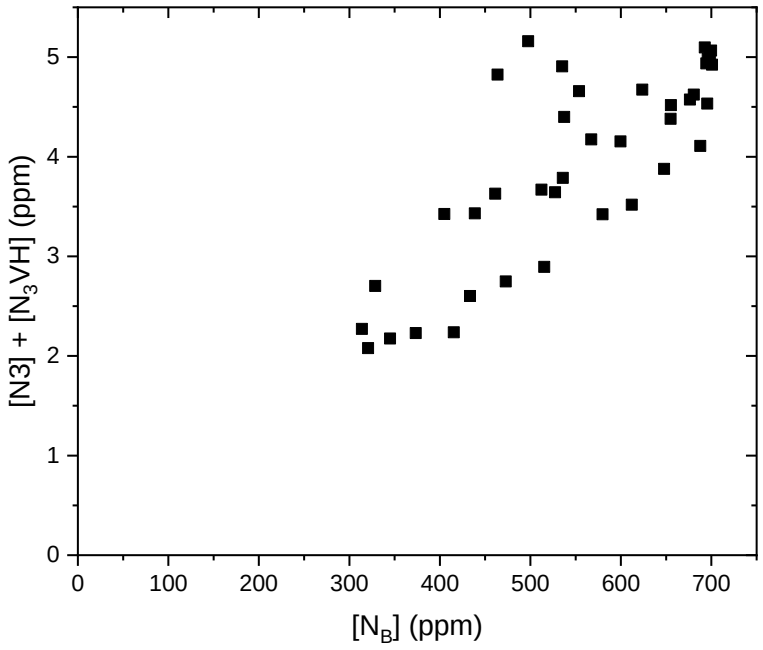

Figure 4.15: A plot of [N_B] vs. [N3] + [N_3VH] for DVK 159.

Linear regression produces a relationship of the following form

$$\left[N_{N3+N_3VH}\right](ppm) = 0.021(0.001) \times [N_B]\,(ppm) \qquad (4.11)$$

With an R^2 value of 0.98. In this sample, the concentration of nitrogen present as N3 and N_3VH centres is around 2.1 % of the nitrogen present as B centres.

Figure 4.16 shows the plot of [N_B] vs. [N3] + [N_3VH] for DVK 160. The spatial resolution is lower for this sample, and so there are only 10 points used to produce a quantification. This means that there are likely additional uncertainties due to the smaller sample size.

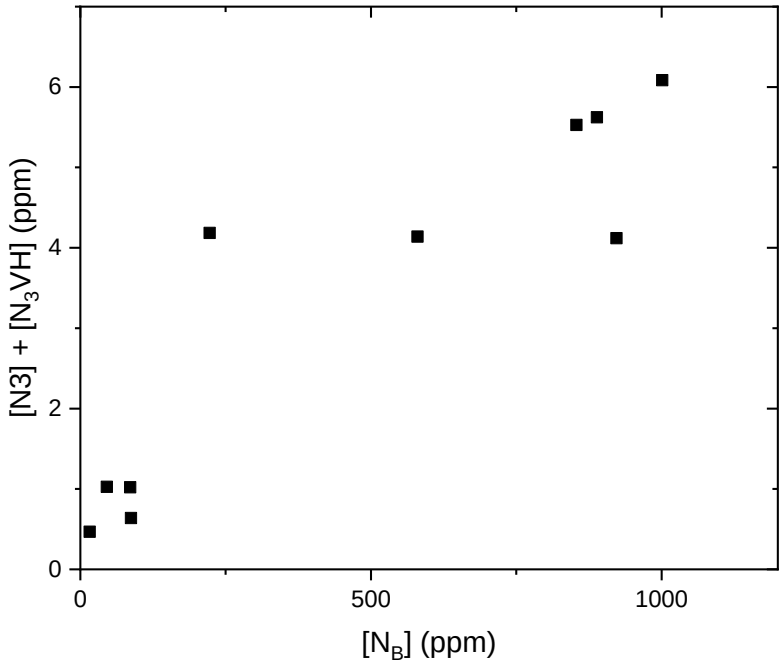

Figure 4.16: A plot of [N_B] vs. [N3] + [N_3VH] for DVK 159.

Linear regression produces the following relationship

$$[N_{N3+N_3VH}](ppm) = 0.018(0.002) \times [N_B]\ (ppm) \qquad (4.12)$$

With an R^2 value of 0.92. This means that, in this sample, the concentration of nitrogen present as N3 and N_3VH centres is around 1.8 % of the nitrogen present as B centres.

Figure 4.17 displays the results for Udachnaya 3143. The rim of the diamond is excluded from this plot due to the high concentrations of N_3VH in order to attempt to produce an estimate for the relative proportions of the defects. There is a clear linear relationship between the variables within the core of the diamond.

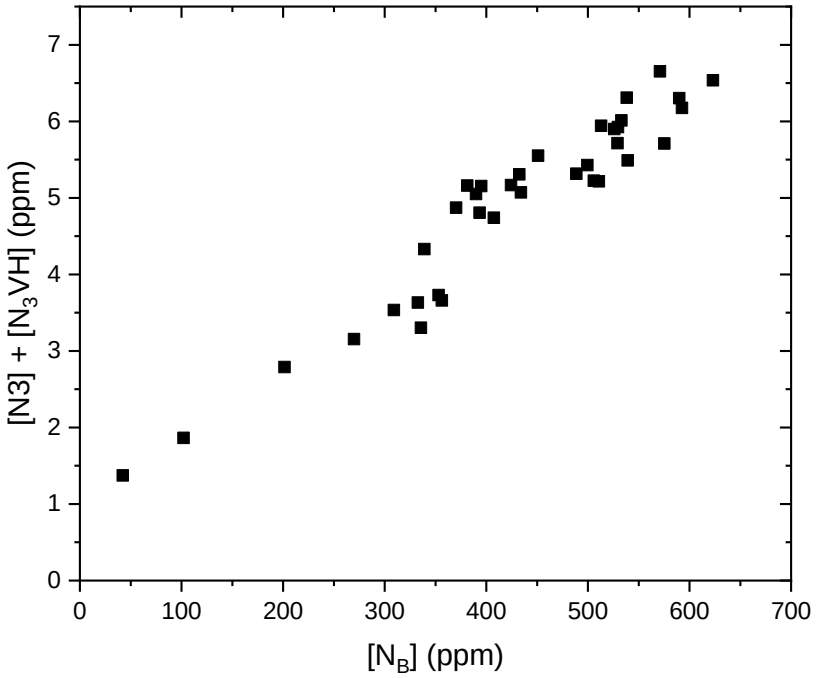

Figure 4.17: A plot of [N_B] vs. [N3] + [N_3VH] for Udachnaya 3143.

Linear regression of the data for Udachnaya 3143 provides the following relationship

$$\left[N_{N3+N_3VH}\right](ppm) = 0.034(0.005) \times [N_B]\ (ppm) \qquad (4.13)$$

With an R^2 value of 0.99. This suggests that the concentration of nitrogen present as N3 and N_3VH centres in this sample is around 3.4 % of the nitrogen present as B centres.

Table 4.3 displays a summation of the proportionality constants in percent of [N_B] generated for each sample in this work. The range of values observed ranges from a concentration of N3 + N_3VH of ~ 1.7 % of the [N_B] in Arg 118 to a maximum of 3.4 % of the [N_B] in Udachnaya 3143. The quality of linear fit varies between samples, with some, such as Udachnaya 3143 displaying a very linear relationship, while others such as DVK 143 which contains a significant amount of scatter within the data.

Sample	Proportionality constant (%)	R^2
Arg 118	1.7	0.95
DVK 143	3.0	0.89
DVK 159	2.1	0.98
DVK 160	1.8	0.92
Udachnaya 3143	3.4	0.99

Table 4.3: A summation of the results of the quantification attempts presented within this chapter. Included is the calculated proportionality constant along with the R^2 value, used as a goodness-of-fit measure of the linear regression.

Figure 4.18 shows the results of the line scans, combined and plotted as [N_B] vs. (a) [N3], (b) [N3] + [N_3VH] and (c) [N_3VH]. A strong positive correlation is observed in both 4.13a and 4.18c, but 4.18b does not appear to show a correlation of any sort. This is consistent with the results displayed for the single spectra in figure 4.6. Linear regression of the data from figure 4.18c with a forced zero y-intercept provides the following relationship within a 95% confidence interval:

$$[N_{N3+N_3VH}]\ (ppm) = 0.024(0.01)\ \times [N_B]\ (ppm) \qquad (4.14)$$

Where $[N_{N3+N_3VH}]$ is the amount of nitrogen present in the form of N3 and N_3VH centres. This relationship has an R^2 value of 0.87 and a PMCC of 0.93 to two decimal places. This suggests that the percentage abundance of nitrogen present as either the N3 or N_3VH centre is ~ 2.5 % of the amount of nitrogen present as B-centres. This value considers the 5 samples studied here as a whole in order to assess a proportionality constant for the relationship between N3, N_3VH and B-centres across the entire dataset.

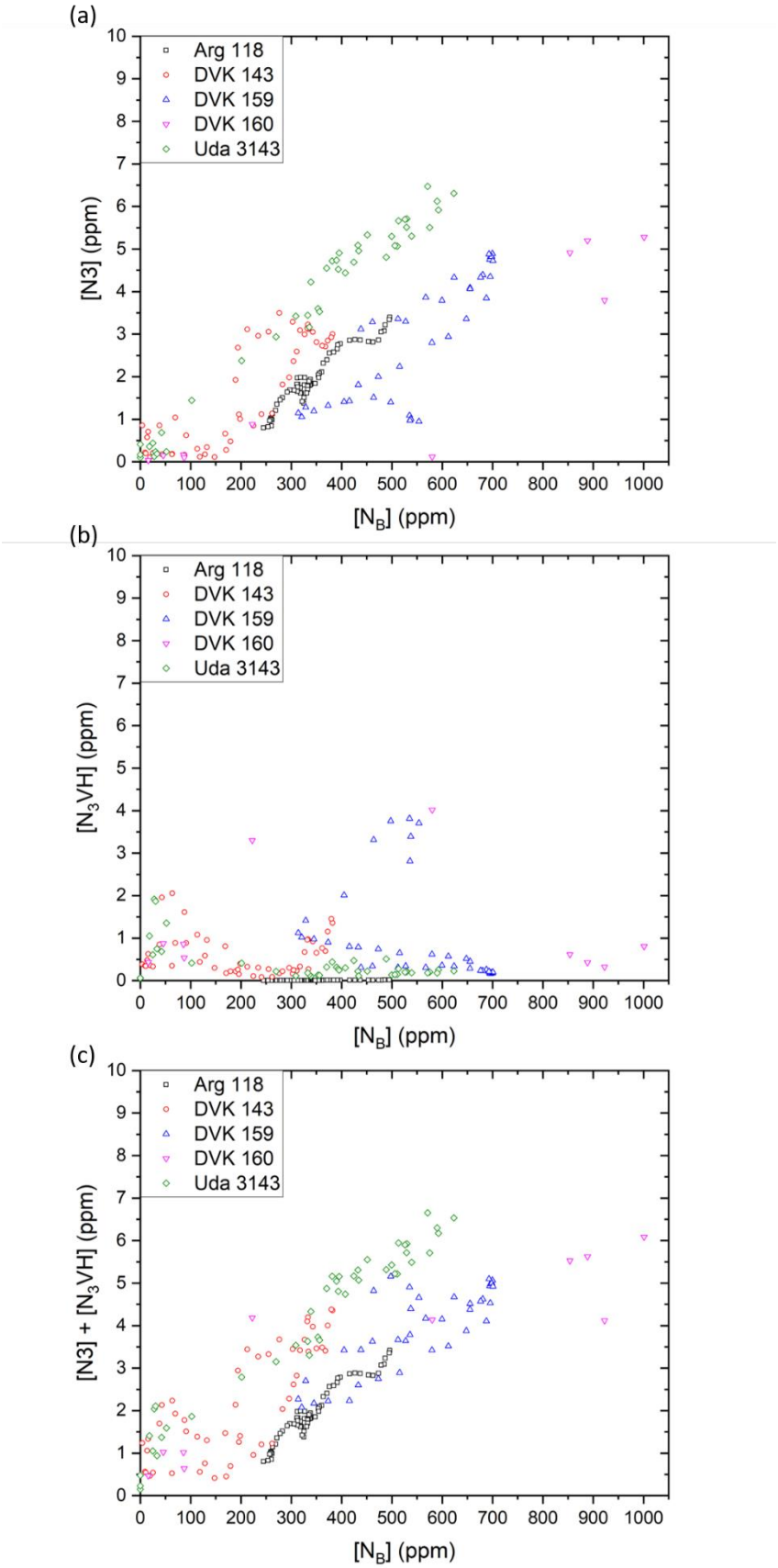

Figure 4.18: Plots of the various relationships between [N_B] (ppm) and (a) [N3] (ppm), (b) [N3] (ppm) and (c) [N_3VH] + [N_3VH] (ppm) for the combined UV-vis and FTIR line scans. Black squares are Arg 118, red circles are DVK 143, blue upward-facing triangles are DVK 159, pink downward-facing triangles are DVK 160 and green diamonds are Udachnaya 3143.

Figure 4.19 shows the combined line scan results plotted onto a log-log plot and colour-coded for [N3] in an analogous way to Figure 4.5.

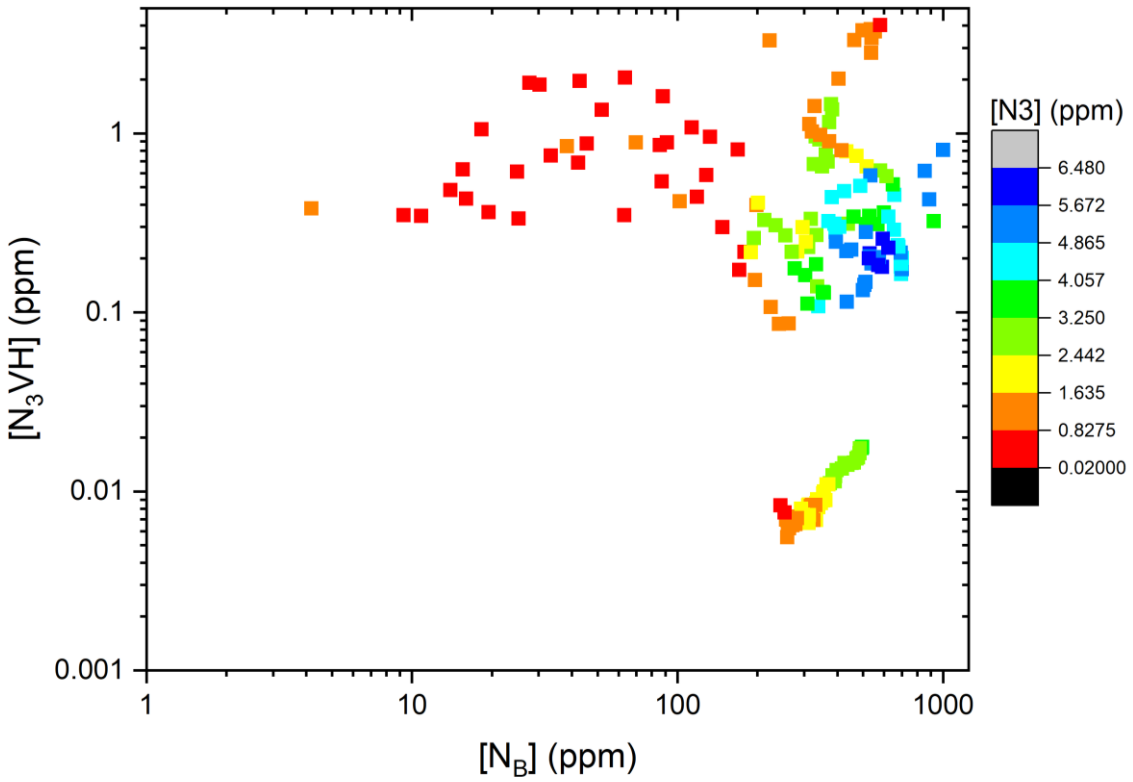

Figure 4.19: a log-log plot of [N_3VH] vs. [N_B], colour-coded for [N3]. All units in ppm.

The [N3] values appear to be enhanced in the points towards the lower right-hand corner of the diagram, as was predicted in the hypotheses laid out earlier in the chapter. This is not entirely the case, with a number of points displaying lower values of N3 than may be expected, but generally meets the prediction that, the further away from the 'limiting envelope' a point lies, the higher the concentration of N3.

4.4 Discussion

The comparison of IR line scans with single UV-vis measurements provided some evidence for the formation of the majority of N_3VH from protonation of an N3 centre in the form of a strong correlation between [N_B] and [N3] + [N_3VH], backed up by the statistics presented in table 4.2. While there was a more linear relationship between these than was observed for either [N3] or [N_3VH] alone – the B-centre concentration does appear to provide a better predictor for the sum of the concentrations of N3 and N_3VH than either alone. However, this was not as clear as would be predicted from the hypothesis described at the beginning of this chapter. This could suggest that there is another reaction pathway for the formation of N_3VH other than the simple protonation discussed here, potentially the trapping of an A-centre by NVH^0 as proposed in earlier theoretical work as the predominant mechanism in CVD diamond (J. P. Goss et al., 2014). It is also possible that the comparisons between a spatially resolved line scan and a single point encompassing several growth zones lead to the obfuscation of trends that could otherwise be observed.

From this evidence alone, it cannot be determined whether the N3 centre is formed in a set proportion to the amount of B centres. The correlation does suggest an element of proportionality, but the relationship is not linear enough to conclude definitively. It has also not been possible to generate the constant of proportionality that would be expected if there was indeed a set fraction of nitrogen aggregates produced as N3. The relationship in Figure 4.6 provides some further evidence to substantiate the hypothesis, as the observed N3 concentration is only significant when there is a relatively weak 3107 cm^{-1} peak compared to the observed B-centre concentration.

A plot investigating the presence of N3 across the [N_B] vs. 3107 cm^{-1} area sample space as discussed earlier appears to show some limited evidence of increased [N3] the further away from the ‘limiting envelope’ (Melton, 2013) within the space an individual diamond lies.

However, a lack of spatial resolution in the UV-vis measurements means all points attributed to a single sample have the same value for [N3], despite the often significant variation in the other features across the various growth zones in the diamonds. This highlights the need for spatially resolved UV-vis measurements in order to provide a stronger test of the hypotheses investigated within this work.

The FTIR and UV-vis line scans show significant complexities in terms of the zonation of these optical features. This illustrates the potential issues with using single spectra. Some samples are more homogenous than others; more homogenous samples may be suitable for single spectra. However, the samples presented here are very heterogenous across the line scans, and clearly the collection of single spectra lead to a large amount of information being overlooked. The line scans allow for a more thorough test of the hypotheses discussed earlier.

As the line scans were collected on two different instruments, there is some uncertainty in terms of the collection of spectra from exact locations within the diamond. However, with careful collection and the use of visible features such as inclusions as markers, it is possible to obtain line scans with confidence in the location. There are uncertainties introduced in terms of quantification efforts from line scans collected on different instrumentation through human error, but both quantitative and qualitative studies of the variation in features are, in theory, possible.

These line scans provide further evidence as to the primary formation mechanism of the N_3VH defect. DVK 143, DVK 159 and DVK 160 all display trends of increases in [N_3VH] when there is a decrease in [N3] relative to the [N_B]. This is especially pronounced at the boundaries between high nitrogen zones and lower nitrogen zones, as highlighted in Fig. 4.8b for DVK 159. This fits with the hypothesis that the formation of N_3VH centres is dependent on the presence of hydrogen within the diamond-forming fluids. The differences in the detected

concentrations of the defects can be rationalised by changes in the environment in which the diamonds are growing. For example, if we consider DVK 159, the observations can be explained by the growth of the nitrogen-rich core occurring under conditions with relatively little hydrogen. This leads to the preservation of an amount of nitrogen in the form of N3 centres. In the nitrogen-poor rim, the conditions are clearly different; not only is there less nitrogen incorporated but there is now a significant concentration of N_3VH centres. This can be rationalised by the growth event occurring in fluids containing significant concentrations of hydrogen in forms conducive to incorporation within the diamond. This hydrogen, once incorporated, would diffuse through the diamond and attach to the dangling carbon bond at the N3 centre, forming N_3VH.

An interesting trend is also observed in Udachnaya 3143, with the amount of N3 showing a significant degree of proportionality with the concentration of B-centres. This is clearer here than in any of the other samples studied. There is an enrichment of N_3VH towards the low-nitrogen rim of the diamond. While this qualitatively supports the trends observed in the Diavik samples, the concentration of B-centres is close to zero. It is therefore surprising that there is a significant concentration of N_3VH, as this would not be predicted by a proportional relationship. This could suggest that the formation of N3 centres is not strictly proportional to the concentration of B-centres in the diamond. It may be the case that the reaction pathways leading to the formation of N3 centres are dependent on other parameters. This is consistent with the mechanisms proposed in equations 4.1 – 4.3. Given that equation 4.3 proposes two mechanisms for the formation of B-centres, only one of which requires a N3 centre as an intermediate, it may not be unsurprising that the relationship is not as quantitatively simple as the hypotheses explored here. The growth history of this diamond can be explained similarly to the Diavik samples, with the initial growth event responsible for the core of the diamond taking place under conditions where very little hydrogen is present. This is then followed by a different

growth event, responsible for the formation of the rim of the diamond. The anomalously high concentrations of N_3VH towards the rim could be caused by overgrowth features such as cuboid growth, which could potentially lead to the preferential incorporation of certain defects such as N_3VH. If this is the case, it could be possible that the hypotheses discussed here are only consistent for diamonds exhibiting regular octahedral growth. The fluids responsible for this overgrowth would appear have a significant concentration of available hydrogen, and therefore the concentration of N_3VH increases.

Arg 118 is unique in this data set, as the concentration of N_3VH is very small compared to the other samples; a maximum concentration of only 0.02 ppm is observed. The general correlation of the N3 centre to the B-centre concentration can therefore be observed. In line with the hypotheses discussed here, this diamond may have formed from fluids that contain very little hydrogen available for incorporation. There appears to be no significant difference in the availability of hydrogen from the core to the rim of the diamond.

An additional piece of evidence for the formation of N_3VH directly from N3 centres is the relative concentrations of the two defects. In this work, both defect concentrations range from negligible to a maximum of ~ 7 ppm. The fact that both centres are present in similar quantities is consistent with the formation mechanism proposed here. It also fits with the suggestion that the controlling factor in the relative amounts of each centre is a separate quantity, in this case the amount of hydrogen present during diamond growth. Alongside this, the fact that N3 and N_3VH are present in roughly the same concentrations could be considered as a secondary verification for the calibration produced for [N_3VH] by Coxon *et al.*, 2020. It is also possible to attempt to refine the Coxon results via optimisation of the fit in Fig 4.18c. When the absorption coefficient for [N_3VH] is varied, the best linear fit is provided with the following relationship

$$[N_3VH^0]_{Wood}(ppm) = 0.07\ ppm\ cm^2\ \times\ I_{3107\ cm^{-1}}\ (cm^{-2})$$

This can potentially be considered as a refined extinction coefficient for the N_3VH centre. The verification and refinement of the Coxon calibration are predicated on the accuracy of the hypotheses presented within this work.

The quantification attempts provide slightly different relative abundances for the different samples. All the attempts provided here, and the data set as a whole, provide a relative abundance of N3 and N_3VH of between 1.5 – 3.5 % of the total B-centre concentration. For Udachnaya 3143, this involved excluding the rim of the diamond. When the rim of the diamond is excluded, a very strong linear relationship is observed.

There is a clear link between the B-centre concentration and the concentration of the N3 and N_3VH centres. However, the variation in proportionality constants for each sample suggests that the exact proportion in which N3 and N_3VH are formed can vary between each sample. The values are all of similar magnitude, but the exact value varies within the range observed. This indicates that there is likely another factor that can affect the relative abundances. As the behaviour of the N3 centre in terms of the kinetics of the interconversions between the aggregates is not well constrained, this could potentially be temperature of storage within the mantle. This could lead to a situation in which, storage at certain temperatures promotes favourable formation of N3. This would then explain the variation in relative abundance observed within this work.

When considering the line scans as a combined data set, a significantly stronger positive correlation is observed for $[N_B]$ vs. [N3] + $[N_3VH]$ than for the single spectra. This is consistent with previous work which correlated the N3 centre alone with the B' and, by extension, the B-centre concentration (Woods, 1986). This allows for the generation of an estimate that the concentration of nitrogen present in the form of N3 or N_3VH is approximately 2.5 % of the

amount of nitrogen present in the form of B-centres. While clearly still a minor aggregate compared to the B-centre, there is a significant amount of nitrogen present in the form of these centres. It must be noted that this correlation is not perfect but does provide further evidence as to the proportionality involved in this reaction process. From the results presented here, it is likely that a correlation is more easily observed when considering a single sample than a set of samples. This can be rationalised, as for each individual sample there is less variation in terms of further history of the diamond than within a group of diamonds. If there are indeed other processes that can affect the relative abundance of these centres, a collective data set across multiple localities would not be expected to provide a dataset capable of quantifying this. If the data set were expanded significantly then a better idea of the processes governing this could potentially be observed.

From the results of this work, it appears that hydrogen can indeed play a role in the quenching of the nitrogen process. If the N3 centre is an intermediate in B-centre formation, and can be removed from the aggregation sequence through the capturing of a hydrogen atom, then the more hydrogen present within the growth medium, the more nitrogen would be removed from the aggregation sequence by generation of N_3VH centres. Due to the multiple reaction mechanisms proposed for B-centre formation, not all of which contain N3, it is difficult to quantify the exact amount to which hydrogen can impact the aggregation state of nitrogen within a diamond.

While the results presented within this chapter are indicative of the potential use of the relative abundance of N3 and N_3VH as a hygrometer, it is worth noting the pitfalls. Udachnaya 3143 highlights the fact that irregular growth conditions may obscure these trends. This means that the results presented here can only be applied to regular diamonds, or regular growth zones within heterogenous diamonds. There is also the inherent uncertainty introduced through the

collection of two separate line scans. Development of instrumentation that could simultaneously collect UV-vis and IR spectra would minimise these uncertainties.

4.5 Conclusions

There were two primary hypotheses discussed earlier, and these will be discussed in turn. The first was that the N3 defect is formed in a set proportion to the concentration of B-centres. This work has provided evidence to support this, with the results from single spectra showing proportionality. This was also supported by the results from the line scans, in particular those of Arg 118 and Udachnaya 3143. These samples showed a significant correlation between the N3 and B-centre concentrations. The single spectra did not show a perfect relationship between the two features, and the Diavik samples showed complex zonation where a correlation could still be observed. This suggests that the proposals of multiple formation mechanisms for B-centres, not all of which contain an intermediate in the form of N3, is likely correct. The results from the line scans allowed for an estimate of the proportionality to be produced for each sample. This suggests that the amount of nitrogen present as N3 and N_3VH centres is between 1.5 – 3.5 % of the amount of nitrogen present as B-centres. The exact factor controlling the value within this range is unknown, but a possible relation to storage temperature of the diamond was discussed. It is likely that proportionality is the case in samples exhibiting normal octahedral growth, but that the exact value of the relative abundances can vary between different diamonds.

The second hypothesis is that the primary formation mechanism of the N_3VH centre is through protonation of an N3 centre. This work has provided evidence that this is the case. With the single spectra, a sum of the N3 and N_3VH centre concentrations provided a stronger relationship with the B-centre concentration than either component alone. Alongside this, the spatially resolved line scans demonstrated a consistent trend of enrichment in the N_3VH centre concentration at regions of the diamond in which there was a lower relative concentration of N3. Along with the concentrations of both defects ranging from negligible to ~ 6 ppm, this

strongly indicates that the formation of the two defects are heavily linked. This is consistent with the formation mechanism proposed above.

A rationale has been discussed for the variations in concentrations being based upon the relative availability of hydrogen during diamond formation. This can explain the trends observed across the line scans. Continuation of this work could expand this data set, and the relative abundance of the N3 and N_3VH defects discussed here may provide information about the availability of hydrogen in diamond-forming fluids across various localities. For example, the observation of high [N_3VH] with low/zero [N3] would perhaps be considered a better indicator of hydrogen content in the diamond-forming fluids than observation of high [N_3VH] alone, with no consideration of N3 concentrations. The relative abundance can therefore be considered as a form of hygrometer. The differences observed in the Diavik samples studied here also suggest a significant change in fluid composition and relative availability of hydrogen with time.

Future work could probe the value of the relative abundances further, building a data set that may allow for comparisons to be made between localities. By doing this, the factors that control the relative abundance of N_B, N3 and N_3VH could be further interrogated.

5. A study of a minor hydrogen-related peak in diamond – clues as to the origin of the 3236 cm^{-1} feature

Declaration

The single spectra in this chapter were collected by Nuzhat Tabassum. However, the line scans and all data processing were undertaken by me. Sample polishing for FTIR studies was carried out by Galina Bulanova.

5.1 Introduction

Although the 3107 cm^{-1} feature is by far the most dominant hydrogen-related peak in the IR spectrum for the majority of samples, there are over 90 lines or absorption systems in the IR and UV-visible range that have been at least tentatively attributed to hydrogen (Fritsch et al., 2007). When the intensity of the 3107 cm^{-1} feature is high, peaks at 2786 cm^{-1} and 3236 cm^{-1} (sometimes reported as 3237 cm^{-1}) can often be observed. The intensity of the 2786 cm^{-1} has been observed to correlate well with the intensity of the 3107 cm^{-1}, and is therefore thought to be part of the same system, specifically attributed to an overtone of the bending mode at 1405 cm^{-1}. The fact that the peak is observed at a slightly lower frequency than would be expected by a simple arithmetic sum can be explained by slight anharmonicity in the vibration (Davies et al., 1984).

Whilst the 3107 cm^{-1} is well-characterised, likely due to its intensity and ubiquity, the origin of the 3236 cm^{-1} feature is a lot more unclear. Originally thought to possibly be a part of the same system as the 3107 cm^{-1} peak, it has since been shown that its intensity is entirely independent of the 3107 cm^{-1} peak, such as in asteriated diamonds with sector-dependent IR signatures (Rondeau et al., 2004), where the relative intensity does not show any preference for certain growth sectors, unlike the 3107 cm^{-1} peak itself. The peak is seen in many types of diamond, but an unusually intense 3236 cm^{-1} is a characteristic of 'grey-blue-violet' diamonds from the Argyle mine in Australia (van der Bogert et al., 2009). The intensity of the feature is often higher in Type IaB diamonds, whatever the colour of the stone, and it has previously been suggested that the feature is less frequently observed in low-nitrogen diamonds (Fritsch et al., 2007). These diamonds are thought to be some of the most hydrogen-rich natural samples in existence, due to the dominance of hydrogen-related features in the IR spectra. An example spectrum from such a sample, RTD002, can be seen in Figure 5.1. The features labelled show

the intensity of the hydrogen-related features in comparison with the intrinsic absorption in the two-phonon region that is characteristic of diamond.

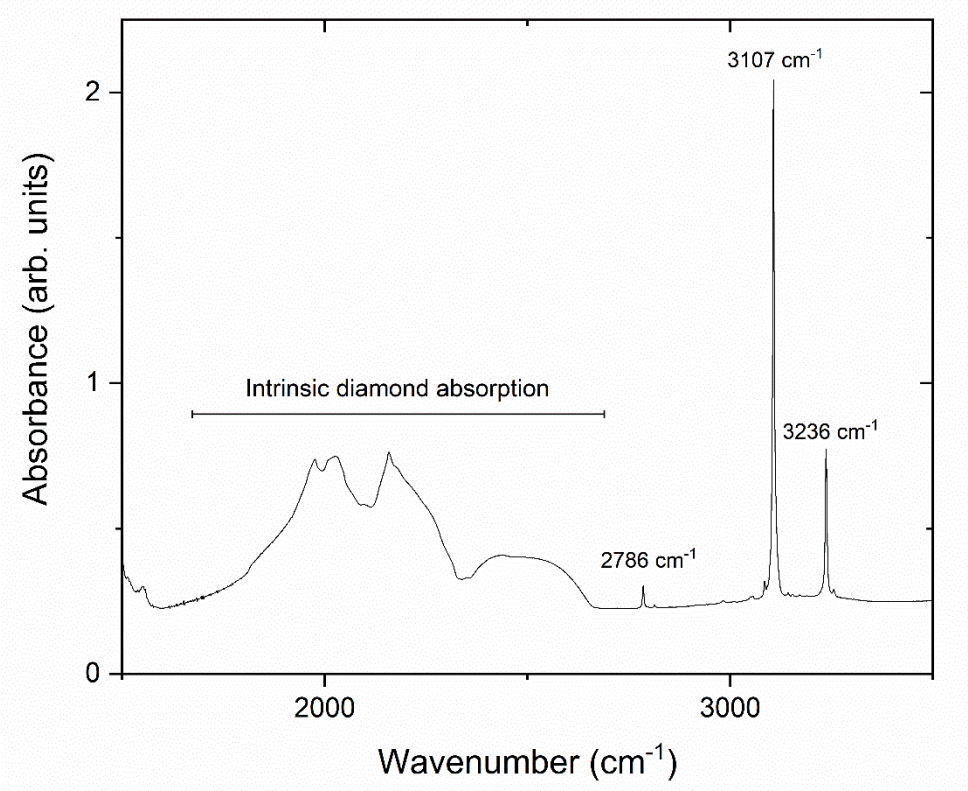

Figure 5.1: An example IR spectrum of a grey-blue-violet 'hydrogen-rich' diamond (in this case RTD002), with the 2786 cm^{-1}, 3107 cm^{-1} and 3236 cm^{-1} features highlighted. The intensity of the 3107 cm^{-1} and 3236 cm^{-1} is exceptionally high compared to that of the intrinsic diamond absorption.

Previous studies have suggested that the feature could be due to an amine (N-H) vibration due to the lack of correlation with various C-H vibrational features (Woods and Collins, 1983). It has also been suggested that the peak could be attributed to an alkyne (C≡C-H) stretch (Iakoubovskii and Adriaenssens, 2002), although, beyond a simple comparison of the vibrational frequency with reference data tables (e.g. Socrates, 2004), no evidence supporting this has been provided. An increase in the intensity of the feature has been observed upon annealing a number of grey diamonds, previously attributed to the mobilisation of hydrogen within the diamond via the breaking down of C-H bonds in graphitic impurities at the temperatures involved (typically around 1800 °C) (Vins and Kononov, 2003). These H atoms can then be trapped at pre-existing defects within the diamond lattice.

Not solely found in natural diamonds, the feature has been observed in synthetic samples, and can be annealed in. High-pressure high-temperature (HPHT) diamonds have also been grown using ^{13}C, and upon this, no isotopic shift was observed in the frequency of the 3236 cm^{-1} peak, which is consistent with the proposal of an N-H stretch being responsible for the feature. The N-H vibration is normally much broader than the observed feature in diamond (Socrates, 2004). However, for a very dilute impurity species, the absorption could be sharp due to the lack of hydrogen bonding with neighbouring groups within the structure, as is seen in substances such as polymers (Fritsch et al., 2007 and ref. within). Furthermore, if a stretching vibration is observed, a corresponding bending mode should be seen around 1600 cm^{-1} (Socrates, 2004). Although this vibration would likely be weaker than the stretching mode, as is the case in the 3107 cm^{-1} system, no likely candidate has been observed. A peak has been observed at 4703 cm^{-1}, the intensity of which correlates well with that of the 3236 cm^{-1} feature, and has thus been attributed to a combination band of the system (Fritsch et al., 2007). If this feature does indeed represent the first combination band, the other fundamental would, through a simple arithmetic sum, be expected to be present at an energy slightly above 1467 cm^{-1}, which is consistent with an amine group being responsible for the feature, although as mentioned above, no likely candidate for this feature has as yet been identified.

The 3236 cm^{-1} feature has been commonly observed in type IaB diamonds from the Mir pipe in Yakutia, observed as having a highest intensity in diamonds with the highest B-centre content (Yuryeva et al., 2017), in accordance with some previous studies of cut gem-quality diamonds (Ferrer and Nogués-Carulla, 1996). It has also been preferentially observed in so called ‘milky’ type IaB diamonds; samples which are cloudy in appearance have been shown to preferentially exhibit the 3236 cm^{-1} feature in comparison to their non-milky type IaB counterparts (Gu and Wang, 2018). In this study, ~ 53 % of milky diamonds contained the feature as opposed to ~ 12 % of non-milky samples. These milky diamonds also commonly

contained a number of optical features associated with plastic deformation, such as deformation lamellae (Hanley et al., 1977). The peak has even been observed in presolar diamonds found in meteorites, such as the Allende meteorite (Braatz et al., 2000).

Recent theoretical work has investigated the possibility of the 3236 cm^{-1} peak being caused by the trapping of a hydrogen atom by a VN_4 defect centred within a platelet (Gu et al., 2020) – see section 1.2.2 for a more in depth discussion of platelets. The computational studies of this configuration suggested that it could be a possible candidate for this IR feature. In addition, it was shown that inclusion of the platelet-centred VN_4H defect quenched other platelet-related IR features, which could be an explanation for the observation of this feature in diamonds not displaying prominent platelet peaks. This suggestion led to the proposal that platelets, with their unique structure and potential for a number of dangling bonds, could act as significant reservoirs of hydrogen within diamonds. The predicted quenching could be thought to make it difficult to test this hypothesis using IR alone, as, if this were true, there would be no observable correlation between the observed platelet peaks and the 3236 cm^{-1} peak. However, due to the possibility of examining the irregularity of diamonds and the amount of platelet degradation, this could be possible to examine. If a platelet-centred defect is responsible for this feature, then it could be expected that the more platelet-degraded a diamond is, the smaller the 3236 cm^{-1} peak would be compared to the 3107 cm^{-1} peak. However, it must be noted that the quenching would naturally lead to the observation of more degraded platelets than may be the case, which must be considered. The study of the platelet feature and how it corresponds to the relative intensity of the 3236 cm^{-1} peak could still provide some information as to the viability of the claim, although there are some issues in terms of quantifying this relationship.

In-depth studies of diamonds from various localities could potentially shed more light on the nature of this feature. By investigating spatial variations of the feature alongside other features

that can be studied through IR, further information may be gleaned as to what is causing this widely observed peak.

5.2 Materials and methods

5.2.1 Samples

A large sample set of previously studied samples was filtered down to a set of 36 parallel plates using the presence of the 3236 cm^{-1} feature in their IR spectra as the selection criterion. These samples originate from four localities: Argyle (Western Australia), Diavik (Canada), Murowa (Zimbabwe) and Bunder (India). The diamonds were polished to thin, central plane-parallel plates oriented parallel to {110}, as discussed in chapter 2 to be most suitable for FTIR studies. A full list of the samples used in this work is presented below in table 5.1.

Locality	**Sample**	**Single spectrum?**	**Line scan?**
Argyle, Australia	Arg 10	N	**Y**
	Arg 31	**Y**	N
	Arg 51	N	**Y**
	Arg 70	**Y**	**Y**
	Arg 71	**Y**	N
	Arg 78	N	**Y**
	Arg 81	**Y**	N
	Arg 83	**Y**	N
	Arg 86	**Y**	N
	Arg 103	**Y**	N
	Arg 128	**Y**	**Y**
	Arg 143	**Y**	N
	Arg 164	**Y**	N
Diavik, Canada	DVK 076	**Y**	**Y**
	DVK 098	**Y**	N
	DVK 115	**Y**	N
	DVK 122	**Y**	**Y**
	DVK 127	**Y**	**Y**
	DVK 131	**Y**	N
	DVK 135	**Y**	N
	DVK 159	**Y**	**Y**
	DVK 160	N	**Y**
	DVK 166	**Y**	N
Murowa, Zimbabwe	Mur 65	**Y**	N
	Mur 107	**Y**	N
	Mur 112	**Y**	N
	Mur 122	**Y**	N
	Mur 141	**Y**	N
	Mur 173	**Y**	N

	Mur 182	**Y**	N
	Mur 265	**Y**	N
	Mur 279	**Y**	N
Bunder, India	Bunder 9	**Y**	N
	Bunder 12	**Y**	N
	Bunder 17	**Y**	N
	Bunder odd	**Y**	N

Table 5.1: A list of the samples used for this study. The table contains the locality and name of each sample, along with whether or not they are part of the single spectra dataset, the line scan dataset, or both.

5.2.2 FTIR

A full write up of the procedure used can be found in chapter 2.

This section contains two approaches to looking at how the spectral features can vary in the samples compared to each other. The first is simply to look at the change in 3236 cm^{-1} peak area with other measurable features such as the various nitrogen aggregate concentrations, and the second is to look at the relative area of the 3236 cm^{-1} peak to the 3107 cm^{-1} peak. Where a ratio is referred to within this chapter, this is meant in the form of *log(3236 area/3107 area)* for ease of visualisation. In practical terms this means that the closer to zero the value of the ratio is, the higher the relative intensity of the 3236 cm^{-1} peak. This chapter contains single spectra collected from individual diamonds, and line scans collected on 10 heterogenous samples.

5.3 Results

5.3.1 Single spectra

Values calculated from the IR spectra in this section can be found in Appendix A.1. Figure 5.2 presents the intensity of the 3236 cm^{-1} peak, provided as peak area in cm^{-2}, plotted against the concentrations of the various nitrogen aggregates and aggregation state, i.e. the percent of nitrogen present as B-centres, with a diamond containing only B-centres falling at 100 % aggregated. The diagrams appear to show a weak positive correlation with $[N_A]$ and a stronger correlation with $[N_B]$, with a Pearson product-moment correlation coefficient (PMCC) of 0.282 and 0.677 respectively. The correlation with $[N_t]$ appears to be stronger still, with a PMCC of 0.809. There is no correlation observed with aggregation state, with the peak being observed in diamonds with low, moderate and highly aggregated nitrogen. There do not appear to be any trends observed within diamonds of specific localities. Figure 5.3 shows the same data as Figure 5.2 but using the ratio of the 3107 cm^{-1} and 3236 cm^{-1} peaks.

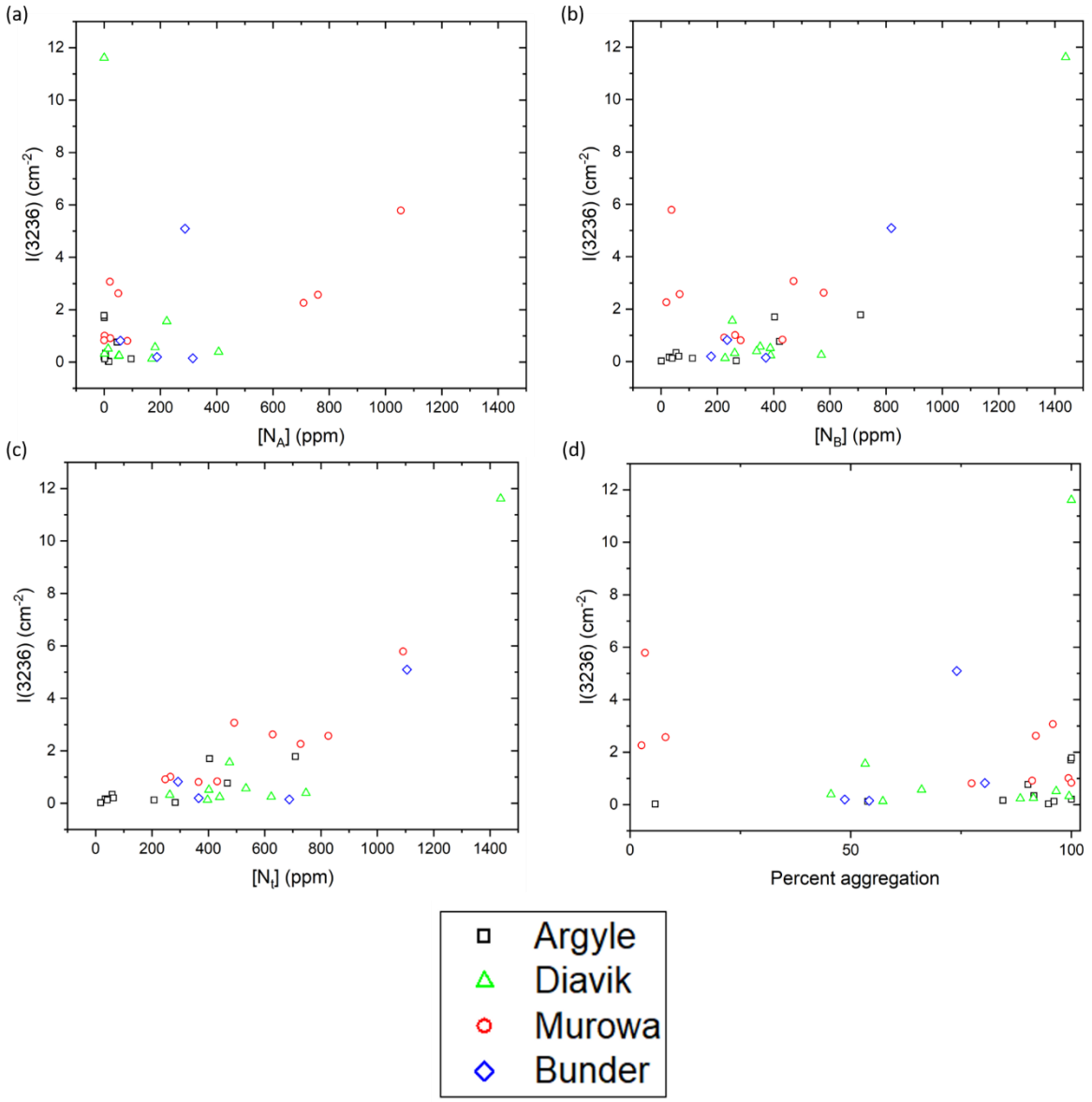

Figure 5.2: A series of plots displaying various nitrogen related features vs. I(3236) in cm^{-2} in order: (a) [N_A], (b) [N_B], (c) [N_t] and (d) displaying percent aggregation. Each point represents a single diamond, black squares are Argyle, red circles from Diavik, green triangles from Murowa and blue diamonds represent stones from Bunder. Error bars are omitted for clarity as they are roughly the same size as the symbols.

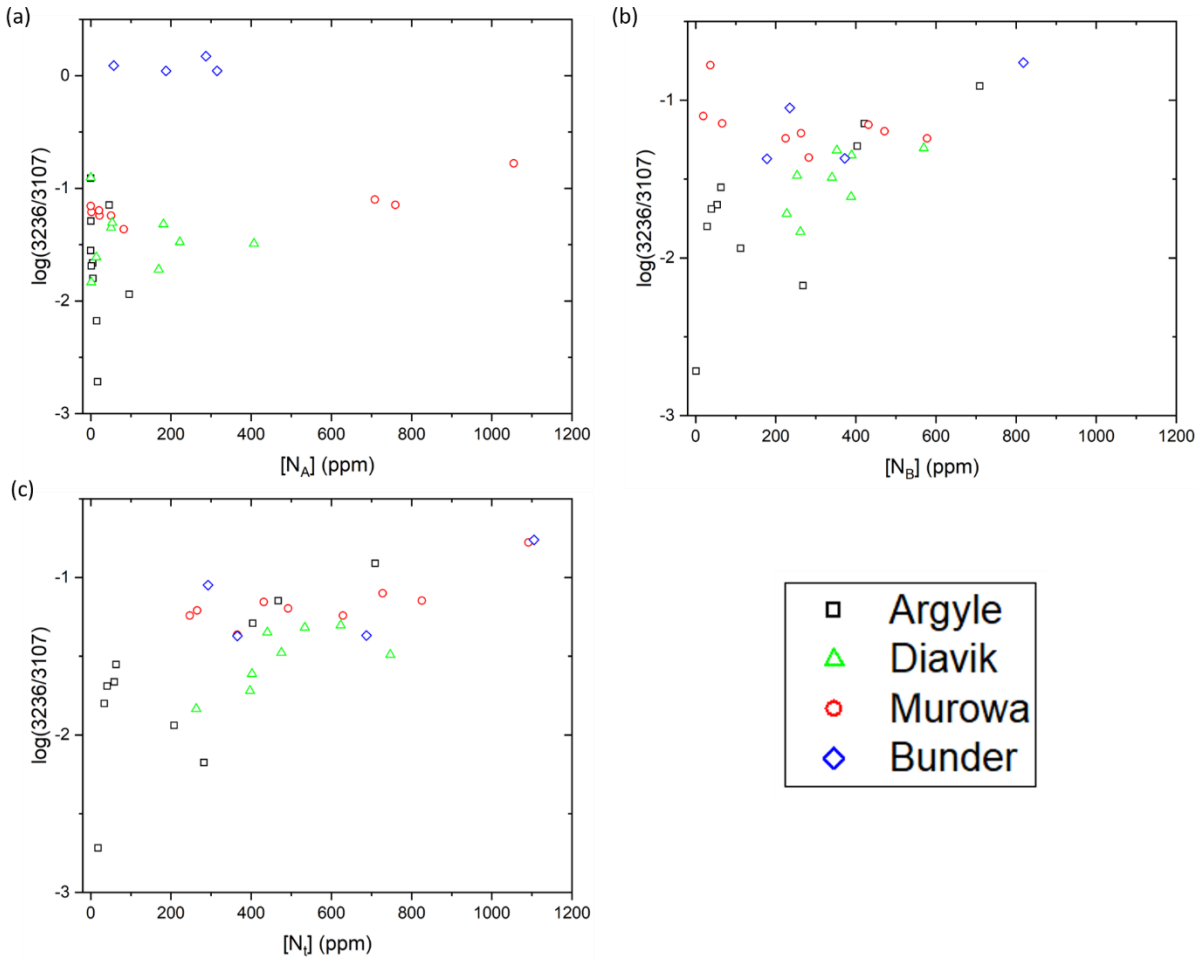

Figure 5.3: series of plots displaying various nitrogen related features vs. log(3236/3107). In order: (a) [N_A], (b) [N_B] and (c) [N_t]. Error bars are omitted as they are roughly the same size as the symbols.

Figure 5.4 shows two relationships: in 5.4a the 3107 cm^{-1} peak area is plotted against the area of the 2786 cm^{-1} peak; thought be to an overtone of the N_3VH bending mode found at 1405 cm^{-1}, as discussed in Section 5.1, and in 5.4b, the area of the 3107 cm^{-1} peak is plotted against the area of the 3236 cm^{-1} peak. Figure 5.4a shows the linear relationship expected from two peaks part of the same system, with a PMCC of 0.993. By contrast, the relationship with the 3107 cm^{-1} peak is more complex, agreeing with previous studies that the two features are not part of the same system. However, whilst not as strong a relationship as with the 2786 cm^{-1}, there does seem to be a link between the two peaks, having a relationship that appears roughly as strong as the relationship in Fig. 5.2c above, with a PMCC of 0.873.

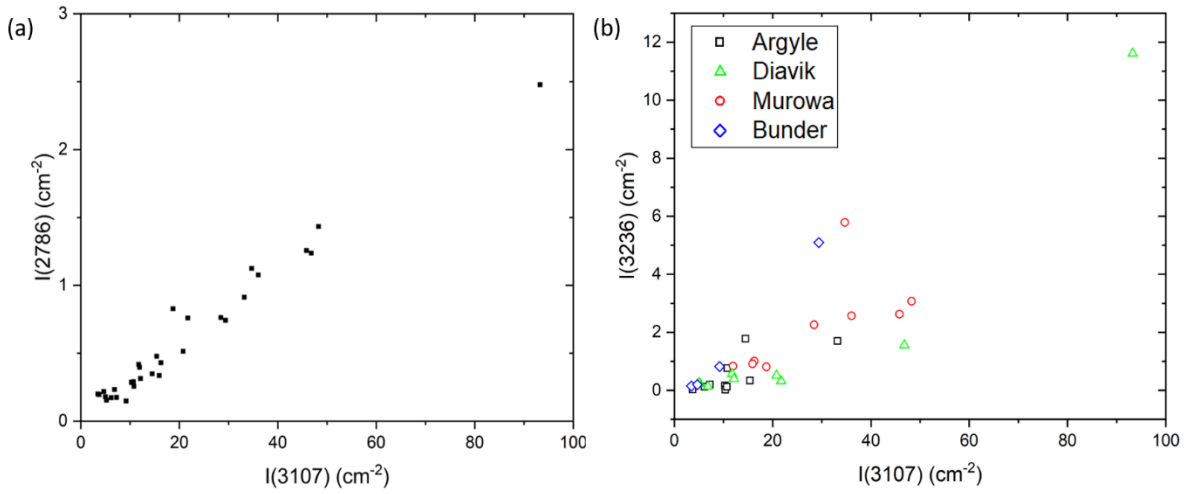

Figure 5.4: (a) the area of the 3107 cm^{-1} peak against the 2786 cm^{-1} peak, thought to be an overtone within the same system (b) the area of the 3107 cm^{-1} peak against the 3236 cm^{-1} peak. Black squares are from Argyle, red circles from Diavik, green triangles from Murowa and blue diamonds are from Bunder. Error bars are omitted as they are roughly the same size as the symbols.

5.3.2 Linescans by region

Figure 5.5 shows the observed relationships between $[N_A]$, $[N_B]$ and $[N_t]$ and the area of the 3236 cm^{-1} peak in 5 heterogeneous diamonds from Argyle. It is worth noting that the diamonds here are highly aggregated, and so have a low concentration of A-centres, in particular Arg 70 and a large number of points from within Arg 78 and Arg 128. Also of note is that Arg 51 contains a number of points that appear anomalously high when compared to the trends observed in the other samples. Whilst not clear-cut, it appears that in general the same trends are observed as in the single spectra, with a general trend of increasing peak area with increasing $[N_B]$ and $[N_t]$.

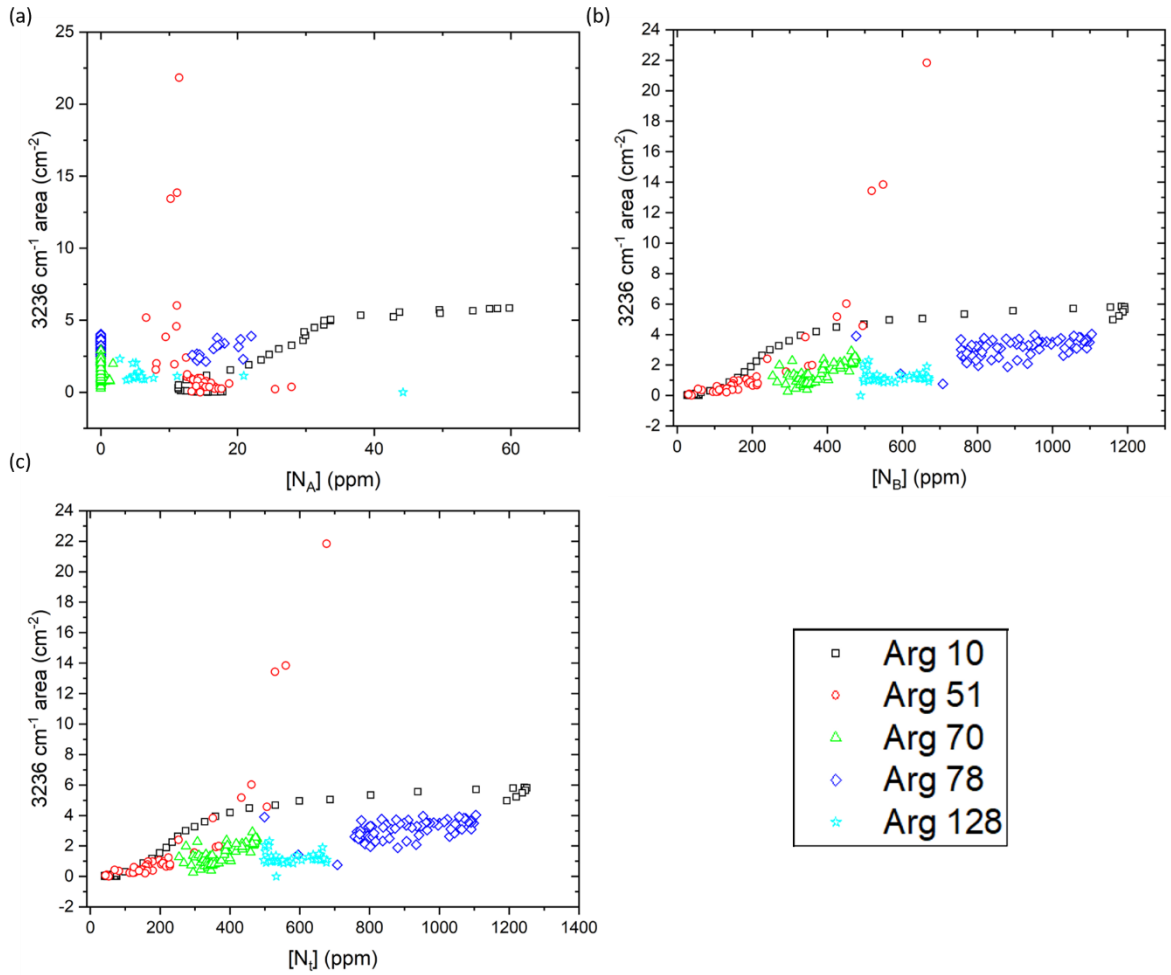

Figure 5.5: plots of the various nitrogen aggregate concentrations against the area of the 3236 cm^{-1} peak for some heterogeneous samples from Argyle; (a) shows [N_A], (b) [N_B] and (c) [N_t]. Black squares represent Arg 10, red circles are Arg 51, green triangles are Arg 70, dark blue diamonds are Arg 78 and light blue stars are Arg 128.

Figure 5.6 shows the relationships of the various nitrogen aggregates with the relative intensity of the 3236 cm^{-1} peak as compared to the 3107 cm^{-1} peak. In a similar way as Figure 5.5a, the concentration of A-centres is low due to the high aggregation states of the nitrogen in theses samples, and so it is difficult to discern trends in the data in Fig 5.6a. However, using a peak area ratio makes it possible to use the anomalously high points discussed above from Arg 51, as calculating a ratio removes the effect of the increased path length due to the crack. Arg 10 shows a distinct trend of an increasing relative intensity of the 3236 cm^{-1} peak with increasing concentrations of all nitrogen aggregates, particularly B-centres and the total nitrogen, before reaching a plateau at a certain concentration and levelling off. Whilst not as clearly displayed as in Arg 10, a similar trend can be seen to be loosely followed in all the Argyle samples,

although interestingly the value on both the x and y axes at which the plateau is reached seems highly variable, with no consistent trend being observed between different samples.

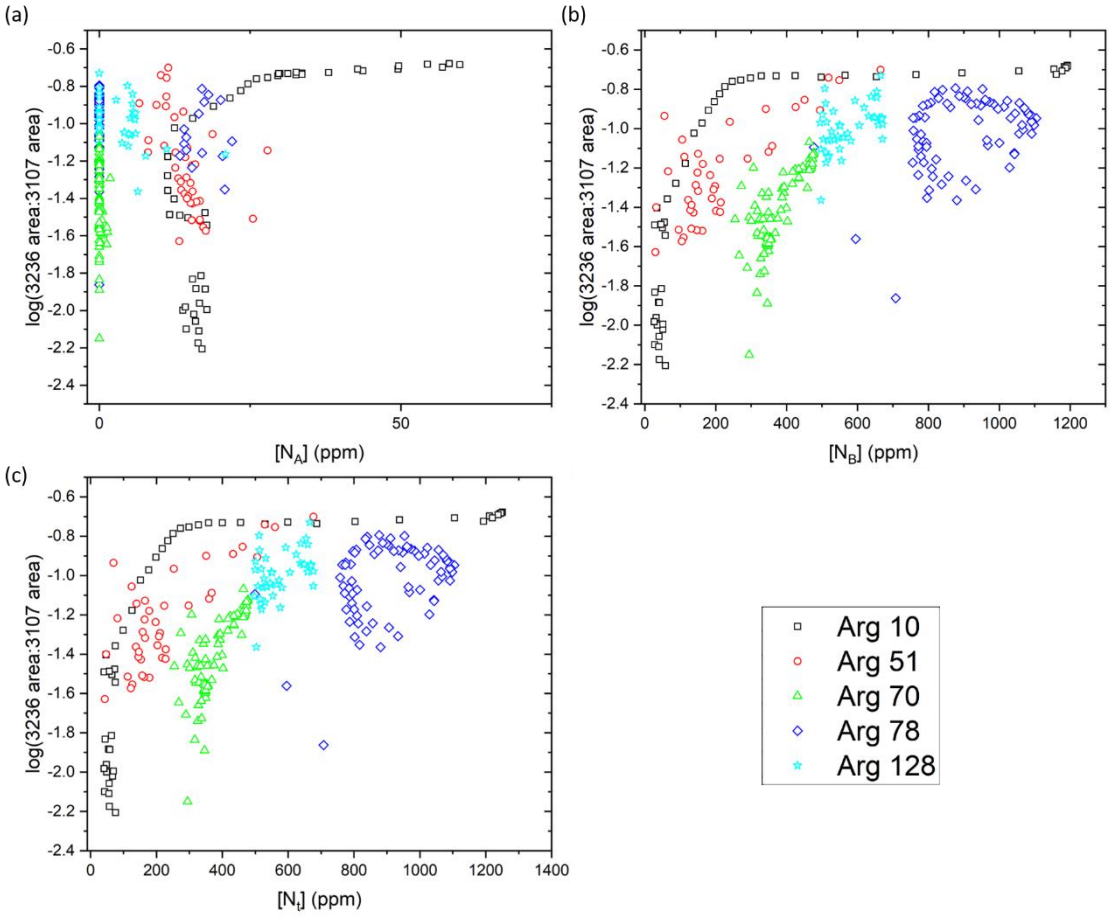

Figure 5.6: plots of the various nitrogen aggregate concentrations against the ratio of the 3236 cm^{-1} and 3107 cm^{-1} peak areas for some heterogeneous samples from Argyle; (a) shows [N_A], (b) [N_B] and (c) [N_I].

Figure 5.7 shows the relationship between the 3107 cm^{-1} peak and the 3236 cm^{-1} peak. A similar trend is present as in the single spectra in Figure 5.4b, with a loose positive correlation being observed across all samples when considered as a whole, although Arg 78 seems to show no correlation, with the intensity of the 3236 cm^{-1} peak appearing independent of 3107 cm^{-1} area entirely.

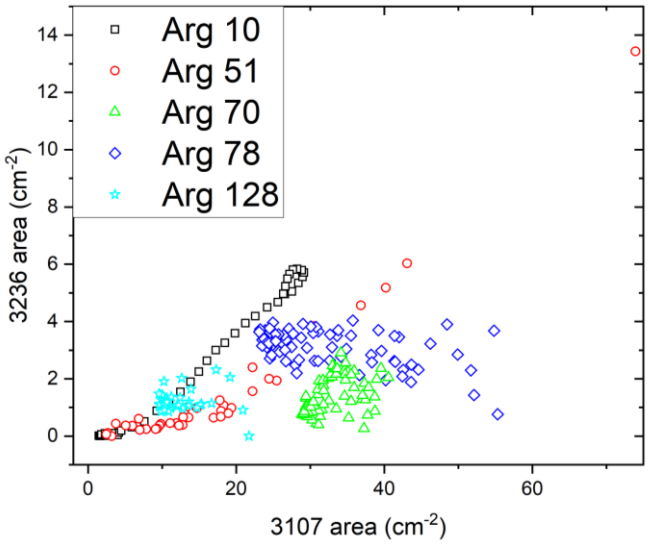

Figure 5.7: The relationship between the area of the 3107 cm^{-1} and 3236 cm^{-1} peaks as observed in 5 heterogenous Argyle diamonds.

Figure 5.8 shows the relationship between the intensity of platelet related features vs. the 3236 cm^{-1} peak area. 5.8a shows the platelet peak area and 5.8b displays the platelet degradation. There appears to be a general trend of increasing 3236 intensity with increasing platelet peak intensity. However, increased platelet degradation appears to lead to a slight decrease in 3236 peak area in all samples other than Arg 128, which is completely degraded.

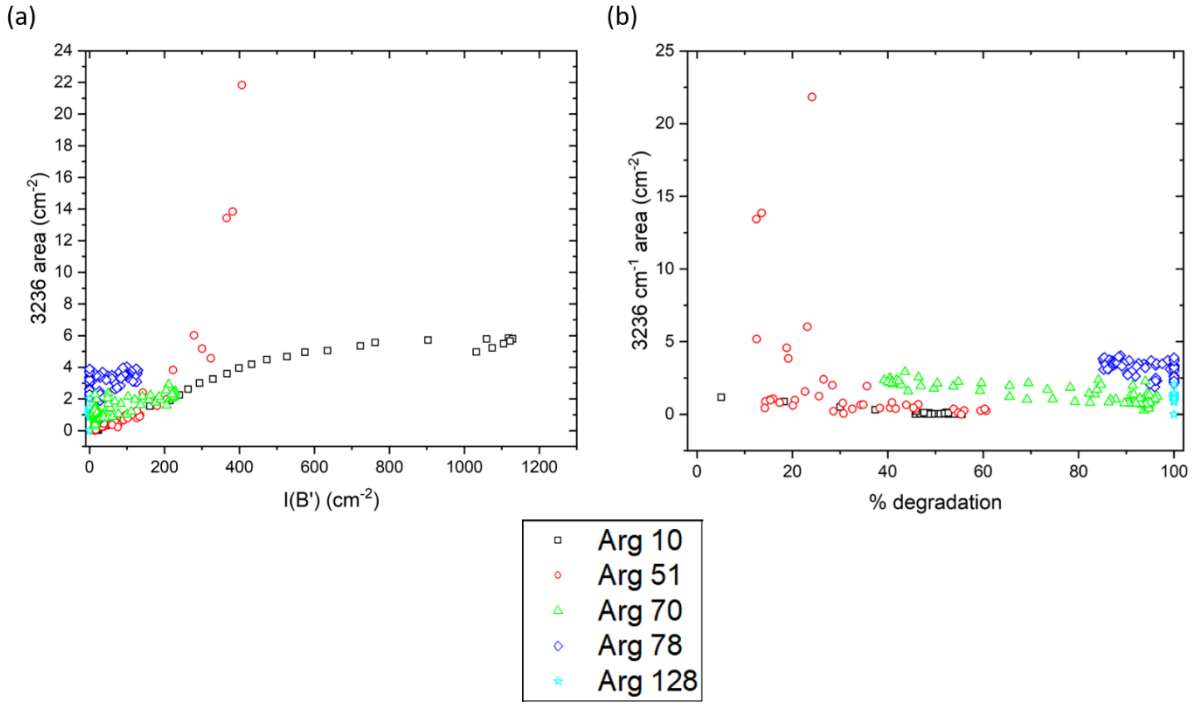

Figure 5.8: plots of the platelet related features against the area of the 3236 cm^{-1} peak for some heterogeneous samples from Argyle; (a) shows I(B') and (b) % degradation.

Figure 5.9 displays the same platelet features but plotted against the ratio of the 3236 and 3107 cm^{-1} peaks. 5.9a displays a similar trend as observed as between $[N_B]$, $[N_t]$ and the peak ratio, with a trend towards a plateau, best illustrated by Arg 10. The degradation plot in 5.9b appears to show a decrease in the relative intensity of the 3236 cm^{-1} peak as degradation increases within each sample.

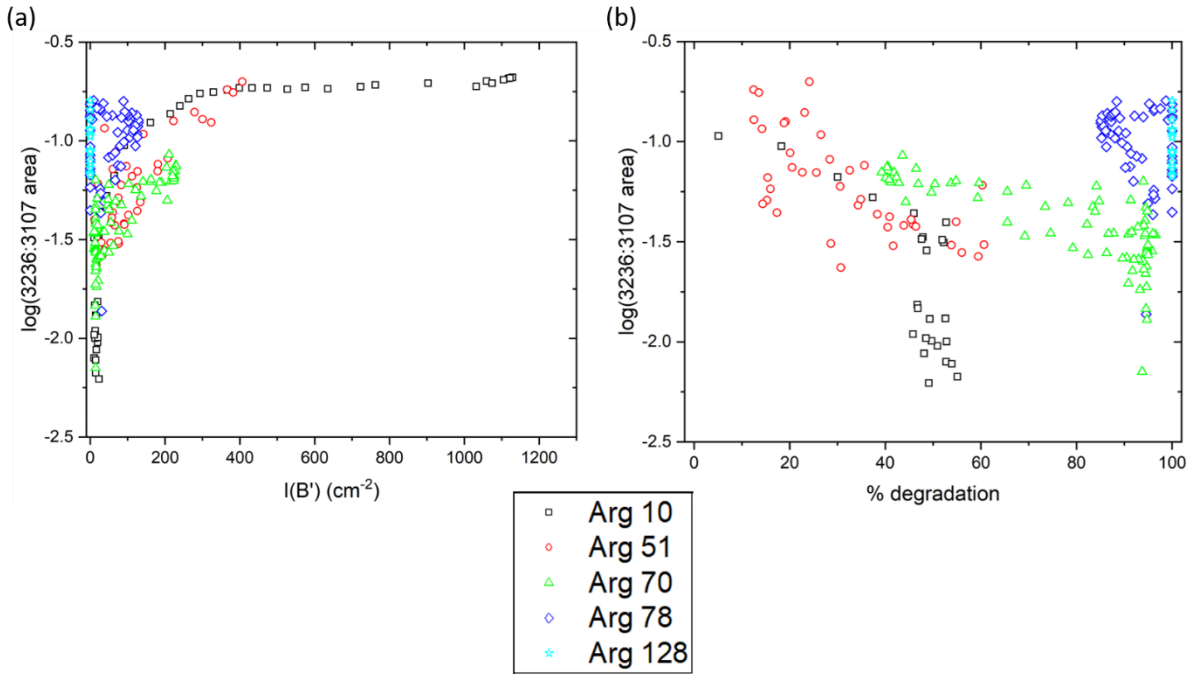

Figure 5.9: plots of the platelet related features against the ratio of the 3236 cm^{-1} and 3107 cm^{-1} peaks for some heterogeneous samples from Argyle; (a) shows I(B') and (b) % degradation.

Figure 5.10 shows the relationships of the various nitrogen aggregates with 5 heterogenous diamonds from the Diavik mine in Canada. Compared to the Argyle samples the trends displayed are more complex, with no observable correlation between any of the aggregates and the intensity of the 3236 cm^{-1} feature. Of note is the fact that, whereas all the Argyle samples contained predominantly B-centres – i.e. highly aggregated nitrogen, this is not the case for the Diavik samples, some of which contain up to 1000 ppm of A-centres with negligible B-centre content.

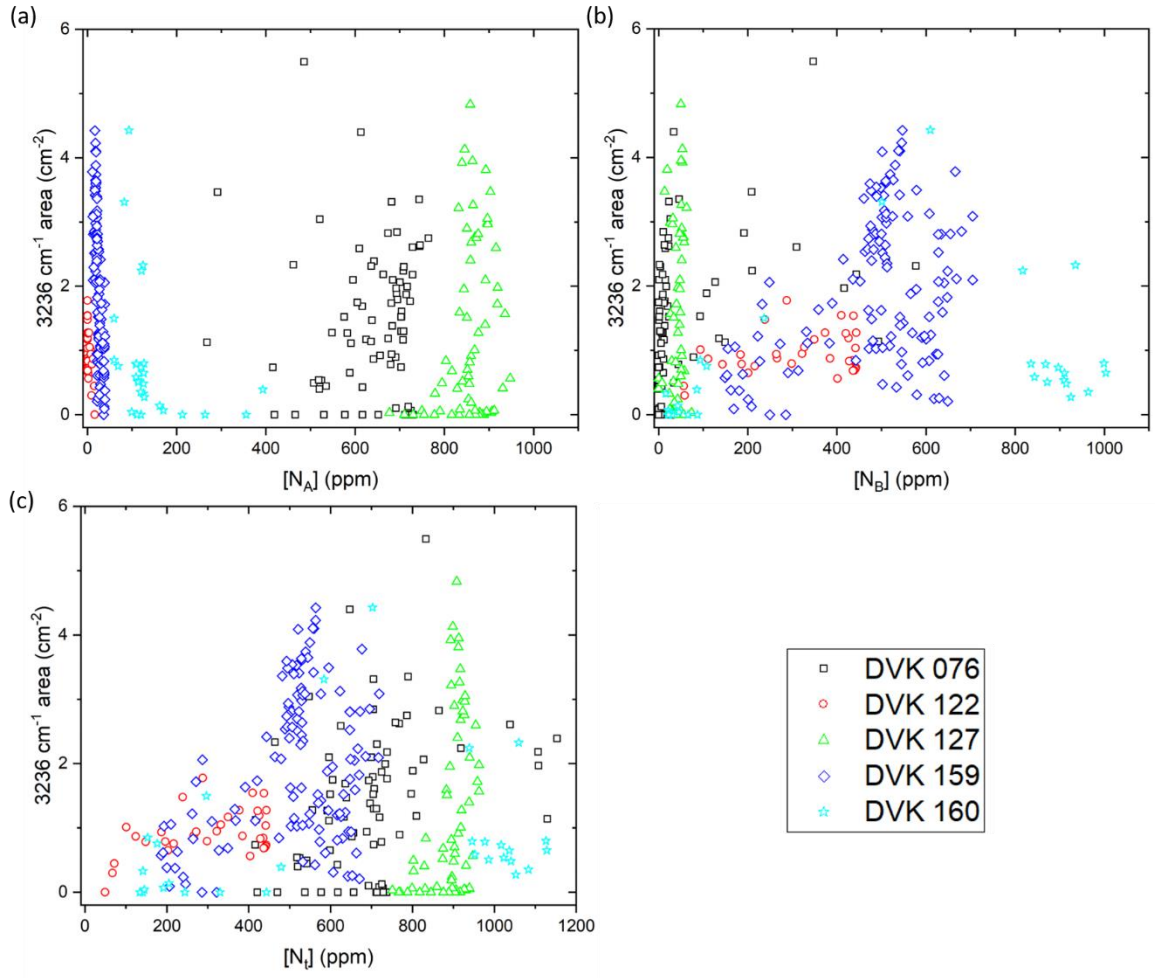

Figure 5.10: plots of the various nitrogen aggregate concentrations against the area of the 3236 cm^{-1} peak for some heterogeneous samples from Diavik; (a) shows [N_A], (b) [N_B] and (c) [N_t]. Black squares represent DVK 076, red circles are DVK 122, green triangles are DVK 127, dark blue diamonds are DVK 159 and light blue stars are DVK 160.

Figure 5.11 shows the relationship of the nitrogen aggregates against the relative intensity of the 3236 cm^{-1} peak. Unlike the Argyle samples, the 3236 cm^{-1} peak does not appear to grow in relative intensity with increasing [N_t], with no appearance of the distinct trend of an increase and then plateau. By contrast, there appears to be no correlation with any of the various nitrogen aggregates, with a range of relative peak intensities being displayed.

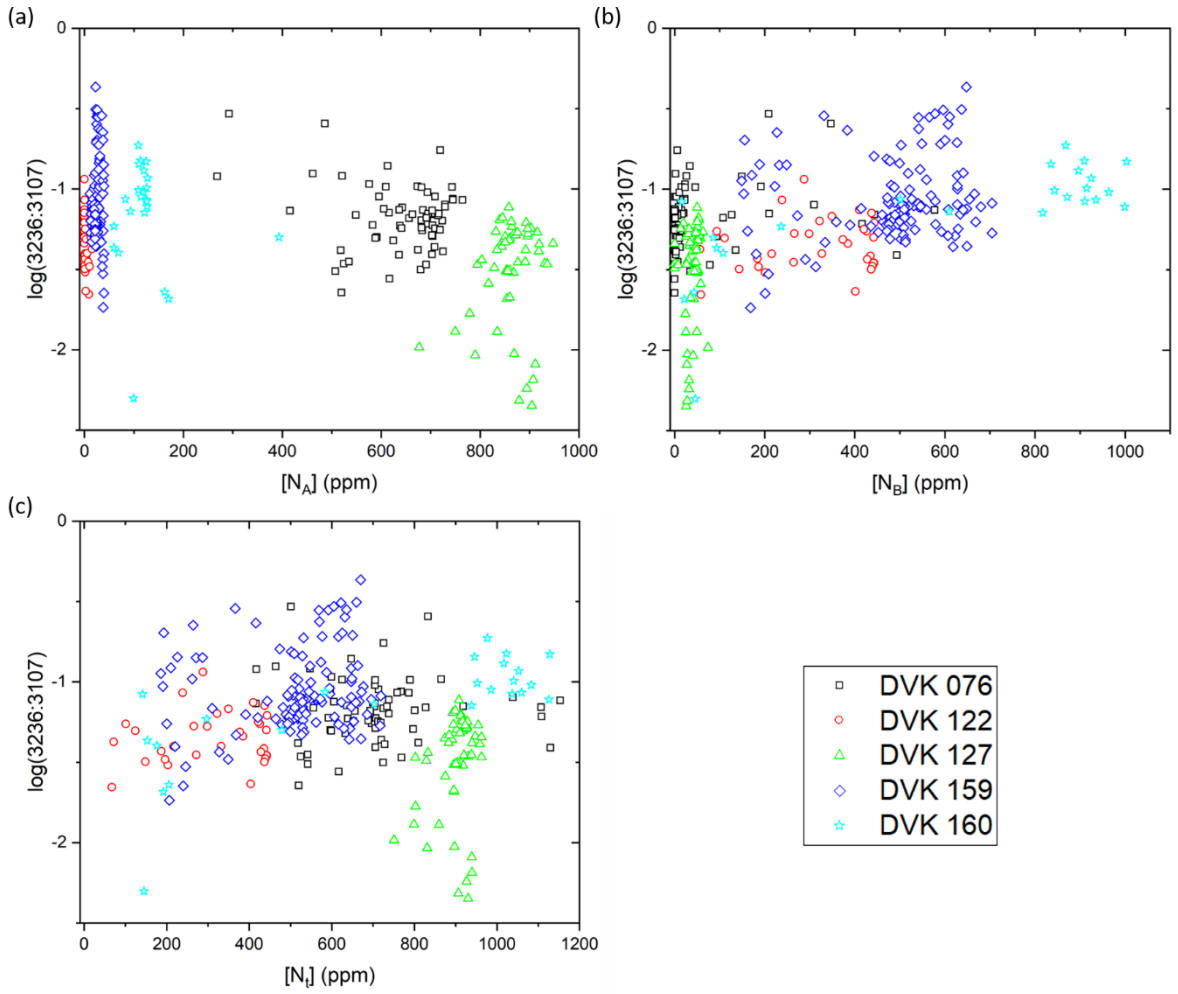

Figure 5.11: plots of the various nitrogen aggregate concentrations against the ratio of the 3236 cm^{-1} and 3107 cm^{-1} peak areas for some heterogeneous samples from Diavik; (a) shows $[N_A]$, (b) $[N_B]$ and (c) $[N_t]$.

Displayed in Figure 5.12 is the relationship observed between the 3107 and 3236 cm^{-1} peaks in the Diavik samples. The figure displays the data with a trendline plotted and assorted statistics shown in the legend. A clear correlation between the intensities of the two peaks is observed, with a PMCC of 0.851. This behaviour is much more distinct than in the Argyle samples.

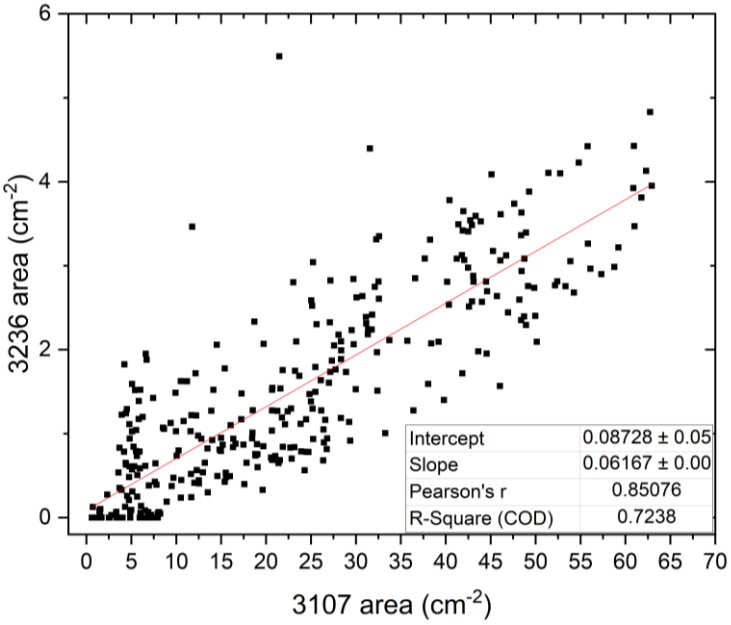

Figure 5.12: a plot of the relationship between the 3107 cm^{-1} and 3236 cm^{-1} peaks in the Diavik samples. This displays all points as one dataset, with a linear trendline plotted and some statistical values annotated on the graph, including the PMCC and R-squared value.

Figure 5.13 shows the platelet-related features vs. 3236 cm^{-1} area for the Diavik samples. There is no observable trend in either plot, with each sample displaying a range of platelet features that seem independent from the 3236 cm^{-1} area.

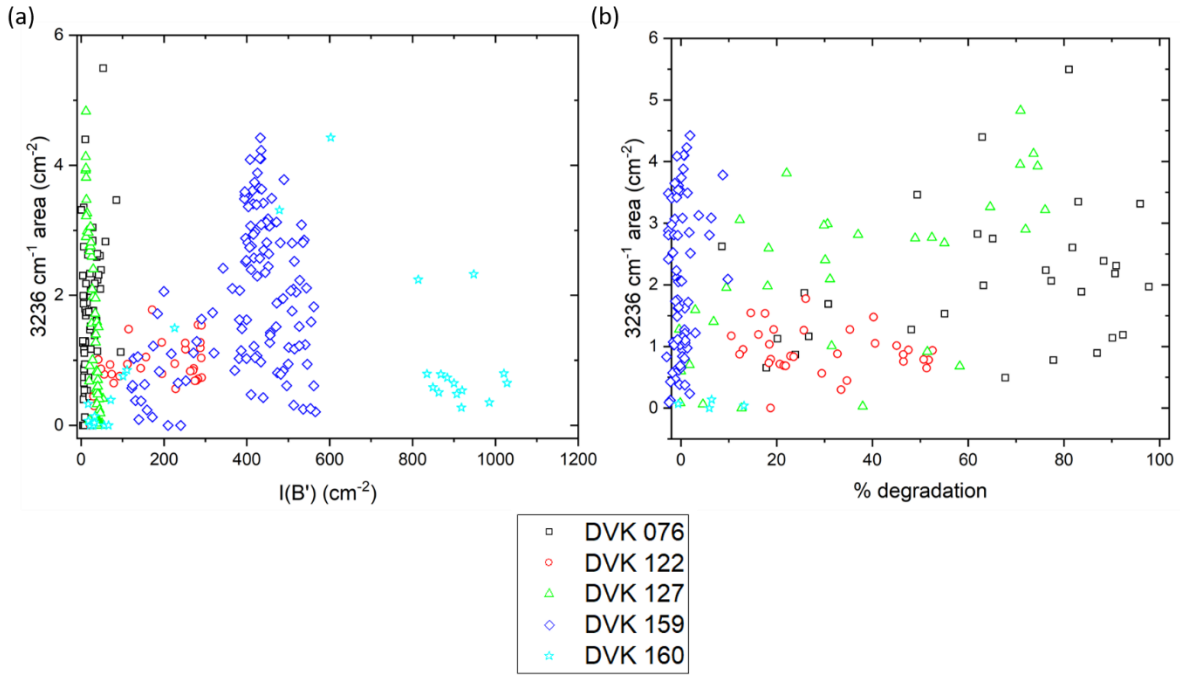

Figure 5.13: plots of the platelet related features against the area of the 3236 cm^{-1} peak for some heterogeneous samples from Diavik; (a) shows I(B') and (b) % degradation.

Figure 5.14 displays the platelet data against the ratio between the 3236 $cm^{-1}$and 3107 cm^{-1} peaks. Similarly to figure 5.13, there is no observable trend between these platelet features and the relative intensity of the 3236 cm^{-1} peak.

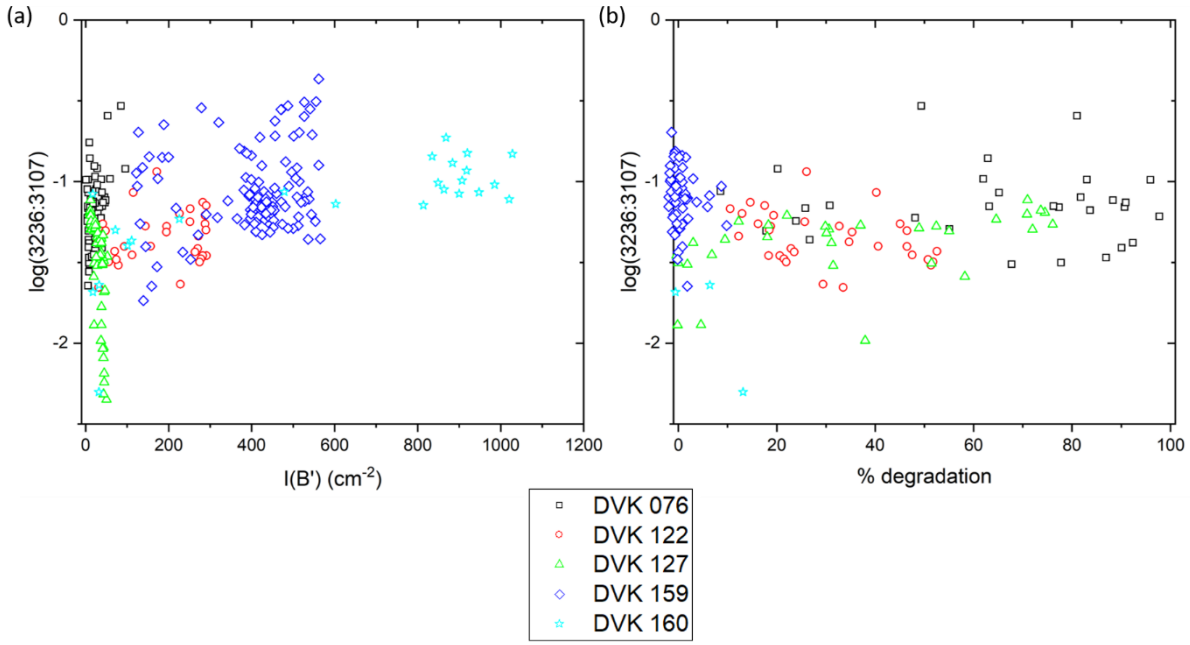

Figure 5.14: plots of the platelet related features against the ratio of the 3236 cm^{-1} and 3107 cm^{-1} peaks for some heterogeneous samples from Argyle; (a) shows I(B') and (b) % degradation.

5.3.3 Spatial variation within samples

Alongside the results in the previous section, it can be useful to consider the way in which the spectral features vary spatially. Figure 5.15 displays the results for the Argyle samples considered above. All the samples contain a low nitrogen rim and a higher nitrogen core, as is commonly observed in diamonds from this locality (Speich, 2017). Consistent with the overall trend seen in the dataset above, a correlation can be seen with nitrogen, with the high nitrogen core often containing a more intense 3236 cm^{-1} peak, which decreases upon transition to the lower nitrogen rim. The trend is similar in the 3107 cm^{-1} peak intensity, with the exception of Arg 70 and 78, in which the intensity of the 3107 cm^{-1} feature shows an increase in the rim that is not observed in the 3236 cm^{-1}.

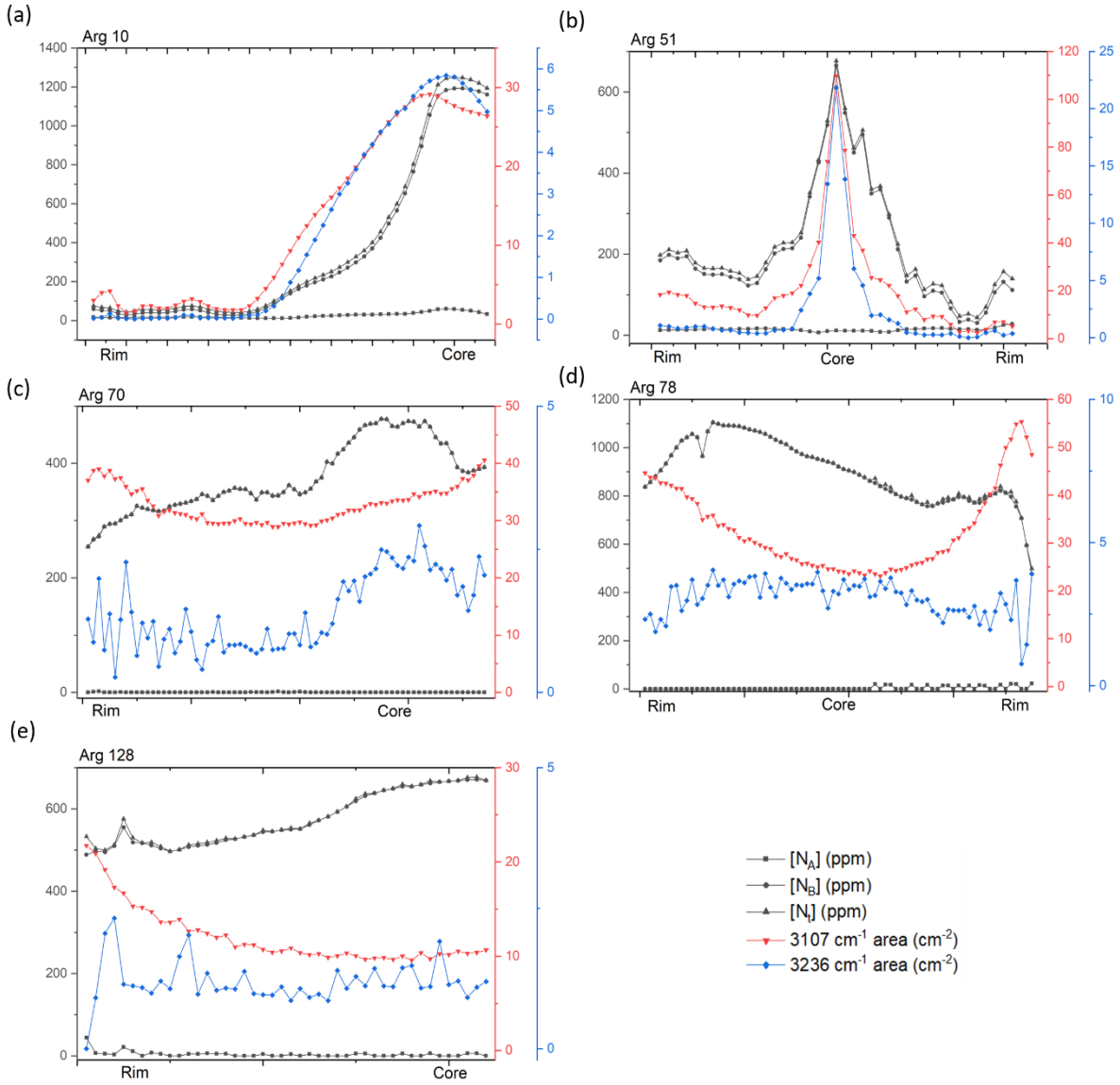

Figure 5.15: A series of plots showing the spatial variation in a number of IR studies of heterogenous diamonds from Argyle. The black lines represent nitrogen, with squares being [N_A], circles being [N_B] and triangles being [N_t]. The upside-down red triangles are the area of the 3107 cm^{-1} peak and the blue diamonds represent the area of the 3236 cm^{-1} peak. (a) is Arg 10, (b) is Arg 51, (c) is Arg 70, (d) is Arg 78 and (e) is Arg 128.

Figure 5.16 shows the same plots as 5.15 for the peak ratio. A similar trend can be observed, with a higher relative intensity of the 3236 cm^{-1} peak in the high-nitrogen core of the diamonds. This is consistent with the overall trends observed in the dataset of Argyle samples. The relationship between total nitrogen and a higher relative intensity can be seen more clearly than in figure 5.15.

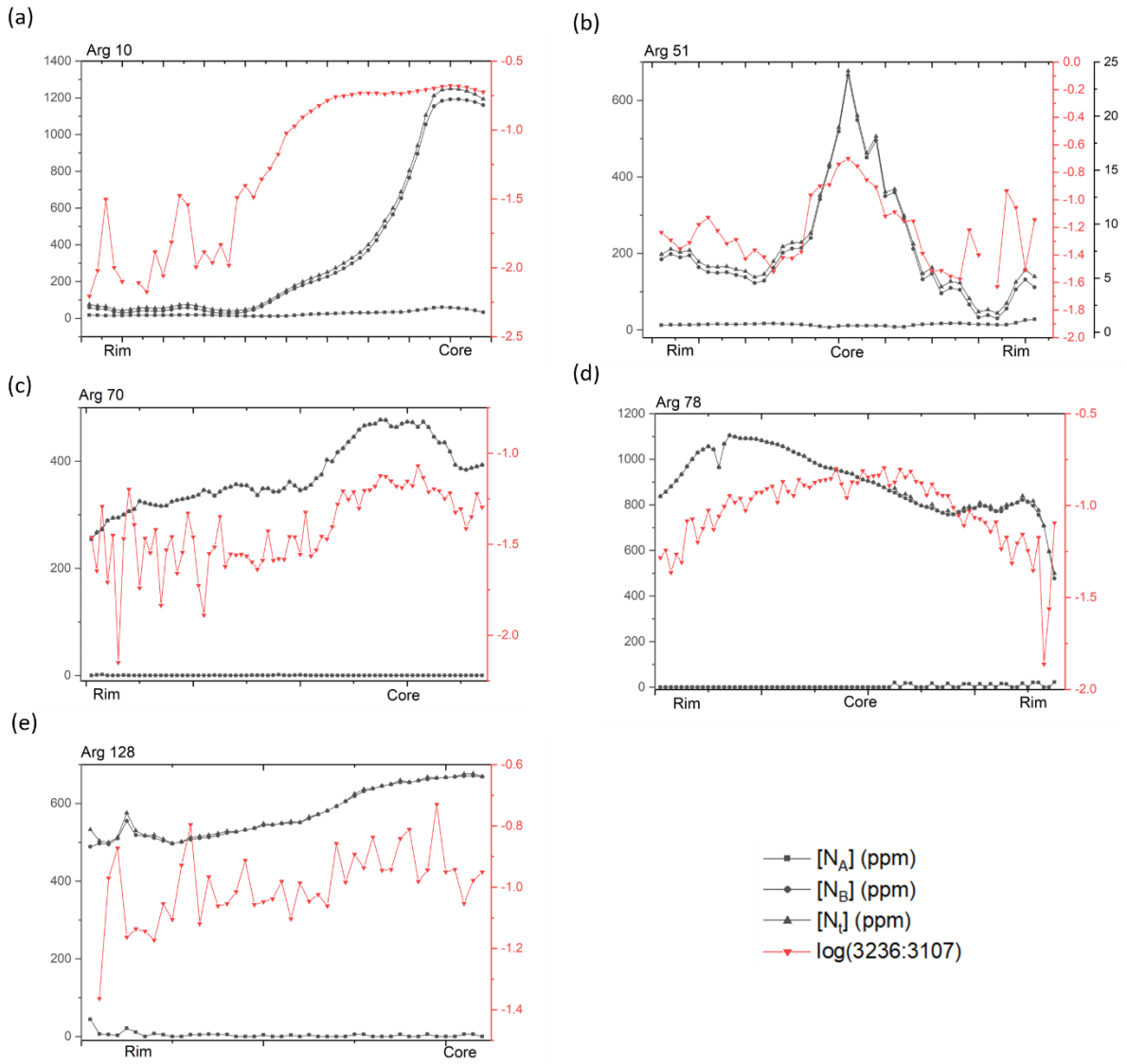

Figure 5.16: A series of plots showing the spatial variation in a number of IR studies of heterogenous diamonds from Argyle. The black lines represent nitrogen, with squares being [N_A], circles being [N_B] and triangles being [N_t]. The upside-down red triangles are the logarithmic ratio of the 3236 cm^{-1} and 3107 cm^{-1} peaks. (a) is Arg 10, (b) is Arg 51, (c) is Arg 70, (d) is Arg 78 and (e) is Arg 128.

Figure 5.17 shows the same variables as Fig. 5.15, but for the Diavik samples. Immediately apparent is that the zonation of the Diavik samples is generally more complex than in the Argyle ones, with more convoluted trends being observed. For example, DVK 076 in Fig. 5.12a shows zonation that is complex enough to make it difficult to discern the number of individual growth zones present using the IR data alone, compared to the Argyle samples which show a much clearer core-rim relationship. The trend of a higher nitrogen core containing a more intense 3236 cm^{-1} feature is not present here, aside from in DVK 127. It is also clear how the 3107 cm^{-1} and 3236 cm^{-1} features correlate more strongly in the Diavik samples than those from Argyle. An interesting feature can be seen in DVK 160, where both the 3107 cm^{-1} and 3236 cm^{-1} peaks can be seen to have a much greater intensity at the boundary between the high nitrogen core and the low nitrogen rim. This behaviour is not observed in other samples.

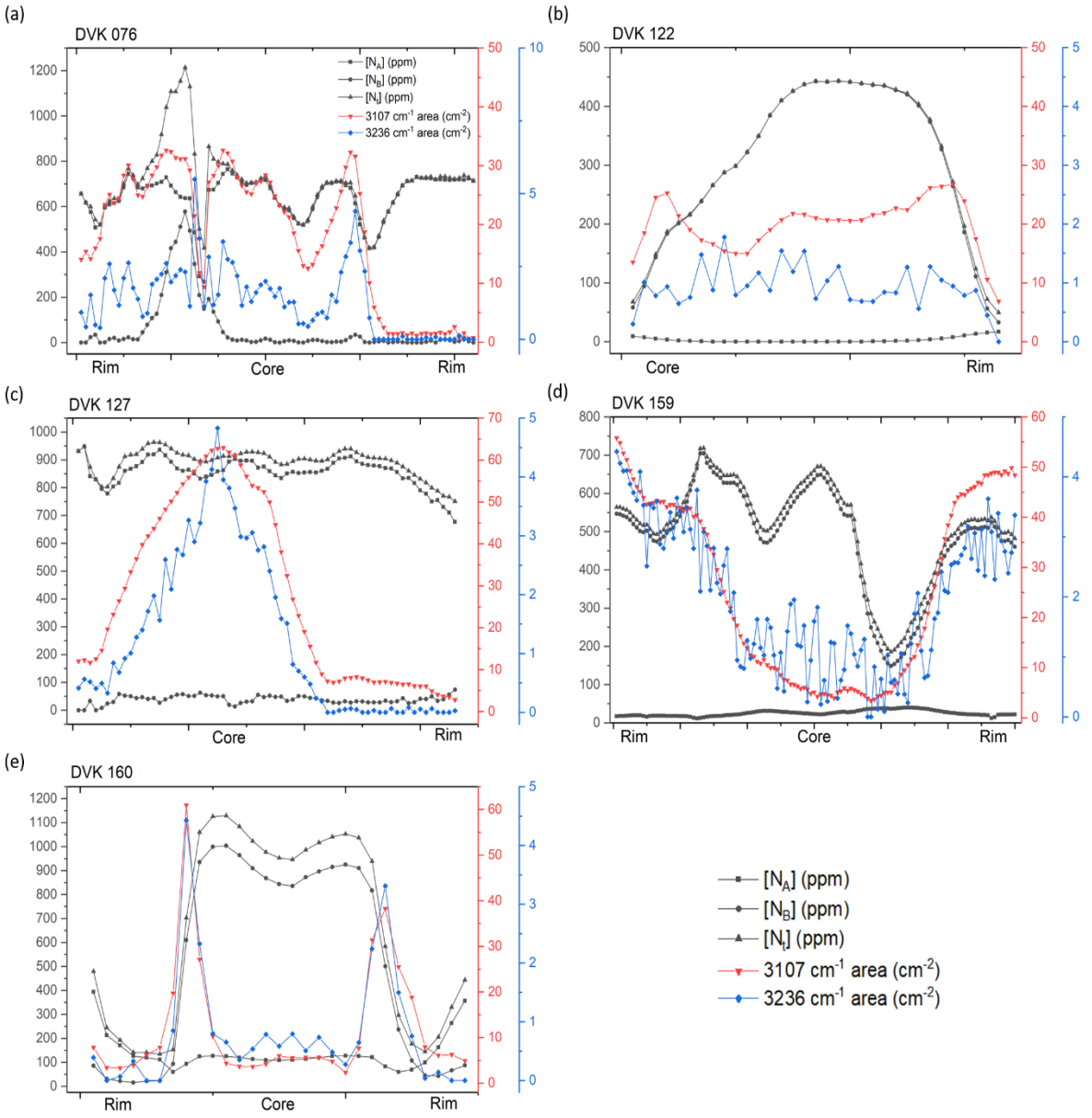

Figure 5.17: a series of plots showing the spatial variation in a number of IR studies of a series of diamonds from Diavik. The black lines represent nitrogen, with squares being [N_A], circles being [N_B] and triangles being [N_I]. The upside-down red triangles are the area of the 3107 cm^{-1} peak and the blue diamonds represent the area of the 3236 cm^{-1} peak. (a) is DVK 076, (b) is DVK 122, (c) is DVK 127, (d) is DVK 159 and (e) is DVK 160.

Figure 5.18 displays the same data for the peak ratio. A number of points where the intensity of the 3236 cm^{-1} peak is zero are omitted for clarity. DVK 076 and DVK 159 clearly illustrate the complex zonation present in these samples. DVK 127 and 160 are the only samples displaying a similar relationship as observed in the Argyle samples, with a higher relative intensity in the high-nitrogen core of the diamond.

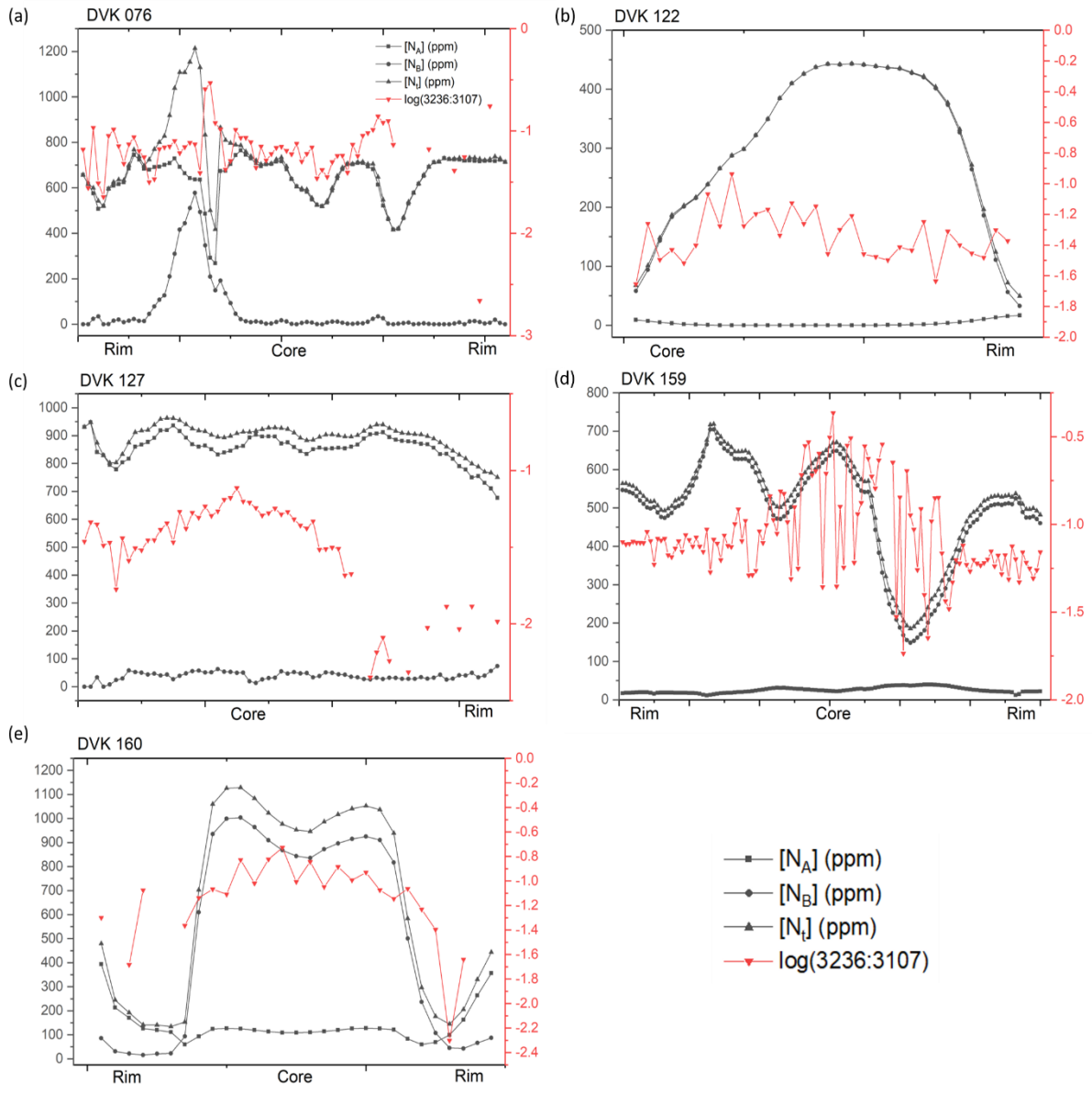

Figure 5.18: a series of plots showing the spatial variation in a number of IR studies of a series of diamonds from Diavik. The black lines represent nitrogen, with squares being [N_A], circles being [N_B] and triangles being [N_t]. The upside-down red triangles represent the logarithmic ratio of the 3236 cm^{-1} and 3107 cm^{-1} peaks. (a) is DVK 076, (b) is DVK 122, (c) is DVK 127, (d) is DVK 159 and (e) is DVK 160.

5.4 Discussion

When considering the previous assertion that a C-H (and specifically, an acetylene C≡C-H bond (Iakoubovskii and Adriaenssens, 2002)) could be responsible for the peak, there appears to be no evidence within this data set consistent with this claim. As such, and given the presence of a correlation with nitrogen, it would seem appropriate to say that the most likely cause of the IR features is an amine-like stretching mode of some form rather than a C-H stretch.

The results from the single spectra would seem to indicate that nitrogen is involved in the structure of the defect responsible for the feature, which is consistent with the feature being an N-H stretch (De Weerdt et al., 2003; Woods and Collins, 1983). However, the fact it does not seem to correlate strongly with any specific nitrogen aggregate, but instead with $[N_t]$, suggests the potential of a complex defect structure compared to the A- and B-centres. This is emphasised by the fact that an intense 3236 cm^{-1} peak can be seen in diamonds that have a low aggregation state. This does not necessarily prohibit some sort of nitrogen aggregate being present in the defect structure but does suggest that the defect could be formed via a separate mechanism than the nitrogen aggregation sequence traditionally observed.

When considering the assertion of a platelet centred VN_4H stretch as a candidate for the peak, the relationship between $[N_t]$ and the peak intensity could be deemed as evidence for this. However, a strong relationship is not observed between the concentration of B centres and the intensity of this peak. If this were indeed the defect responsible for this peak then a reasonable hypothesis would be that a higher concentration of B centres would lead to a higher intensity of the 3236 cm^{-1} feature, however a stronger correlation is observed between $[N_t]$ and the peak intensity. This does not preclude this defect being the cause of this peak, as it could be the case that significant concentrations of the platelet centred VN_4H decrease the observable B centre concentration enough to obscure the relationship that would be observed.

The results from the Argyle line scans paint a clear picture, with all samples appearing to follow a clear trend where the 3236 cm^{-1} feature grows in relative to the 3107 cm^{-1} as total nitrogen increases, before reaching a point and levelling off. This suggests that, whatever the defect structure, nitrogen is likely present in the environment. This further supports the claim of an N-H stretch being responsible for the feature. The fact that the trend appears also to be present when looking at [N_B] may be of significance, potentially indicating a high-order nitrogen aggregate comprising part of the defect system. However, it is worth noting that the diamonds here contain aggregation states upwards of 90 %, and so this trend could simply be a representation of the trend observed in [N_t].

The fact that the plateau is reached at differing nitrogen levels between samples, also lying at different intensities on the y-axis, suggest that there is another controlling factor at play in the relative abundance of the defects causing the two infrared features than can be studied via a 2D plot such as this one. This could potentially be the inclusion of another element in the defect structure that is invisible in the IR spectrum, such as a transition metal or an element such as boron, which, where observed, is commonly seen as a substitutional impurity with a characteristic IR signature (Gaillou et al., 2012; Mainwood, 1979). This could also be caused by the presence of nitrogen in another form than the aggregates measured here, such as a less common, possibly infrared-inactive species in the nitrogen aggregation process. The Argyle samples all contain highly aggregated nitrogen, which also suggests the presence of some form of higher-order nitrogen aggregate, present in significantly lower concentration than the nitrogen aggregates usually observed within diamonds.

The general trend observed in the Argyle samples of a decreasing relative intensity of the 3236 cm^{-1} peak as the platelet degradation increases within the samples can be considered as supporting evidence for the platelet-centred VN_4H defect structure. A trend can also be seen of increasing 3236 cm^{-1} peak intensity with increasing *I(B')*, however, as discussed in the

introduction, the theorised quenching of the platelet peak causes some difficulty when assessing the hypothesis. This means that, although this could be considered tentative evidence to support the claim, further, more detailed studies of the platelets through methods aside from IR may be needed to confirm the defect structure.

There are numerous species that have been observed in the EPR spectra of diamonds that have not yet been identified as being optically active that could potentially be responsible for a peak such as this. One such candidate is a series of nickel-nitrogen vacancy complexes known as the NE_n centres (Johnston and Mainwood, 2003; Nadolinny et al., 1999). These centres are generally found within diamonds that have been grown in nickel-containing catalysts and then subsequently annealed. Whilst there has been observation of the coexistence of nickel-related defects and the 3236 cm^{-1} peak in diamonds (Iakoubovskii and Adriaenssens, 2002), there has not been concrete observation of nickel as a part of this defect structure. Detailed studies of these nickel related features are often undertaken using EPR, which suffers from a lack of spatial resolution compared to optical techniques – for example, the N_s^0 defect is one of the most widely studied EPR-active forms of nitrogen in diamonds, and yet obtaining spatial resolutions lower than 100 µm proves difficult (Newton, 2006). This is a potential barrier when attempting to study the spatial distribution of these NE_n centres compared to IR studies, as the spatial variation achievable in IR is significantly higher. If this were able to be undertaken, it may be possible to gain further understanding as to whether or not a nickel-nitrogen related centre could be related to the defect structure causing the 3236 cm^{-1} feature.

However, the samples from Diavik do not appear to show similar relationships, with no clear trend being observed other than a distinct correlation between the 3107 cm^{-1} and 3236 cm^{-1} peaks. This does not support the conclusions drawn from the Argyle samples, but could be a consequence of the more complex zonation that is present within the Diavik samples. This zonation could potentially mask relationships that are clearer in two-stage diamonds such as

many of the Argyle samples. A number of the Diavik samples studied for spatial variation contain lower concentrations of aggregated nitrogen than those in the Argyle dataset. If the platelet centred VN_4H defect is responsible for the peak, then the low concentrations of B centres could mask the relationship that would be expected between the B centre concentration and the 3236 cm^{-1} peak intensity.

5.5 Conclusions and Future Work

The results presented in this chapter shed some light on to the behaviour of this peak, although the problem is by no means completely solved. Whilst the results from one set of samples appear to paint a picture of the behaviour this defect exhibits when considered with other IR-active defects, the inclusion of data from other localities merely muddies the waters. Work of this nature can provide suggestions as to the components of various defects, although complementary techniques are required in order to confirm the validity of the ideas that have arisen.

The relationships observed between the various nitrogen aggregates and the peak intensity strongly indicate the presence of some form of nitrogen within the defect structure. The results from Argyle suggest the possibility of a higher-order nitrogen aggregate possibly being present, which does not preclude the recent assertion that a platelet-centred VN_4H stretch is a candidate for the feature.

The differences between the Argyle and Diavik samples – specifically the link between nitrogen aggregates in the Argyle samples and the 3107 cm^{-1} peak in the Diavik samples – are stark. This likely means that, whatever the requisite conditions are for growth of this defect, the mantle storage conditions vary enough across these two localities to lead to significantly different behaviour in the various intensities of the IR active features discussed within this chapter.

Future work into this peak and defect system could include studies of diamonds from other localities in order to expand the range of samples investigated and build a larger dataset to draw from. Building a larger library of diamonds could allow for relationships to be observed that are not able to be accounted for when studying smaller groups of samples. The use of EPR studies could also provide additional information, which could potentially suggest whether or not any of the myriad EPR-active features (such as the NE_n centres discussed above) could be potential candidates for this defect, along with whether or not there are any other elements aside from nitrogen and hydrogen that could be included within the defect structure.

6. Conclusions and outlook

The aim of this work was to add to the knowledge of hydrogen within natural diamonds, a ubiquitous but elusive impurity. The most common observation of hydrogen within diamonds comes from the 3107 cm^{-1} peak in infrared spectroscopy, which arises from the N_3VH centre. However, it has been suggested that there may be other IR-inactive forms of hydrogen within diamonds, and the amount of hydrogen present is poorly understood. Based upon the proton-proton scattering measurements described within chapter 3 of this thesis, it appears that the IR features are not a valid representation of bulk hydrogen contents within diamonds, with the amount of hydrogen predicted by IR alone falling at least 20 times below the observed concentrations. This raises the question of where the hydrogen is located, which is a clear area for further study. A number of ideas such as extended defects, including voidites, were discussed as potential traps of IR-inactive hydrogen. These could signal directions for future work.

The rest of this thesis has focussed on the use of IR to interrogate environments in which hydrogen is incorporated. This was achieved using IR alone in chapter 5; a minor H-containing feature at 3236 cm^{-1} was investigated, with some clues provided as to the underlying cause. The results here are somewhat consistent with a platelet-centred nitrogen aggregate as part of the defect structure. This, along with the discussion around chapter 3, further highlight the possibility of extended defects as candidates for hydrogen incorporation within diamonds.

In chapter 4, evidence from IR and UV-vis was provided for the formation of N_3VH centres through direct protonation of N3. The links between the N3 centre and N_3VH likely plays a direct role in the nitrogen aggregation sequence in diamonds, and these findings indicate the potential of hydrogen to quench this process. This chapter explored using the relative abundances as indicators of hydrogen availability during different diamond growth events within samples. The relative abundance of N3 and N_3VH centres can, from the methodology

discussed here, be taken forward as a way of investigating this across different samples and localities, essentially functioning as a hygrometer.

Photoluminescence and IR studies were used to investigate diamond growth events in a number of samples in chapter 6. This used the coexistence of peaks in hydrogen and nickel-related features at zone boundaries to suggest a small cuboid period of growth between the standard octahedral growth zones within these samples. While not diagnostic, this highlights the valuable information that can be learned from the correlation and PL and IR features within diamonds.

This project has advanced our understanding of hydrogen in natural diamonds and provided new ways in which hydrogen can be used to shed light on the geological conditions under which diamonds form and are stored within the mantle of the Earth. However, many questions around hydrogen remain unanswered, with a significant amount of work needed to fully understand this impurity in diamonds. Given the ubiquity of hydrogen as an impurity, it is likely that there is a lot still to be learned about the mantle from the incorporation of this light element into diamonds.

Appendix A – Supplementary material for Chapter 4

A.1 FTIR and UV-vis summary table

This section contains a table summarising the results of the UV-vis and IR results for all samples studied as single UV-vis spectra. All values are presented to 2 d.p.

Sample	Thickness (mm)	[N3] (ppm)	[N_A] (ppm)	[N_B] (ppm)	[N_t] (ppm)	3107 cm^{-1} intensity (cm^{-2})	[N_3VH] (Liggins) (ppm)	[N_3VH] (Coxon) (ppm)	[N3] + [N_3VH] (Liggins) (ppm)	[N3] + [N_3VH] (Coxon) (ppm)
Aikhal 2100P	1.87	3.51	119.48	231.23	350.71	3.15	0.63	0.35	4.14	3.86
Arg 117	1.46	3.26	193.01	486.03	679.04	3.49	0.70	0.38	3.96	3.64
Arg 118	1.2	1.77	361.42	354.16	715.59	0.09	0.02	0.01	1.78	1.78
Arg 13	1.09	0.09	6.21	20.97	27.18	7.19	1.44	0.79	1.53	0.88
Arg 136	1.7	0.00	1.68	207.62	209.30	12.36	2.47	1.36	2.47	1.36
Arg 158	1.6	0.21	149.21	79.73	228.94	0.06	0.01	0.01	0.22	0.21
Arg 16	1.12	3.83	239.24	591.83	831.07	3.59	0.72	0.39	4.55	4.22
Arg 167	1.47	0.16	236.08	234.89	236.08	20.43	4.09	2.25	4.25	2.41
Arg 25	1.13	0.03	5.36	22.88	27.12	3.81	0.76	0.42	0.79	0.45
Arg 46	1.11	0.12	8.30	89.61	97.91	7.03	1.41	0.77	1.53	0.90
Arg 56	1.06	0.11	14.42	112.80	127.22	10.83	2.17	1.19	2.27	1.30
Arg 65	0.63	0.00	2.05	383.66	385.71	25.28	5.06	2.78	5.06	2.78
Arg 72	1.09	0.30	63.69	77.81	141.50	3.86	0.77	0.42	1.07	0.72
Arg 75	0.85	0.00	3.73	12.10	15.82	1.51	0.30	0.17	0.30	0.17
Arg 78	0.69	0.09	0.00	769.49	769.49	43.83	8.77	4.82	8.86	4.91
Arg 90	0.88	0.03	16.49	46.62	63.11	20.39	4.08	2.24	4.11	2.27
Arg 92	0.87	0.17	0.00	39.38	39.38	3.05	0.61	0.34	0.78	0.51
Arg 93	0.93	0.09	0.08	64.91	64.99	7.68	1.54	0.84	1.62	0.93
DVK044	0.59	0.28	133.07	145.88	278.94	10.77	2.15	1.18	2.43	1.46

DVK076	0.44	0.00	643.36	59.94	703.31	18.12	3.62	1.99	3.62	1.99
DVK127	1.07	0.14	820.18	34.72	854.90	25.32	5.06	2.78	5.21	2.93
DVK143	0.54	1.00	111.92	178.99	290.90	5.40	1.08	0.59	2.08	1.60
DVK159	0.55	1.38	25.02	485.62	510.64	25.37	5.07	2.79	6.45	4.17
DVK160	0.39	3.90	139.74	506.30	646.03	11.83	2.37	1.30	6.27	5.20
Mir 1164	0.54	0.34	758.42	113.12	871.54	1.34	0.27	0.15	0.61	0.49
Mur 112	0.28	0.00	8.11	219.18	227.29	7.75	1.55	0.85	1.55	0.85
Mur 235	0.85	1.48	238.88	304.21	543.09	3.53	0.71	0.39	2.19	1.87
Mur 265	0.34	1.36	165.19	164.53	329.72	7.53	1.51	0.83	2.87	2.19
Mur 83	0.34	0.25	124.77	90.22	214.99	1.48	0.30	0.16	0.55	0.42
Uda 3009E	0.63	5.17	246.89	433.53	680.43	30.01	6.00	3.30	11.17	8.47
Uda 3097	1.29	1.69	367.23	293.24	660.48	28.33	5.67	3.12	7.35	4.80
Uda 3143P	0.71	2.68	63.58	338.31	401.89	5.06	1.01	0.56	3.70	3.24

A.2 Representative FTIR spectra

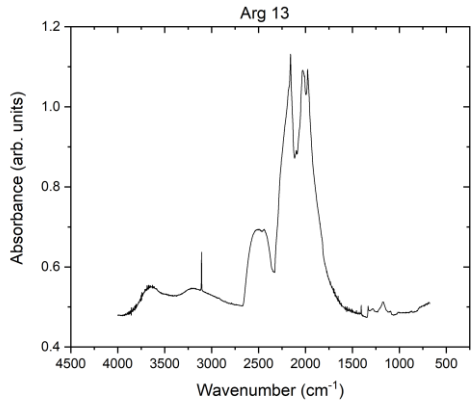

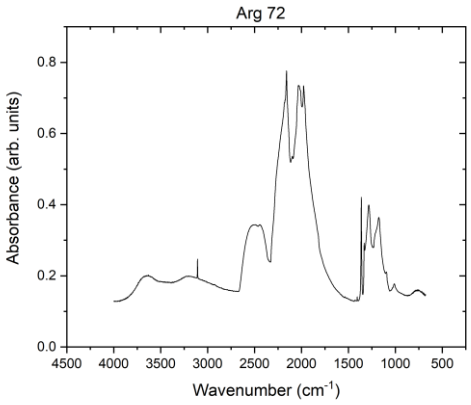

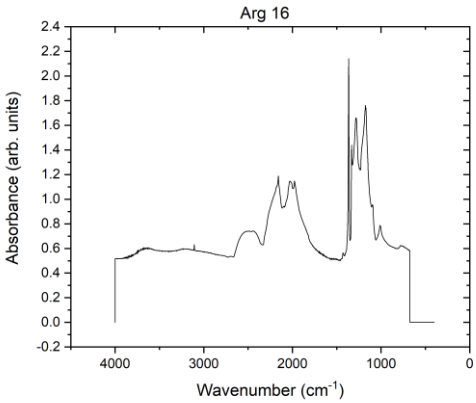

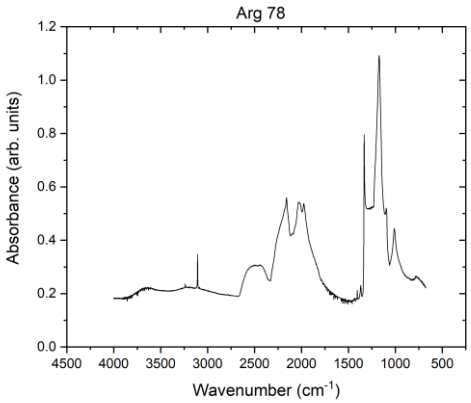

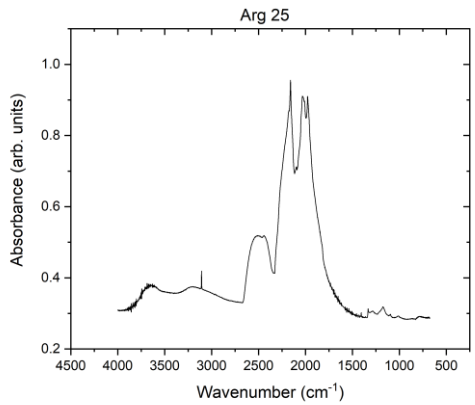

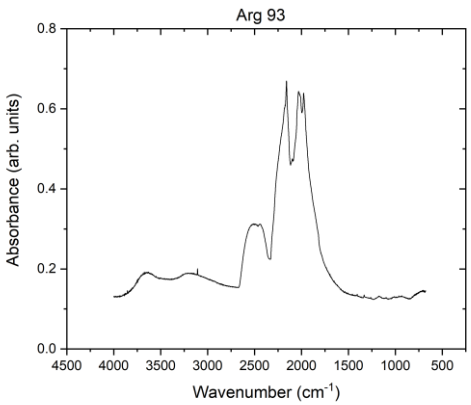

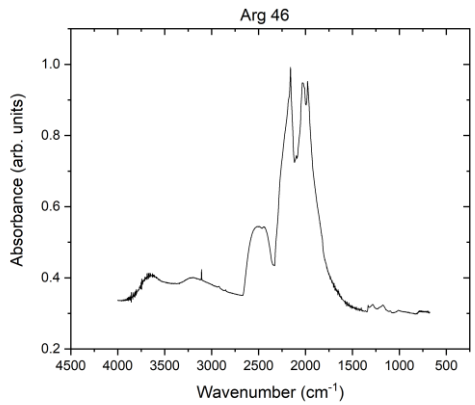

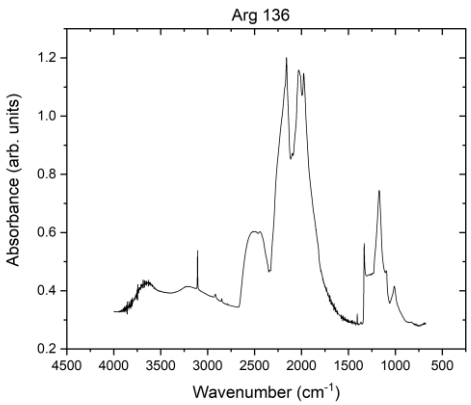

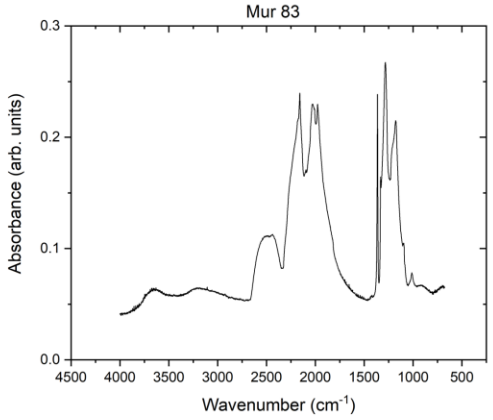
Mur 83
Absorbance (arb. units)
Wavenumber (cm-1)

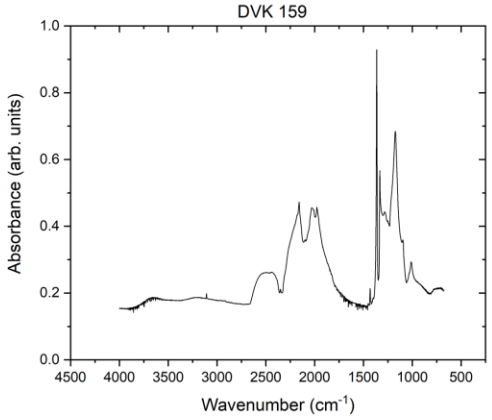
DVK 159
Absorbance (arb. units)
Wavenumber (cm-1)

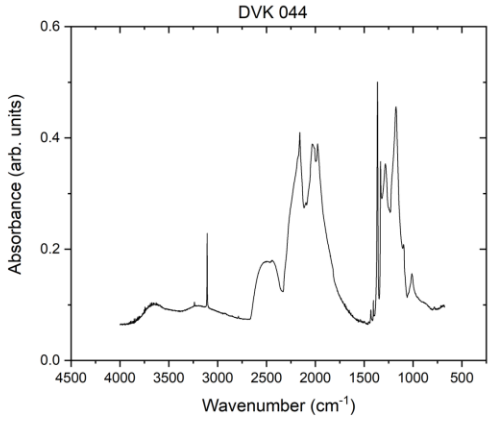
DVK 044
Absorbance (arb. units)
Wavenumber (cm-1)

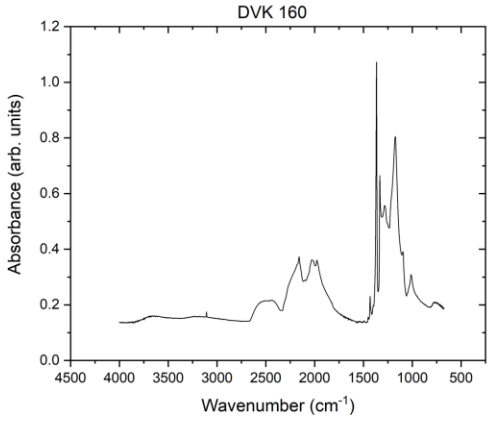
DVK 160
Absorbance (arb. units)
Wavenumber (cm-1)

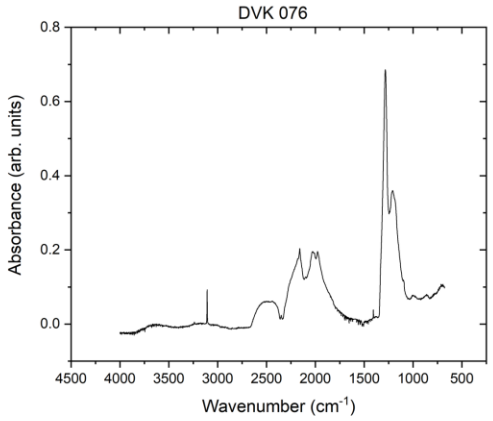
DVK 076
Absorbance (arb. units)
Wavenumber (cm-1)

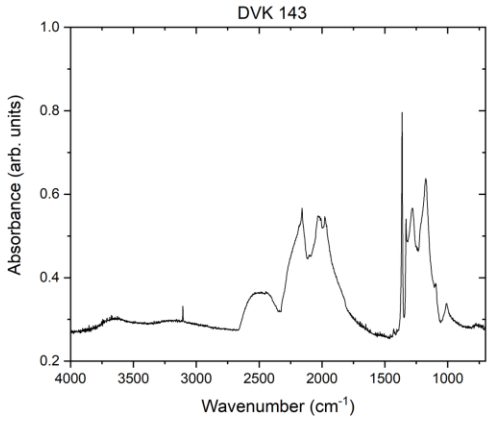
DVK 143
Absorbance (arb. units)
Wavenumber (cm-1)

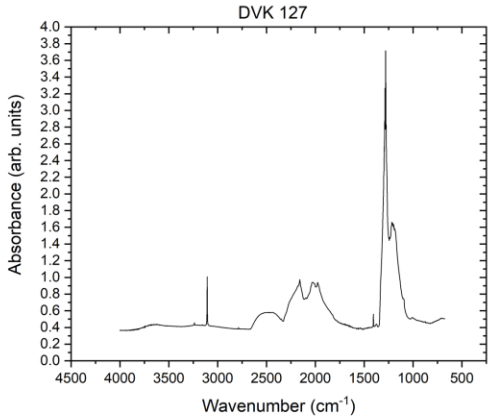
DVK 127
Absorbance (arb. units)
Wavenumber (cm-1)

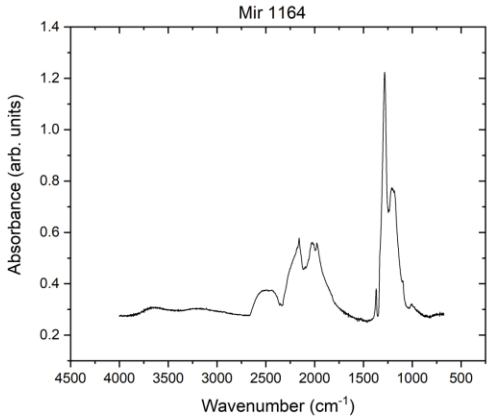
Mir 1164
Absorbance (arb. units)
Wavenumber (cm-1)

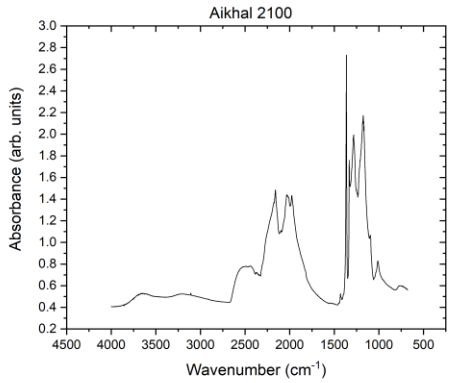
Aikhal 2100
Absorbance (arb. units)
Wavenumber (cm-1)

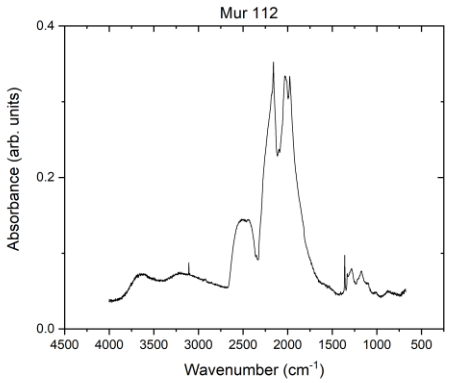
Mur 112
Absorbance (arb. units)
Wavenumber (cm-1)

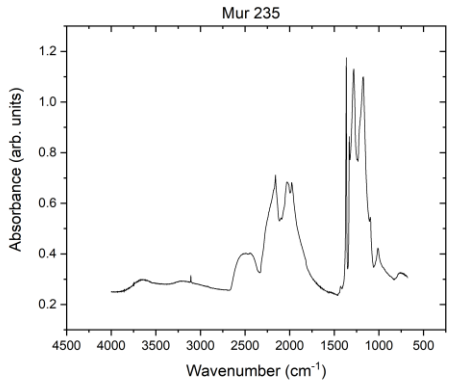
Mur 235
Absorbance (arb. units)
Wavenumber (cm-1)

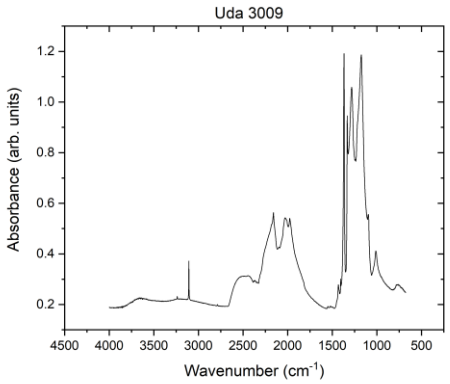
Uda 3009
Absorbance (arb. units)
Wavenumber (cm-1)

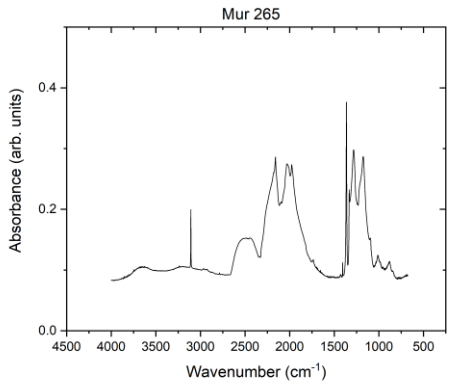
Mur 265
Absorbance (arb. units)
Wavenumber (cm-1)

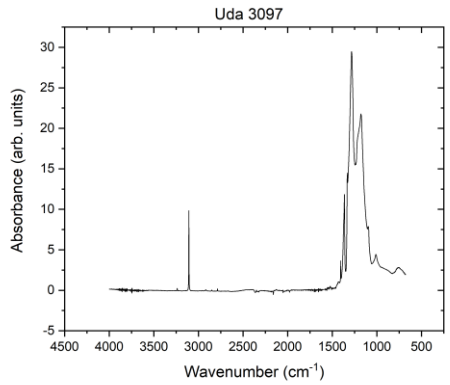
Uda 3097
Absorbance (arb. units)
Wavenumber (cm-1)

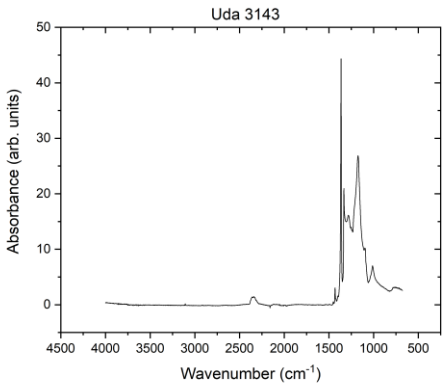
Uda 3143
Absorbance (arb. units)
Wavenumber (cm-1)

A.3 Representative UV-vis spectra

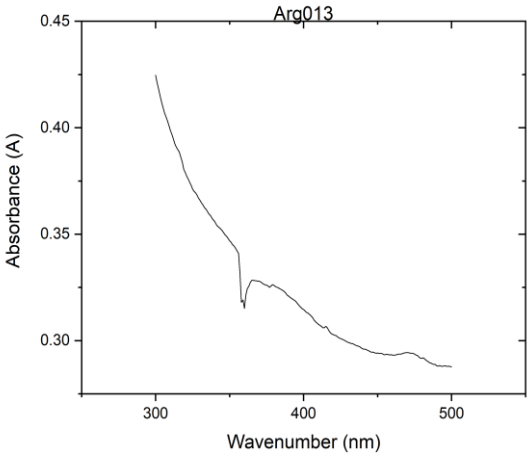

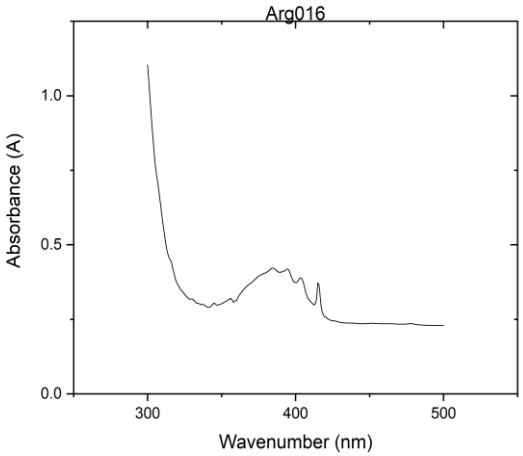

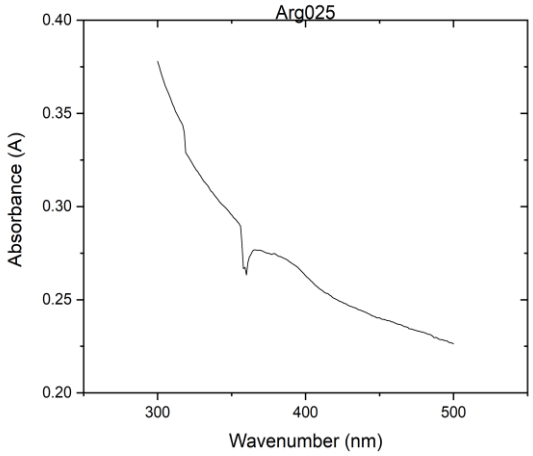

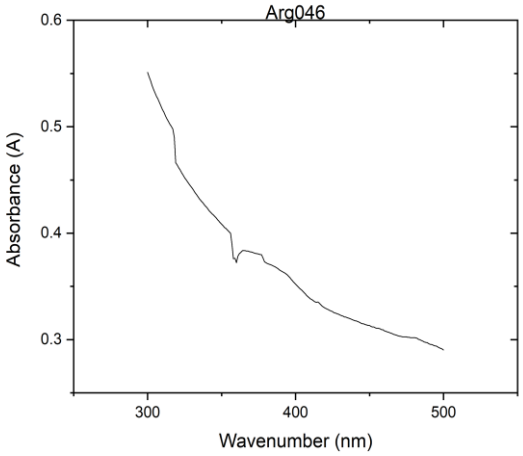

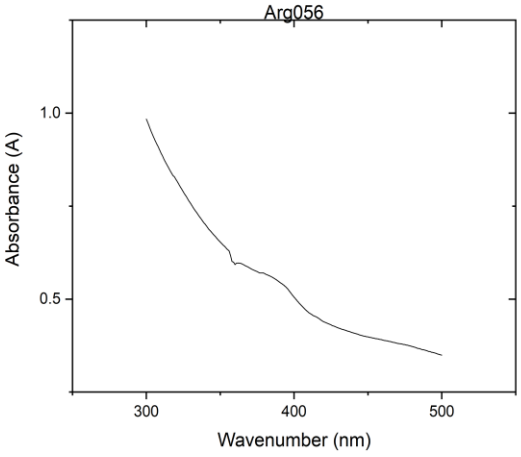

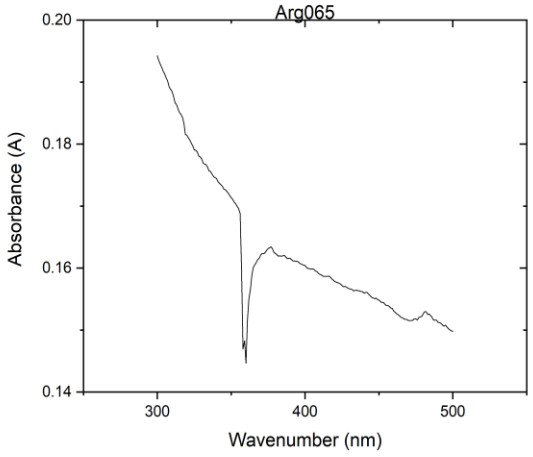

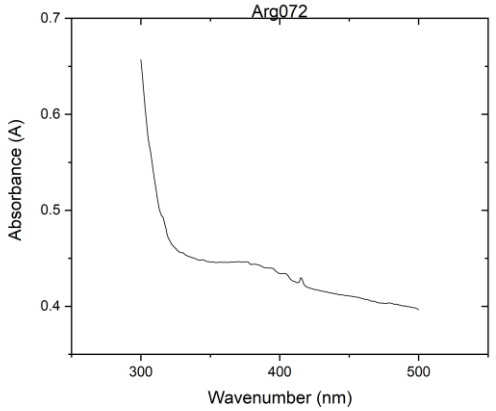
Arg072
Absorbance (A)
0.7
0.6
0.5
0.4
300
400
500
Wavenumber (nm)

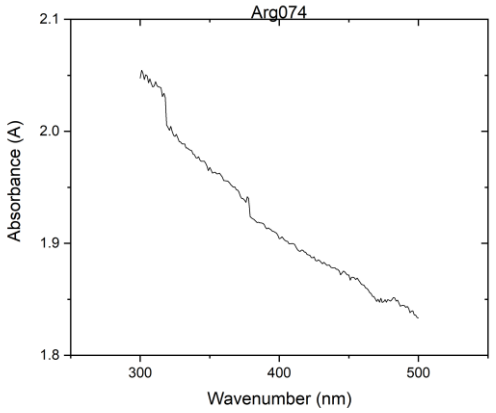
Arg074
Absorbance (A)
2.1
2.0
1.9
1.8
300
400
500
Wavenumber (nm)

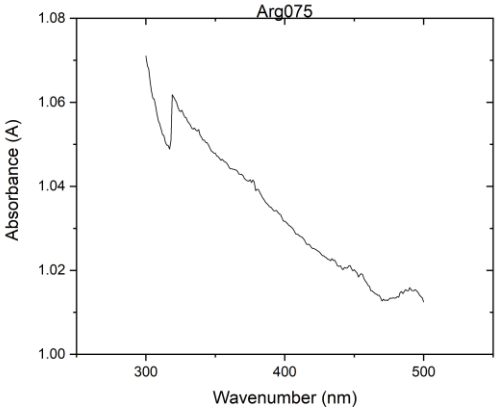
Arg075
Absorbance (A)
1.08
1.06
1.04
1.02
1.00
300
400
500
Wavenumber (nm)

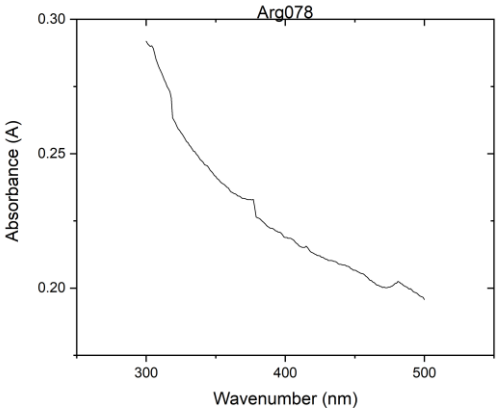
Arg078
Absorbance (A)
0.30
0.25
0.20
300
400
500
Wavenumber (nm)

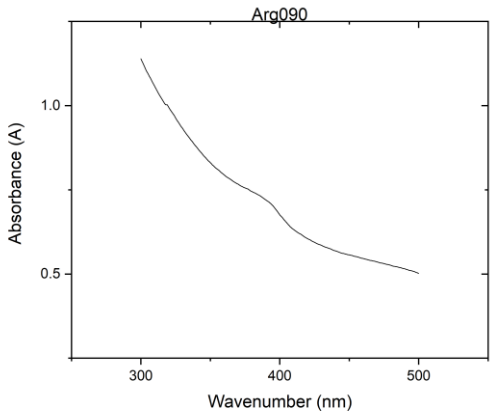
Arg090
Absorbance (A)
1.0
0.5
300
400
500
Wavenumber (nm)

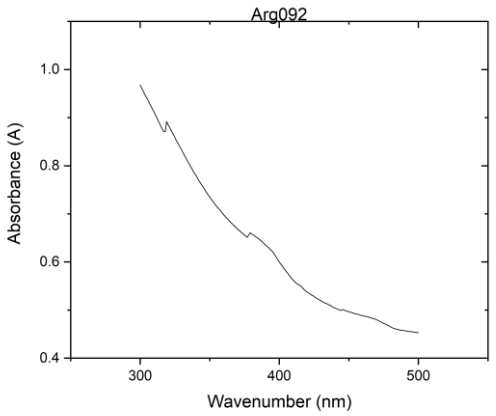
Arg092
Absorbance (A)
1.0
0.8
0.6
0.4
300
400
500
Wavenumber (nm)

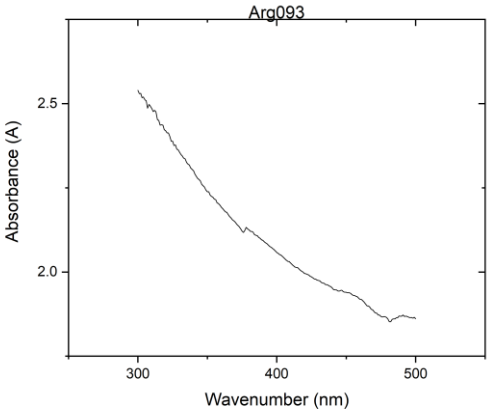
Arg093
Absorbance (A)
2.5
2.0
300
400
500
Wavenumber (nm)

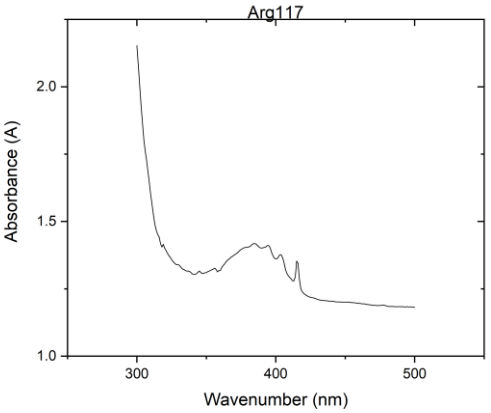
Arg117
Absorbance (A)
2.0
1.5
1.0
300
400
500
Wavenumber (nm)

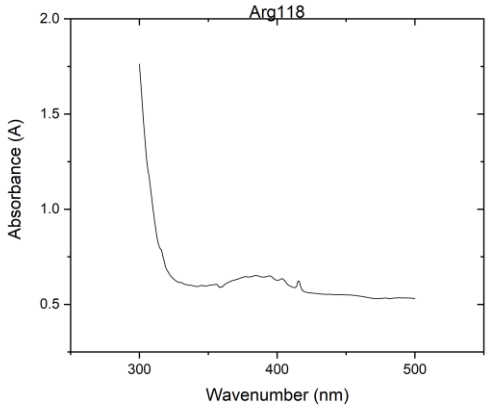
Arg118
Absorbance (A)
Wavenumber (nm)

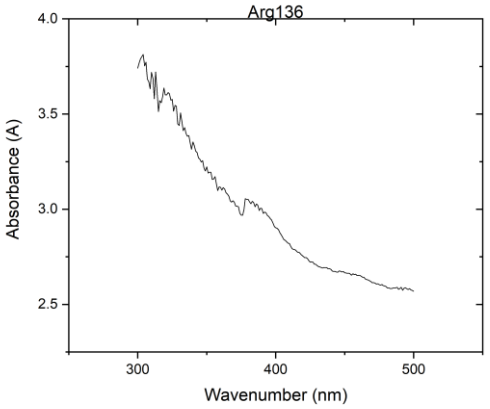
Arg136
Absorbance (A)
Wavenumber (nm)

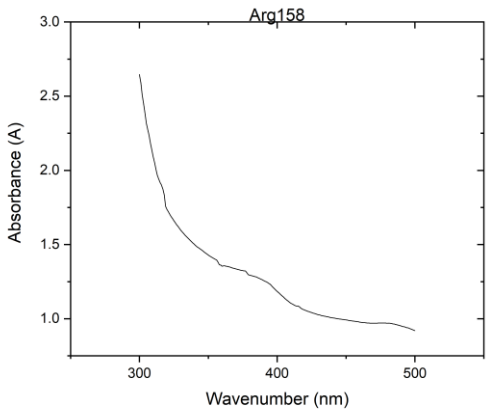
Arg158
Absorbance (A)
Wavenumber (nm)

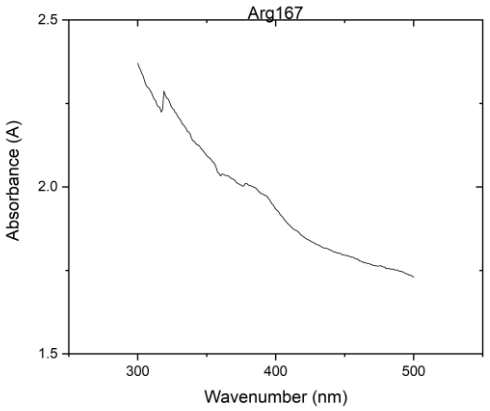
Arg167
Absorbance (A)
Wavenumber (nm)

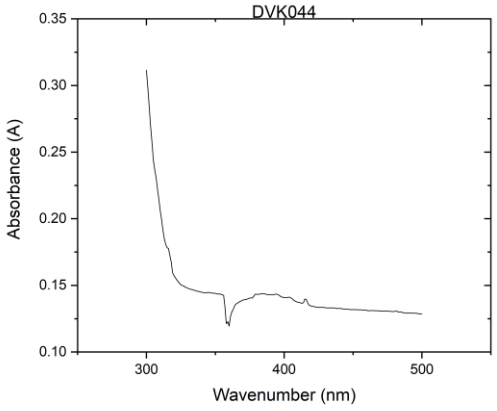
DVK044
Absorbance (A)
Wavenumber (nm)

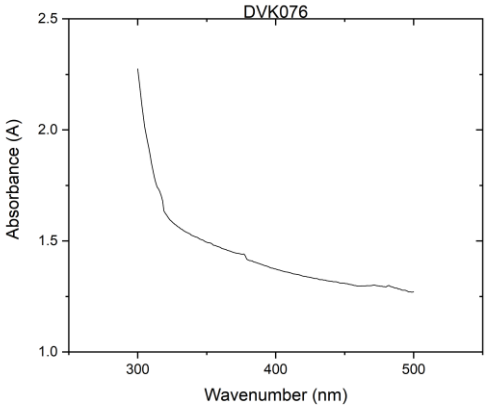
DVK076
Absorbance (A)
Wavenumber (nm)

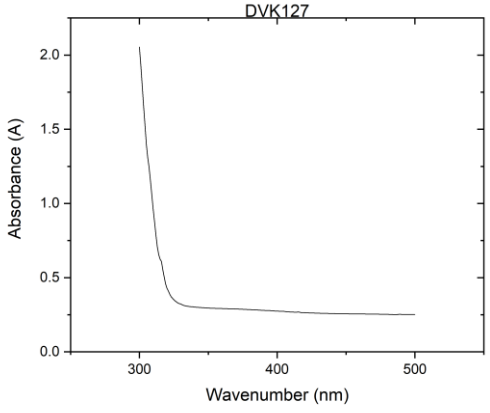
DVK127
Absorbance (A)
Wavenumber (nm)

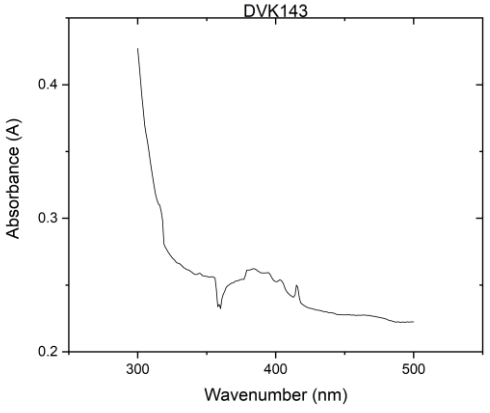
DVK143
Absorbance (A)
Wavenumber (nm)

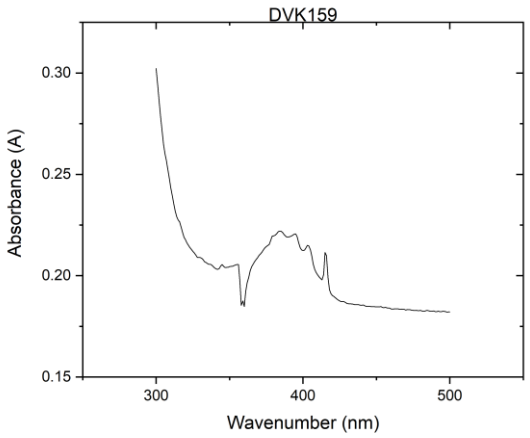
DVK159
Absorbance (A)
0.30
0.25
0.20
0.15
300
400
500
Wavenumber (nm)

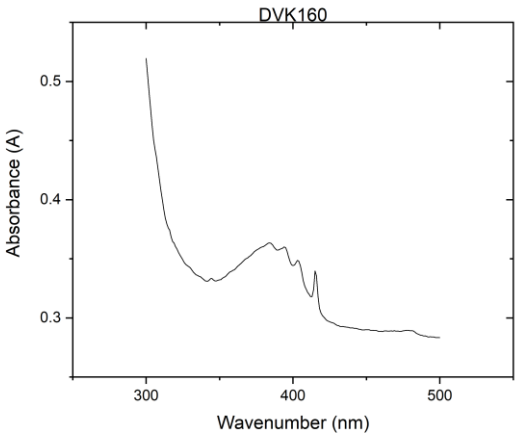
DVK160
Absorbance (A)
0.5
0.4
0.3
300
400
500
Wavenumber (nm)

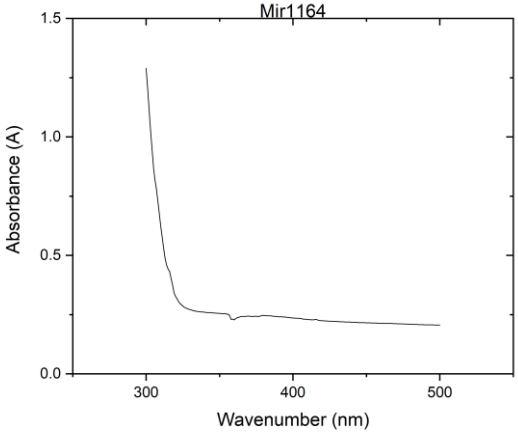
Mir1164
Absorbance (A)
1.5
1.0
0.5
0.0
300
400
500
Wavenumber (nm)

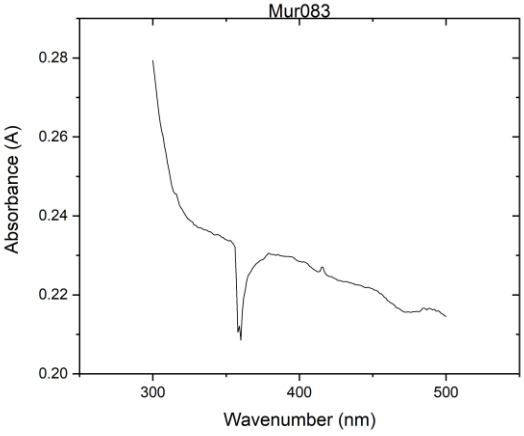
Mur083
Absorbance (A)
0.28
0.26
0.24
0.22
0.20
300
400
500
Wavenumber (nm)

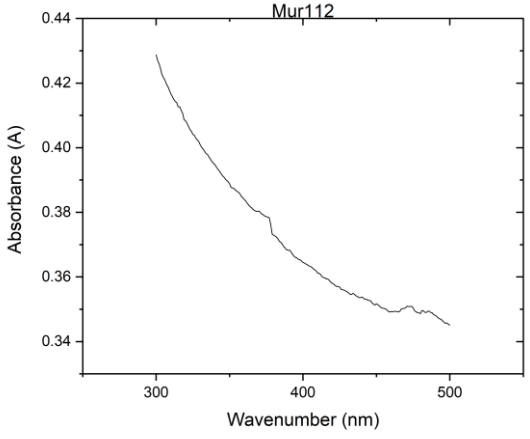
Mur112
Absorbance (A)
0.44
0.42
0.40
0.38
0.36
0.34
300
400
500
Wavenumber (nm)

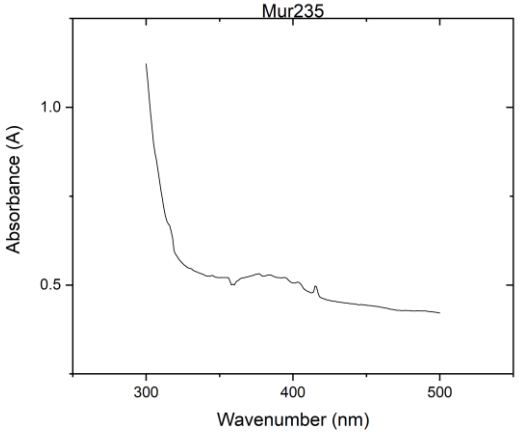
Mur235
Absorbance (A)
1.0
0.5
300
400
500
Wavenumber (nm)

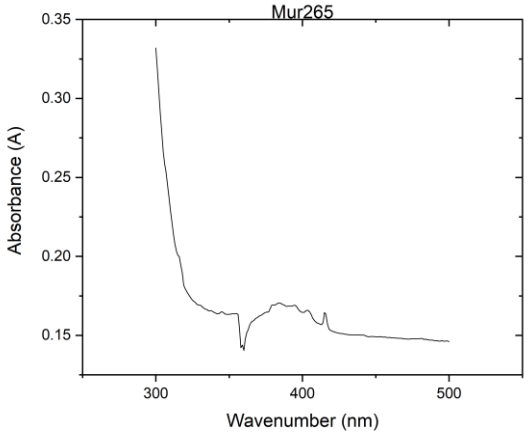
Mur265
Absorbance (A)
0.35
0.30
0.25
0.20
0.15
300
400
500
Wavenumber (nm)

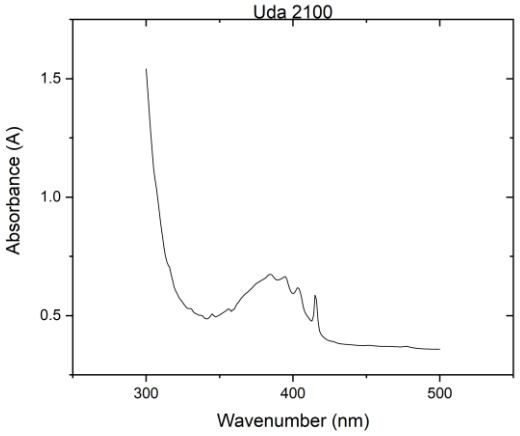
Uda 2100
Absorbance (A)
1.5
1.0
0.5
300
400
500
Wavenumber (nm)

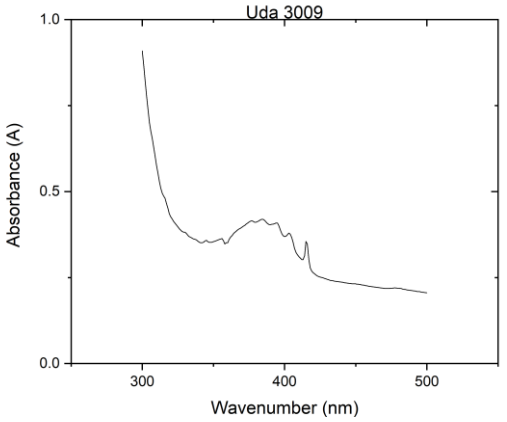
Uda 3009
Absorbance (A)
1.0
0.5
0.0
300
400
500
Wavenumber (nm)

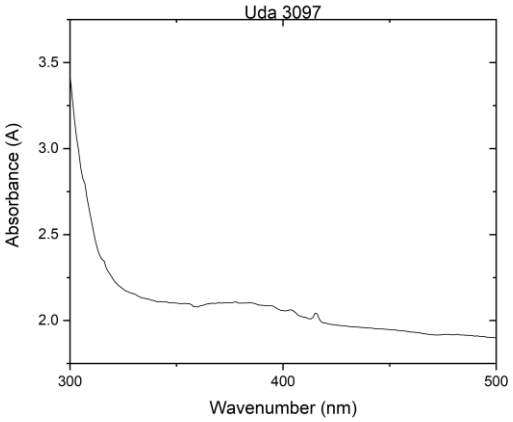
Uda 3097
Absorbance (A)
3.5
3.0
2.5
2.0
300
400
500
Wavenumber (nm)

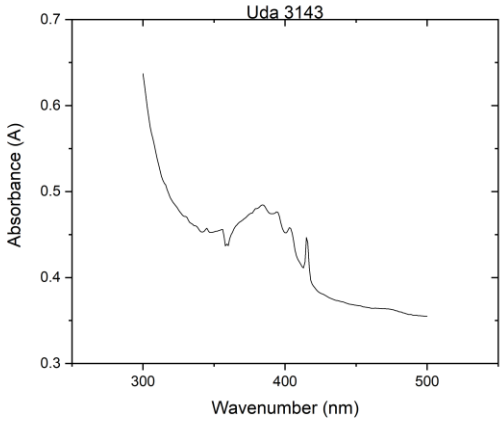
Uda 3143
Absorbance (A)
0.7
0.6
0.5
0.4
0.3
300
400
500
Wavenumber (nm)

Appendix B – Supplementary material for Chapter 5

B.1 FTIR results for single spectra

This section contains the FTIR results for the single spectra used in chapter 5. All values are presented to 2 d.p.

Sample	[N_A] (ppm)	[N_B] (ppm)	[N_t] (ppm)	Percent aggregation	I(3107) (cm^{-2})	I(3236) (cm^{-2})	log(3236/3107)	Platelet peak area (cm^{-2})
Arg 31	14.65	267.58	282.23	94.81	3.72	0.02	-2.18	66.81
Arg 70	0.58	403.48	404.07	99.86	33.21	1.70	-1.29	55.61
Arg 71	5.24	28.51	33.75	84.47	10.29	0.16	-1.80	4.25
Arg 81	4.97	53.61	58.57	91.52	15.39	0.33	-1.66	7.02
Arg 83	17.21	1.04	18.25	5.70	10.37	0.02	-2.72	1.98
Arg 86	0.00	63.44	63.44	100.00	7.25	0.20	-1.55	7.49
Arg 103	46.04	421.46	467.50	90.15	10.78	0.77	-1.15	307.10
Arg 128	0.00	709.46	709.46	100.00	14.48	1.78	-0.91	0.00
Arg 143	95.90	111.90	207.80	53.85	10.72	0.12	-1.94	94.15
Arg 164	1.62	39.53	41.15	96.07	6.15	0.13	-1.69	0.00
DVK 76	708.49	19.18	727.67	2.64	28.43	2.26	-1.10	7.29
DVK 98	1054.65	36.94	1091.59	3.38	34.71	5.78	-0.78	10.39
DVK 115	82.65	282.72	365.38	77.38	18.73	0.81	-1.36	114.17
DVK 122	1.76	263.38	265.14	99.34	16.27	1.00	-1.21	68.47
DVK 127	759.64	66.33	825.97	8.03	36.05	2.57	-1.15	19.03
DVK 131	21.99	224.99	246.98	91.10	15.92	0.91	-1.24	192.30
DVK 135	0.00	431.51	431.51	100.00	11.95	0.83	-1.16	86.88
DVK 159	20.70	471.40	492.09	95.79	48.29	3.07	-1.20	396.79
DVK 166	50.68	577.95	628.64	91.94	45.82	2.62	-1.24	483.76

Mur 65	50.93	389.25	440.19	88.43	5.23	0.23	-1.35	338.75
Mur 107	53.64	569.68	623.33	91.39	5.00	0.25	-1.30	438.87
Mur 112	0.00	1437.96	1437.96	100.00	93.26	11.62	-0.90	1202.59
Mur 122	1.42	261.53	262.95	99.46	21.74	0.32	-1.83	4.01
Mur 141	181.20	352.38	533.58	66.04	11.76	0.57	-1.32	341.24
Mur 173	222.09	253.12	475.22	53.27	46.81	1.56	-1.48	215.90
Mur 182	406.83	340.17	747.00	45.54	12.11	0.39	-1.49	302.21
Mur 265	169.65	227.48	397.13	57.28	6.84	0.13	-1.72	218.70
Mur 279	13.92	388.15	402.07	96.54	20.78	0.51	-1.61	0.00
Bun 9	315.01	372.34	687.35	54.17	3.46	0.15	-1.37	267.96
Bun 12	187.74	177.85	365.59	48.65	4.67	0.20	-1.37	138.40
Bun 17	57.32	235.01	292.33	80.39	9.20	0.82	-1.05	190.49
Bun odd	287.18	818.13	1105.32	74.02	29.39	5.09	-0.76	1072.18

B.2 Representative spectra

Single spectra were obtained and are presented as corrected.

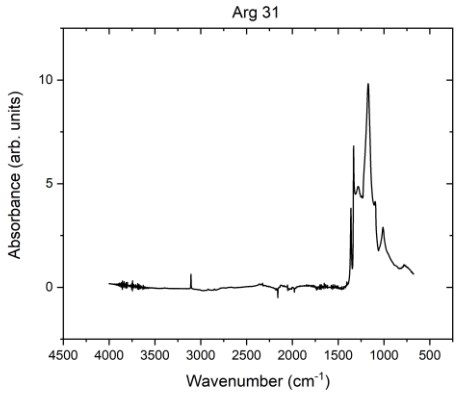

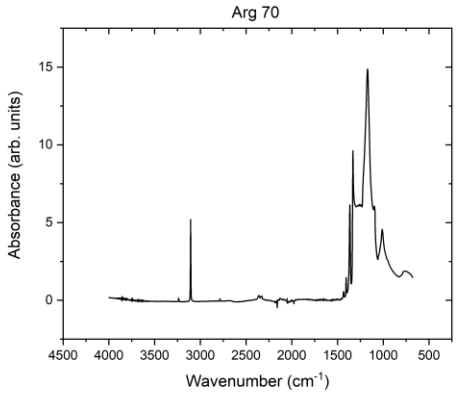

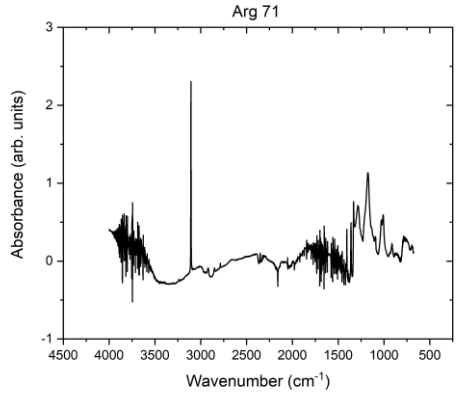

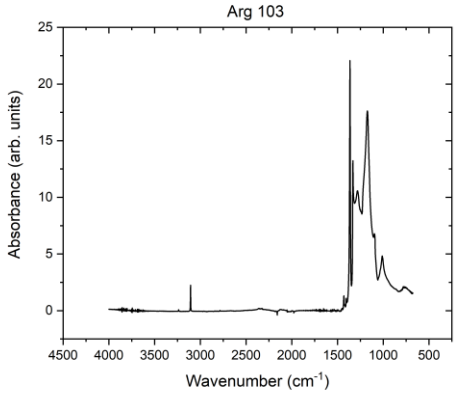

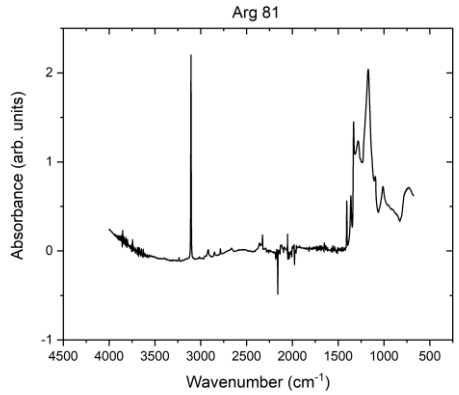

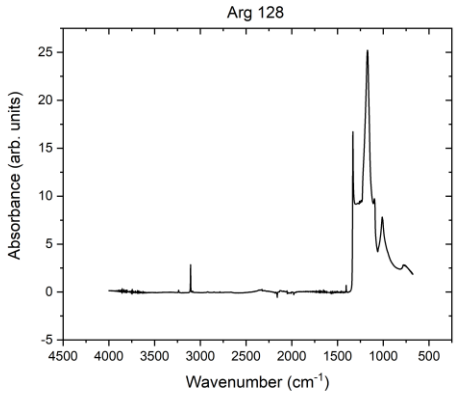

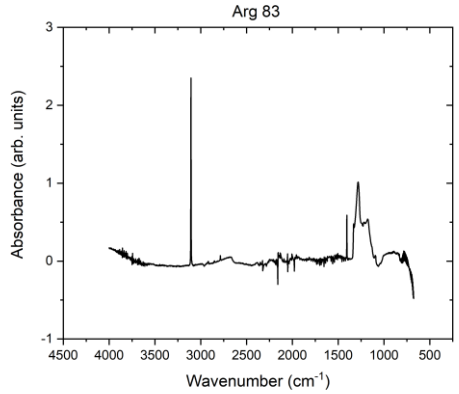

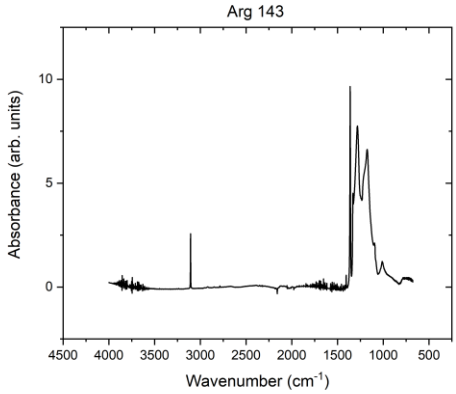

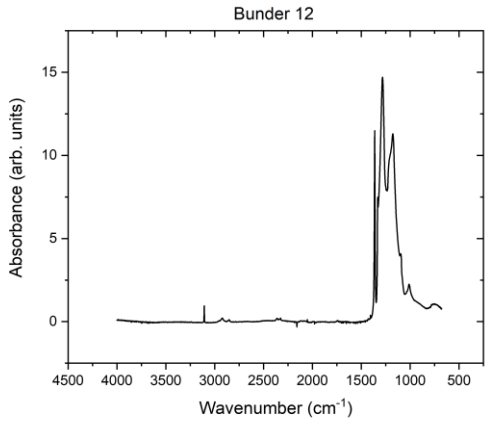
Bunder 12
Absorbance (arb. units)
Wavenumber (cm-1)

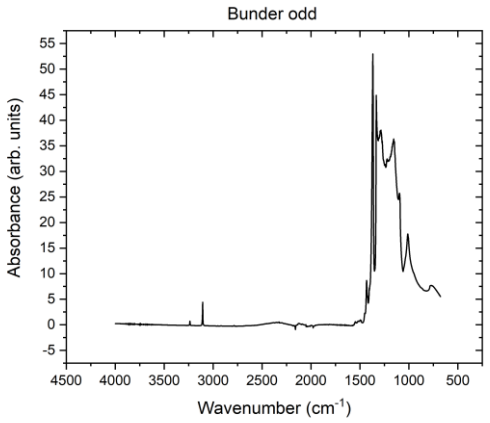
Bunder odd
Absorbance (arb. units)
Wavenumber (cm-1)

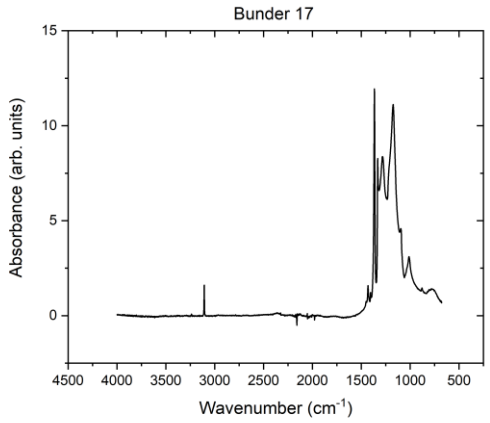
Bunder 17
Absorbance (arb. units)
Wavenumber (cm-1)

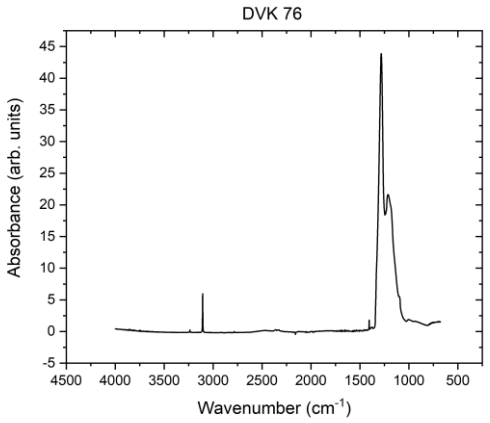
DVK 76
Absorbance (arb. units)
Wavenumber (cm-1)

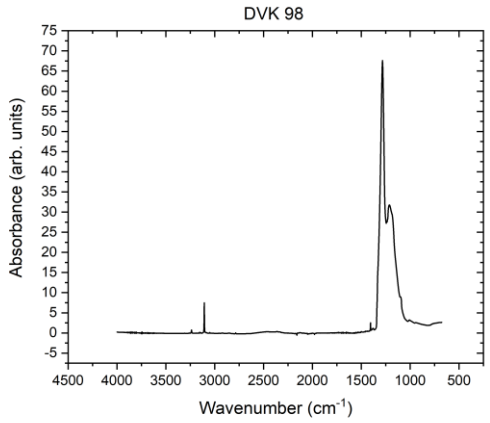
DVK 98
Absorbance (arb. units)
Wavenumber (cm-1)

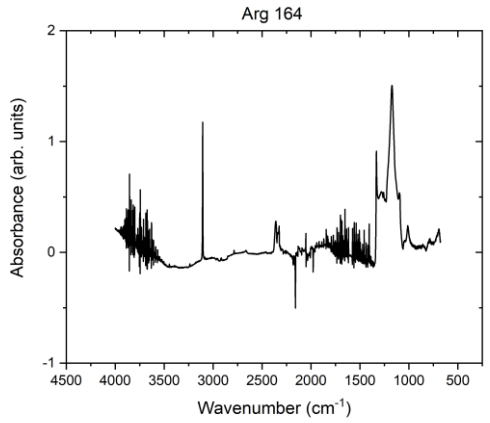
Arg 164
Absorbance (arb. units)
Wavenumber (cm-1)

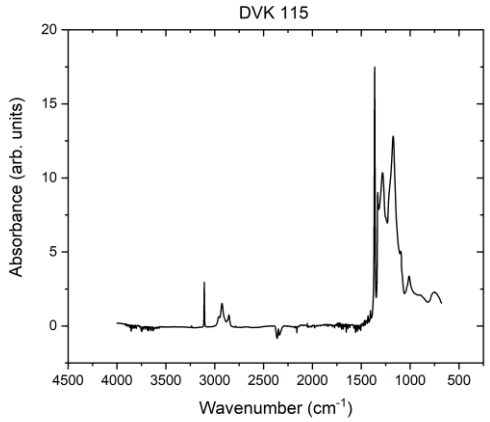
DVK 115
Absorbance (arb. units)
Wavenumber (cm-1)

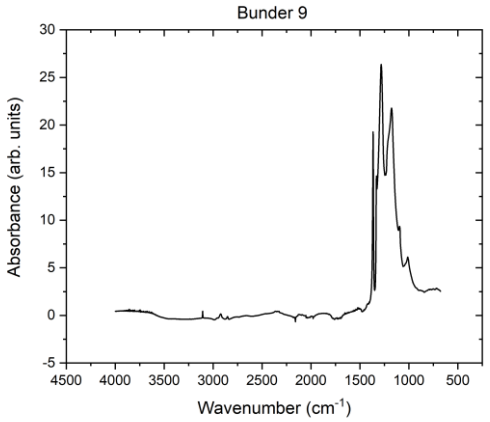
Bunder 9
Absorbance (arb. units)
Wavenumber (cm-1)

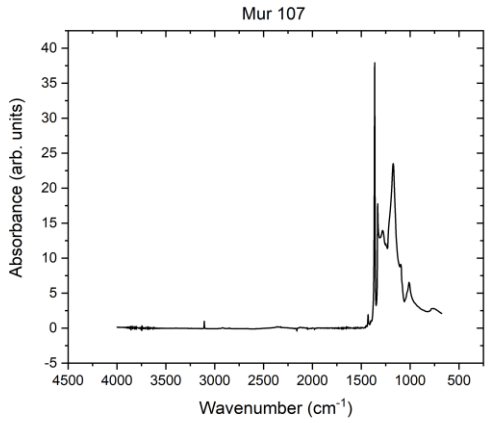
Mur 107
Absorbance (arb. units)
Wavenumber (cm-1)

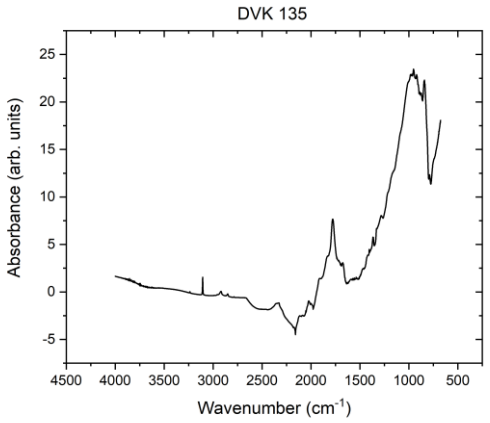
DVK 135
Absorbance (arb. units)
Wavenumber (cm-1)

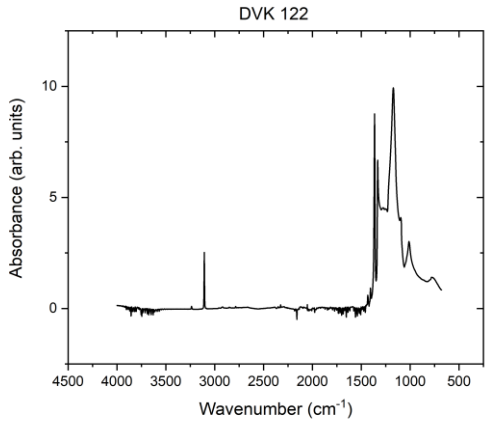
DVK 122
Absorbance (arb. units)
Wavenumber (cm-1)

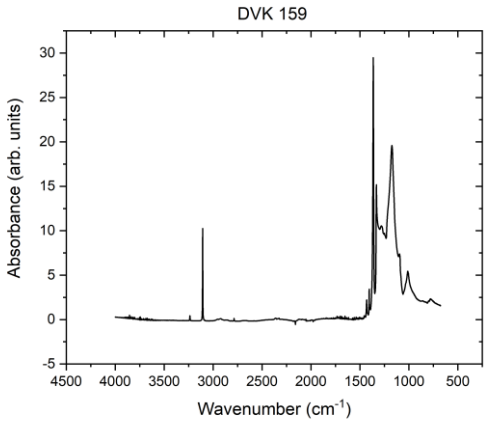
DVK 159
Absorbance (arb. units)
Wavenumber (cm-1)

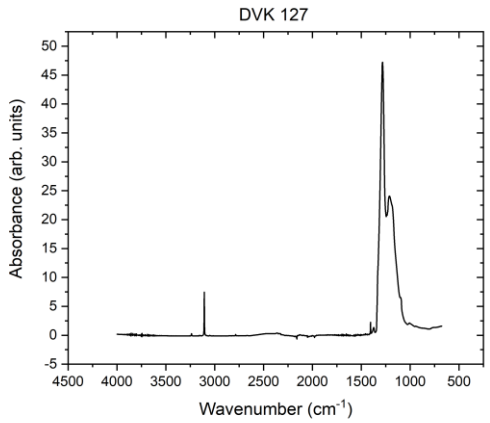
DVK 127
Absorbance (arb. units)
Wavenumber (cm-1)

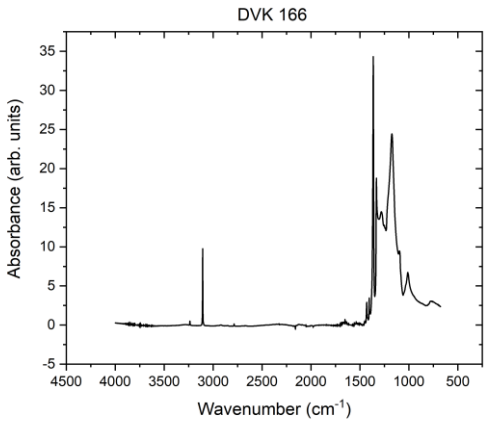
DVK 166
Absorbance (arb. units)
Wavenumber (cm-1)

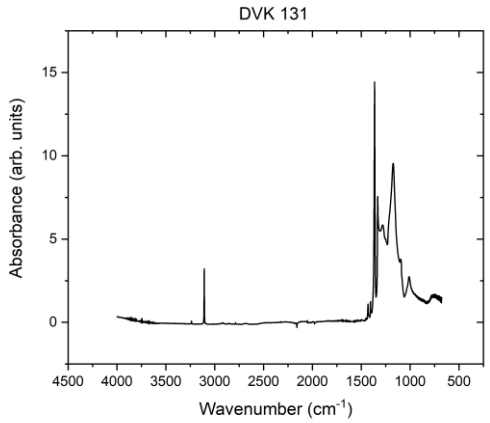
DVK 131
Absorbance (arb. units)
Wavenumber (cm-1)

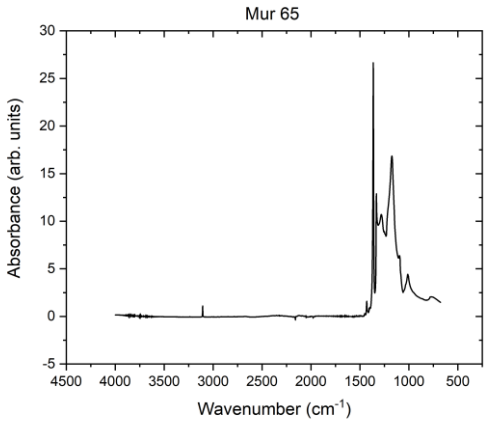
Mur 65
Absorbance (arb. units)
Wavenumber (cm-1)

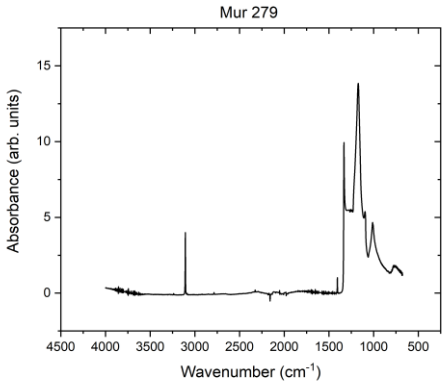
Mur 279
Absorbance (arb. units)
Wavenumber (cm-1)

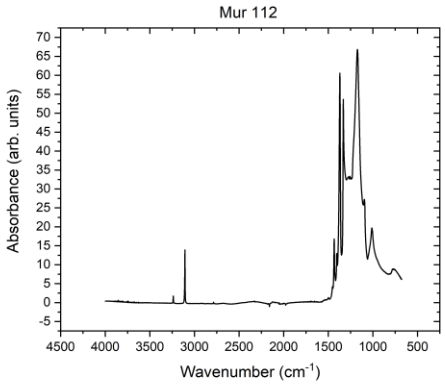
Mur 112
Absorbance (arb. units)
Wavenumber (cm-1)

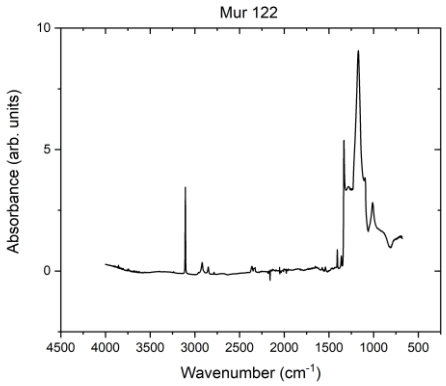
Mur 122
Absorbance (arb. units)
Wavenumber (cm-1)

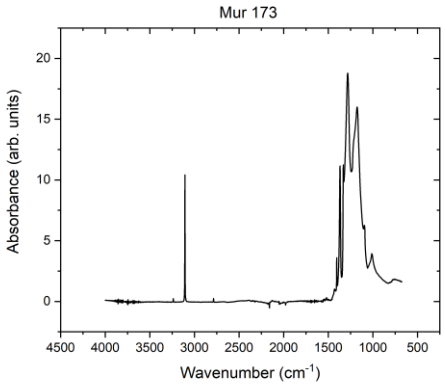
Mur 173
Absorbance (arb. units)
Wavenumber (cm-1)

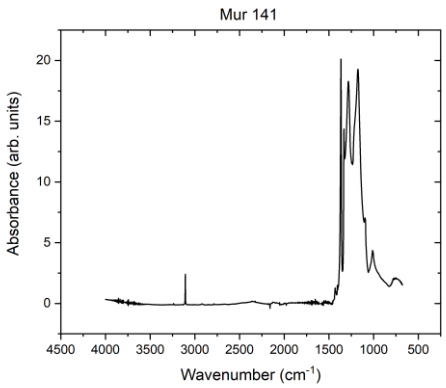
Mur 141
Absorbance (arb. units)
Wavenumber (cm-1)

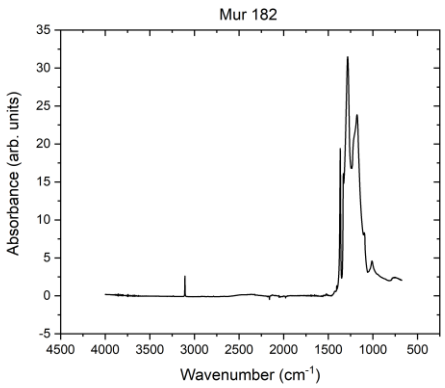
Mur 182
Absorbance (arb. units)
Wavenumber (cm-1)

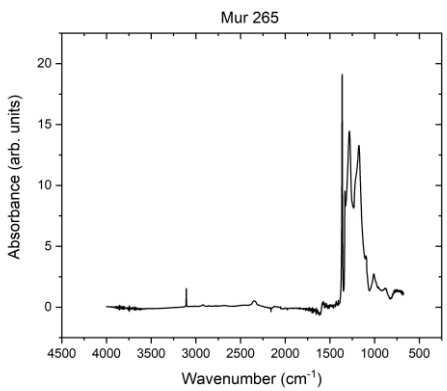
Mur 265
Absorbance (arb. units)
Wavenumber (cm-1)

Appendix C – Photoluminescence studies and attempts at correlation with IR

This appendix covers the results of a series of photoluminescence studies on some of the diamonds presented within the body of this thesis. Along with IR line scans, these PL experiments provide some minor indications of cuboid growth events within the growth history of the crystals.

As was discussed in Section 1.2.6, the growth mechanism of natural diamonds is understood to be a layer-by-layer crystallisation. This mechanism leads to the presence of internal growth structures which can be complex, containing any number of different growth zones. The most commonly observed growth mechanism is octahedral growth. However, there are other mechanisms observed, such as non-faceted growth on curved surfaces, which averages out to a mean orientation defined by simple cubic crystal axes, e.g. {100} (Bulanova, 1995), but locally could be inclined at up to 30 ° from true cube orientation. This non-faceted growth is known as 'cuboid growth'.

The features associated with hydrogen in natural diamonds are often found associated with cuboid growth within diamonds – see section 1.2.3.2 for details. This has been observed in both pure cuboid and pure cubic crystals (Welbourn et al., 1989), as well as having been observed in the cuboid sectors of mixed-habit diamonds, such as the visually striking growth sectors in asteriated diamonds (Rondeau et al., 2004). However, they cannot serve as a unique fingerprint of cuboid growth due to their prevalence in other growth environments as discussed at length within this thesis, along with their presence within the fibrous structures of diamond coat (Chrenko et al., 1967).

Features related to transition metals – including the focus of this study, nickel – have been observed in diamonds for many years (Yelisseyev and Kanda, 2007). Due to the common use of nickel within the growth media for HPHT diamond, nickel is often found as an impurity within synthetic samples (Collins, 2000; Kanda and Watanabe, 1999). The effect of nickel on

nitrogen aggregation within HPHT samples has also been studied (Fisher and Lawson, 1998). Nickel has even been proposed as being responsible for the optical features of chameleon diamonds (Fritsch and Delaunay, 2018). One common form of nickel incorporation is as a series of atomic scale defects containing both nickel and nitrogen, termed the NE_n series. Much of the detailed knowledge of these complexes comes from studies of synthetic HPHT diamonds (Wentorf, 1971). The first of the series, named NE1, NE2 and NE3, exhibit a characteristic EPR signal as well as a bright yellow PL signal under near-UV illumination, containing a number of vibronic systems already well known (Nadolinny and Yelisseyev, 1994). Further EPR investigations expanded this family, adding NE5 – NE8 to the family (Nadolinny et al., 1999, 1997; Yelisseyev and Nadolinny, 1995). These Ni-N complexes are all derived from the basic structure of NE4, displayed in figure C.1. The defining feature of this family of defects

is a Ni ion occupying a distorted site at the centre of a carbon divacancy (Lang et al., 2004). These vacancies allow for the inclusion of the large Ni ion without major distortion of the host diamond lattice.

Through the comparison of EPR and optical properties in certain samples, the optical analogues of the NE1 – NE3 centres have been identified, aided by PL-excitation spectroscopy and decay-time measurements in order to distinguish between overlapping vibronic systems. These are presented in table C.1.

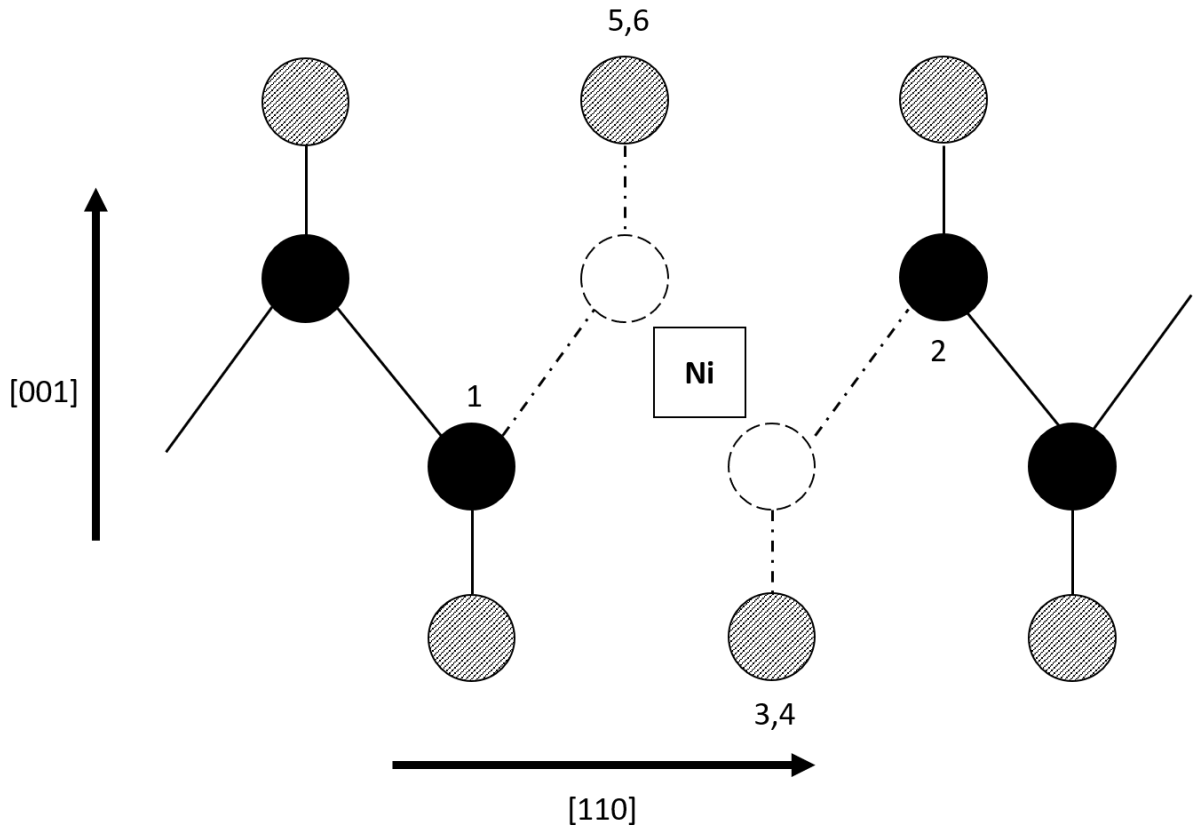

Figure C.1: A schematic of the NE4 defect structure, shown in projection on a (110) plane. This consists of a chain of carbon atoms (solid black circles), two carbon vacancies (dashed circles) and the Ni ion (open square) in between the sites of the carbon vacancies. Hatched circles represent carbon atoms distant $a_0/2\sqrt{2}$ above and below the plane. The six nearest neighbours are indicated by the numbers 1 to 6 and are represented as undistorted from their normal positions in the lattice for ease of visualisation.

EPR centre	Optical system	Zero-phonon line (nm)
NE1	S3	496.7
NE2	S2	488.9
NE3	523	523.2

Table C.1: The names and ZPLs of the optical analogues corresponding to the EPR centres NE1 – NE3.

A variety of other PL features have been observed in diamonds and related to the presence of nickel within the crystal. One worthy of discussion is found at 613 nm (sometimes referred to as the 612 nm system). This has been observed and related to nickel in the past within natural samples (Lindblom et al., 2005), including purple diamonds from Siberia (Titkov et al., 2008). This PL feature has also been observed in polycrystalline diamonds from the Mengyin kimberlite in China (Yang et al., 2012) and samples from Yakutia, alongside other nickel-related features such as the 523 system (Stepanov et al., 2017). Among diamonds from the Mir kimberlite, the peak was observed in high-nitrogen IaB stones. However, it was also observed in colourless diamonds with low A and B centre content (Yuryeva et al., 2017), which potentially poses an issue when considering the optical system as a nickel- and nitrogen-related feature.

Given the preferential incorporation of nickel under certain growth conditions, the study of the distribution of nickel-related features within diamonds could provide an insight into the prevalence of unique diamond growth such as cuboid growth. Along with this, the higher observed intensity for hydrogen-related IR features, specifically the 3107 cm^{-1} centre, can allow for further study into these conditions. A correlation between high 3107 cm^{-1} intensity and nickel-related features, while likely not diagnostic, could provide indications as to periods of cuboid growth within the formation of specific diamonds.

Methods

Samples

Samples were selected based on existing IR studies with variable intensity of the 3107 cm^{-1} peak. This included several samples with a peak observed in the 3107 cm^{-1} intensity at the boundary between growth zones within the diamond.

FTIR

A full write-up of the methods used to collect FTIR data can be found in chapter 2. This section contains high quality line scans.

Photoluminescence (PL) spectroscopy

Photoluminescence (PL) spectroscopy is a non-destructive optical technique in which a material is illuminated by a light source, and the resulting emission is collected and recorded as a plot of emitted intensity against wavelength. A perfect, defect-free diamond would be transparent to light in the visible to near-UV spectrum due to its high band gap energy of 5.5 eV, however, impurities can introduce defect states within this band gap, and can allow transitions to take place.

PL maps were collected using a Thermo Scientific DXRi Raman Microscope, which has the ability to use several modular lasers. The possible excitation wavelengths are 455 nm, 532 nm, 633 nm and 780 nm. Measurements were collected with spatial resolutions of 3 – 10 μm using a typical collection time of 8 hours for each excitation wavelength in order to increase the signal-to-noise ratio. The availability of different excitation wavelengths is useful when determining whether or not a spectral feature is a Raman or PL feature; a Raman feature, such as the intrinsic diamond peak at 1332 cm^{-1}, is present regardless of the excitation wavelength used, whereas a PL feature will only be present if a sufficient excitation wavelength is used. The live spectrum feature was used to determine sufficient experimental parameters in order to

maximise signal without saturating the detector. Peaks observed were fitted with a linear baseline within the OMNICxi software in order to produce maps of intensity of the relevant feature.

Combining IR and PL measurements

In order to assess the distributions in various optical features across different techniques efforts must be made to ensure that the spectra are taken across the same place in the diamond. In this work, microscopy images were used to make sure that the measurements were collected on the same face of the diamond. Line scans were collected in IR, and then PL measurements were collected along the same area of the diamond. Features such as the edge of the diamond and visual inclusions were used to identify the same areas and ensure that they were studied across both techniques. The uncertainties involved in this have been discussed in chapter 4 surrounding the correlation of IR and UV-vis line scans; the same uncertainties are present here. As PL is an inherently non-quantitative technique, some of these uncertainties are reduced by collecting PL maps around the IR line scan instead of attempting to match specific points. There are still uncertainties associated with using data from two separate techniques, but a qualitative evaluation of trends is possible.

Results

Figure C.2 presents the results of some optical studies of DVK 143. Fig. C.2a shows a plot of the 3107 cm^{-1} intensity as you move from the rim of the diamond to the core. Aside from the high intensity in the core, a region of higher-intensity 3107 cm^{-1} can be observed in the middle, corresponding to the boundary between a high-nitrogen core and a lower-nitrogen rim. C.2b displays a map of the 613 nm feature (discussed in section 6.1) along the path of the IR line scan. This feature shows a strong increase in intensity at the edges of the 3107 cm^{-1} rich zone. C.2c shows another PL feature at 576 nm which has been observed in nitrogen-containing natural diamonds (Zaitsev, 2013), which shows a similar enrichment towards the edges of the 3107 cm^{-1} rich zone. The increased intensity of these PL features does not directly correlate with the increased 3107 cm^{-1} intensity but instead appears to be present towards the edge of the 3107 cm^{-1} rich zone.

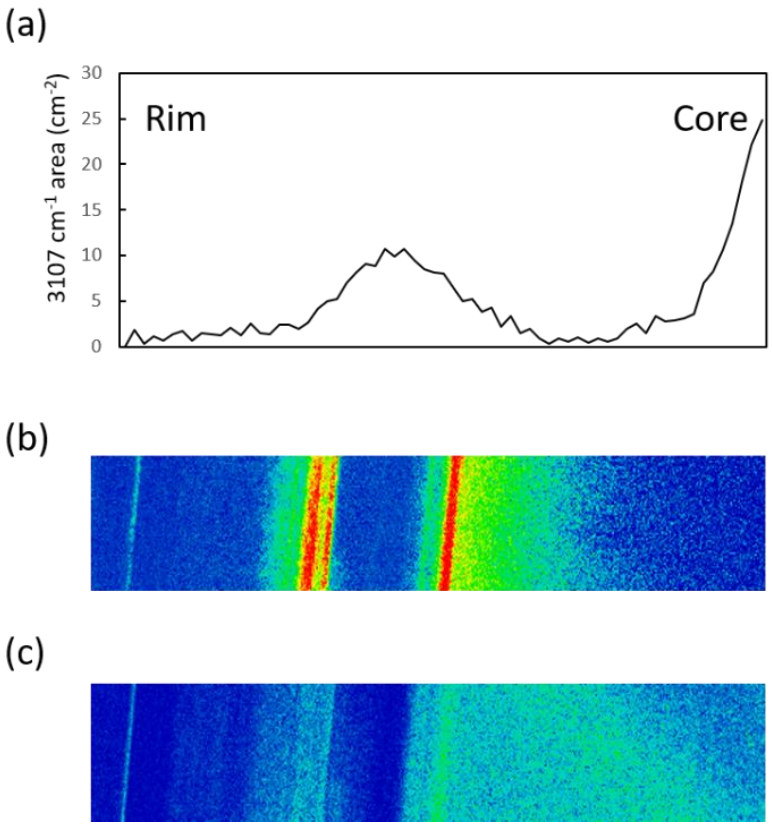

Figure C.2: A selection of optical studies of DVK 143. (a) A map of the area of the 3107 cm^{-1} feature. (b) A map of the 613 nm feature (associated with the S2 and S3 defects) along the path of the FTIR line scan. (c) A map of a PL feature observed at 576 nm in nitrogen-containing natural diamonds.

Figure C.3 shows data for DVK 076. C.3a is the variation in 3107 cm^{-1} area. Clearly visible is the complex zonation present in this sample. There is significant difficulty distinguishing between growth zones through the IR results alone. C.3b shows a map of a feature observed at 710 nm under 633 nm excitation. This feature could be one that has previously been reported in synthetic diamonds grown using nickel catalysts, and has been correlated to other nickel containing features (Yeliseyev and Nadolinnyy, 1992; Yelisseyev and Nadolinny, 1995). C.3c shows a map of a ZPL at 496 nm under 455 nm excitation that is associated with the S3 defect (Nadolinny and Yelisseyev, 1994; Zaitsev, 2013). The 710 nm feature can be seen to spike in intensity at areas that also contain spikes in 3107 cm^{-1} intensity. There also appear to be peaks at other points that do not correspond to peaks in the 3107 cm^{-1} intensity. The S3 defect can be seen to behave similarly at two points, indicated by the outer dashed lines on the diagram. However, the S3 defect appears to have a higher intensity outside of these regions. The complex zonation in the IR makes visualisation of these trends difficult. The enrichment towards the edges of the spikes in 3107 cm^{-1} intensity observed in DVK 143 are not observed here.

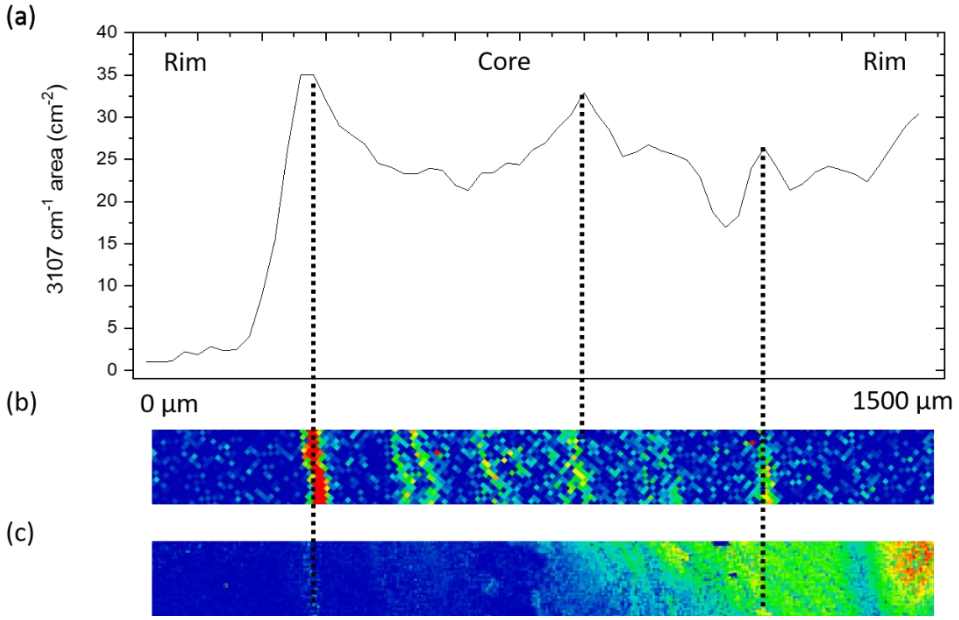

Figure C.3: a selection of optical studies from DVK 076. (a) A map of the area of the 3107 cm^{-1} feature (b) A map of a PL feature observed at 710 nm along the path of the FTIR line scan (c) A map of the 496 nm feature (associated with the S3 defect) along the path of the FTIR line scan.

Figure C.4 displays optical studies of a621-17-02. C.4b shows the distribution of a feature at 760 nm under 633 nm excitation that has previously been observed in natural type I diamonds (Solin, 1972). C.4c displays a map of the 467 nm feature under 455 nm illumination. This feature has been associated with the S3 centre, and is related to the NE1 and NE2 centres (Nadolinny et al., 1997; Yelisseyev and Nadolinny, 1995). Both of these features show a significant increase in intensity across the region with the largest 3107 cm^{-1} intensity. There is also inhomogeneity in intensity within the enriched zones of both features, suggesting complexity in the structure of the zone.

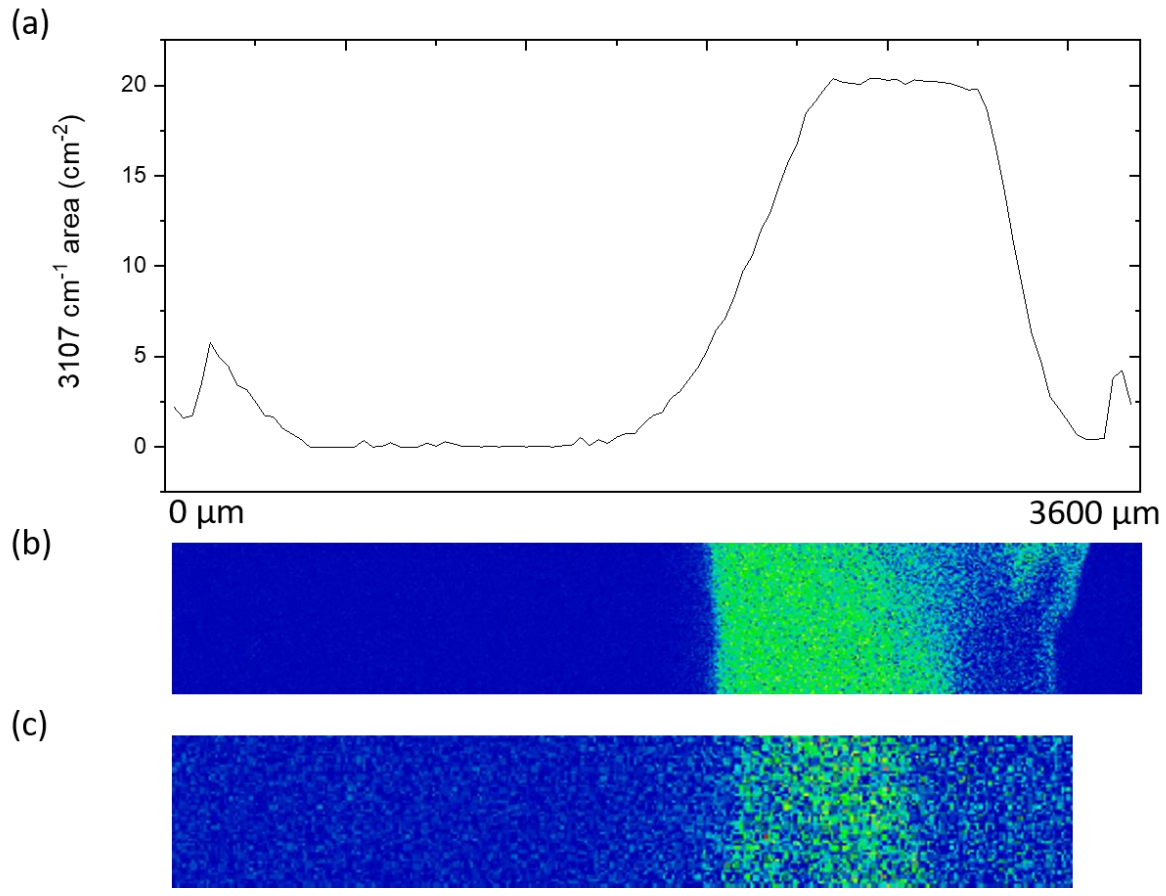

Figure C.4: a selection of optical studies from a621-17-02. (a) A map of the area of the 3107 cm^{-1} feature (b) A map of a PL feature observed at 760 nm along the path of the FTIR line scan (c) A map of a feature at 467 nm along the path of the FTIR line scan, which is associated with the S3 centre.

Figure C.5 shows results for a621-02-01. The map in C.5a displays the spatial variation in the ZPL at ~ 503 nm under 455 nm illumination. This could be the H3 centre, which is associated with the N_2V^0 defect (Zaitsev, 2013). However, the ZPLs of the H3, 3H (a characteristic centre present in irradiated diamond (Zaitsev, 2013)) and S1 centre are all at ~ 503 nm. This makes distinguishing between the different centres difficult, and in many cases impossible. The H3 is often a dominant feature, but it is not possible to state with certainty which of the features is being observed here. Fig. C.5c shows a broad luminescence observed from 650 – 750 nm under 633 nm excitation. This broad luminescence corresponds to the core of the sample where there is low 3107 cm^{-1} and H3 intensity. The two bands of H3 intensity at the left of C.5b correspond to a spike in the 3107 cm^{-1} intensity. These are indicated by the dashed lines on the diagrams. By contrast, the region on the right of C.5a with an increased 3107 cm^{-1} intensity compared to the core of the diamond does not see a similarly enriched 503 nm absorption. This is indicative of a complex growth history.

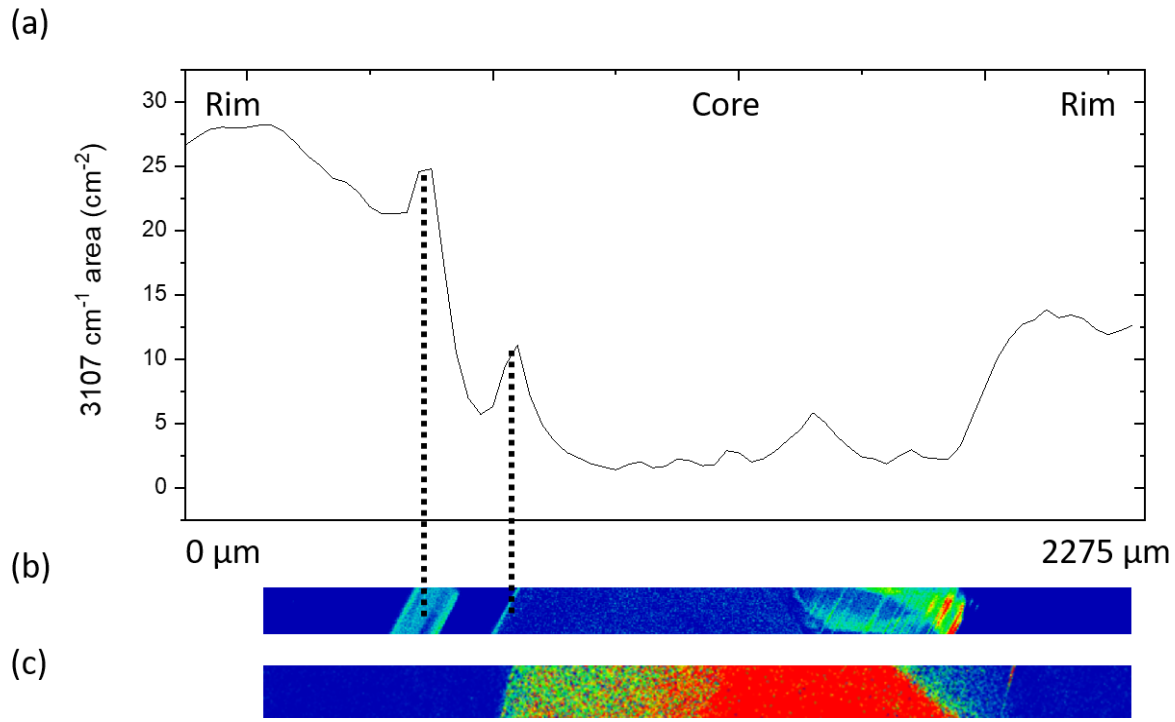

Figure C.5: a selection of optical studies from a621-02-01. (a) A map of the area of the 3107 cm^{-1} feature (b) A map of what is likely the ZPL of the H3 defect at 503 nm along the path of the FTIR line scan (c) A map of a broad luminescence observed under 633 nm excitation along the path of the FTIR line scan.

Figure C.6 displays the results for DVK 044. C.6b shows the variation in the absorbance from the feature at 503 nm under 455 nm excitation. This feature is likely either the H3 centre, S1 centre or 3H centre (Zaitsev, 2013). The 3107 cm^{-1} intensity is high in the core of the diamond. The intensity also peaks at the boundaries between the core and the rim, indicated by the lines on the diagram. These peaks coincide with regions with significant H3 intensity, although there is negligible H3 intensity in the core. The H3 luminescence is more diffuse than the peaks observed in the 3107 cm^{-1} intensity.

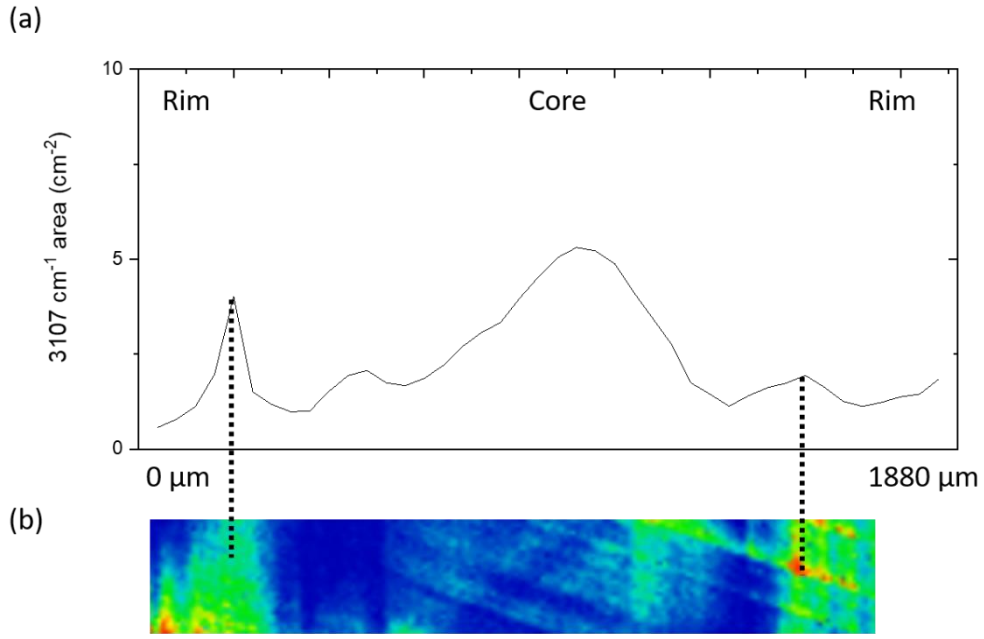

Figure C.6: a selection of optical studies from DVK 044. (a) A map of the area of the 3107 cm^{-1} feature (b) A map of what is likely the ZPL of the H3 defect at 503 nm along the path of the FTIR line scan.

Figure C.7 shows the results for DVK 122. C.7b shows a map of a feature observed at 572 nm under 532 nm illumination. This could be either a feature observed in natural diamonds which exhibit yellow luminescence (Field, 1992; Zaitsev, 2013) or a line previously observed in synthetic diamonds grown in a Ni-containing catalyst (Nadolinny et al., 1999; Zaitsev, 2013). The core shows significant intensity of this feature, whereas the rim does not. This coincides with the trend observed in the 3107 cm^{-1} defect, which has a significantly higher intensity in the core of the sample. C.7c shows the variation in the intensity of the 503 nm feature under 455 nm illumination (Zaitsev, 2013). There is appreciable intensity throughout the majority of the diamond, but there is a noticeable peak in the intensity at the rim on the right-hand side of the diagrams.

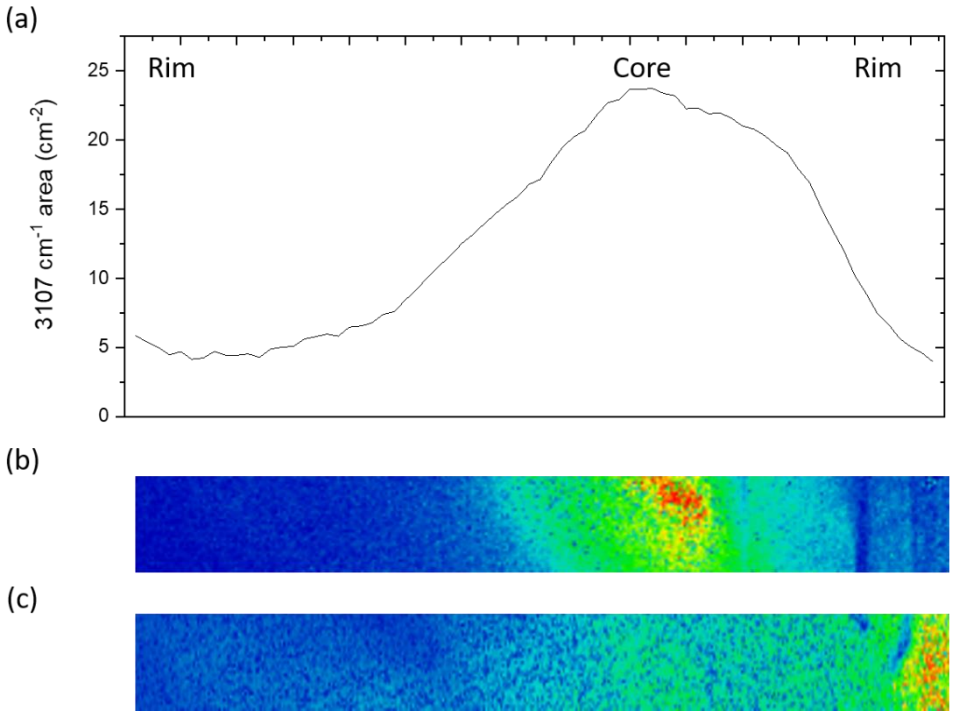

Figure C.7: A selection of optical studies from DVK 122. (a) A line scan of the area of the 3107 cm^{-1} feature (b) A map of a feature at 572 nm under 532 nm excitation (c) A map of what is likely the ZPL of the H3 defect at 503 nm under 455 nm excitation along the path of the FTIR line scan.

Figure C.8 displays the results for DVK 160. C.8b shows a map of the intensity of a feature observed at 656 nm under 633 nm illumination. This could be a feature previously observed in synthetic diamonds grown in nickel- and silicon-containing media (Sittas et al., 1996; Zaitsev, 2013). Figure C.8c then shows the variation in the intensity of the H3 feature at 503 nm. The 656 nm defect shows a high intensity in the core, along with two thin bands of increased intensity corresponding to the two peaks observed in the 3107 cm^{-1} intensity. By contrast, the H3 defect is not present in the core of the diamond, or the boundary between the growth-zones. Instead, the H3 feature is only observed in the rim of the diamond.

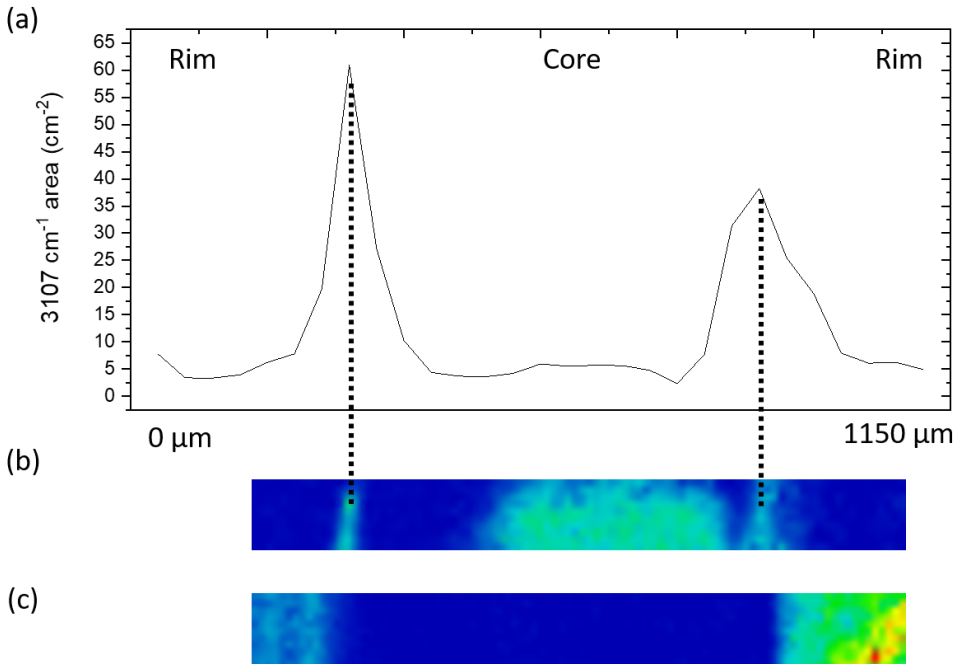

Figure C.8: A selection of optical studies from DVK 160. (a) A line scan of the area of the 3107 cm^{-1} feature (b) A map of a feature at 572 nm under 532 nm excitation (c) A map of what is likely the ZPL of the H3 defect at 503 nm under 455 nm excitation along the path of the FTIR line scan.

Figure C.9 shows the data for Mur 265. The IR shows a high 3107 cm^{-1} intensity in the core, a low intensity in the rim and two peaks at the zone boundary. C.9b shows a feature at 467 nm under 455 nm illumination, that has a high intensity in the core, along with smaller peaks

corresponding to the zone boundaries. This is likely the same feature observed in a621-17-02, which has been associated with the S3 centre (Nadolinny et al., 1997; Yelisseyev and Nadolinny, 1995). C.9c shows the intensity of two features, observed at 658 and 788 nm under 633 nm illumination. The 788 nm feature could be a feature previously observed in natural diamonds of mixed cubo-octahedral habit that correlates with the S2 centre (Zaitsev, 2013), and therefore may be nickel related. The 658 nm feature could be one observed in synthetic diamonds grown in Ni-containing media (Sittas et al., 1996; Yelisseyev and Nadolinny, 1995). These show a narrow band of intensity at the zone boundary. Fig. C.9d shows a narrow band of intensity of a feature at 613 nm under 532 nm excitation, corresponding with a zone boundary. This could be a feature that has previously been associated with the S2 and S3 centres (Zaitsev, 2013).

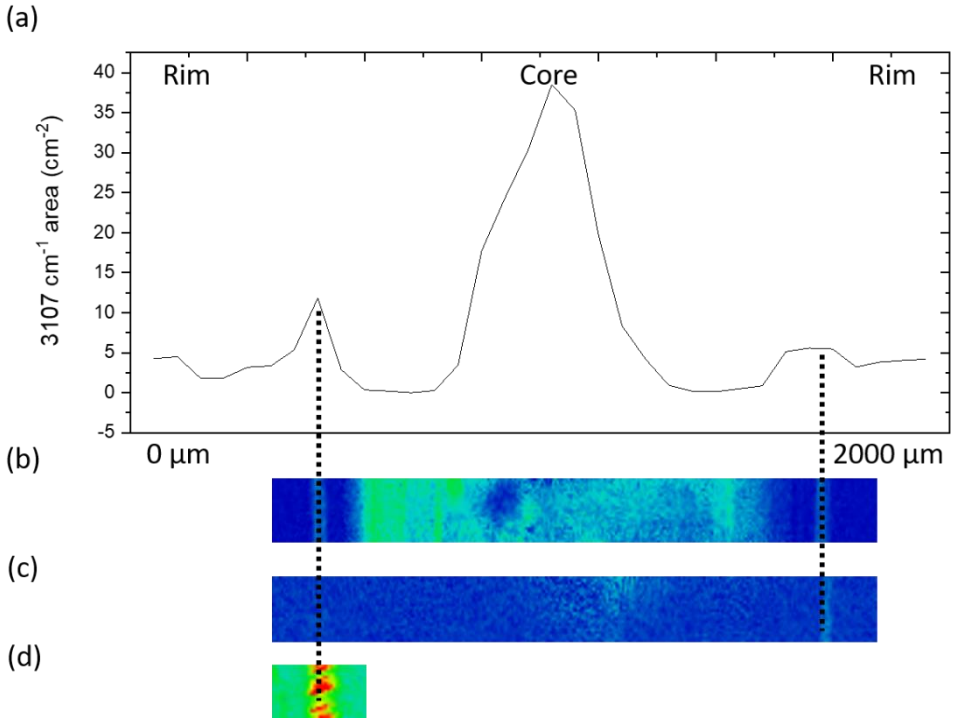

Figure C.9: A selection of optical studies from Mur 265. (a) A line scan of the area of the 3107 cm^{-1} feature (b) A map of the distribution of a feature at 467 nm under 455 nm illumination (c) A map of the distribution of two features: a peak at 658 nm and a peak at 788 nm, both under 633 nm illumination (d) A map of a feature at 612 nm under 532 nm excitation along the path of the FTIR line scan.

Table C.2 summarises the results from this work. This displays the wavelength of the features observed, and their locations within the diamond. This also shows the relative intensity of the 3107 cm^{-1} peak at the same locations within the diamonds. The * for DVK 076 indicates that the intensity of the 3107 cm^{-1} peak at the rims is asymmetric, with one side containing high intensity and the other low. A † indicates that the exact identity of the centre responsible for the luminescence is uncertain.

Locality	**Sample**	**3107 cm^{-1} intensity (relative)**			**PL features observed**		
		Core	**Boundary**	**Rim**	**Core**	**Boundary**	**Rim**
Orapa, Botswana	A621-02-01	Low	High peaks	High	633 nm	***H3*†**	None
	A621-17-02	High	Low	Moderate	***S3***, ***467 nm***	None	None
Diavik, Canada	DVK 044	High	High peak	Low	None	***H3*†**	None
	DVK 076	High	Complex	High*	***710 nm***	***710 nm***, ***496 nm***	None
	DVK 122	High	Moderate	Low	***572 nm***, ***H3*†**	***H3*†**	***H3*†**
	DVK 143	High	Moderate peak	Low	None	***613 nm***, 576 nm	None
	DVK 160	Low	High peaks	Low	***656 nm***	***656 nm***	***H3*†**
Murowa, Zimbabwe	Mur 265	High	Moderate peaks	Low	***467 nm***	***467 nm, 658 nm, 788 nm, 612 nm***	None

*Table C.2: A summary of the results from this work, showing the locality of each sample and the PL features observed in the core and rim, along with the boundary between the core and rim. Features that have been related to nickel or cuboid growth are highlighted in bold italics. The * indicates asymmetry in the distribution of the 3107 cm^{-1} intensity. The † indicates that, while represented as the H3 centre, this could potentially be either the S1 or 3H centre.*

Discussion and Conclusions

The samples studied here primarily show nickel-related features in the PL spectra. Using the known relationship between nickel and cuboid growth, a correlation between these features and the intensity of the 3107 cm^{-1} centre discussed at length within this thesis could be an indicator of cuboid growth.

All diamonds studied here contain very heterogenous distribution of the PL features studied. This highlights the complex zonation that can provide a substantial amount of information on growth history. The significant variation in PL intensity reinforces that studies using single PL spectra encompassing a whole diamond are insufficient to truly understand the growth conditions of a significant portion of diamonds, with a large amount of information potentially being obscured.

The diamonds presented here all show features that have been previously related to the presence of nickel within the diamond lattice. As the diamonds are from several different localities, this supports the idea that nickel is present in the growth media of diamonds from many places across the world. While there are many other transition metals that have been introduced into synthetic diamond, only a few, including chromium, cobalt and nickel have been observed as optical centres (Yelisseyev and Kanda, 2007; Zaitsev, 2000). This does not mean that other metals such as iron are not incorporated into the diamond lattice. It may be the case that any iron-based defects are optically inactive and diamagnetic, meaning that they cannot be observed with ease. This could lead to ideas of an overabundance of nickel in diamond-forming fluids. As such, it is important to note the possibility of an oversampling of nickel due to the ease at which it is incorporated into optical centres.

DVK 044, 076, 143 and 160 and Mur 265 all contain peaks in 3107 cm^{-1} intensity at the boundary between growth zones. In these diamonds, this corresponds to a similar peak in nickel-related features. The exact nature of the nickel-related feature observed can vary, with

a number of different centres being seen in the PL spectra. This suggests the possibility of a small period of cuboid growth in between two zones of standard octahedral growth. The fact that diamonds often contain zones of different ages and growth conditions likely indicates that the conditions under which an individual diamond forms can change significantly, with geologically significant periods of time between growth events. Between these growth events it is possible that there are periods of diamond growth followed by resorption events that are not recorded in the diamond that is exhumed to the Earth's surface.

The zones show different behaviour in terms of the shape of the luminescence at the boundary. In DVK 143, the Ni-related features appear to grow in sharply at the edges of the 3107 cm^{-1}-rich zone before decaying as you move away from this region. This could suggest a small octahedral growth event captured between small regions of cuboid growth indicated by the Ni-related features. In the majority of samples, this is not the case. For most samples, the Ni-related features appear to grow synchronously with the 3107 cm^{-1} peak. This more strongly suggests the possibility of a small period of cuboid growth contained between octahedral growth zones.

It is not possible from this work to determine the exact sequence of growth events. For example, it could be possible that there are three separate growth sequences: an octahedral event, some cuboid overgrowth, succeeded by another octahedral growth event. It is also possible that there is a slight discontinuity between the crystal structures of the two octahedral events. In this case, it might be expected that there could be a small period of defective growth in between these two zones. Any defective growth could lead to the preferential incorporation of impurities such as nickel or hydrogen. Both of these scenarios are possible, and it is difficult to determine which is more likely.

The variation in exact behaviour of the nickel-related luminescence in the different samples is distinct. For example, a number of the diamonds such as DVK 122 and a621-17-02 exhibit nickel-related features in the core of the diamond, and DVK 143 shows Ni-related features that grow in at the edges of the H-rich zone. This reinforces that these defects are not diagnostic of cuboid growth and can be present in other areas of the diamonds.

A number of the diamonds here display what is most likely the H3 centre in their PL spectra. This is observed all throughout DVK 122, at the zone boundary in a621-02-01 and DVK 044 and in the rim of DVK 160. This feature is the most common naturally occurring optical feature in nitrogen-containing diamonds (Zaitsev, 2013). This is often accompanied by the N3 centre, which is discussed at length in chapter 4. The N3 centre could not be studied here due to the unavailability of a laser with a sufficient excitation wavelength. The H3 defect has been thought to decorate individual dislocations (Lang, 1977; Zaitsev, 2013). The incorporation of dislocations decorated with H3 centres could potentially explain the complex zonation of this luminescence within a621-02-01. In synthetic diamonds, the H3 defect has also been observed to form preferentially in {100} growth sectors (Dismukes, 1993; Malogolovets et al., 1979; Zaitsev, 2013). This could suggest that the presence of H3 in the zone boundaries may be another indicator of periods of cuboid growth. Once again, this cannot be considered diagnostic, but the combination of several features that are preferentially incorporated in cuboid zones provides a stronger suggestion of the presence of this defective growth event.

It is important to emphasize, as has been stated previously, that the presence of nickel and hydrogen concurrently is not necessarily diagnostic of cuboid growth, but merely a suggestion. The defect distributions and speculations here do, however, provide suggestions of explanations as to why these defects are found in such thin bands of increased intensity within the diamonds studied here. It is also clear that this is not the case in many diamonds. Those samples presented here are a selection of a larger dataset, many of which were not observed to

contain any significant luminescence features. This is perhaps expected for diamonds containing homogenous IR features, indicative of only one growth event. It is likely that the conditions leading to small periods of defective, possibly cuboid growth are unique, and that they can occur across a wide range of localities.

This work has presented optical studies of eight inhomogeneous diamonds from three localities and attempted to correlate the 3107 cm^{-1} peak intensity with PL centres. A variety of different PL features have been observed, with all diamonds exhibiting luminescence from centres that have previously been linked to the presence of nickel within the crystal.

Many of the diamonds show peaks in 3107 cm^{-1} intensity at the boundary between growth zones. This correlates with an enhanced intensity in many of the nickel-related features. Due to the known preferential incorporation of both nickel-related features and the 3107 cm^{-1} peak into cuboid growth zones, this is a possible indication of a small period of cuboid growth between growth zones in these diamonds.

While not diagnostic, a rationale has been discussed for the preservation of a small cuboid growth event in between periods of standard octahedral growth. The exact nature of this is likely to vary between samples, as indicated by the range of behaviours exhibited by the Ni-related luminescence features. The correlation of PL and IR features can provide an additional source of information into diamond growth events. Further study could expand the dataset and examine additional inhomogeneous diamonds that exhibit a peak in 3107 cm^{-1} intensity at growth zone boundaries. This could validate the ideas discussed here and use the study of hydrogen to further probe diamond growth events.

References

Abbott, R.N., 2018. Trace element thermometry of garnet-clinopyroxene pairs, revisited. Am. Mineral. 103, 1169–1171. https://doi.org/10.2138/am-2018-6487

Ahrens, T.J., 1989. Water storage in the mantle. Nature. https://doi.org/10.1038/342122a0

Ashfold, M.N.R., May, P.W., Rego, C.A., Everitt, N.M., 1994. Thin film diamond by chemical vapour deposition methods. Chem. Soc. Rev. 23, 21. https://doi.org/10.1039/cs9942300021

Aubaud, C., Hauri, E.H., Hirschmann, M.M., 2004. Hydrogen partition coefficients between nominally anhydrous minerals and basaltic melts. Geophys. Res. Lett. 31. https://doi.org/10.1029/2004GL021341

Bachmann, P.K., Leers, D., Lydtin, H., 1991. Towards a general concept of diamond chemical vapour deposition. Diam. Relat. Mater. 1, 1–12. https://doi.org/10.1016/0925-9635(91)90005-U

Bai, Q., Kohlstedt, D.L., 1993. Effects of chemical environment on the solubility and incorporation mechanism for hydrogen in olivine. Phys. Chem. Miner. 19, 460–471. https://doi.org/10.1007/BF00203186

Bali, E., Audétat, A., Keppler, H., 2013. Water and hydrogen are immiscible in Earth's mantle. Nature 495, 220–222. https://doi.org/10.1038/nature11908

Ballutaud, D., Jomard, F., Theys, B., Mer, C., Tromson, D., Bergonzo, P., 2001. Hydrogen diffusion and stability in polycrystalline CVD undoped diamond. Diam. Relat. Mater. 10, 405–410. https://doi.org/10.1016/S0925-9635(00)00590-2

Barry, J.C., 1986. Voidites in diamond - do they contain nitrogen? Ultramicroscopy 20, 169–176. https://doi.org/10.1016/0304-3991(86)90183-X

Bech Nielsen, B., Hoffmann, L., Budde, M., Jones, R., Goss, J.P., Öberg, S., 1995. H Interacting with Intrinsic Defects in Si. Mater. Sci. Forum 196–201, 933–938. https://doi.org/10.4028/www.scientific.net/MSF.196-201.933

Bell, D.R., Rossman, G.R., Maldener, J., Endisch, D., Rauch, F., 2003. Hydroxide in olivine: A quantitative determination of the absolute amount and calibration of the IR spectrum. J. Geophys. Res. Solid Earth 108. https://doi.org/10.1029/2001jb000679

Bolfan-Casanova, N., 2005. Water in the Earth's mantle. Mineral. Mag. 69, 229–257. https://doi.org/10.1180/0026461056930248

Bolfan-Casanova, N., Keppler, H., Rubie, D.C., 2000. Water partitioning between nominally anhydrous minerals in the MgO-SiO2-H2O system up to 24 GPa: Implications for the distribution of water in the Earth's mantle. Earth Planet. Sci. Lett. 182, 209–221. https://doi.org/10.1016/S0012-821X(00)00244-2

Bonney, G., 1900. The parent-rock of the diamond in South Africa. Proc. R. Soc. London 65, 223–236. https://doi.org/10.1098/rspl.1899.0028

Borysiuk, M., Ros, L., Kristiansson, P., Skogby, H., Abdel, N., Elfman, M., Golubev, P., Nilsson, E.J.C., Pallon, J., 2013. Hydrogen analysis and profiling with a position sensitive detector. Nucl. Instruments Methods Phys. Res. Sect. B Beam Interact. with Mater. Atoms 306, 49–53. https://doi.org/10.1016/j.nimb.2012.12.040

Boyd, F.R., Gurney, J.J., 1986. Diamonds and the African Lithosphere. Science (80-.). 232, 472–477. https://doi.org/10.1126/science.232.4749.472

Boyd, S.R., Kiflawi, I., Woods, G.S., 1995. Infrared absorption by the B nitrogen aggregate in diamond. Philos. Mag. Part B 72, 351–361. https://doi.org/10.1080/13642819508239089

Boyd, S.R., Kiflawi, I., Woods, G.S., 1994. The relationship between infrared absorption and the A defect concentration in diamond. Philos. Mag. Part B 69, 1149–1153. https://doi.org/10.1080/01418639408240185

Braatz, A., Ott, U., Henning, T., Jäger, C., Jeschke, G., 2000. Infrared, ultraviolet, and electron paramagnetic resonance measurements on presolar diamonds: Implications for optical features and origin. Meteorit.

Planet. Sci. 35, 75–84. https://doi.org/10.1111/j.1945-5100.2000.tb01975.x

Breeding, C.M., Shigley, J.E., 2009. The “Type” Classification System of Diamonds and Its Importance in Gemology. Gems Gemol. 45, 96–111. https://doi.org/10.5741/GEMS.45.2.96

Brey, G.P., Köhler, T., 1990. Geothermobarometry in Four-phase Lherzolites II. New Thermobarometers, and Practical Assessment of Existing Thermobarometers. J. Petrol. 31, 1353–1378. https://doi.org/10.1093/petrology/31.6.1353

Brozel, M.R., Evans, T., Stephenson, R.F., 1978. Partial Dissociation of Nitrogen Aggregates in Diamond by High Temperature-High Pressure Treatments. Proc. R. Soc. A Math. Phys. Eng. Sci. 361, 109–127. https://doi.org/10.1098/rspa.1978.0094

Bulanova, G.P., 1995. The formation of diamond. J. Geochemical Explor. 53, 1–23. https://doi.org/10.1016/0375-6742(94)00016-5

Bulanova, G.P., Pearson, D.G., Hauri, E.H., Griffin, B.J., 2002. Carbon and nitrogen isotope systematics within a sector-growth diamond from the Mir kimberlite, Yakutia. Chem. Geol. 188, 105–123. https://doi.org/http://dx.doi.org/10.1016/S0009-2541(02)00075-X

Bulanova, G.P., Speich, L., Smith, C.B., Gaillou, E., Kohn, S.C., Wibberley, E., Chapman, J.G., Howell, D., Davy, A.T., 2018. The unique nature of Argyle fancy diamonds: internal structure, paragenesis and reasons for color. Econ Geol.

Bulanova, G.P., Varshavsky, A.V., Kotegov, V.A., 2005. A venture into the interior of natural diamond: genetic information and implications for the gem industry. J. Gemmol. 29, 377–386. https://doi.org/10.15506/JoG.2005.29.7.377

Bundy, F.P., Hall, H.T., Strong, H.M., Wentorf, R.H., 1955. Man-Made diamonds. Nature 176, 51–55. https://doi.org/10.1038/176051a0

Bursill, L.A., 1983. Small and extended defect structures in gem-quality type I diamonds. Endeavour 7, 70–77. https://doi.org/10.1016/S0160-9327(83)80005-2

Canil, D., Fedortchouk, Y., 1999. Garnet dissolution and the emplacement of kimberlites. Earth Planet. Sci. Lett. 167, 227–237. https://doi.org/10.1016/S0012-821X(99)00019-9

Cartigny, P., 2005. Stable Isotopes and the Origin of Diamond. Elements 1, 79–84. https://doi.org/10.2113/gselements.1.2.79

Charette, J.J., 1959. Le spectre infra-rouge a grande dispersion des trois types de diamants et ses variations en fonction de la temperature. Physica 25, 1303–1312. https://doi.org/10.1016/0031-8914(59)90053-9

Chen, Y.-C., Griffiths, B., Weng, L., Nicley, S.S., Ishmael, S.N., Lekhai, Y., Johnson, S., Stephen, C.J., Green, B.L., Morley, G.W., Newton, M.E., Booth, M.J., Salter, P.S., Smith, J.M., 2019. Laser writing of individual nitrogen-vacancy defects in diamond with near-unity yield. Optica 6, 662. https://doi.org/10.1364/optica.6.000662

Cherniak, D.J., Watson, E.B., Meunier, V., Kharche, N., 2018. Diffusion of helium, hydrogen and deuterium in diamond: Experiment, theory and geochemical applications. Geochim. Cosmochim. Acta 232, 206–224. https://doi.org/10.1016/j.gca.2018.04.029

Chevallier, J., Jomard, F., Teukam, Z., Koizumi, S., Kanda, H., Sato, Y., Deneuville, A., Bernard, M., 2002. Hydrogen in n-type diamond. Diam. Relat. Mater. 11, 1566–1571. https://doi.org/10.1016/S0925-9635(02)00063-8

Chevallier, J., Theys, B., Lusson, A., Grattepain, C., Deneuville, A., Gheeraert, E., 1998. Hydrogen-boron interactions in <math display="inline"> <mi>p</mi> </math> -type diamond. Phys. Rev. B 58, 7966–7969. https://doi.org/10.1103/PhysRevB.58.7966

Chrenko, R.M., McDonald, R.S., Darrow, K.A., 1967. Infra-red spectra of diamond coat. Nature 213, 474–476. https://doi.org/10.1038/213474a0

Chrenko, R.M., Tuft, R.E., Strong, H.M., 1977. Transformation of the state of nitrogen in diamond. Nature 270, 141–144. https://doi.org/10.1038/270141a0

Chu, W.-K., Mayer, J.W., Nicolet, M.-A., 1978. Backscattering spectroscopy.

Clackson, S.G., Moore, M., Walmsley, J.C., Woods, G.S., 1990. The relationship between platelet size and the frequency of the B' infrared absorption peak in type la diamond. Philos. Mag. B Phys. Condens. Matter; Stat. Mech. Electron. Opt. Magn. Prop. 62, 129–137. https://doi.org/10.1080/13642819008226980

Cohen, B.L., Fink, C.L., Degnan, J.H., 1972. Nondestructive Analysis for Trace Amounts of Hydrogen. J. Appl. Phys. 43, 19–25. https://doi.org/10.1063/1.1660806

Collins, A.T., 2001. The colour of diamond and how it may be changed. J. Gemmol. 27, 341–359. https://doi.org/10.15506/JoG.2001.27.6.341

Collins, A.T., 2000. Spectroscopy of defects and transition metals in diamond. Diam. Relat. Mater. 9, 417–423. https://doi.org/10.1016/S0925-9635(99)00314-3

Collins, A.T., Stanley, M., 1985. Absorption and luminescence studies of synthetic diamond in which the nitrogen has been aggregated, J. Phys. D: Appl. Phys.

Coxon, D.J.L., Staniforth, M., Breeze, B.G., Greenough, S.E., Goss, J.P., Monti, M., Lloyd-Hughes, J., Stavros, V.G., Newton, M.E., 2020. An Ultrafast Shakedown Reveals the Energy Landscape, Relaxation Dynamics and Concentration of the N3VH0 Defect in Diamond. J. Phys. Chem. Lett. acs.jpclett.0c01806. https://doi.org/10.1021/acs.jpclett.0c01806

Crank, J., 1979. The mathematics of diffusion. Oxford university press.

Dasgupta, R., Hirschmann, M.M., 2010. The deep carbon cycle and melting in Earth's interior. Earth Planet. Sci. Lett. 298, 1–13. https://doi.org/10.1016/j.epsl.2010.06.039

Davies, G., 1999. Current problems in diamond: towards a quantitative understanding. Phys. B Condens. Matter 273–274, 15–23. https://doi.org/10.1016/S0921-4526(99)00398-1

Davies, G., 1981. Decomposing the IR absorption spectra of diamonds. Nature 290, 40–41. https://doi.org/10.1038/290040a0

Davies, G., 1976. The A nitrogen aggregate in diamond-its symmetry and possible structure. J. Phys. C Solid State Phys. 9, L537–L542. https://doi.org/10.1088/0022-3719/9/19/005

Davies, G., 1974. Vibronic spectra in diamond. J. Phys. C Solid State Phys. 7, 3797–3809. https://doi.org/10.1088/0022-3719/7/20/019

Davies, G., Collins, A.T., Spear, P., 1984. Sharp infra-red absorption lines in diamond. Solid State Commun. 49, 433–436. https://doi.org/10.1016/0038-1098(84)90657-4

Dawson, J.B., Stephens, W.E., 1975. Statistical Classification of Garnets from Kimberlite and Associated Xenoliths. J. Geol. 83, 589–607. https://doi.org/10.1086/628143

De Beers Group, 2019. The diamond insight report, 2019.

De Vries, R.C., 1975. Plastic deformation and "work-hardening" of diamond. Mater. Res. Bull. 10, 1193–1199. https://doi.org/10.1016/0025-5408(75)90026-4

De Weerdt, F., Pal'yanov, Y.N., Collins, A.T., 2003. Absorption spectra of hydrogen in 13 C diamond produced by high-pressure, high-temperature synthesis, J. Phys.: Condens. Matter.

Deines, P., Gurney, J.J., Harris, J.W., 1984. Associated chemical and carbon isotopic composition variations in diamonds from Finsch and Premier kimberlite, South Africa. Geochim. Cosmochim. Acta 48, 325–342. https://doi.org/10.1016/0016-7037(84)90254-0

Demouchy, S., Bolfan-Casanova, N., 2016. Distribution and transport of hydrogen in the lithospheric mantle: A review. Lithos 240–243, 402–425. https://doi.org/10.1016/j.lithos.2015.11.012

Dismukes, J.P., 1993. Proceedings of the Third International Symposium on Diamond Materials. The Electrochemical Society.

Doyle, B.P., Maclear, R.D., Connell, S.H., Formenti, P., Machi, I.Z., Butler, J.E., Schaaff, P., Sellschop, J.P.F., Sideras-Haddad, E., Bharuth-Ram, K., 1997. 3-D-micro-ERDA microscopy of trace hydrogen distributions in diamond using a 2-D-PSD with event reconstruction. Nucl. Instruments Methods Phys.

Res. Sect. B Beam Interact. with Mater. Atoms 130, 204–210. https://doi.org/10.1016/S0168-583X(97)00367-4

Dyer, H.B., Raal, F.A., Du Preez, L., Loubser, J.H.N., 1965. Optical absorption features associated with paramagnetic nitrogen in diamond. Philos. Mag. 11, 763–774. https://doi.org/10.1080/14786436508230081

Eggler, D.H., 1983. Upper mantle oxidation state: Evidence from olivine-orthopyroxene-ilmenite assemblages. Geophys. Res. Lett. 10, 365–368. https://doi.org/10.1029/GL010i005p00365

Eugster, H.P., 1957. Heterogeneous Reactions Involving Oxidation and Reduction at High Pressures and Temperatures. J. Chem. Phys. 26, 1760–1761. https://doi.org/10.1063/1.1743626

Evans, T., Harris, J.W., 1989. Nitrogen aggregation, inclusion equilibration temperatures and the age of diamonds. Kimberlites Relat. rocks 2, 1001–1006.

Evans, T., Qi, Z., 1982. The Kinetics of the Aggregation of Nitrogen Atoms in Diamond. Proc. R. Soc. A Math. Phys. Eng. Sci. 381, 159–178. https://doi.org/10.1098/rspa.1982.0063

Ferrer, N., Nogués-Carulla, J.M., 1996. Characterisation study of cut gem diamond by IR spectroscopy. Diam. Relat. Mater. 5, 598–602. https://doi.org/10.1016/0925-9635(95)00479-3

Field, J.E., 1992. The properties of natural and synthetic diamond. Academic Press.

Fisher, D., Lawson, S.C., 1998. The effect of nickel and cobalt on the aggregation of nitrogen in diamond. Diam. Relat. Mater. 7, 299–304. https://doi.org/10.1016/S0925-9635(97)00246-X

Fritsch, E., Delaunay, A., 2018. What Truly Characterises a Chameleon Diamond? An Example of an Atypical 25.85 ct Stone. J. Gemmol. 36, 142–151. https://doi.org/10.15506/JoG.2018.36.2.142

Fritsch, E., Hainschwang, T., Massi, L., Rondeau, B., 2007. Hydrogen-Related Optical Centers in Natural Diamond: An Update. New Diam. Front. Carbon Technol. 17.

Fritsch, E., Scarratt, K., 1993. Gemmological properties of Type Ia diamonds with an unusually high hydrogen content. J. Gemmol. 23, 451–460. https://doi.org/10.15506/JoG.1993.23.8.451

Fritsch, E., Scarratt, K., Collins, A.T., 1991. Optical properties of diamonds with an unusually high hydrogen content, in: Materials Research Society International Conference Proceedings, Second International Conference on New Diamond Science and Technology, Washington DC, Sept. pp. 23–27.

Frost, D.J., McCammon, C.A., 2008. The Redox State of Earth's Mantle. Annu. Rev. Earth Planet. Sci. 36, 389–420. https://doi.org/10.1146/annurev.earth.36.031207.124322

Fuchs, F., Wild, C., Schwarz, K., Müller-Sebert, W., Koidl, P., 1995. Hydrogen induced vibrational and electronic transitions in chemical vapor deposited diamond, identified by isotopic substitution. Appl. Phys. Lett. 66, 177–179. https://doi.org/10.1063/1.113126

Gaillou, E., Post, J.E., Rost, D., Butler, J.E., 2012. Boron in natural type IIb blue diamonds: Chemical and spectroscopic measurements. Am. Mineral. 97, 1–18. https://doi.org/10.2138/am.2012.3925

Gicquel, A., Hassouni, K., Silva, F., Achard, J., 2001. CVD diamond films: from growth to applications. Curr. Appl. Phys. 1, 479–496. https://doi.org/https://doi.org/10.1016/S1567-1739(01)00061-X

Goss, J P, Briddon, P.R., Hill, V., Jones, R., Rayson, M.J., 2014. Identification of the structure of the 3107 cm(-1) H-related defect in diamond. J. Phys. Condens. Matter 26, 145801. https://doi.org/10.1088/0953-8984/26/14/145801

Goss, J. P., Briddon, P.R., Hill, V., Jones, R., Rayson, M.J., 2014. Identification of the structure of the 3107 cm-1 H-related defect in diamond. J. Phys. Condens. Matter 26. https://doi.org/10.1088/0953-8984/26/14/145801

Goss, J. P., Briddon, P.R., Jones, R., Sque, S., 2003a. The vacancy-nitrogen-hydrogen complex in diamond: A potential deep centre in chemical vapour deposited material. J. Phys. Condens. Matter 15. https://doi.org/10.1088/0953-8984/15/39/014

Goss, J. P., Briddon, P.R., Jones, R., Teukam, Z., Ballutaud, D., Jomard, F., Chevallier, J., Bernard, M.,

Deneuville, A., 2003b. Deep hydrogen traps in heavily B-doped diamond. Phys. Rev. B - Condens. Matter Mater. Phys. 68, 235209. https://doi.org/10.1103/PhysRevB.68.235209

Goss, J P, Coomer, B.J., Jones, R., Fall, C.J., Briddon, P.R., Öberg, S., 2003. Extended defects in diamond: The interstitial platelet. Phys. Rev. B 67, 165208. https://doi.org/10.1103/PhysRevB.67.165208

Graham, R.J., Buseck, P.R., 1994. Cathodoluminescence of brown diamonds as observed by transmission electron microscopy. Philos. Mag. B 70, 1177–1185. https://doi.org/10.1080/01418639408240282

Grütter, H.S., Gurney, J.J., Menzies, A.H., Winter, F., 2004. An updated classification scheme for mantle-derived garnet, for use by diamond explorers. Lithos 77, 841–857. https://doi.org/10.1016/j.lithos.2004.04.012

Gu, T., Ritterbex, S., Tsuchiya, T., Wang, W., 2020. Novel configurations of VN4 and VN4H defects in diamond platelets: Structure, energetics and vibrational properties. Diam. Relat. Mater. 108, 107957. https://doi.org/10.1016/j.diamond.2020.107957

Gu, T., Wang, W., 2018. Optical defects in milky type IaB diamonds. Diam. Relat. Mater. 89, 322–329. https://doi.org/10.1016/j.diamond.2018.09.010

Gurney, J.J., 1986. Diamonds, in: International Kimberlite Conference: Extended Abstracts. pp. 363–367.

Hainschwang, T., Notari, F., Fritsch, E., Massi, L., 2006. Natural, untreated diamonds showing the A, B and C infrared absorptions (“ABC diamonds”), and the H2 absorption. Diam. Relat. Mater. 15, 1555–1564. https://doi.org/10.1016/j.diamond.2005.12.029

Hainschwang, T., Simic, D., Fritsch, E., Deljanin, B., Woodring, S., DelRe, N., 2005. A gemological study of a collection of chameleon diamonds. Gems Gemol. 41, 20–35. https://doi.org/10.5741/GEMS.41.1.20

Hanley, P.L., Kiflawi, I., Lang, A.R., 1977. On topographically identifiable sources of cathodoluminescence in natural diamonds. Philos. Trans. R. Soc. London. Ser. A, Math. Phys. Sci. 284, 329–368. https://doi.org/10.1098/rsta.1977.0012

Harley, S.L., 1984. An experimental study of the partitioning of Fe and Mg between garnet and orthopyroxene. Contrib. to Mineral. Petrol. 86, 359–373. https://doi.org/10.1007/BF01187140

Harris, J., Hutchison, M.T., Hursthouse, M., Light, M., Harte, B., 1997. A new tetragonal silicate mineral occurring as inclusions in lower-mantle diamonds. Nature 387, 486–488. https://doi.org/10.1038/387486a0

Harte, B., 2010. Diamond formation in the deep mantle: the record of mineral inclusions and their distribution in relation to mantle dehydration zones. Mineral. Mag. 74, 189–215. https://doi.org/10.1180/minmag.2010.074.2.189

Harte, B., 1994. Lower Mantle Mineral Associations Preserved in Diamonds. Mineral. Mag. 58A, 384–385. https://doi.org/10.1180/minmag.1994.58A.1.201

Hirsch, P.B., Hutchison, J.L., Titchmarsh, J., 1986. Voidites in diamond Evidence for a crystalline phase containing nitrogen. Philos. Mag. A Phys. Condens. Matter, Struct. Defects Mech. Prop. 54, 93-L54. https://doi.org/10.1080/01418618608242890

Hirschmann, M.M., 2006. Water, Melting, and the Deep Earth H2O Cycle. Annu. Rev. Earth Planet. Sci. 34, 629–653. https://doi.org/10.1146/annurev.earth.34.031405.125211

Hirschmann, M.M., Aubaud, C., Withers, A.C., 2005. Storage capacity of H2O in nominally anhydrous minerals in the upper mantle. Earth Planet. Sci. Lett. 236, 167–181. https://doi.org/10.1016/j.epsl.2005.04.022

Hogberg, K., Stachel, T., Stern, R.A., 2016. Carbon and nitrogen isotope systematics in diamond: Different sensitivities to isotopic fractionation or a decoupled origin? Lithos 265, 16–30. https://doi.org/10.1016/j.lithos.2016.06.020

Hudson, P.R.W., Tsong, I.S.T., 1977. Hydrogen impurity in natural gem diamond, JOURNAL OF MATERIALS SCIENCE.

Humble, P., 1982. The structure and mechanism of formation of platelets in natural type Ia diamond. Proc. R.

Soc. London. A. Math. Phys. Sci. 381, 65–81. https://doi.org/10.1098/rspa.1982.0059

Hunt, L., Stachel, T., Morton, R., Grütter, H., Creaser, R.A., 2009. The Carolina kimberlite, Brazil - Insights into an unconventional diamond deposit. Lithos 112, 843–851. https://doi.org/10.1016/j.lithos.2009.04.018

Hutton, L.A., Iacobini, J.G., Bitziou, E., Channon, R.B., Newton, M.E., Macpherson, J. V, 2013. Examination of the Factors Affecting the Electrochemical Performance of Oxygen-Terminated Polycrystalline Boron-Doped Diamond Electrodes. https://doi.org/10.1021/ac401042t

Iakoubovskii, K., Adriaenssens, G.., 2002. Optical characterization of natural Argyle diamonds. Diam. Relat. Mater. 11, 125–131. https://doi.org/10.1016/S0925-9635(01)00533-7

Irifune, T., Kurio, A., Sakamoto, S., Inoue, T., Sumiya, H., Funakoshi, K. ichi, 2004. Formation of pure polycrystalline diamond by direct conversion of graphite at high pressure and high temperature. Phys. Earth Planet. Inter. 143, 593–600. https://doi.org/10.1016/j.pepi.2003.06.004

Izraeli, E.S., Harris, J.W., Navon, O., 2004. Fluid and mineral inclusions in cloudy diamonds from Koffiefontein, South Africa. Geochim. Cosmochim. Acta 68, 2561–2575. https://doi.org/10.1016/j.gca.2003.09.005

Izraeli, E.S., Harris, J.W., Navon, O., 2001. Brine inclusions in diamonds: a new upper mantle fluid. Earth Planet. Sci. Lett. 187, 323–332. https://doi.org/10.1016/S0012-821X(01)00291-6

Jablon, B.M., Navon, O., 2016. Most diamonds were created equal, Earth and Planetary Science Letters. https://doi.org/10.1016/j.epsl.2016.03.013

Jambon, A., Zimmermann, J.L., 1990. Water in oceanic basalts: evidence for dehydration of recycled crust. Earth Planet. Sci. Lett. 101, 323–331. https://doi.org/10.1016/0012-821X(90)90163-R

Jelezko, F., Gaebel, T., Popa, I., Domhan, M., Gruber, A., Wrachtrup, J., 2004. Observation of coherent oscillation of a single nuclear spin and realization of a two-qubit conditional quantum gate. Phys. Rev. Lett. 93, 130501. https://doi.org/10.1103/PhysRevLett.93.130501

Johnston, K., Mainwood, A., 2003. Properties of nickel nitrogen complexes in diamond: Stability and electronic structure. Diam. Relat. Mater. 12, 516–520. https://doi.org/10.1016/S0925-9635(02)00389-8

Kaiser, W., Bond, W.L., 1959. Nitrogen, A Major Impurity in Common Type I Diamond. Phys. Rev. 115, 857–863. https://doi.org/10.1103/PhysRev.115.857

Kanda, H., Watanabe, K., 1999. Distribution of nickel related luminescence centers in HPHT diamond. Diam. Relat. Mater. 8, 1463–1469. https://doi.org/http://dx.doi.org/10.1016/S0925-9635(99)00070-9

Kanda, H., Watanabe, K., 1997. Distribution of the cobalt-related luminescence center in HPHT diamond. Diam. Relat. Mater. 6, 708–711. https://doi.org/10.1016/s0925-9635(96)00666-8

Kelley, S.P., Wartho, J.A., 2000. Rapid kimberlite ascent and the significance of Ar-Ar ages in xenolith phlogopites. Science (80-.). 289, 609–611. https://doi.org/10.1126/science.289.5479.609

Kiflawi, I., Bruley, J., 2000. The nitrogen aggregation sequence and the formation of voidites in diamond. Diam. Relat. Mater. 9, 87–93. https://doi.org/10.1016/S0925-9635(99)00265-4

Kiflawi, I., Fisher, D., Kanda, H., Sittas, G., 1996. The creation of the 3107 cm−1 hydrogen absorption peak in synthetic diamond single crystals. Diam. Relat. Mater. 5, 1516–1518. https://doi.org/http://dx.doi.org/10.1016/S0925-9635(96)00568-7

Kiflawi, I., Mayer, A.E., Spear, P.M., Van Wyk, J.A., Woods, G.S., 1994. Infrared absorption by the single nitrogen and a defect centres in diamond. Philos. Mag. B Phys. Condens. Matter; Stat. Mech. Electron. Opt. Magn. Prop. 69, 1141–1147. https://doi.org/10.1080/01418639408240184

Klein-BenDavid, O., Izraeli, E.S., Hauri, E., Navon, O., 2007. Fluid inclusions in diamonds from the Diavik mine, Canada and the evolution of diamond-forming fluids. Geochim. Cosmochim. Acta 71, 723–744. https://doi.org/10.1016/j.gca.2006.10.008

Klein-BenDavid, O., Logvinova, A.M., Schrauder, M., Spetius, Z. V., Weiss, Y., Hauri, E.H., Kaminsky, F. V., Sobolev, N. V., Navon, O., 2009. High-Mg carbonatitic microinclusions in some Yakutian diamonds-a

new type of diamond-forming fluid. Lithos 112, 648–659. https://doi.org/10.1016/j.lithos.2009.03.015

Koga, K., Hauri, E., Hirschmann, M., Bell, D., 2003. Hydrogen concentration analyses using SIMS and FTIR: Comparison and calibration for nominally anhydrous minerals. Geochemistry, Geophys. Geosystems 4. https://doi.org/10.1029/2002GC000378

Koga, K.T., Van Orman, J.A., Walter, M.J., 2003. Diffusive relaxation of carbon and nitrogen isotope heterogeneity in diamond: a new thermochronometer. Phys. Earth Planet. Inter. 139, 35–43. https://doi.org/10.1016/S0031-9201(03)00141-9

Kohlstedt, D.L., Keppler, H., Rubie, D.C., 1996. Solubility of water in the α, β and γ phases of (Mg,Fe) 2 SiO 4. Contrib. to Mineral. Petrol. 123, 345–357. https://doi.org/10.1007/s004100050161

Kohn, S.C., Speich, L., Smith, C.B., Bulanova, G.P., 2016. FTIR thermochronometry of natural diamonds: A closer look. Lithos 265, 148–158. https://doi.org/10.1016/j.lithos.2016.09.021

Kramers, J.D., 1979. Lead, uranium, strontium, potassium and rubidium in inclusion-bearing diamonds and mantle-derived xenoliths from Southern Africa. Earth Planet. Sci. Lett. 42, 58–70. https://doi.org/10.1016/0012-821X(79)90190-0

Krebs, M.Y., Pearson, D.G., Stachel, T., Laiginhas, F., Woodland, S., Chinn, I., Kong, J., 2019. A common parentage-low abundance trace element data of gem diamonds reveals similar fluids to fibrous diamonds. Lithos 324–325, 356–370. https://doi.org/10.1016/j.lithos.2018.11.025

Krogh, E.J., 1988. The garnet-clinopyroxene Fe-Mg geothermometer - a reinterpretation of existing experimental data. Contrib. to Mineral. Petrol. 99, 44–48. https://doi.org/10.1007/BF00399364

Lai, M.Y., Breeding, C.M., Stachel, T., Stern, R.A., 2019. Spectroscopic features of natural and HPHT-treated yellow diamonds. Diam. Relat. Mater. 107642. https://doi.org/10.1016/j.diamond.2019.107642

Lanford, W.A., 1992. Analysis for Hydrogen By Nuclear-Reaction and Energy Recoil Detection. Nucl. Instruments Methods Phys. Res. Sect. B-Beam Interact. with Mater. Atoms 66, 65–82.

Lang, A.R., 1977. Defects in natural diamonds: Recent observations by new methods. J. Cryst. Growth 42, 625–631. https://doi.org/10.1016/0022-0248(77)90258-5

Lang, A.R., 1974a. Glimpses into the growth history of natural diamonds. J. Cryst. Growth 24–25, 108–115. https://doi.org/10.1016/0022-0248(74)90287-5

Lang, A.R., 1974b. Glimpses into the growth history of natural diamonds. J. Cryst. Growth 24–25, 108–115. https://doi.org/10.1016/0022-0248(74)90287-5

Lang, A.R., Yelisseyev, A.P., Pokhilenko, N.P., Steeds, J.W., Wotherspoon, A., 2004. Is dispersed nickel in natural diamonds associated with cuboid growth sectors in diamonds that exhibit a history of mixed-habit growth? J. Cryst. Growth 263, 575–589. https://doi.org/10.1016/j.jcrysgro.2003.11.116

Lewis, H.C., 1887. IV.—On a Diamantiferous Peridotite and the Genesis of the Diamond. Geol. Mag. 4, 22–24. https://doi.org/10.1017/S0016756800188399

Liggins, S., 2010. Identification of point defects in treated single crystal diamond.

Lindblom, J., Hölsä, J., Papunen, H., Häkkänen, H., 2005. Luminescence study of defects in synthetic as-grown and HPHT diamonds compared to natural diamonds. Am. Mineral. 90, 428–440. https://doi.org/10.2138/am.2005.1681

Logvinova, A.M., Taylor, L.A., Fedorova, E.N., Yelisseyev, A.P., Wirth, R., Howarth, G., Reutsky, V.N., Sobolev, N.V., 2015. A unique diamondiferous peridotite xenolith from the Udachnaya kimberlite pipe, Yakutia: role of subduction in diamond formation. Russ. Geol. Geophys. 56, 306–320. https://doi.org/10.1016/j.rgg.2015.01.022

Luth, R.W., Stachel, T., 2014. The buffering capacity of lithospheric mantle: implications for diamond formation. Contrib. to Mineral. Petrol. 168, 1083. https://doi.org/10.1007/s00410-014-1083-6

Luth, R.W., Virgo, D., Boyd, F.R., Wood, B.J., 1990. Ferric iron in mantle-derived garnets - Implications for thermobarometry and for the oxidation state of the mantle. Contrib. to Mineral. Petrol. 104, 56–72. https://doi.org/10.1007/BF00310646

Mainwood, A., 1994. Nitrogen and nitrogen-vacancy complexes and their formation in diamond. Phys. Rev. B 49, 7934–7940. https://doi.org/10.1103/PhysRevB.49.7934

Mainwood, A., 1979. Substitutional impurities in diamond. J. Phys. C Solid State Phys. 12, 2543–2549. https://doi.org/10.1088/0022-3719/12/13/018

Malogolovets, V.G., Vishnevskii, A.S., Camoilovich, M.I., 1979. IR Spectroscopy and Cathodoluminescence of Synthetic Semiconducting Diamonds. Dokl. Akad. Nauk SSSRAN UkrSSR 366–370.

Matjuschkin, V., Woodland, A.B., Frost, D.J., Yaxley, G.M., 2020. Reduced methane-bearing fluids as a source for diamond. https://doi.org/10.1038/s41598-020-63518-2

McCollom, T.M., Shock, E.L., 1998. Fluid-rock interactions in the lower oceanic crust: Thermodynamic models of hydrothermal alteration. J. Geophys. Res. Solid Earth 103, 547–575. https://doi.org/10.1029/97jb02603

Melton, C.E., Giardini, A.A., 1975. Experimental results and a theoretical interpretation of gaseous inclusions found in Arkansas natural diamonds. Am. Mineral. J. Earth Planet. Mater. 60, 413–417.

Melton, C.E., Giardini, A.A., 1974. The composition and significance of gas released from natural diamonds from Africa and Brazil. Am. Mineral. J. Earth Planet. Mater. 59, 775–782.

Melton, G.L., 2013. Elemental impurities , defects and carbon isotopes in mantle diamond.

Melton, G.L., Stachel, T., Stern, R.A., Carlson, J., Harris, J.W., 2013. Infrared spectral and carbon isotopic characteristics of micro- and macro-diamonds from the Panda kimberlite (Central Slave Craton, Canada). Lithos 177, 110–119. https://doi.org/10.1016/j.lithos.2013.06.019

Mendelssohn, M.J., Milledge, H.J., 1995. Geologically Significant Information from Routine Analysis of the Mid-Infrared Spectra of Diamonds. Int. Geol. Rev. 37, 95–110. https://doi.org/10.1080/00206819509465395

Moser, M., Reichart, P., Bergmaier, A., Greubel, C., Schiettekatte, F., Dollinger, G., 2016. Hydrogen analysis depth calibration by CORTEO Monte-Carlo simulation. Nucl. Instruments Methods Phys. Res. Sect. B Beam Interact. with Mater. Atoms 371, 161–166. https://doi.org/10.1016/j.nimb.2015.09.069

Nadolinny, V.A., Shatsky, V.S., Yuryeva, O.P., Rakhmanova, M.I., Yu Komarovskikh, A., Kalinin, A.A., Palyanov, Y.N., 2020. Formation features of N 3 V centers in diamonds from the Kholomolokh placer in the Northeast Siberian Craton 47, 4. https://doi.org/10.1007/s00269-019-01070-w

Nadolinny, V.A., Yelisseyev, A.P., 1994. New paramagnetic centres containing nickel ions in diamond. Diam. Relat. Mater. 3, 17–21. https://doi.org/10.1016/0925-9635(94)90024-8

Nadolinny, V.A., Yelisseyev, A.P., Baker, J.M., Newton, M.E., Twitchen, D.J., Lawson, S.C., Yuryeva, O.P., Feigelson, B.N., 1999. A study of 13 C hyperfine structure in the EPR of nickel-nitrogen-containing centres in diamond and correlation with their optical properties. J. Phys. Condens. Matter 11, 7357–7376. https://doi.org/10.1088/0953-8984/11/38/314

Nadolinny, V.A., Yelisseyev, A.P., Yuryeva, O.P., Feygelson, B.N., 1997. EPR study of the transformations in nickel containing centres at heated synthetic diamonds. Appl. Magn. Reson. 12, 543–554. https://doi.org/10.1007/BF03164134

Nadolinny, V.A., Yurjeva, O.P., Pokhilenko, N.P., 2009. EPR and luminescence data on the nitrogen aggregation in diamonds from Snap Lake dyke system. Lithos 112, 865–869. https://doi.org/10.1016/j.lithos.2009.05.045

Navon, O., Hutcheon, I.D., Rossman, G.R., Wasserburg, G.J., 1988. Mantle-derived fluids in diamond micro-inclusions. Nature 335, 784–789. https://doi.org/10.1038/335784a0

Navon, O., Wirth, R., Schmidt, C., Jablon, B.M., Schreiber, A., Emmanuel, S., 2017. Solid molecular nitrogen (δ-N2) inclusions in Juina diamonds: Exsolution at the base of the transition zone. Earth Planet. Sci. Lett. 464, 237–247. https://doi.org/10.1016/j.epsl.2017.01.035

Nestola, F., Smyth, J.R., 2016. Diamonds and water in the deep Earth: a new scenario. Int. Geol. Rev. 58, 263–276. https://doi.org/10.1080/00206814.2015.1056758

Newton, M.E., 2006. EPR, ENDOR and EPR Imaging of Defects in Diamond, in: Gilbert, B.C., Davies, M.B.,

Murphy, D.M. (Eds.), Electron Paramagnetic Resonance: Volume 20. pp. 131–156. https://doi.org/10.1039/9781847557568-00131

Nikkinen, J., Savitski, V., Reilly, S., Dziechciarczyk, L., Harkonen, A., Kemp, A., Guina, M., 2018. Sub-100 ps Monolithic Diamond Raman Laser Emitting at 573 nm. IEEE Photonics Technol. Lett. 30, 981–984. https://doi.org/10.1109/LPT.2018.2806183

Nimis, P., Grütter, H., 2010. Internally consistent geothermometers for garnet peridotites and pyroxenites. Contrib. to Mineral. Petrol. 159, 411–427. https://doi.org/10.1007/s00410-009-0455-9

Nimis, P., Taylor, W.R., 2000. Single clinopyroxene thermobarometry for garnet peridotites. Part I. Calibration and testing of a Cr-in-Cpx barometer and an enstatite-in-Cpx thermometer. Contrib. to Mineral. Petrol. 139, 541–554. https://doi.org/10.1007/s004100000156

O'Neill, H.S.C., Wood, B.J., 1979. An experimental study of Fe-Mg partitioning between garnet and olivine and its calibration as a geothermometer. Contrib. to Mineral. Petrol. 70, 59–70. https://doi.org/10.1007/BF00371872

Ohtani, E., 2015. Hydrous minerals and the storage of water in the deep mantle. Chem. Geol. 418, 6–15. https://doi.org/10.1016/j.chemgeo.2015.05.005

Palot, M., Pearson, D.G., Stachel, T., Harris, J.W., Bulanova, G.P., Chinn, I., 2013. Multiple Growth Episodes or Prolonged Formation of Diamonds? Inferences from Infrared Absorption Data, in: Proceedings of 10th International Kimberlite Conference. Springer India, New Delhi, pp. 281–296. https://doi.org/10.1007/978-81-322-1170-9_18

Parman, S.W., Kurz, M.D., Hart, S.R., Grove, T.L., 2005. Helium solubility in olivine and implications for high 3He/ 4He in ocean island basalts. Nature 437, 1140–1143. https://doi.org/10.1038/nature04215

Pearson, D.G., Brenker, F.E., Nestola, F., McNeill, J., Nasdala, L., Hutchison, M.T., Matveev, S., Mather, K., Silversmit, G., Schmitz, S., Vekemans, B., Vincze, L., 2014. Hydrous mantle transition zone indicated by ringwoodite included within diamond. Nature 507, 221–224. https://doi.org/10.1038/nature13080

Peslier, A.H., Woodland, A.B., Wolff, J.A., 2008. Fast kimberlite ascent rates estimated from hydrogen diffusion profiles in xenolithic mantle olivines from southern Africa. Geochim. Cosmochim. Acta 72, 2711–2722. https://doi.org/10.1016/j.gca.2008.03.019

Prado, C., Wilkins, S.J., Gründler, P., Marken, F., Compton, R.G., 2003. Electrodeposition of Lead at Boron-Doped Diamond Film Electrodes: Effect of Temperature. Electroanalysis 15, 1011–1016. https://doi.org/10.1002/elan.200390121

Pritchard, R.E., Ashwin, M.J., Tucker, J.H., Newman, R.C., 1998. Isolated interstitial hydrogen molecules in hydrogenated crystalline silicon. Phys. Rev. B 57, R15048–R15051. https://doi.org/10.1103/PhysRevB.57.R15048

Rakhmanova, M.I., Nadolinny, V.A., Yuryeva, O.P., Pokhilenko, N.P., Logvinova, A.M., 2015. Peculiarities of nitrogen impurity aggregation in diamonds from the Sytykanskaya pipe, Yakutia. Eur. J. Mineral. 27, 51–56. https://doi.org/10.1127/ejm/2014/0026-2413

Read, T.L., Cobb, S.J., Macpherson, J. V., 2019. An sp 2 Patterned Boron Doped Diamond Electrode for the Simultaneous Detection of Dissolved Oxygen and pH. ACS Sensors 4, 756–763. https://doi.org/10.1021/acssensors.9b00137

Reddy, S.M., Saxey, D.W., Rickard, W.D.A., Fougerouse, D., Montalvo, S.D., Verberne, R., Riessen, A., 2020. Atom Probe Tomography: Development and Application to the Geosciences. Geostand. Geoanalytical Res. 44, 5–50. https://doi.org/10.1111/ggr.12313

Reichart, P., 2004. Three-Dimensional Hydrogen Microscopy in Diamond. Science (80-.). 306, 1537–1540. https://doi.org/10.1126/science.1102910

Reichart, P., Dollinger, G., 2009. Hydrogen analysis by proton-proton scattering. Handb. Mod. Ion Beam Mater. Anal. 187–205.

Reichart, P., Dollinger, G., Bergmaier, A., Datzmann, G., Hauptner, A., Körner, H.-J., Krücken, R., 2004. 3D hydrogen microscopy with sub-ppm detection limit. Nucl. Instruments Methods Phys. Res. Sect. B Beam

Interact. with Mater. Atoms 219–220, 980–987. https://doi.org/10.1016/j.nimb.2004.01.200

Reichart, P., Dollinger, G., Bergmaier, A., Datzmann, G., Hauptner, A., Körner, H.J., 2002. Sensitive 3D hydrogen microscopy by proton proton scattering. Nucl. Instruments Methods Phys. Res. Sect. B Beam Interact. with Mater. Atoms 197, 134–149. https://doi.org/10.1016/S0168-583X(02)01479-9

Reinitz, I.M., Buerki, P.R., Shigley, J.E., McClure, S.F., Moses, T.M., 2000. Identification of HPHT-Treated Yellow to Green Diamonds. Gems Gemol. 36, 128–137. https://doi.org/10.5741/GEMS.36.2.128

Robertson, R., Fox, J.J., Martin, A.E., 1933. Two types of diamond. Philos. Trans. R. Soc. London. Ser. A, Contain. Pap. a Math. or Phys. Character 232, 463–535. https://doi.org/10.1098/rsta.1934.0013

Rondeau, B., Fritsch, E., Guiraud, M., Chalain, J.-P., Notari, F., 2004. Three historical 'asteriated' hydrogen-rich diamonds: growth history and sector-dependent impurity incorporation. Diam. Relat. Mater. 13, 1658–1673. https://doi.org/10.1016/j.diamond.2004.02.002

Ros, L., Kristiansson, P., Borysiuk, M., Abdel, N., Elfman, M., Nilsson, E.J.C., Pallon, J., 2015. Deuterium/hydrogen microscopy in astrogeological material using an elastic recoil approach. Nucl. Instruments Methods Phys. Res. Sect. B Beam Interact. with Mater. Atoms 348, 273–277. https://doi.org/10.1016/j.nimb.2014.12.038

Rosenhauer, M., Woermann, E., Knecht, B., Ulmer, C., 2019. The stability of graphite and diamond as a function of the oxygen fugasity in the mantle, in: International Kimberlite Conference Extended Abstracts: 1977. University of Alberta, pp. 285–287. https://doi.org/10.29173/ikc1048

Rudloff-Grund, J., Brenker, F.E., Marquardt, K., Howell, D., Schreiber, A., O'Reilly, S.Y., Griffin, W.L., Kaminsky, F. V., 2016. Nitrogen nanoinclusions in milky diamonds from Juina area, Mato Grosso State, Brazil. Lithos 265, 57–67. https://doi.org/10.1016/j.lithos.2016.09.022

Runciman, W.A., Carter, T., 1971. High resolution infra-red spectra of diamond. Solid State Commun. 9, 315–317. https://doi.org/10.1016/0038-1098(71)90001-9

Rupertus, V., 2011. Ion Beam Spectrochemical Analysis (IBSCA), in: Surface and Thin Film Analysis: A Compendium of Principles, Instrumentation, and Applications, Second Edition. Wiley-VCH, Weinheim, Germany, pp. 357–366. https://doi.org/10.1002/9783527636921.ch22

Saguy, C., 2004. Diffusion of Light Elements in Diamond. Defect Diffus. Forum 226–228, 31–48. https://doi.org/10.4028/www.scientific.net/DDF.226-228.31

Saguy, C., Cytermann, C., Fizgeer, B., Richter, V., Avigal, Y., Moriya, N., Kalish, R., Mathieu, B., Deneuville, A., 2003. Diffusion of hydrogen in undoped, p-type and n-type doped diamonds. Diam. Relat. Mater. 12, 623–631. https://doi.org/10.1016/S0925-9635(02)00403-X

Satoh, S., Sumiya, H., 1995. Synthesis of High Purity Diamond Single Crystal. Rev. High Press. Sci. Technol. 4, 308–314.

Schirhagl, R., Raatz, N., Meijer, J., Markham, M., Gerstl, S.S.A., Degen, C.L., 2015. Nanometer-scale isotope analysis of bulk diamond by atom probe tomography. Diam. Relat. Mater. 60, 60–65. https://doi.org/10.1016/j.diamond.2015.10.016

Sellschop, J.P.F., Connell, S.H., Madiba, C.C.P., Sideras-Haddad, E., Stemmet, M.C., Bharuth-Ram, K., Appel, H., Kundig, W., Patterson, B., Holzschuh, E., 1992. Hydrogen in and on natural and synthetic diamond. Nucl. Instruments Methods Phys. Res. Sect. B Beam Interact. with Mater. Atoms 68, 133–140. https://doi.org/10.1016/0168-583X(92)96064-6

Seshadri, K.S., Jones, R.N., 1963. The shapes and intensities of infrared absorption bands-A review. Spectrochim. Acta 19, 1013–1085. https://doi.org/10.1016/0371-1951(63)80187-3

Shirey, S.B., Cartigny, P., Frost, D.J., Keshav, S., Nestola, F., Nimis, P., Pearson, D.G., Sobolev, N. V., Walter, M.J., 2013. Diamonds and the Geology of Mantle Carbon. Rev. Mineral. Geochemistry 75, 355–421. https://doi.org/10.2138/rmg.2013.75.12

Sideras-Haddad, E., Connell, S.., Sellschop, J.P.., Machi, I.., Rebuli, D., Maclear, R.., Doyle, B.., 2001. Hydrogen and oxygen chemistry and dynamics in diamond studied by nuclear microscopic techniques. Nucl. Instruments Methods Phys. Res. Sect. B Beam Interact. with Mater. Atoms 181, 419–425.

https://doi.org/10.1016/S0168-583X(01)00595-X

Sittas, G., Kanda, H., Kiflawi, I., Spear, P.M., 1996. Growth and characterization of Si-doped diamond single crystals grown by the HTHP method. Diam. Relat. Mater. 5, 866–869. https://doi.org/10.1016/0925-9635(95)00449-1

Smit, K. V., Shirey, S.B., Stern, R.A., Steele, A., Wang, W., 2016a. Diamond growth from C–H–N–O recycled fluids in the lithosphere: Evidence from CH4 micro-inclusions and δ13C–δ15N–N content in Marange mixed-habit diamonds. Lithos. https://doi.org/10.1016/j.lithos.2016.03.015

Smit, K. V., Shirey, S.B., Stern, R.A., Steele, A., Wang, W., 2016b. Diamond growth from C–H–N–O recycled fluids in the lithosphere: Evidence from CH4micro-inclusions and δ13C–δ15N–N content in Marange mixed-habit diamonds. Lithos 265, 68–81. https://doi.org/10.1016/j.lithos.2016.03.015

Smith, E.M., Kopylova, M.G., Frezzotti, M.L., Afanasiev, V.P., 2015. Fluid inclusions in Ebelyakh diamonds: Evidence of CO2 liberation in eclogite and the effect of H2O on diamond habit. Lithos 216–217, 106–117. https://doi.org/10.1016/J.LITHOS.2014.12.010

Smith, E.M., Shirey, S.B., Richardson, S.H., Nestola, F., Bullock, E.S., Wang, J., Wang, W., 2018. Blue boron-bearing diamonds from Earth's lower mantle. Nature 560, 84–87. https://doi.org/10.1038/s41586-018-0334-5

Smith, W. V., Sorokin, P.P., Gelles, I.L., Lasher, G.J., 1959. Electron-spin resonance of nitrogen donors in diamond. Phys. Rev. 115, 1546–1552. https://doi.org/10.1103/PhysRev.115.1546

Sobolev, N. V, YG, L., LN, P., Sobolev, E. V, 1969. Chrome pyropes from Yakutian diamonds. Dokl. Akad. Nauk SSSR 189, 162-+.

Socrates, G., 2004. Infrared and Raman characteristic group frequencies: tables and charts. John Wiley & Sons.

Sokol, A.G., Palyanov, Y., Tomilenko, A.A., 2004. Diamond Crystallization in Fluid and Carbonate–Fluid Systems under Mantle P–T Conditions: 1. Fluid Composition, Translated from Geokhimiya.

Solin, S.A., 1972. Photoluminescence of natural type I and type IIb diamonds. Phys. Lett. A 38, 101–102. https://doi.org/http://dx.doi.org/10.1016/0375-9601(72)90506-3

Sparks, R.S.J., Baker, L., Brown, R.J., Field, M., Schumacher, J., Stripp, G., Walters, A., 2006. Dynamical constraints on kimberlite volcanism. J. Volcanol. Geotherm. Res. 155, 18–48. https://doi.org/10.1016/j.jvolgeores.2006.02.010

Speich, L., 2017. Platelets in diamond as a tool to decipher the thermal history of the lithospheric mantle.

Speich, L., Kohn, S.C., 2020. QUIDDIT - QUantification of Infrared active Defects in Diamond and Inferred Temperatures. Comput. Geosci. 104558. https://doi.org/10.1016/j.cageo.2020.104558

Speich, L., Kohn, S.C., Bulanova, G.P., Smith, C.B., 2018. The behaviour of platelets in natural diamonds and the development of a new mantle thermometer. Contrib. to Mineral. Petrol. 173, 39. https://doi.org/10.1007/s00410-018-1463-4

Speich, L., Kohn, S.C., Wirth, R., Bulanova, G.P., Smith, C.B., 2017. The relationship between platelet size and the B ′ infrared peak of natural diamonds revisited. Lithos 278–281, 419–426. https://doi.org/10.1016/j.lithos.2017.02.010

Stachel, T., Brey, G.P., Harris, J.W., 2005. Inclusions in Sublithospheric Diamonds: Glimpses of Deep Earth. Elements 1, 73–78. https://doi.org/10.2113/gselements.1.2.73

Stachel, T., Harris, J.W., 2008. The origin of cratonic diamonds — Constraints from mineral inclusions. Ore Geol. Rev. 34, 5–32. https://doi.org/10.1016/J.OREGEOREV.2007.05.002

Stachel, T., Harris, J.W., 1997. Diamond precipitation and mantle metasomatism - evidence from the trace element chemistry of silicate inclusions in diamonds from Akwatia, Ghana. Contrib. to Mineral. Petrol. 129, 143–154. https://doi.org/10.1007/s004100050328

Stachel, T., Luth, R.W., 2015. Diamond formation — Where, when and how? Lithos 220–223, 200–220. https://doi.org/10.1016/j.lithos.2015.01.028

Stagno, V., Ojwang, D.O., McCammon, C.A., Frost, D.J., 2013. The oxidation state of the mantle and the extraction of carbon from Earth's interior. Nature 493, 84–88. https://doi.org/10.1038/nature11679

Stepanov, A.S., Korsakov, A. V., Yuryeva, O.P., Nadolinniy, V.A., Perraki, M., De Gussem, K., Vandenabeele, P., 2011. Brown diamonds from an eclogite xenolith from Udachnaya kimberlite, Yakutia, Russia, in: Spectrochimica Acta - Part A: Molecular and Biomolecular Spectroscopy. pp. 41–48. https://doi.org/10.1016/j.saa.2011.01.006

Stepanov, F.A., Emelyanova, A.S., Rakevich, A.L., Mironov, V.P., Zedgenizov, D.A., Shatskiy, V.S., Martynovich, E.F., 2017. Localization of 523 and 794 Defects in Diamond. Izv. Ross. Akad. Nauk. Seriya Fiz. 81, 1220–1226. https://doi.org/10.3103/S1062873817090246

Sweeney, R.., Prozesky, V.., Viljoen, K.., Connell, S., 1999. The sensitive determination of H in diamond by infrared (FTIR) spectroscopy and micro-elastic-recoil (μ-ERDA) techniques. Nucl. Instruments Methods Phys. Res. Sect. B Beam Interact. with Mater. Atoms 158, 582–587. https://doi.org/10.1016/S0168-583X(99)00367-5

Taylor, W.R., Green, D.H., 1986. The role of reduced COH fluids in mantle partial melting, in: International Kimberlite Conference: Extended Abstracts. pp. 211–213.

Teukam, Z., Ballutaud, D., Jomard, F., Chevallier, J., Bernard, M., Deneuville, A., 2003. Trap limited diffusion of hydrogen in boron-doped diamond. Diam. Relat. Mater. 12, 647–651. https://doi.org/10.1016/S0925-9635(02)00240-6

Thomson, A.R., Kohn, S.C., Bulanova, G.P., Smith, C.B., Araujo, D., Walter, M.J., 2016. Trace element composition of silicate inclusions in sub-lithospheric diamonds from the juina-5 kimberlite: Evidence for diamond growth from slab melts. Lithos. https://doi.org/10.1016/j.lithos.2016.08.035

Thomson, A.R., Kohn, S.C., Bulanova, G.P., Smith, C.B., Araujo, D., Walter, M.J., Walter, M.J., 2014. Origin of sub-lithospheric diamonds from the Juina-5 kimberlite (Brazil): constraints from carbon isotopes and inclusion compositions. Contrib. to Mineral. Petrol. 168, 1081. https://doi.org/10.1007/s00410-014-1081-8

Titkov, S. V., Shigley, J.E., Breeding, C.M., Mineeva, R.M., Zudin, N.G., Sergeev, A.M., 2008. Natural-Color Purple Diamonds from Siberia. Gems Gemol. 44, 56–64. https://doi.org/10.5741/GEMS.44.1.56

Titus, E., Ali, N., Cabral, G., Madaleno, J.C., Neto, V.F., Gracio, J., Ramesh Babu, P., Sikder, A.K., Okpalugo, T.I., Misra, D.S., 2006. Nitrogen and hydrogen related infrared absorption in CVD diamond films. Thin Solid Films 515, 201–206. https://doi.org/10.1016/j.tsf.2005.12.062

Tomlinson, E.L., McMillan, P.F., Zhang, M., Jones, A.P., Redfern, S.A.T., 2007. Quartz-bearing C-O-H fluid inclusions diamond: Retracing the pressure-temperature path in the mantle using calibrated high temperature IR spectroscopy. Geochim. Cosmochim. Acta 71, 6030–6039. https://doi.org/10.1016/j.gca.2007.09.013

Tschauner, O., Huang, S., Greenberg, E., Prakapenka, V.B., Ma, C., Rossman, G.R., Shen, A.H., Zhang, D., Newville, M., Lanzirotti, A., Tait, K., 2018. Ice-VII inclusions in diamonds: Evidence for aqueous fluid in Earth's deep mantle. Science (80-.). 359, 1136–1139. https://doi.org/10.1126/science.aao3030

Tsong, I.S.T., McLaren, A.G., 1975. An ion beam spectrochemical analyser with application to the analysis of silicate minerals. Spectrochim. Acta Part B At. Spectrosc. 30, 343–351. https://doi.org/10.1016/0584-8547(75)80032-2

Uzan-Saguy, C., Reznik, A., Cytermann, C., Brener, R., Kalish, R., Bustarret, E., Bernard, M., Deneuville, A., Gheeraert, E., Chevallier, J., 2001. Hydrogen diffusion in B-ion-implanted and B-doped homo-epitaxial diamond: Passivation of defects vs. passivation of B acceptors. Diam. Relat. Mater. 10, 453–458. https://doi.org/10.1016/S0925-9635(00)00568-9

van der Bogert, C.H., Smith, C.P., Hainschwang, T., McClure, S.F., 2009. Gray-to-Blue-to-Violet Hydrogen-Rich Diamonds from The Argyle Mine, Australia. Gems Gemol. 45, 20–37. https://doi.org/10.5741/GEMS.45.1.20

Vasilev, E., Petrovsky, V., Kozlov, A., Antonov, A., Kudryavtsev, A., Orekhova, K., 2019. The story of one diamond: the heterogeneous distribution of the optical centres within a diamond crystal from the Ichetju placer, northern Urals. Mineral. Mag. 83, 515–522. https://doi.org/10.1180/mgm.2019.32

Vasilev, E.A., Zedgenizov, D.A., Klepikov, I. V, 2020. The enigma of cuboid diamonds: the causes of inverse distribution of optical centers within the growth zones. A.P. Karpinsky Russ. Geol. Res. Inst. 65, 59–70. https://doi.org/10.3190/jgeosci.301

Vins, V.G., Kononov, O. V., 2003. A model of HPHT color enhancement mechanism in natural gray diamonds. Diam. Relat. Mater. 12, 542–545. https://doi.org/10.1016/S0925-9635(03)00062-1

Virtanen, P., Gommers, R., Oliphant, T.E., Haberland, M., Reddy, T., Cournapeau, D., Burovski, E., Peterson, P., Weckesser, W., Bright, J., van der Walt, S.J., Brett, M., Wilson, J., Millman, K.J., Mayorov, N., Nelson, A.R.J., Jones, E., Kern, R., Larson, E., Carey, C.J., Polat, İ., Feng, Y., Moore, E.W., VanderPlas, J., Laxalde, D., Perktold, J., Cimrman, R., Henriksen, I., Quintero, E.A., Harris, C.R., Archibald, A.M., Ribeiro, A.H., Pedregosa, F., van Mulbregt, P., Vijaykumar, A., Bardelli, A. Pietro, Rothberg, A., Hilboll, A., Kloeckner, A., Scopatz, A., Lee, A., Rokem, A., Woods, C.N., Fulton, C., Masson, C., Häggström, C., Fitzgerald, C., Nicholson, D.A., Hagen, D.R., Pasechnik, D. V., Olivetti, E., Martin, E., Wieser, E., Silva, F., Lenders, F., Wilhelm, F., Young, G., Price, G.A., Ingold, G.L., Allen, G.E., Lee, G.R., Audren, H., Probst, I., Dietrich, J.P., Silterra, J., Webber, J.T., Slavič, J., Nothman, J., Buchner, J., Kulick, J., Schönberger, J.L., de Miranda Cardoso, J.V., Reimer, J., Harrington, J., Rodríguez, J.L.C., Nunez-Iglesias, J., Kuczynski, J., Tritz, K., Thoma, M., Newville, M., Kümmerer, M., Bolingbroke, M., Tartre, M., Pak, M., Smith, N.J., Nowaczyk, N., Shebanov, N., Pavlyk, O., Brodtkorb, P.A., Lee, P., McGibbon, R.T., Feldbauer, R., Lewis, S., Tygier, S., Sievert, S., Vigna, S., Peterson, S., More, S., Pudlik, T., Oshima, T., Pingel, T.J., Robitaille, T.P., Spura, T., Jones, T.R., Cera, T., Leslie, T., Zito, T., Krauss, T., Upadhyay, U., Halchenko, Y.O., Vázquez-Baeza, Y., 2020. SciPy 1.0: fundamental algorithms for scientific computing in Python. Nat. Methods 17, 261–272. https://doi.org/10.1038/s41592-019-0686-2

Walker, J., 1979. Optical absorption and luminescence in diamond. Reports Prog. Phys. 42, 1605. https://doi.org/10.1088/0034-4885/42/10/001

Wallace, P.J., 2003. From mantle to atmosphere: magma degassing, explosive eruptions, and volcanic volatile budgets. Dev. Volcanol. 5, 105–127. https://doi.org/10.1016/S1871-644X(03)80026-8

Watson, E.B., Brenan, J.M., 1987. Fluids in the lithosphere, 1. Experimentally-determined wetting characteristics of CO2H2O fluids and their implications for fluid transport, host-rock physical properties, and fluid inclusion formation. Earth Planet. Sci. Lett. 85, 497–515. https://doi.org/10.1016/0012-821X(87)90144-0

Wegdén, M., Kristiansson, P., Skogby, H., Auzelyte, V., Elfman, M., Malmqvist, K.G., Nilsson, C., Pallon, J., Shariff, A., 2005. Hydrogen depth profiling by p-p scattering in nominally anhydrous minerals, in: Nuclear Instruments and Methods in Physics Research, Section B: Beam Interactions with Materials and Atoms. North-Holland, pp. 524–529. https://doi.org/10.1016/j.nimb.2005.01.111

Weiss, Y., McNeill, J., Pearson, D.G., Nowell, G.M., Ottley, C.J., 2015. Highly saline fluids from a subducting slab as the source for fluid-rich diamonds. Nature 524, 339–342. https://doi.org/10.1038/nature14857

Welbourn, C.M., Rooney, M.-L.T., Evans, D.J.F., 1989. A study of diamonds of cube and cube-related shape from the Jwaneng mine. J. Cryst. Growth 94, 229–252. https://doi.org/10.1016/0022-0248(89)90622-2

Wentorf, R.H., 1971. Diamond growth rates. J. Phys. Chem. 75, 1833–1837. https://doi.org/10.1021/j100681a013

Willardson, R.K., Weber, E.R., Stavola, M., 1998. Identification of Defects in Semiconductors. Academic Press.

Woods, G.S., 1986. Platelets and the infrared Absorption of Type Ia Diamonds. Proc. R. Soc. A Math. Phys. Eng. Sci. 407, 219–238. https://doi.org/10.1098/rspa.1986.0094

Woods, G.S., Collins, A.T., 1983. Infrared absorption spectra of hydrogen complexes in type I diamonds. J. Phys. Chem. Solids 44, 471–475. https://doi.org/10.1016/0022-3697(83)90078-1

Yang, X., Keppler, H., Li, Y., 2016. Molecular hydrogen in mantle minerals. Lett. Geochemical Perspect. Lett. Geochem. Persp. Let 2, 160–168. https://doi.org/10.7185/geochemlet.1616

Yang, Z., Liang, R., Zeng, X., Peng, M., Mal´ymal´y, P., Misiewicz, J., Polimeni, A., 2012. A Microscopy and FTIR and PL Spectra Study of Polycrystalline Diamonds from Mengyin Kimberlite Pipes. Int. Sch. Res. Netw. ISRN Spectrosc. 2012. https://doi.org/10.5402/2012/871824

Yeliseyev, A.P., Nadolinnyy, V.A., 1992. New Nickel-Containing Paramagnetic Centers in Diamond, in:

Transactions (Doklady) of the Russian Academy of Sciences, Earth Science Sections. Scripta Technica Inc., p. 149.

Yelisseyev, A., Kanda, H., 2007. Optical Centers Related to 3d Transition Metals in Diamond, New Diamond and Frontier Carbon Technology.

Yelisseyev, A.P., Nadolinny, V.A., 1995. Photoinduced absorption lines related to nickel impurity in annealed synthetic diamonds. Diam. Relat. Mater. 4, 177–185. https://doi.org/10.1016/0925-9635(94)00240-1

Yuryeva, O.P., Rakhmanova, M.I., Zedgenizov, D.A., 2017. Nature of type IaB diamonds from the Mir kimberlite pipe (Yakutia): evidence from spectroscopic observation. Phys. Chem. Miner. https://doi.org/10.1007/s00269-017-0890-5

Zaitsev, A., 2000. Vibronic spectra of impurity-related optical centers in diamond. Phys. Rev. B - Condens. Matter Mater. Phys. 61, 12909–12922. https://doi.org/10.1103/PhysRevB.61.12909

Zaitsev, A.M., 2013. Optical properties of diamond: a data handbook. Springer Science & Business Media.

Zaitsev, A.M., 2001. Optical Properties of Diamond. Springer Berlin Heidelberg, Berlin, Heidelberg. https://doi.org/10.1007/978-3-662-04548-0

Zhang, C., Duan, Z., 2009. A model for C-O-H fluid in the Earth's mantle. Geochim. Cosmochim. Acta 73, 2089–2102. https://doi.org/10.1016/j.gca.2009.01.021

Zhu, C., Byrd, R.H., Lu, P., Nocedal, J., 1997. Algorithm 778: L-BFGS-B: Fortran Subroutines for Large-Scale Bound-Constrained Optimization. ACM Trans. Math. Softw. 23, 550–560. https://doi.org/10.1145/279232.279236